

Novel Surface-Volume-Surface Electric Field
Integral Equations for Electromagnetic Analysis of
3-D Metal-Dielectric Objects and \mathcal{H} -matrix
Strategies for Their Fast Direct Solution

by

Reza Gholami

A Thesis Submitted to the Faculty of Graduate Studies of

The University of Manitoba

in partial fulfilment of the requirements of the degree of

DOCTOR OF PHILOSOPHY

Department of Electrical and Computer Engineering

University of Manitoba

Winnipeg, Manitoba, Canada

Copyright © 2019 by Reza Gholami

Abstract

The hierarchical (\mathcal{H})-matrix acceleration method plays important role in electromagnetic analysis of large-scale problems. This thesis is about fast direct solution of 3-D full-wave scattering and radiation problems with \mathcal{H} -matrix acceleration of the method of moments (MoM) for the novel surface-volume-surface electric field integral equation (SVS-EFIE) and the Locally Corrected Nyström (LCN) method for traditional magnetic field integral equation (MFIE). Two new formulations of the SVS-EFIE are proposed. First, new SVS-EFIE formulation is developed for the scattering and radiation problems on metal-dielectric composite objects with arbitrary number of regions situated in free space. Second, new SVS-EFIE formulation is developed for scattering and radiation problems on dielectric-dielectric composite objects situated in multilayered medium. The proposed SVS-EFIE formulations introduce independent surface electric current density on the boundary of each region. Thus, in the new formulations, the scatterer regions can be meshed independently according to their local material properties. This improves the flexibility and efficiency of the proposed formulations in the analysis of both multiscale and large-scale composite structures. An \mathcal{H} -matrix based fast direct solution strategies are proposed for acceleration of the MoM solution of the new SVS-EFIE formulations. The method is largely insensitive to the poor conditioning of the MoM matrix equation. The required theory for applying \mathcal{H} -matrices to the new formulations as well as the construction of the block- \mathcal{H} -matrices pertinent to MoM discretization of the composite SVS-EFIE is described in details. Numerical validation shows that the proposed methods have a wide-range of applications and generate accurate results using only the small fraction of memory and total CPU time needed by conventional MoM solution of the SVS-EFIE. Fast error-controlled direct solution of the traditional integral equations for scattering problems on metal objects with \mathcal{H} -matrices is also pioneered in this work. The proposed strategy for acceleration of the higher-order LCN method with \mathcal{H} -matrices exhibits $O(h^p)$ error behaviour in the fast direct solution of the scattering problems on smooth metal objects with characteristic mesh elements size h and order of solution approximation p .

Acknowledgments

Firstly, I would like to express my sincere gratitude to my advisor, Dr. Vladimir Okhmatovski, for his continuous support and guidance in my PhD research, for his patience and motivation. I appreciate all his contributions of times, experts in the area of computational electromagnetics, and his ample knowledge. It has been a privilege to be his graduate student and I can not thank him enough. I would like to thank my co-advisor, Dr. David Barber, for his guidance and confidence in my research work.

I would like to thank my internal examining committee: Dr. Puyan Mojabi and Dr. Tim Papakyriakou for all their efforts in evaluation of my thesis as well as their comments and feedback.

I would also like to thank my external examiner Dr. Andrew F. Peterson from Georgia Institute of Technology for evaluation of this work.

Special thanks to my colleagues in the Computational Electromagnetics Group; Shucheng Zheng, Anton Menshov, Jamiu Mojolagbe, Dr. Ian Jeffrey, Zhuotong Chen, Dr. Farhad Sheikhhossieni, Jamil Feroj, Sikandar Hossein, Dr. Mohammad Shafiepour, Dr. Jonatan Aronsson, and Dr. Osman Goni for their collaborations and support.

I would like to extend my gratitude to the Natural Sciences and Engineering Research Council of Canada, University of Manitoba Faculty of Graduate Studies, the Center for Earth Observation Science (CEOS) for funding my research, and many thanks to Compute Canada for providing the computing resources throughout this research program.

Last but not the least, I would like to express my deepest gratitude to my family for their love and support throughout my PhD research. I would also like to thank my friends for all their support.

*To my Parents Parvaneh and Abbasali, my sister Parisa, and brother Peiman, and
my nephews Ashkan, Paya, and Shahan.*

Contributions

The author contributed to the following publications while working towards the PhD degree.

Articles in International Journals

- **Paper 1:** **R. Gholami**, S. Zheng, and V. Okhmatovski, “Surface-volume-surface EFIE for electromagnetic analysis of 3-D composite dielectric objects in multilayered media,” *IEEE J. Multiscale and Multiphys. Comput. Techn.*, Under Review.
- **Paper 2:** **R. Gholami** and V. Okhmatovski, “Surface-volume-surface EFIE formulation for fast direct solution of scattering problem on general 3-D composite metal-dielectric objects,” *IEEE Trans. Antennas Propag.*, to be published.
- **Paper 3:** **R. Gholami**, A. Menshov, and V. Okhmatovski, “ \mathcal{H} -matrix accelerated solution of surface-volume-surface EFIE for fast analysis of scattering on composite dielectric objects,” *IEEE J. Multiscale and Multiphys. Comput. Techn.*, vol. 4, no. 1, pp. 152–162, 2019.
- **Paper 4:** **R. Gholami**, J. Mojolagbe, A. Menshov, F. Sheikh Hosseini Lori, and V. Okhmatovski, “ \mathcal{H} -matrix arithmetic for fast direct and iterative method of moment solution of surface-volume-surface EFIE for 3-D radiation problems,” *Progress In Electromagnetics Research B*, vol. 82, pp. 189–210, 2018.
- **Paper 5:** S. Zheng, **R. Gholami**, and V. Okhmatovski, “Surface-volume-surface electric field integral equation for solution of scattering problems on 3-D dielectric objects in multilayered media,” *IEEE Trans. Microw. Theory Tech.* vol. 66, no. 12, pp. 5399–5414, Dec. 2018.
- **Paper 6:** Z. Chen, **R. Gholami**, J. Mojolagbe, and V. Okhmatovski, “Formulation of surface-volume-surface EFIE for solution of three-dimensional scattering problems on composite dielectric objects,” *IEEE Antennas Wireless Propag. Lett.* vol. 17, no. 6, pp. 1043–1047, Jun. 2018.

- **Paper 7:** F.L.S. Hosseini, A. Menshov, **R. Gholami**, J. Mojolagbe, and V. Okhmatovski, “Novel single-source integral equation for scattering problems by 3D dielectric objects,” *IEEE Trans. Antennas Propag.* vol. 66, no. 2, pp. 797–807, Feb. 2018.

Articles in Conferences Proceedings

- S. Zheng, **R. Gholami**, and V. Okhmatovski, “Surface-volume-surface EFIE for analysis of 3-D microwave circuits in multilayered substrate with finite dielectric inclusions”, in *IEEE Int. Microw. Symp. (IMS2020)*, submitted.
- **R. Gholami**, S. Zheng, and V. Okhmatovski, “Overview of surface-volume-surface electric field integral equation formulations for 3-D composite metal-dielectric objects,” in *IEEE Europ. Conf. Antennas and Propag. (EuCAP2020)*, accepted.
- A. Aljamal, **R. Gholami**, S. Zheng, and V. Okhmatovski, “Delta-gap source excitation model in surface-volume-surface electric field integral equation for 3-D interconnect characterization”, in *IEEE Electr. Perform. Electron. Packaging Systems (EPEPS)*, Montreal, Canada, Oct. 2019, to be published.
- **R. Gholami**, Z. Chen, and V. Okhmatovski, “On the error study of surface-volume-surface EFIE for solving the 3-D scattering problems on composite dielectric objects”, in *Proceedings of 18th Int. Symp. on Antenna Techn. and Applied Electromagn. (ANTEM)*, Waterloo, Canada, Aug. 2018, pp. 1-2.
- S. Zheng, **R. Gholami**, D. Isleifson, D. Barber, and V. Okhmatovski, “Analysis of scattering on arctic sea ice in C-Band with layered medium formulation of surface-volume-surface electric field integral equation”, in *USNC-URSI Radio Sci. Meet.* Boston, MA, Jul. 2018, pp. 1345-1346.
- Z. Chen, **R. Gholami**, and V. Okhmatovski, “Formulation of surface-volume-surface-EFIE for solution of 2-D scattering problems on composite dielectric objects under TM polarization”, in *USNC-URSI Radio Sci. Meet.* Boston, MA, Jul. 2018, pp. 2345-2346.
- J. Mojolagbe, **R. Gholami**, and V. Okhmatovski, “On complexity reduction in solution of scattering problems on well-conducting 3D objects with surface-volume-surface EFIE”, in *Appl. Comput. Electromag. Conf. (ACES)*, Denver, CO, March 2018. pp. 1-2.

Conferences Abstracts

- **R. Gholami**, Z. Chen, M. Shafieipour, and V. Okhmatovski, “Fast direct error-controlled solution of scattering problems via \mathcal{H} -matrix accelerated Locally Corrected Nyström discretization of combined field integral equation”, *Progress Electromagn. Research Symp. (PIERS)*, Xiamen, China, Dec. 2019, accepted.
- **R. Gholami**, S. Zheng, and V. Okhmatovski, “Surface-volume-surface electric field integral equation for solution of scattering problems on composite dielectric objects in stratified media,” *Progress Electromagn. Research Symp. (PIERS)*, Xiamen, China, Dec. 2019, accepted.
- **R. Gholami** and V. Okhmatovski, “Surface-volume-surface electric field integral equation for solution of scattering problems on 3-D composite metal-dielectric objects”, accepted and to be presented in *UNSC-URSI Radio Sci. Meet.*, Atlanta, GA, Jul. 2019.
- **R. Gholami**, S. Zheng, and V. Okhmatovski, “ \mathcal{H} -matrix accelerated MoM solution of surface-volume-surface electric field integral equation for scattering problems on homogeneous dielectric objects in multilayered medium”, in *IEEE MTT-S Int. Conf. Numerical Electromagn. Multiphys. Modeling Optimization (NEMO)*, Boston, MA, May 2019.
- **R. Gholami**, J. Mojolagbe, A. Menshov, F. L. S. Hosseini, and V. Okhmatovski, “Fast direct method of moments solution of surface-volume-surface integral equation with \mathcal{H} -matrix”, in *URSI Atlan. Radio Sci. Meet. (AT-RASC)*, Gran Canaria, Spain, Jun. 2018.
- **R. Gholami**, J. Mojolagbe, A. Menshov, and V. Okhmatovski, “ \mathcal{H} -matrix arithmetic for a new single-source integral equation for 3-D scattering from homogeneous objects”, in *UNSC-URSI Radio Sci. Meet.*, Boston, MA, Jul. 2018.
- **R. Gholami**, J. Mojolagbe, A. Menshov, and V. Okhmatovski, “An \mathcal{H} -matrix accelerated method of moments solution of a new single-source integral equation for scattering problems”, in *USNC-URSI Radio Sci. Meet.*, San-Diego, CA, Jul. 2017.
- F. L. S. Hosseini, **R. Gholami**, A. Menshov, and V. Okhmatovski, “Novel single-source integral equation for scattering problems on homogeneous dielectric objects”, in *USNC-URSI Rad. Sci. Meet.*, Fajardo, Puerto-Rico, June 2016.

Author's Contributions to Research Results Included in this Thesis

It should be noted that since a majority of the author's research was conducted in collaboration with other researchers, the author's contributions as a first author of the published and submitted papers are described below.

Chapter 2 (Paper 1): \mathcal{H} -Matrix Arithmetic for Fast Direct and Iterative Method of Moment Solution of Surface-Volume-Surface EFIE for 3-D Radiation Problems

The author derived and generalized the \mathcal{H} -matrix arithmetic for both direct and iterative MoM solution of SVS-EFIE for 3-D homogeneous object, implemented a computer code, and validated the accelerated method numerically. This improves the performance of the SVS-EFIE by significantly reducing its memory cost and CPU time complexities.

Chapter 3 (Paper 2): \mathcal{H} -Matrix Accelerated Solution of Surface-Volume-Surface EFIE for Fast Analysis of Scattering on Composite Dielectric Objects

The author proposed an \mathcal{H} -matrix fast direct framework for MoM solution of SVS-EFIE for 3-D scattering and radiation problems on composite dielectric objects, derived and generalized the \mathcal{H} -matrix arithmetic for the new solver, implemented a computer code, and validated the accelerated method numerically. The proposed solver is particularly suitable for the problems with large-scale geometries and multiple dielectric regions.

Chapter 4 (Paper 3): Surface-Volume-Surface EFIE Formulation for Fast Direct Solution of Scattering Problem on 3-D Composite Metal-Dielectric Objects

The author proposed a new SVS-EFIE formulation for electromagnetic analysis of scattering and radiation problems of general composite metal-dielectric objects, implemented an \mathcal{H} -matrix acceleration of the new formulation, and validated the accelerated method. The new formulation introduces independent current on the boundary of each region which makes it particularly suitable for multiscale problems.

Chapter 5 (Paper 4): Surface-Volume-Surface EFIE for Electromagnetic Analysis of 3-D Composite Dielectric Objects in Multilayered Media

The author derived a new SVS-EFIE formulation for electromagnetic analysis of multiscale scattering problems of general composite dielectric objects embedded in layered

media, implemented an \mathcal{H} -matrix acceleration of the new solver, and validated the accelerated method.

Chapter 6: Fast Direct Error-Controlled Solution of Scattering Problems via \mathcal{H} -matrix Accelerated Locally Corrected Nyström Discretization of Magnetic Field Integral Equation

The author proposed the \mathcal{H} -matrix strategy for high-order Locally Corrected Nyström (LCN) discretization of the magnetic field integral equation (MFIE) for 3-D scattering problems, implemented a computer code, and validated the accelerated method. The numerical simulations of the proposed framework validate the capability of the solver for large-scale problems while achieving the higher-order error behavior.

Author's Contributions to Research Results not Included in this Thesis

There are other three journal publications in which the candidate is not the first author, but the candidate's contributions are described below.

Paper 5: Novel Single-Source Integral Equation for Scattering Problems by 3D Dielectric Objects

The author accelerated the conventional MoM solution of SVS-EFIE, developed numerical prototypes, and validated the accelerated numerical techniques.

Paper 6: Formulation of Surface-Volume-Surface EFIE for Solution of Three-Dimensional Scattering Problems on Composite Dielectric Objects

The author generalized the SVS-EFIE formulation for 3-D composite dielectric objects, implemented a computer code, and validate the method.

Paper 7: Surface-Volume-Surface Electric Field Integral Equation for Solution of Scattering Problems on 3-D Dielectric Objects in Multilayered Media

The author developed and implemented the \mathcal{H} -matrix accelerated method for the layered medium SVS-EFIE to enable the solver for 3-D large-scale sea-ice scattering problems buried in layered medium and validated the numerical techniques.

Table of Contents

List of Tables	xv
List of Figures	xvi
1 Introduction	1
1.1 Derivation of SVS-EFIE for a 3-D Scattering Problem on Homogeneous Dielectric Objects	4
1.1.1 Traditional exterior surface equivalence principle	4
1.1.2 Traditional interior surface equivalence principle	6
1.1.3 Generalized exterior surface equivalence principle	7
1.1.4 Generalized interior surface equivalence principle	8
1.1.5 Single-source representation of the generalized surface equivalence principle	9
1.1.6 Volume equivalence principle	11
1.1.7 Surface-volume-surface electric field integral equation derivation	11
1.2 Outline of Thesis	13
2 \mathcal{H}-Matrix Arithmetic for Fast Direct and Iterative Method of Moment Solution of Surface-Volume-Surface EFIE for 3-D Radiation Problems	15
2.1 Abstract	15
2.2 Introduction	16
2.3 Formulations and Equations of SVS-EFIE and Its MoM Solution . . .	18
2.4 \mathcal{H} -Matrix Acceleration of MoM Solution	21
2.4.1 Multilevel Geometry Partitioning	22
2.4.2 \mathcal{H} -Matrix Structure for the SVS-EFIE Operators	23
2.4.3 Filling \mathcal{H} -Matrices of the SVS-EFIE Operators	24
2.5 \mathcal{H} -Matrix Fast Iterative and Direct Solutions	25
2.6 Memory and Computational Complexity Analysis for \mathcal{H} -matrix SVS-EFIE	32
2.6.0.1 Memory Complexity for SVS-EFIE \mathcal{H} -matrices	34

2.6.0.2	Computational Complexity of \mathcal{H} -GMRES Based Iterative Solver	36
2.6.0.3	Computational Complexity of \mathcal{H} -LU Based Direct Solver	36
2.7	Numerical Results	40
2.7.1	Dielectric Sphere	41
2.7.2	Dielectric NASA Almond	44
2.7.3	Austin Benchmark Suite for Computational Bioelectromagnetics	49
2.7.3.1	Homogeneous Human Head-Sized Sphere	50
2.7.3.2	Homogeneous Human Body-Sized Spheroid	50
2.8	Conclusion	52
3	\mathcal{H}-Matrix Accelerated Solution of Surface-Volume-Surface EFIE for Fast Analysis of Scattering on Composite Dielectric Objects	53
3.1	Abstract	53
3.2	Introduction	54
3.3	Synopsis of SVS-EFIE for 3-D Composite Scatterers and Its MoM Solution	56
3.4	\mathcal{H} -Matrix Based Fast Direct MoM Solution of SVS-EFIE for 3-D Composite Scatterer	62
3.4.1	Geometry Partitioning and Construction of \mathcal{H} -matrix	63
3.4.2	Assembling of Final \mathcal{Z}_{SVS} MoM \mathcal{H} -matrix	65
3.4.3	Direct Solution Using Block \mathcal{H} -LU Decomposition	66
3.4.4	Forward and Backward Substitutions	68
3.5	Computational Complexity of \mathcal{H} -Matrix SVS-EFIE for 3-D Composite Scatterer (3.15)	68
3.5.1	Memory Complexity for a Composite Scatterer Consisting of \mathcal{L} Regions	69
3.5.2	Computational Complexity of \mathcal{H} -LU Based Direct Solver	70
3.6	Numerical Results	72
3.6.1	Three Piece-wise Homogeneous Head-Sized Spheres	72
3.6.2	Homogeneous Human Head Model	76
3.7	Conclusion	77
4	Surface-Volume-Surface EFIE Formulation for Fast Direct Solution of Scattering Problem on General 3-D Composite Metal-Dielectric Objects	82
4.1	Introduction	84
4.2	Problem Formulation	85
4.3	\mathcal{H} -matrix-Based Direct Solution	91
4.4	Numerical Results	93
4.4.1	Multilayer sphere	94
4.4.2	Bifurcated sphere	96

4.5	Conclusion	100
5	Surface-Volume-Surface EFIE for Electromagnetic Analysis of 3-D Composite Dielectric Objects in Multilayered Media	104
5.1	Abstract	104
5.2	Introduction	105
5.3	SVS-EFIE Formulation for Composite Dielectric Objects in Layered Media	109
5.4	\mathcal{H} -matrix-Based Fast Direct MoM Solution of the Proposed SVS-EFIE	113
5.5	Numerical Results	117
5.5.1	Dielectric Bifurcated Capsule	118
5.5.2	Dielectric Coated Sphere	121
5.5.3	Rough Surface of Composite Snow Sea-Ice Model	122
5.6	Conclusion	128
6	Fast Direct Error-Controlled Solution of Scattering problem via \mathcal{H}-matrix Accelerated Locally Corrected Nyström Discretization of Magnetic Field Integral Equation	132
6.1	Abstract	132
6.2	Introduction	133
6.3	Synopsis OF Locally Corrected Nyström Discretization Of MFIE . . .	134
6.4	\mathcal{H} -Matrix-Based Fast Direct Solution of LCN-MFIE	137
6.4.1	Geometry Partitioning and Construction of the \mathcal{H} -matrix . . .	137
6.4.2	Direct Solution Using Block \mathcal{H} -LU Decomposition	138
6.5	Numerical Results	139
6.6	Conclusion	144
7	Conclusions, Comments and Future Work	145
7.1	Conclusions	145
7.2	Addressing Prof. Peterson's Comments	146
7.2.1	Comment 1	146
7.2.2	Comment 2	147
7.2.3	Comment 3	151
7.2.4	Comment 4	151
7.2.5	Comment 5	152
7.2.6	Comment 6	153
7.2.7	Comment 7	153
7.2.8	Comment 8	154
7.2.9	Comment 9	154
7.2.10	Comment 10	154
7.3	Future Works	155

References

List of Tables

2.1	Memory compression ratio (5.12) for the \mathcal{H} -matrix accelerated MoM solution of the SVS-EFIE for the dielectric sphere excitation problem with different mesh densities ($h = \lambda/10, \lambda/20, \text{ and } \lambda/30$).	42
2.2	Values of tissue-equivalent material relative dielectric permittivity and conductivity [74].	49
3.1	Computational complexity comparison for the proposed solver and PMCHWT [11] equations for the case of $N = P^\alpha$ ($1 < \alpha < 1.5$) and fixed number of regions \mathcal{L}	72
3.2	Time and memory for the \mathcal{H} -matrix accelerated MoM solutions of both SVS-EFIE and PMCHWT [11] for the radiation problem of the three piecewise homogeneous head-sized sphere model at 402 MHz.	76
3.3	Time and memory for the \mathcal{H} -matrix accelerated MoM solutions of both SVS-EFIE and PMCHWT [11] for the radiation problem of the homogeneous head at 2.45 GHz.	77
4.1	Computational complexity comparison for the SVS-S-EFIE and PMCHWT [11] equations for the case of $N = P^\alpha$ ($1 < \alpha < 1.5$) and fixed number of penetrable regions \mathcal{R}_1 and PEC regions \mathcal{R}_2 for both naïve and \mathcal{H} -matrix accelerated MoM.	95
6.1	Memory compression ratio (5.12) for the results in Fig. 6.1 using the proposed solver as a function of the solution order p and the number of elements N_e	142
7.1	Scaling in fill time with number of regions \mathcal{L} in SVS-EFIE and PMCHWT formulations.	148
7.2	Scaling in solve time with number of regions \mathcal{L} in SVS-EFIE and PMCHWT formulations.	150

List of Figures

- 1.1 To derivation of SVS-EFIE in the scattering problem of 3-D object excited by incident field \mathbf{E}^{inc} . (a) A scatterer with volume V bounded by surface ∂V situated in free-space background medium with permittivity ε_0 . Complex relative permittivity of volume V is represented as ϵ . (b) Traditional surface equivalence principle exterior to V with true electric \mathcal{J}^e and magnetic \mathcal{J}^m surface current densities producing true field \mathbf{E} , \mathbf{H} outside V and zero fields in V . (c) Traditional surface equivalence principle interior to V with true electric \mathcal{J}^e and magnetic \mathcal{J}^m surface current densities producing true fields \mathbf{E} , \mathbf{H} in V and zero fields outside V . (d) Generalized surface equivalence principle exterior to V with fictitious electric \mathbf{J}^e and magnetic \mathbf{J}^m surface current densities (single source amenable) producing true fields \mathbf{E} , \mathbf{H} outside V and unconstrained fields \mathbf{E}_{in} and \mathbf{H}_{in} in V . (e) Generalized surface equivalence principle interior to V with fictitious electric \mathbf{J}^e and magnetic \mathbf{J}^m surface current densities (single source amenable) producing true fields \mathbf{E} , \mathbf{H} in V and unconstrained fields \mathbf{E}_{∞} , \mathbf{H}_{∞} outside V . (f) Volume equivalence principle (true fields \mathbf{E}_0 , \mathbf{H}_0 in V_{∞} and \mathbf{E} , \mathbf{H} in V produced by volume polarization current \mathbf{j} in V). 5
- 2.1 System of linear equations structure resulting from MoM discretization of the SVS-EFIE (2.1). Here, P is the number of RWG basis functions on the boundary ∂V and N is the number of tetrahedron elements in the volume V 20
- 2.2 Hierarchical partitioning of RWG basis/testing functions for surface mesh and piece-wise basis/testing functions for volume mesh into an L -level hierarchy of clusters. T_S and T_V represent surface and volume cluster trees, respectively. 23

- 2.3 \mathcal{H} -matrix representation of the volume-to-surface MoM impedance matrix $\mathbf{Z}_0^{\partial V, V}$ arising from $T_{S \times V}$ interaction tree. The structure is constructed using an spheroid model with its surface tree T_S as observer tree and volume tree T_V as source tree with tree depth $L = 3$. Red blocks represent inadmissible blocks and green blocks represent admissible blocks. 25
- 2.4 Assembly of Z_{SVS} MoM \mathcal{H} -matrix from the individual \mathcal{H} -matrices of SVS-EFIE operators: $Z_\epsilon^{\partial V, \partial V}$ arising from $T_{S \times S}$ interaction tree, $\mathbf{Z}_0^{\partial V, V}$ arising from $T_{S \times V}$, and $\mathbf{Z}_\epsilon^{V, \partial V}$ arising from $T_{V \times S}$ via formatted multiplication and addition (2.14) required by a \mathcal{H} -LU based direct solution of the SVS-EFIE. 26
- 2.5 (a) Recursive function $\mathcal{H}\text{-Approx}\mathcal{F}(M \rightarrow M''')$ converting an \mathcal{F} -block M to an \mathcal{H} -matrix M''' . This procedure can also be implemented in the opposite order as $\mathcal{F}\text{-Approx}\mathcal{H}(M''' \rightarrow M)$. (b) Recursive function $\mathcal{H}\text{-Approx}\mathcal{R}(M \rightarrow M''')$ converting an \mathcal{R} block M to an \mathcal{H} -matrix M''' . If \mathcal{H} -matrix M''' has depth of L , then L -step recursion (e.g. $M \rightarrow M''$) and one final step (e.g. $M'' \rightarrow M'''$) are needed for both cases (a) and (b). Here, to simplify the depiction, the depth of M''' is considered to be $L = 2$ which leads to 3 steps conversion. 30
- 2.6 Recursive function $\mathcal{R}\text{mul}\mathcal{H}(\mathcal{R}, \mathcal{H})$ performing formatted multiplication of \mathcal{R} - and \mathcal{H} -blocks and storing the result in \mathcal{R} -format. The recursive function $\mathcal{H}\text{mul}\mathcal{R}(\mathcal{H}, \mathcal{R})$ is defined similarly with an opposite order of operations. Here, to simplify the depiction, the depth of \mathcal{H} -matrix is considered to be $L = 1$. In general, \mathcal{H} -blocks of various depths occur. 32
- 2.7 Procedures to re-compress the addition of two matrices. a) Function $\text{Trun}_{k'' \leftarrow k+k'}^{\mathcal{R}+\mathcal{R}}(\dots)$ for addition and truncation of two matrices in \mathcal{R} -format. b) Recursive function $\text{Trun}_{k'' \leftarrow k+k'}^{\mathcal{H}+\mathcal{H}}(\dots)$ for addition and truncation of two \mathcal{H} -matrices. Again, to simplify the depiction, the depth of \mathcal{H} -matrices in (b) is considered to be $L = 1$. The resultant compressed blocks with revealed rank k'' are represented as dashed blocks. 33
- 2.8 Average relative error δ of both \mathcal{H} -matrix accelerated MoM solution for dielectric sphere excitation problem with different mesh densities ($h = \lambda/10, \lambda/20$, and $\lambda/30$) with respect to the Mie series solution as a function of ACA truncation tolerance τ . The error in the direct MoM solution of SVS-EFIE [13] is shown for reference. 42
- 2.9 Scaling behavior of both \mathcal{H} -matrix (dashed lines) and naïve (solid lines) MoM SVS-EFIE for the dielectric sphere with mesh density $h = \lambda/10$ across the frequency range from 4 GHz to 10 GHz. (a) Memory for $Z_\epsilon^{\partial V, \partial V}$. (b) Memory for $\mathbf{Z}_0^{\partial V, V} + \mathbf{Z}_\epsilon^{V, \partial V}$. (c) Set up time for $Z_\epsilon^{\partial V, \partial V}$. (d) Set up time for $\mathbf{Z}_0^{\partial V, V}$ and $\mathbf{Z}_\epsilon^{V, \partial V}$ 45

2.10	Scaling behavior of both \mathcal{H} -matrix (dashed lines) and naïve (solid lines) MoM SVS-EFIE for the dielectric sphere with mesh density $h = \lambda/10$ across the frequency range from 4 GHz to 10 GHz. (a) Set up time for Z_{SVS} as a part of \mathcal{H} -LU-based direct solver. (b) Solution time for \mathcal{H} -LU-based direct method (\mathcal{H} -LU factorization and back substitution) (c) Solution time for \mathcal{H} -GMRES-based iterative method (fixed $N_{\text{it}} = 1000$ and fixed residual 10^{-6} cases).	46
2.11	Scaling behavior of both \mathcal{H} -matrix (dashed lines) and naïve (solid lines) MoM SVS-EFIE for the dielectric sphere with relative permittivity of $\epsilon = 1.5$ at 3 GHz. (a) Memory for $Z_{\epsilon}^{\partial V, \partial V}$. (b) Memory for $\mathbf{Z}_0^{\partial V, V} + \mathbf{Z}_{\epsilon}^{V, \partial V}$. (c) Set up time for $Z_{\epsilon}^{\partial V, \partial V}$. (d) Set up time for $\mathbf{Z}_0^{\partial V, V}$ and $\mathbf{Z}_{\epsilon}^{V, \partial V}$	47
2.12	Scaling behavior of both \mathcal{H} -matrix (dashed lines) and naïve (solid lines) MoM SVS-EFIE for the dielectric sphere with relative permittivity of $\epsilon = 1.5$ at 3 GHz. (a) Set up time for Z_{SVS} as a part of \mathcal{H} -LU-based direct solver. (b) Solution time for \mathcal{H} -LU-based direct method (\mathcal{H} -LU factorization and back substitution) (c) Solution time for \mathcal{H} -GMRES-based iterative method (fixed $N_{\text{it}} = 1000$ and fixed residual 10^{-6} cases).	48
2.13	Magnitude of the total electric field at 3 GHz inside the dielectric NASA almond model with the relative dielectric permittivity $\epsilon = 12$. A 3-D representation of the total electric field obtained from \mathcal{H} -matrix SVS-EFIE is in the left plot. The distribution of the magnitude of the total electric field along the x and y axes for the \mathcal{H} -matrix SVS-EFIE and FEKO solutions are shown in the right plots.	49
2.14	Magnitude of the total electric field inside the human head-sized sphere produced by a z -directed electric dipole situated at $x' = 0$ m, $y' = 0$ m, $z' = 0.4$ m obtained by the \mathcal{H} -matrix solver at (a) 900 MHz (b) 2.45 GHz. The relative error distribution with respect to the Mie series solution is shown in (c) and (d).	51
2.15	Magnitude of the total electric field inside the human body-sized spheroid produced by a uniform \hat{z} -polarized plane-wave traveling in the $+x$ direction at 402 MHz and 900 MHz obtained by the \mathcal{H} -matrix SVS-EFIE. The distribution of the magnitude of total electric field along the x and z axes for \mathcal{H} -matrix SVS-EFIE and FEKO solutions are shown in the right.	51

3.1 To derivation of SVS-EFIE in the scattering problem of 3-D composite dielectric object excited by incident field E^{inc} . (a) Original scattering problem of a two-region composite scatterer with volumes V_1 and V_2 bounded by surfaces $\partial V_1 = \partial V_{01} + \partial V_{21}$ and $\partial V_2 = \partial V_{02} + \partial V_{12}$, and situated in free-space background medium with permittivity ϵ_0 . Complex relative permittivity of volume V_1 and V_2 are ϵ_1 and ϵ_2 , respectively. (b) Volume equivalence principle to generate the true fields E_0, H_0 in V_∞ by volume polarization currents \mathbf{j}_1 and \mathbf{j}_2 . (c) Generalized surface equivalence principle interior to V_1 with single fictitious electric surface current density \mathbf{J}_1 producing true fields E_1, H_1 in V_1 and unconstrained field E_1^∞ outside V_1 . (d) Generalized surface equivalence principle interior to V_2 with single fictitious electric surface current density \mathbf{J}_2 producing true fields E_2, H_2 in V_2 and unconstrained field E_2^∞ outside V_2 57

3.2 Assembly of \mathcal{Z}_{SVS} MoM \mathcal{H} -matrix for composite scatterer featuring two regions from the individual \mathcal{H} -matrices of SVS-EFIE operators: $\mathcal{Z}_\epsilon^{\partial V, \partial V}$, $\mathcal{Z}_0^{\partial V, V}$, and $\mathcal{Z}_\epsilon^{V, \partial V}$ via formatted multiplication and addition (3.22) required by \mathcal{H} -LU based direct solution of the SVS-EFIE. Admissible blocks (green) corresponding to far interactions and inadmissible blocks (red) corresponding to near interactions. The number of RWG basis functions on the boundaries ∂V_1 and ∂V_2 are P_1 and P_2 , respectively, with $P = P_1 + P_2$ being the total number of RWG basis functions. The number of tetrahedron elements in the volumes V_1 and V_2 are N_1 and N_2 , respectively, with $N = N_1 + N_2$ being the total number of tetrahedrons discretizing the object volume $V_1 + V_2$ (Fig. 3.1). 63

3.3 The geometry of the three piece-wise homogeneous human head-sized spheres 73

3.4 (a) Magnitude of the total electric field inside the three piece-wise human head-sized spheres produced by a z -directed electric dipole computed by the proposed solver (3.15) at 402 MHz. (b) The distribution of the relative error in total electric field with respect to the Mie series analytical solution. 74

3.5 Scaling behavior of both \mathcal{H} -matrix (dashed lines) and naïve (solid lines) MoM discretization of SVS-EFIE for the radiation problem of the three piece-wise spheres at 402 MHz varying number of mesh elements. (a) Memory. (b) Fill time (time to construct the MoM matrices of the SVS-EFIE). (c) Solution time (including of creation of final \mathcal{Z}_{SVS} , block \mathcal{H} -LU decomposition, and block \mathcal{H} -substitutions). 75

3.6 A 3-D representation of the magnitude of the total electric field inside the homogeneous human head model produced by a z -directed electric dipole situated at $x' = 0.065$ m, $y' = 0.03$ m, and $z' = 0.1$ m obtained by the proposed solver. 78

- 3.7 Magnitude of the total electric field inside the homogeneous human head model with observation lines along x , y , and z axis obtained by the proposed solver and FEKO at 900 MHz and 2.45 GHz 79
- 3.8 Scaling behavior of both \mathcal{H} -matrix (dashed lines) and conventional (solid lines) MoM discretization of SVS-EFIE for the radiation problem of homogeneous human head at 2.45 GHz varying number of mesh elements. (a) Memory. (b) Fill time (time to construct the MoM matrices of the SVS-EFIE). (c) Solution time (including of creation of final \mathcal{Z}_{SVS} , block \mathcal{H} -LU decomposition, and block \mathcal{H} -substitutions). 80
- 4.1 (a) Derivation of SVS-S-EFIE for the scattering problem of a 3-D composite metal-dielectric object excited by E^{inc} for a three-region scatterer with volumes V_1 , V_2 , and V_3 bounded by surfaces $\partial V_1 = \partial V_{01} + \partial V_{21} + \partial V_{31}$, $\partial V_2 = \partial V_{02} + \partial V_{12} + \partial V_{32}$, and $\partial V_3 = \partial V_{03} + \partial V_{13} + \partial V_{23}$. The composite object situated in free-space background medium. The dielectric regions V_1 and V_2 have complex relative permittivities of ϵ_1 and ϵ_2 , respectively, and V_3 being PEC. The original scattering problem is decomposed to: (b) exterior volume-surface equivalence problem (true fields E_0 , H_0 in V_∞ produced by volume polarization currents \mathbf{j}_1 and \mathbf{j}_2 and surface equivalence current \mathcal{J}_3), (c) interior to V_1 generalized surface equivalence problem with single fictitious electric surface current density \mathbf{J}_1 producing true field in V_1 and unconstrained field E_1^∞ outside V_1 , and (d) interior to V_2 generalized surface equivalence problem with single fictitious electric surface current density \mathbf{J}_2 producing true field in V_2 and unconstrained field E_2^∞ outside V_2 86
- 4.2 System of matrix equations resulting from MoM discretization of the SVS-S-EFIE (formulations (4.8) and (4.9)) for a composite metal-dielectric scatterer of Fig. 4.1(a). The number of RWG functions on the boundaries ∂V_1 , ∂V_2 , and ∂V_3 are P_1 , P_2 and P_3 , respectively, with $P = P_1 + P_2 + P_3$ being the total number of RWG basis functions. The number of tetrahedron elements in the dielectrics with volumes V_1 and V_2 are N_1 and N_2 , respectively. The vectors of unknowns and RHS are not appeared in the system of matrix equations. 91
- 4.3 Assembly of \mathcal{Z}_{SVS} MoM \mathcal{H} -matrix for composite metal-dielectric scatterer featuring three regions (Fig. 4.1(a)). The \mathcal{Z}_{SVS} \mathcal{H} -matrix computed from the individual \mathcal{H} -matrices operators $\mathcal{Z}_{\epsilon/0}^{\partial V_i, \partial V_j}$, $\mathcal{Z}_0^{\partial V_i, V_j}$, and $\mathcal{Z}_\epsilon^{V_i, \partial V_j}$ via formatted multiplication and addition required by \mathcal{H} -LU based direct solution. Green blocks are corresponding to the far interactions and red blocks are corresponding to the near interactions. The number of RWG basis functions on the boundaries ∂V_1 , ∂V_2 , and ∂V_3 are P_1 , P_2 , and P_3 , respectively. The number of tetrahedron elements in the volumes V_1 and V_2 are N_1 and N_2 94

4.4	(a) Magnitude of \mathbf{E} -field in the dielectric region of the two-region composite metal-dielectric multilayer sphere model obtained by the \mathcal{H} -matrix accelerated of the SVS-S-EFIE. (b) Relative error in the solution of the two-region model compared against Mie series. (c) Magnitude of \mathbf{E} -field in the dielectric region of the three-region composite metal-dielectric multilayer sphere model obtained by the \mathcal{H} -matrix accelerated of the SVS-S-EFIE. (d) Relative error in the solution of the three-region model compared against Mie series. (e) Non-conformal mesh representation of the three-region composite metal-dielectric multilayer sphere model.	97
4.5	Scaling behavior of both \mathcal{H} -matrix (dashed lines) and naïve (solid lines) MoM discretization of SVS-S-EFIE for the radiation problem of the three-region multilayer sphere model. (a) Memory. (b) Fill time (time to construct the MoM matrices of the SVS-S-EFIE). (c) Solution time (including of creation of final \mathcal{Z}_{SVS} , block \mathcal{H} -LU decomposition, and block \mathcal{H} -substitutions).	98
4.6	(a) A 3-D representation of the magnitude of \mathbf{E} -field inside the dielectric region of a composite metal-dielectric bifurcated sphere discretized with uniform mesh using the \mathcal{H} -matrix accelerated SVS-S-EFIE. (b) Non-conformal mesh representation of the model with uniform discretization of dielectric and PEC regions. (c) Magnitude of \mathbf{E} -field along x axis obtained by the proposed solver and FEKO for the uniform mesh model. (d) The 3-D representation of magnitude of \mathbf{E} -field inside the dielectric region of the multiscale mesh model using the proposed solver. (e) Non-conformal mesh representation of the model with multiscale discretization of the dielectric region. (f) Magnitude of the total electric field along x axis after mesh refinement compared against the FEKO.	101
4.7	Scaling behavior of both \mathcal{H} -matrix (dashed lines) and naïve (solid lines) MoM discretization of SVS-S-EFIE for the radiation problem of bifurcated sphere with regular mesh model. (a) Memory. (b) Fill time (time to construct the MoM matrices of the SVS-S-EFIE). (c) Solution time (including of creation of final \mathcal{Z}_{SVS} , block \mathcal{H} -LU decomposition, and block \mathcal{H} -substitutions).	102
4.8	Scaling behavior of both \mathcal{H} -matrix (dashed lines) and naïve (solid lines) MoM discretization of SVS-S-EFIE for the radiation problem of bifurcated sphere with multiscale mesh model. (a) Memory. (b) Fill time (time to construct the MoM matrices of the SVS-S-EFIE). (c) Solution time (including of creation of final \mathcal{Z}_{SVS} , block \mathcal{H} -LU decomposition, and block \mathcal{H} -substitutions).	103

- 5.1 Radiation problem of extraneous currents \mathbf{j}^{ext} producing incident field \mathbf{E}^{inc} , which scatters on a 3-D composite dielectric object consisting of two regions with volumes V_{R1} and V_{R2} bounded by surfaces ∂V_{R1} and ∂V_{R2} , and having complex relative permittivities $\epsilon_{R1} = \epsilon_{R1} + \sigma_{R1}/(\omega\epsilon_0)$ and $\epsilon_{R2} = \epsilon_{R2} + \sigma_{R2}/(\omega\epsilon_0)$, respectively. The composite object is situated in general $(n + 1)$ -layer non-magnetic planar layered medium. The partial volumes $V_{L1,R1}$ and $V_{L2,R1}$ forming first region of the object V_{R1} and the partial surfaces $\partial V_{L1,R1}$ and $\partial V_{L2,R1}$ forming first region surface ∂V_{R1} denote parts of the first region confined to the first and second layers, respectively. Similarly, partial volumes $V_{L2,R2}$ and $V_{L3,R2}$ forming the second region of the object V_{R2} and the partial surfaces $\partial V_{L2,R2}$ and $\partial V_{L3,R2}$ forming the second region surface ∂V_{R2} denote parts of the objects confined to the second and third layers, respectively. 108
- 5.2 Matrix structure resulting from MoM discretization of the SVS-EFIE formulation (5.9) for a generic two-region composite dielectric objects situated in layered media Fig. 5.1. The number of RWG functions on the boundaries ∂V_{R1} and ∂V_{R2} are I_{R1} and I_{R2} , respectively, with $I = I_{R1} + I_{R2}$ being the total number of RWG basis functions. The number of tetrahedron elements in the dielectrics with volumes V_{R1} and V_{R2} are N_{R1} and N_{R2} , respectively. The total number of tetrahedron elements in the models is $N = N_{R1} + N_{R2}$. Also, $N_{L1,R1}$ and $N_{L2,R1}$ are the number of tetrahedrons of parts of the region $R1$ confined to the first and second layers, respectively. Similarly, $N_{L2,R2}$ and $N_{L3,R2}$ are the number of tetrahedrons of parts of the region $R2$ confined to the second and third layers, respectively, with $N_{R2} = N_{L2,R2} + N_{L3,R2}$. Coefficients $\alpha_{m,p'}$ in the MoM matrix corresponding to the volume-to-surface operator are equal to $k_0^2(\epsilon_{Rm} - \epsilon_{Lp'})$ (see formulation (5.9)). . 112

- 5.3 \mathcal{H} -matrix structure of the MoM discretization of the proposed solver for a generic two-region composite dielectric objects situated in layered media of Fig. 5.1. Green blocks represent the admissible blocks, which are compressed using ACA algorithm. The red blocks represent the inadmissible blocks. Creation of the final \mathcal{Z}_{SVS} MoM \mathcal{H} -matrix using formatted multiplication and addition [39] is required for fast block \mathcal{H} -LU based direct solution of the matrix equation. Symbols \otimes and \oplus denote operations of formatted multiplication and addition. Dashed lines represent the pertinent \mathcal{H} -matrix blocks for clustering of the regions corresponding to the strategy honouring the structure of the layers of the medium. In such strategy the clusters of elements are not allowed to straddle the dielectric interfaces of the layers. However, in this work we adopt the strategy of mesh elements clustering such that groups of elements are formed regardless of the structure of the layers of the medium (i.e. the clusters can straddle the interfaces between the layers) as it is done in the case of composite scatterers situated in free space [39]. The actual \mathcal{H} -matrix blocks introduced according to the clustering strategy adopted in this work are represented with solid lines. 114
- 5.4 Depiction of a composite dielectric bifurcated capsule with 0.5 m radius and 0.25 m height is embedded in the three layer medium. Complex relative permittivity of the objects are $\epsilon_{R1} = 2$ and $\epsilon_{R2} = 4$. The model is excited by a electric dipole. 118
- 5.5 Magnitude of the total electric field inside the dielectric bifurcated capsule for object in free space (top) and object buried in the layered media (bottom) for the problem in Fig. 5.4. The field distribution inside the object obtained by the free space SVS-EFIE formulation [39] and SVS-EFIE layered media formulation (5.9) are shown in the left. Also, the fields inside the object with observation lines at $(-0.45 \leq x \leq 0.45, y = 0.0, z = -0.325)$ m, $(x = 0.0, -0.45 \leq y \leq 0.45, z = -0.325)$ m and $(x = 0.0, y = 0.0, -0.0625 \leq z \leq 0.0625)$ m obtained by the SVS-EFIE and FEKO are shown in the right for comparison. . 120
- 5.6 Memory cost and CPU time complexity of both \mathcal{H} -matrix (dashed lines) and naïve (solid lines) MoM discretization of SVS-EFIE for the scattering problem of the bifurcated capsule model buried in layered medium. (a) Memory. (b) Fill time. (c) Direct solve time (including of creation of final \mathcal{Z}_{SVS} , block \mathcal{H} -LU decomposition, and block \mathcal{H} -substitution). 121

- 5.7 Depiction of a coated sphere with inner radius of 0.15 m and outer radius of 0.25 m embedded in three layer medium. Complex relative permittivity of the regions are $\epsilon_{R1} = 5$ and $\epsilon_{R2} = 3$ for inner and outer spheres, respectively. The model is excited by electric dipole located in far zone. 123
- 5.8 Visualization of the Green's function component in mixed-potential Michalski-Zheng's formulation used in MoM solution of SVS-EFIE at 300MHz for 2-layer sphere buried in 3-layer medium (Fig. 5.7). The Green's function data at $\rho = 0.035$ m and $\rho = 0.69$ m from four databases used to compute the Green's function components K_{xx}^A , K_{xz}^A , K_{yz}^A , K_{zz}^A and K_ϕ , where K_{xz}^A can be evaluated as $\iota \cos(\phi) \partial K_{tz} / \partial \rho$, and K_{yz}^A can be evaluated as $\iota \sin(\phi) \partial K_{tz} / \partial \rho$ 124
- 5.9 Magnitude of the total electric field inside the dielectric coated sphere situated in free space (top) and situated in the layered media (bottom) for the problem in Fig. 5.7 at 300MHz. The field distribution inside the object obtained by the free space SVS-EFIE formulation [39] and SVS-EFIE layered media formulation (5.9) is shown in the left. Also, the fields inside the object with observation lines along x , y , and z axis obtained by the SVS-EFIE and FEKO are shown in the right for comparison. 125
- 5.10 Memory cost and CPU time complexity of both \mathcal{H} -matrix (dashed lines) and naïve (solid lines) MoM discretization of SVS-EFIE for the scattering problem of the coated sphere model buried in layered medium. (a) Memory. (b) Fill time. (c) Direct solve time (including of creation of final \mathcal{Z}_{SVS} , block \mathcal{H} -LU decomposition, and block \mathcal{H} -substitution). 126
- 5.11 Depiction of a rough surface snow sea-ice model as a composite object. The top region of the model is covered by snow with 0.005 m thickness and complex relative permittivity of $\epsilon_{R1} = 1.5$ and the bottom region is sea-ice with 0.015 m thickness and relative permittivity and conductivity of $\epsilon_{R2} = 3.18$ and $\sigma_{R2} = 0.021$ S/m and is half buried in air and the sea-ice layer. 127
- 5.12 Magnitude of the total electric field inside the model of rough surface snow sea-ice model (Fig. 5.11) at 1GHz. The field distribution inside the model is shown in the left where the observation surface is on the interface between air layer and the sea ice layer $z = 0.04$ m. The fields computed using FEKO are shown in the right for comparison with observation lines at $(0.001 \leq x \leq 0.169, y = 0.085, z = 0.04)$ m, $(x = 0.085, 0.001 \leq y \leq 0.169, z = 0.04)$ m and $(x = 0.085, y = 0.085, 0.031 \leq z \leq 0.049)$ m. 129

5.13 Memory cost and CPU time complexity of both \mathcal{H} -matrix (dashed lines) and naïve (solid lines) MoM discretization of SVS-EFIE for the scattering problem of the snow sea-ice model buried in layered medium. (a) Memory. (b) Fill time. (c) Direct solve time (including of creation of final \mathcal{Z}_{SVS} , block \mathcal{H} -LU decomposition, and block \mathcal{H} -substitution). 130

6.1 The mean relative error in the current as a function of the element size and solution order in the \mathcal{H} -matrix acceleration of LCN discretization of MFIE. The relative error is computed using $\text{MeanErr}(J) = \frac{1}{2QN_e} \sum_{i=0}^{2QN_e} \frac{|J_i^{\text{LCN}} - J_i^{\text{Ref}}|}{|J_i^{\text{Ref}}|}$ with respect to the Mie-series analytic solution as a reference. 140

6.2 Memory cost and CPU time complexity performance of the \mathcal{H} -matrix accelerated LCN discretization of MFIE for the results in Fig. 6.1 as a function of the total number of unknowns N and solution order p . (a) Memory cost. (b) Fill time (time to construct the LCN matrices in (6.7)). (c) Solution time (using block \mathcal{H} -LU direct algorithm). The complexity of the conventional LCN discretization (solid line) of MFIE is also plotted for comparison. 141

6.3 The magnitude of the surface current density J on the PEC sphere as a function of θ using the proposed solver and the Mie-series analytic solution at $f = 100$ MHz for the first-order solution with $N = 786, 432$ number of unknowns. 143

1

Introduction

Electromagnetic problems of general composite metal-dielectric and dielectric-dielectric objects play an important role in analysis of field interactions with the biological tissues [1, 2], antenna design [3, 4], remote sensing [5], and various other areas [6, 7]. Since these complex objects contain inhomogeneous and/or anisotropic materials the methods of computational electromagnetics (CEM) based on the direct discretization of the Maxwell Equations such as Finite-Difference Time-Domain (FDTD) [8] and the Finite Element Method (FEM) [9] have become the most popular frameworks for solution of these problems. Besides the versatility of these approaches, they have some disadvantages such as: limitation of error accumulation when solving large-scale problems, requirement of discretizing both the scatterer and its surrounding space, and dependency on accurate enforcement of the absorbing boundary conditions truncating the mesh.

Alternatively, such problems can be solved using integral equations (IEs) with method of moments (MoM) [10] discretization. The IE based solutions allow to reduce dimensionality of the boundary value problems by introducing the unknown field quantities only at the boundaries of the objects [11]. This enables development of computational frameworks free of above listed disadvantages encountered in FDTD and FEM.

While in the traditional surface integral equations (SIEs) two unknown surface current densities [12] are required on the surface of the scatterer, in our previous

work [13], we proposed a new type of single source integral equation (SSIE) known as surface-volume-surface electric field integral equation (SVS-EFIE) which needs only a single surface current density on the scatterer. Also, the proposed SVS-EFIE has only electric-field type integral operator with non hyper-singular integrals under MoM discretization [14]*.

On the other hand, the MoM discretization of the IEs produces dense matrices which need the development of fast algorithms [15] in order to reduce the memory cost and CPU time of the solver. Fast iterative algorithms such as Multi-Level-Fast-Multipole-Method (MLFMM) [16–19], Fast Fourier Transform (FFT)-based methods [20–22], Adaptive Cross Approximation (ACA) [23,24], and other methods [25,26] can be used to accelerate the required matrix-vector product iteratively. However, since the pertinent integral equations discretized with boundary element schemes (e.g. MoM) typically produce a poorly conditioned matrix equation for the scattering and radiation problems of complex non-smooth geometries, multiscale discretization, and high disparity in the material properties, the above fast iterative schemes are commonly plagued with convergence problems.

Fast direct algorithms [27–34], on the other hand, are much less sensitive to the poor conditioning of the MoM matrix equation due to their non-iterative nature. In this thesis, we propose such fast direct framework in order to accelerate the new SVS-EFIE solutions. In [35], we developed a fast direct method using hierarchical (\mathcal{H})-matrix [27,36] for acceleration of the MoM solution of the SVS-EFIE for homogeneous dielectric objects in free space. The \mathcal{H} -matrix accelerated SVS-EFIE is shown to produce accurate results using only a fraction of the resources needed by conventional MoM both in terms of memory and total CPU time. The implementation of the \mathcal{H} -matrix framework for MoM discretization of the SVS-EFIE is described in detail in this thesis.

In [35,37], SVS-EFIE and its \mathcal{H} -matrix acceleration have been developed for homogeneous dielectric scatterers. In [38], the SVS-EFIE formulation is developed

* In MoM discretization of SVS-EFIE, the basis and testing functions are chosen in such a way that the solver features integrals with singularities no stronger than $1/R$, R being the distance from the source to the observation point. The integrals with singularities stronger than $1/R$ (e.g. $1/R^2$) considered as hyper-singular integrals and are difficult to be computed.

for the case of piece-wise homogeneous dielectric-dielectric regions. The novel \mathcal{H} -matrix strategy is developed in [39] to accelerate matrix-matrix multiplications, LU-decomposition, and back-substitution of the proposed solver for the composite objects with arbitrary number of homogeneous dielectric regions.

Next, in [40], the new formulation of the SVS-EFIE is developed for scattering and radiation problems on piece-wise homogeneous metal-dielectric regions in free space. In the proposed formulation, independent electric surface current densities are introduced at the boundary of each dielectric-dielectric and metal-dielectric regions. This feature enables the proposed formulation to create non-conformal meshes at material junctions while decreasing the total number of unknowns in comparison to the traditional SIEs [41, 42]. It also makes the proposed solver particularly suitable for the practical scattering and radiation problems with multiscale meshes. The \mathcal{H} -matrix framework is also developed for the new formulation in [40] to enable the solver for simulation of large-scale problems.

Furthermore, since the SVS-EFIE formulation only features the electric field dyadic Green's functions, it is suitable for the solution of scattering and radiation problems on objects situated in planar multilayered media [37]. Hence, in [43], the SVS-EFIE formulation is developed to the case of piece-wise homogeneous dielectric objects situated in multilayered medium. The new \mathcal{H} -matrix strategy of creation of clusters of element crossing the dielectric interfaces between the layers is shown to preserve the compressibility of the pertinent \mathcal{H} -matrix blocks. The numerical results confirm that the \mathcal{H} -matrix implemented for the layered medium solver in [43] has the same computational complexity performance as the one implemented for the free space solver provided the layered medium Green's function components are computed with the tolerance level which is below the tolerance level of the compression scheme used in formation of the \mathcal{H} -matrix blocks [39].

In this thesis, the \mathcal{H} -matrix accelerated framework developed for different SVS-EFIE formulations is for the case of low-order (LO) MoM discretization of pertinent formulations. In order to extend the application of the proposed fast direct \mathcal{H} -matrix framework to the case of higher-order (HO) method, the HO Locally Corrected Nyström (LCN) discretization of the magnetic field integral equation (MFIE)

is developed in the final chapter. Unlike the MoM discretization where the interactions are element-based methods, the LCN discretization is defined as a point-based method where the HO solution can be obtained efficiently [44]. The computational complexity and the error performance of the proposed fast error-controlled direct solver is studied numerically for the PEC smooth objects. The new framework is shown to produce the HO results while using only the small fraction of resources needed by conventional (unaccelerated) LCN.

1.1 Derivation of SVS-EFIE for a 3-D Scattering Problem on Homogeneous Dielectric Objects

In this section, we review the background of this thesis by deriving the SVS-EFIE formulation for scattering problem of a 3-D homogeneous dielectric object. Consider scattering problem of time-harmonic incident field \mathbf{E}^{inc} with frequency ω on a 3-D homogeneous dielectric object with volume V and complex relative permittivity of $\epsilon = \epsilon + \sigma/(i\omega\epsilon_0)$ (Fig. 1.1(a)). The scatterer is situated in free space with permittivity ϵ_0 . Time factor $e^{-i\omega t}$ is suppressed throughout the thesis and $i = \sqrt{-1}$.

1.1.1 Traditional exterior surface equivalence principle

The total field $\mathbf{E}(\mathbf{r})$ and $\mathbf{H}(\mathbf{r})$ outside the volume V can be defined using exterior to V surface equivalence principle (Fig. 1.1(b)) which involves the equivalent surface electric current \mathcal{J}^e and magnetic current \mathcal{J}^m densities on the boundary ∂V , as follows [11, 45]:

$$\begin{aligned} \mathbf{E}^{\text{inc}}(\mathbf{r}) + i\omega\mu_0 \oint_{\partial V} \overline{\overline{\mathbf{G}}}_{e0}(\mathbf{r}, \mathbf{r}') \cdot \mathcal{J}^e(\mathbf{r}') ds' \\ + \oint_{\partial V} \overline{\overline{\mathbf{G}}}_{m0}(\mathbf{r}, \mathbf{r}') \cdot \mathcal{J}^m(\mathbf{r}') ds' = \begin{cases} \mathbf{E}(\mathbf{r}), & \mathbf{r} \in V_\infty \setminus \partial V, \\ \mathbf{0}, & \mathbf{r} \in V \setminus \partial V, \end{cases} \end{aligned} \quad (1.1)$$

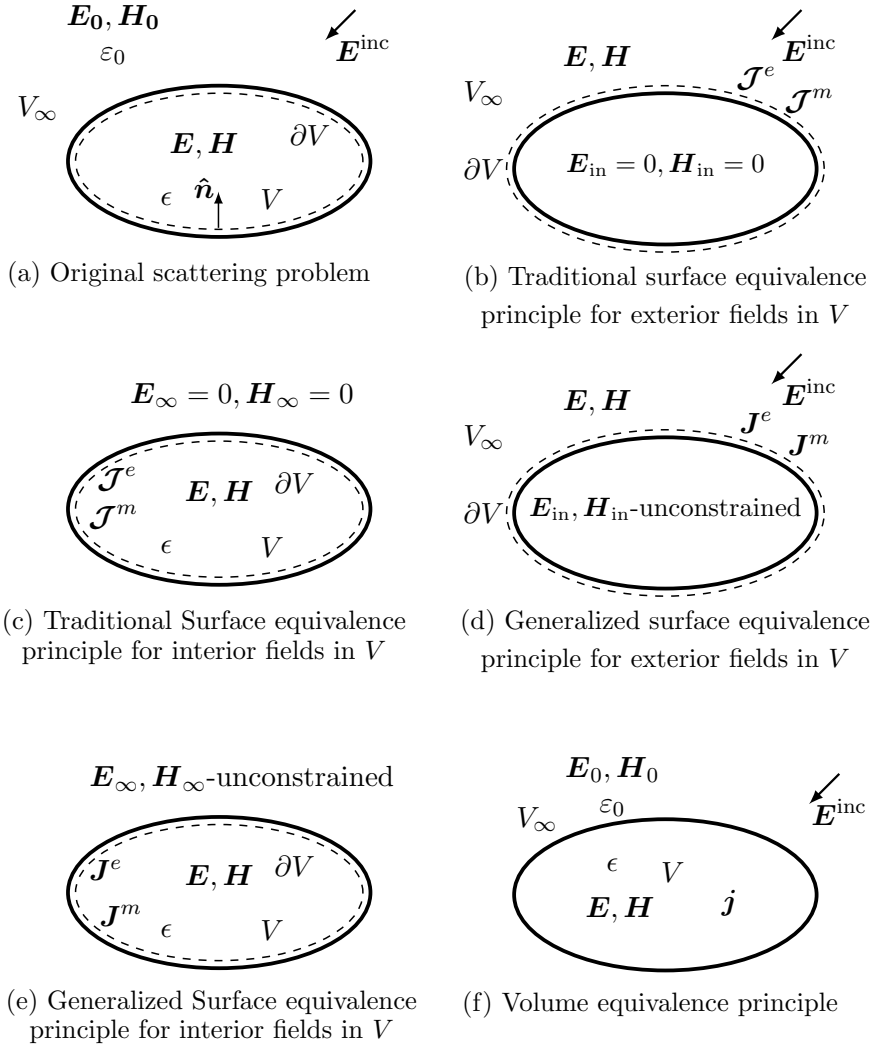


Figure 1.1: To derivation of SVS-EFIE in the scattering problem of 3-D object excited by incident field \mathbf{E}^{inc} . (a) A scatterer with volume V bounded by surface ∂V situated in free-space background medium with permittivity ϵ_0 . Complex relative permittivity of volume V is represented as ϵ . (b) Traditional surface equivalence principle exterior to V with true electric \mathcal{J}^e and magnetic \mathcal{J}^m surface current densities producing true field \mathbf{E} , \mathbf{H} outside V and zero fields in V . (c) Traditional surface equivalence principle interior to V with true electric \mathcal{J}^e and magnetic \mathcal{J}^m surface current densities producing true fields \mathbf{E} , \mathbf{H} in V and zero fields outside V . (d) Generalized surface equivalence principle exterior to V with fictitious electric \mathbf{J}^e and magnetic \mathbf{J}^m surface current densities (single source amenable) producing true fields \mathbf{E} , \mathbf{H} outside V and unconstrained fields \mathbf{E}_{in} and \mathbf{H}_{in} in V . (e) Generalized surface equivalence principle interior to V with fictitious electric \mathbf{J}^e and magnetic \mathbf{J}^m surface current densities (single source amenable) producing true fields \mathbf{E} , \mathbf{H} in V and unconstrained fields \mathbf{E}_{∞} , \mathbf{H}_{∞} outside V . (f) Volume equivalence principle (true fields \mathbf{E}_0 , \mathbf{H}_0 in V_{∞} and \mathbf{E} , \mathbf{H} in V produced by volume polarization current \mathbf{j} in V).

$$\begin{aligned}
 \mathbf{H}^{\text{inc}}(\mathbf{r}) - \oint_{\partial V} \overline{\overline{G}}_{m0}(\mathbf{r}, \mathbf{r}') \cdot \mathcal{J}^e(\mathbf{r}') ds' \\
 - i\omega\epsilon_0 \oint_{\partial V} \overline{\overline{G}}_{e0}(\mathbf{r}, \mathbf{r}') \cdot \mathcal{J}^m(\mathbf{r}') ds' = \begin{cases} \mathbf{H}(\mathbf{r}), & \mathbf{r} \in V_\infty \setminus \partial V, \\ \mathbf{0}, & \mathbf{r} \in V \setminus \partial V, \end{cases}
 \end{aligned} \tag{1.2}$$

where $\overline{\overline{G}}_{e0}(\mathbf{r}, \mathbf{r}') = (k_0^{-2} \nabla \nabla + \overline{\overline{I}}) e^{-ik_0 |\mathbf{r} - \mathbf{r}'|} / (4\pi |\mathbf{r} - \mathbf{r}'|)$ is the electric field 3-D dyadic Green's function of free space which satisfies inhomogeneous dyadic wave equation

$$\nabla \times \nabla \times \overline{\overline{G}}_{e0}(\mathbf{r}, \mathbf{r}') - k_0^2 \overline{\overline{G}}_{e0}(\mathbf{r}, \mathbf{r}') = \overline{\overline{I}} \delta(\mathbf{r} - \mathbf{r}'). \tag{1.3}$$

where k_0 is the wavenumber and $\overline{\overline{I}}$ is the idem-factor. In (1.1) and (1.2) the equivalent surface electric current density $\mathcal{J}^e = \hat{\mathbf{n}} \times \mathbf{H}$ defined on boundary ∂V as the tangential component of the true magnetic field \mathbf{H} outside V . The equivalent surface magnetic current density $\mathcal{J}^m = -\hat{\mathbf{n}} \times \mathbf{E}$ defined on boundary ∂V as the tangential component of the true electric field \mathbf{E} outside V . Also, $\overline{\overline{G}}_{m0}(\mathbf{r}, \mathbf{r}') = \nabla \times \overline{\overline{G}}_{e0}(\mathbf{r}, \mathbf{r}')$ is the magnetic field dyadic Green's function of free space. The physical meaning of the above is that the total fields $\mathbf{E}(\mathbf{r})$ and $\mathbf{H}(\mathbf{r})$ outside the volume V is generated by the true source outside V (here is \mathbf{E}^{inc}) as well as the equivalence surface currents \mathcal{J}^e and \mathcal{J}^m impressed on the boundary ∂V .

1.1.2 Traditional interior surface equivalence principle

Similarly, the total field $\mathbf{E}(\mathbf{r})$ and $\mathbf{H}(\mathbf{r})$ inside the volume V can be defined using interior to V surface equivalence principle (Fig. 1.1(c))

$$\begin{aligned}
 -i\omega\mu_0 \oint_{\partial V} \overline{\overline{G}}_{ee}(\mathbf{r}, \mathbf{r}') \cdot \mathcal{J}^e(\mathbf{r}') ds' \\
 - \oint_{\partial V} \overline{\overline{G}}_{me}(\mathbf{r}, \mathbf{r}') \cdot \mathcal{J}^m(\mathbf{r}') ds' = \begin{cases} \mathbf{0}, & \mathbf{r} \in V_\infty \setminus \partial V, \\ \mathbf{E}(\mathbf{r}), & \mathbf{r} \in V \setminus \partial V, \end{cases}
 \end{aligned} \tag{1.4}$$

$$\begin{aligned}
 & \oint_{\partial V} \overline{\overline{G}}_{m\epsilon}(\mathbf{r}, \mathbf{r}') \cdot \mathcal{J}^e(\mathbf{r}') ds' \\
 & + i\omega\epsilon \oint_{\partial V} \overline{\overline{G}}_{e\epsilon}(\mathbf{r}, \mathbf{r}') \cdot \mathcal{J}^m(\mathbf{r}') ds' = \begin{cases} \mathbf{0}, & \mathbf{r} \in V_\infty \setminus \partial V, \\ \mathbf{H}(\mathbf{r}), & \mathbf{r} \in V \setminus \partial V, \end{cases} \quad (1.5)
 \end{aligned}$$

where $\overline{\overline{G}}_{e\epsilon}(\mathbf{r}, \mathbf{r}') = (k_\epsilon^{-2} \nabla \nabla + \overline{\overline{I}}) e^{-ik_\epsilon |\mathbf{r} - \mathbf{r}'|} / (4\pi |\mathbf{r} - \mathbf{r}'|)$ is the electric field 3-D dyadic Green's function of homogeneous medium with complex relative permittivity of ϵ which satisfies inhomogeneous dyadic wave equation

$$\nabla \times \nabla \times \overline{\overline{G}}_{e\epsilon}(\mathbf{r}, \mathbf{r}') - k_\epsilon^2 \overline{\overline{G}}_{e\epsilon}(\mathbf{r}, \mathbf{r}') = \overline{\overline{I}} \delta(\mathbf{r} - \mathbf{r}'), \quad (1.6)$$

where $k_\epsilon = k_0 \sqrt{\epsilon}$ is the wavenumber of the homogeneous medium.

Moreover, the total field is zero if the observation point is located inside the scatterer, which is given by the lower part of the right-hand side of (1.1) and (1.2). This is known as the *extinction theorem* which implies that the equivalent surface electric and magnetic currents generate a field that cancels \mathbf{E}^{inc} inside the scatterer. Similarly, the total field is zero if the observation point is located outside V , which is given by the upper part of the right-hand side of (1.4) and (1.5).

1.1.3 Generalized exterior surface equivalence principle

The generalized exterior equivalence principle allows the field inside the scatterer to be arbitrary (Fig. 1.1(d)), instead of being forced to zero as in the traditional equivalence exterior integral representation in (1.1) and (1.2) [11]. Detailed justification for generalized integral field representation the reader can find in [46]. Thus, for the total field $\mathbf{E}(\mathbf{r})$ and $\mathbf{H}(\mathbf{r})$ outside the volume V we have the following formulations as the generalized exterior equivalence representation

$$\begin{aligned}
 & \mathbf{E}^{\text{inc}}(\mathbf{r}) + i\omega\mu_0 \oint_{\partial V} \overline{\overline{G}}_{e0}(\mathbf{r}, \mathbf{r}') \cdot \mathbf{J}^e(\mathbf{r}') ds' \\
 & + \oint_{\partial V} \overline{\overline{G}}_{m0}(\mathbf{r}, \mathbf{r}') \cdot \mathbf{J}^m(\mathbf{r}') ds' = \begin{cases} \mathbf{E}(\mathbf{r}), & \mathbf{r} \in V_\infty \setminus \partial V, \\ \mathbf{E}_{\text{in}}(\mathbf{r}), & \mathbf{r} \in V \setminus \partial V, \end{cases} \quad (1.7)
 \end{aligned}$$

$$\begin{aligned}
 \mathbf{H}^{\text{inc}}(\mathbf{r}) - \oint_{\partial V} \overline{\overline{\mathbf{G}}}_{m0}(\mathbf{r}, \mathbf{r}') \cdot \mathbf{J}^e(\mathbf{r}') ds' \\
 - i\omega\varepsilon_0 \oint_{\partial V} \overline{\overline{\mathbf{G}}}_{e0}(\mathbf{r}, \mathbf{r}') \cdot \mathbf{J}^m(\mathbf{r}') ds' = \begin{cases} \mathbf{H}(\mathbf{r}), & \mathbf{r} \in V_\infty \setminus \partial V, \\ \mathbf{H}_{\text{in}}(\mathbf{r}), & \mathbf{r} \in V \setminus \partial V. \end{cases} \quad (1.8)
 \end{aligned}$$

In (1.7) and (1.8), $\mathbf{J}^e = \hat{n} \times [\mathbf{H} - \mathbf{H}_{\text{in}}]$ is the fictitious equivalent surface electric current density which introduces the jump on boundary ∂V between the tangential component of the true magnetic field \mathbf{H} outside V and unconstrained magnetic field \mathbf{H}_{in} inside V . Also, $\mathbf{J}^m = -\hat{n} \times [\mathbf{E} - \mathbf{E}_{\text{in}}]$ is the fictitious equivalent surface magnetic current density which introduces the jump on boundary ∂V between the tangential component of the true electric field \mathbf{E} outside the object and unconstrained electric field \mathbf{E}_{in} inside the object.

1.1.4 Generalized interior surface equivalence principle

Similarly, the generalized interior equivalence principle (Fig. 1.1(e)) allow us to represent the total field $\mathbf{E}(\mathbf{r})$ and $\mathbf{H}(\mathbf{r})$ inside the volume V as

$$\begin{aligned}
 -i\omega\mu_0 \oint_{\partial V} \overline{\overline{\mathbf{G}}}_{ee}(\mathbf{r}, \mathbf{r}') \cdot \mathbf{J}^e(\mathbf{r}') ds' \\
 - \oint_{\partial V} \overline{\overline{\mathbf{G}}}_{me}(\mathbf{r}, \mathbf{r}') \cdot \mathbf{J}^m(\mathbf{r}') ds' = \begin{cases} \mathbf{E}_\infty(\mathbf{r}), & \mathbf{r} \in V_\infty \setminus \partial V, \\ \mathbf{E}(\mathbf{r}), & \mathbf{r} \in V \setminus \partial V, \end{cases} \quad (1.9)
 \end{aligned}$$

$$\begin{aligned}
 \oint_{\partial V} \overline{\overline{\mathbf{G}}}_{me}(\mathbf{r}, \mathbf{r}') \cdot \mathbf{J}^e(\mathbf{r}') ds' \\
 + i\omega\varepsilon \oint_{\partial V} \overline{\overline{\mathbf{G}}}_{ee}(\mathbf{r}, \mathbf{r}') \cdot \mathbf{J}^m(\mathbf{r}') ds' = \begin{cases} \mathbf{H}_\infty(\mathbf{r}), & \mathbf{r} \in V_\infty \setminus \partial V, \\ \mathbf{H}(\mathbf{r}), & \mathbf{r} \in V \setminus \partial V, \end{cases} \quad (1.10)
 \end{aligned}$$

where $\mathbf{J}^e = \hat{n} \times [\mathbf{H} - \mathbf{H}_\infty]$ is the fictitious equivalent surface electric current density defined on boundary ∂V which introduces the jump between the tangential component of the true magnetic field \mathbf{H} inside the object and unconstrained magnetic field \mathbf{H}_∞ outside the object. Also, $\mathbf{J}^m = -\hat{n} \times [\mathbf{E} - \mathbf{E}_\infty]$ is the fictitious equivalent surface magnetic current density defined on boundary ∂V which introduces the jump between

the tangential component of the true electric field \mathbf{E} inside ∂V and unconstrained electric field \mathbf{E}_∞ outside ∂V .

1.1.5 Single-source representation of the generalized surface equivalence principle

The ambiguity in the definition of the unconstrained electric and magnetic fields inside the objects in (1.7) and (1.8) allows to represent the fictitious equivalent currents in terms of a single fictitious equivalent currents $\mathbf{J} = \hat{\mathbf{t}}J_0$ as $\mathbf{J}^e = a\mathbf{J}$ and $\mathbf{J}^m = b\hat{\mathbf{n}} \times \mathbf{J}$, where a and b are constants and $\hat{\mathbf{t}}$ is the tangential vector to the surface ∂V . The reader can find detailed justification for such single-source field representation (also known as “combined source” representation [47]) in [46] and [14]. Therefore, the generalized exterior equivalence principle (1.7) and (1.8) can be represented in the form of a single-source field representation, as follows:

$$\begin{aligned} \mathbf{E}^{\text{inc}}(\mathbf{r}) + i\omega\mu_0 \oint_{\partial V} \overline{\overline{\mathbf{G}}}_{e0}(\mathbf{r}, \mathbf{r}') \cdot a\mathbf{J}(\mathbf{r}') ds' \\ + \oint_{\partial V} \overline{\overline{\mathbf{G}}}_{m0}(\mathbf{r}, \mathbf{r}') \cdot b\hat{\mathbf{n}} \times \mathbf{J}(\mathbf{r}') ds' = \begin{cases} \mathbf{E}(\mathbf{r}), & \mathbf{r} \in V_\infty \setminus \partial V, \\ \mathbf{E}_{\text{in}}(\mathbf{r}), & \mathbf{r} \in V \setminus \partial V, \end{cases} \end{aligned} \quad (1.11)$$

$$\begin{aligned} \mathbf{H}^{\text{inc}}(\mathbf{r}) - \oint_{\partial V} \overline{\overline{\mathbf{G}}}_{m0}(\mathbf{r}, \mathbf{r}') \cdot a\mathbf{J}(\mathbf{r}') ds' \\ - i\omega\varepsilon_0 \oint_{\partial V} \overline{\overline{\mathbf{G}}}_{e0}(\mathbf{r}, \mathbf{r}') \cdot b\hat{\mathbf{n}} \times \mathbf{J}(\mathbf{r}') ds' = \begin{cases} \mathbf{H}(\mathbf{r}), & \mathbf{r} \in V_\infty \setminus \partial V, \\ \mathbf{H}_{\text{in}}(\mathbf{r}), & \mathbf{r} \in V \setminus \partial V. \end{cases} \end{aligned} \quad (1.12)$$

Similarly, the generalized interior equivalence principle (1.9) and (1.10) can also be represented in the form of a single-source field representation, as follows:

$$\begin{aligned}
 & -i\omega\mu_0 \oint_{\partial V} \overline{\overline{G}}_{e\epsilon}(\mathbf{r}, \mathbf{r}') \cdot a\mathbf{J}(\mathbf{r}') ds' \\
 & - \oint_{\partial V} \overline{\overline{G}}_{m\epsilon}(\mathbf{r}, \mathbf{r}') \cdot b\hat{\mathbf{n}} \times \mathbf{J}(\mathbf{r}') ds' = \begin{cases} \mathbf{E}_\infty(\mathbf{r}), & \mathbf{r} \in V_\infty \setminus \partial V, \\ \mathbf{E}(\mathbf{r}), & \mathbf{r} \in V \setminus \partial V, \end{cases} \quad (1.13)
 \end{aligned}$$

$$\begin{aligned}
 & \oint_{\partial V} \overline{\overline{G}}_{m\epsilon}(\mathbf{r}, \mathbf{r}') \cdot a\mathbf{J}(\mathbf{r}') ds' \\
 & + i\omega\epsilon \oint_{\partial V} \overline{\overline{G}}_{e\epsilon}(\mathbf{r}, \mathbf{r}') \cdot b\hat{\mathbf{n}} \times \mathbf{J}(\mathbf{r}') ds' = \begin{cases} \mathbf{H}_\infty(\mathbf{r}), & \mathbf{r} \in V_\infty \setminus \partial V, \\ \mathbf{H}(\mathbf{r}), & \mathbf{r} \in V \setminus \partial V. \end{cases} \quad (1.14)
 \end{aligned}$$

In our previous works [13], [14] and this thesis, the particular case of $a = 1$ and $b = 0$ are considered for (1.11)-(1.14) which yields these formulations consisting of only the E -field operators. Hence, (1.11) and (1.12) can be rewritten as

$$\mathbf{E}^{\text{inc}}(\mathbf{r}) + i\omega\mu_0 \oint_{\partial V} \overline{\overline{G}}_{e0}(\mathbf{r}, \mathbf{r}') \cdot \mathbf{J}(\mathbf{r}') ds' = \begin{cases} \mathbf{E}(\mathbf{r}), & \mathbf{r} \in V_\infty \setminus \partial V, \\ \mathbf{E}_{\text{in}}(\mathbf{r}), & \mathbf{r} \in V \setminus \partial V, \end{cases} \quad (1.15)$$

$$\mathbf{H}^{\text{inc}}(\mathbf{r}) - \oint_{\partial V} \overline{\overline{G}}_{m0}(\mathbf{r}, \mathbf{r}') \cdot \mathbf{J}(\mathbf{r}') ds' = \begin{cases} \mathbf{H}(\mathbf{r}), & \mathbf{r} \in V_\infty \setminus \partial V, \\ \mathbf{H}_{\text{in}}(\mathbf{r}), & \mathbf{r} \in V \setminus \partial V. \end{cases} \quad (1.16)$$

Similarly, expressions (1.13) and (1.14) can be rewritten as

$$-i\omega\mu_0 \oint_{\partial V} \overline{\overline{G}}_{e\epsilon}(\mathbf{r}, \mathbf{r}') \cdot \mathbf{J}(\mathbf{r}') ds' = \begin{cases} \mathbf{E}_\infty(\mathbf{r}), & \mathbf{r} \in V_\infty \setminus \partial V, \\ \mathbf{E}(\mathbf{r}), & \mathbf{r} \in V \setminus \partial V, \end{cases} \quad (1.17)$$

$$\oint_{\partial V} \overline{\overline{G}}_{m\epsilon}(\mathbf{r}, \mathbf{r}') \cdot \mathbf{J}(\mathbf{r}') ds' = \begin{cases} \mathbf{H}_\infty(\mathbf{r}), & \mathbf{r} \in V_\infty \setminus \partial V, \\ \mathbf{H}(\mathbf{r}), & \mathbf{r} \in V \setminus \partial V, \end{cases} \quad (1.18)$$

where in (1.15)-(1.18) $\mathbf{J}(\mathbf{r}) = \hat{\mathbf{t}}(\mathbf{r})J_0(\mathbf{r})$ is the fictitious unknown function defined on the boundary ∂V [46]. The above expressions are used to derive the SVS-EFIE as discussed next.

1.1.6 Volume equivalence principle

The electric field inside and outside the penetrable scatterers can be defined as an integral over the volume polarization current density (Fig. 1.1(f)) [11]

$$\mathbf{E}(\mathbf{r}) = \mathbf{E}^{\text{inc}}(\mathbf{r}) + \int_V \overline{\overline{\mathbf{G}}}_{e0}(\mathbf{r}, \mathbf{r}') \cdot \mathbf{j}(\mathbf{r}') dv', \quad \mathbf{r} \in V, V_\infty, \quad (1.19)$$

where $\mathbf{j}(\mathbf{r}) = k_0^2(\epsilon - 1)\mathbf{E}(\mathbf{r})$ is the polarization current density inside V with complex relative permittivity of ϵ .

1.1.7 Surface-volume-surface electric field integral equation derivation

In [13], [14], we have introduced a single-source integral equations known as SVS-EFIE. To derive the SVS-EFIE, the single source surface field representation throughout the volume of a dielectric scatterer is constrained using volume equivalence principle instead of the traditional constraining of it with the surface equivalence principle [46]. Therefore, substitution of the interior single source field representation (1.17) into the volume equivalence principle (1.19) followed by the restriction of the observation point to the boundary of the scatterer from inside V yields the desired SVS-EFIE

$$\begin{aligned} & -i\omega\mu_0\hat{\mathbf{t}} \cdot \oint_{\partial V} \overline{\overline{\mathbf{G}}}_{e\epsilon}(\mathbf{r}, \mathbf{r}') \cdot \mathbf{J}(\mathbf{r}') ds' + i\omega\mu_0k_0^2(\epsilon - 1)\hat{\mathbf{t}} \cdot \\ & \int_V \overline{\overline{\mathbf{G}}}_{e0}(\mathbf{r}, \mathbf{r}') \cdot \oint_{\partial V} \overline{\overline{\mathbf{G}}}_{e\epsilon}(\mathbf{r}', \mathbf{r}'') \cdot \mathbf{J}(\mathbf{r}'') ds'' dv' = \hat{\mathbf{t}} \cdot \mathbf{E}^{\text{inc}}(\mathbf{r}), \quad \mathbf{r} \in \partial V. \end{aligned} \quad (1.20)$$

where $\hat{\mathbf{t}}$ is the tangential vector to the boundary ∂V . Note, since \mathbf{J} is a tangential vector function defined on the boundary of the scatterer, therefore, in order to balance the range and domain of the SVS-EFIE in (1.20), the V-EFIE has to be satisfied only for the observation point on the boundary ∂V .

In general, SVS-EFIE (1.20) is a class of SSIEs while in this thesis is used for the solution of electromagnetic wave scattering and radiation problems. The SVS-EFIE (1.20) has several advantages over the other traditional IEs. First, it only features the electric field dyadic Green's function which due to its derivative-free MoM discretization, it is particularly advantageous for solution of the problems with object situated in a multilayered media. Therefore, SVS-EFIE does not required extra accuracy in evaluation of costly Sommerfeld integrals [37]. This property of SVS-EFIE improves the efficiency and flexibility of the proposed layered medium formulation combined with the fast \mathcal{H} -matrix framework used for acceleration of pertinent MoM blocks as it enables the MoM matrix corresponding to well-separated clusters of the basis and test functions situated in multilayered medium remain well compressible. In chapter 5, such compressibility is observed when the ACA tolerance is set to be above the error level associated with the error occurring during numerical evaluation of the layered medium Green's function values and evaluation of MoM reaction integrals. Note, that the PMCHWT, EFIE, MFIE and Muller formulations also feature magnetic current density as the unknown function in addition to the electric current density. As a result, they require magnetic field dyadic Green's function which introduces extra layered media Green's function kernels and requires evaluation of the derivatives from the curl operator [37]. The latter cannot be fully eliminated through the use of either gradient or divergence theorems. As a result, those derivatives from curl operator have to be either moved inside the Sommerfeld integrals and slow down their convergence or be evaluated numerically after the Sommerfeld integrals are computed. In this case, one needs extra accuracy in evaluation of the already costly Sommerfeld integrals since the differential operators act as amplifiers of the error in the numerically evaluated Green's function kernels. Second, the SVS-EFIE features fewer integral operators than the alternative SSIEs [14]. Third, the SVS-EFIE formulations for composite dielectric-dielectric objects in chapter 3 and composite metal-dielectric objects in chapter 4 introduce independent electric surface current densities on the boundaries of regions, therefore the corresponding regions can be meshed independently according to their respective material properties. This property of SVS-EFIE eliminates the difficulties associated with representation of

the surface current densities at material junctions featured in the traditional SIEs and allows to generate non-conformal meshes. However, in SVS-EFIE, due to the field translations performed from surface to volume domains and back, the proposed formulations require the discretization of both surface and volume of the dielectric objects unlike the PMCHWT formulation with being purely surface discretization approach.

1.2 Outline of Thesis

This thesis has 6 chapters synopsis of which is provided below:

- **Chapter 1:** The introduction of the thesis is given. Also, a brief background of SVS-EFIE is reviewed and its formulation is derived to the case of a 3-D homogeneous dielectric object in free space.
- **Chapter 2:** The implementation of the \mathcal{H} -matrix framework for fast direct and iterative MoM solution of the SVS-EFIE for scattering and radiation problems of 3-D homogeneous dielectric object is explained in detail. Also, the \mathcal{H} -matrix arithmetic and the computational complexity of the proposed solver is derived.
- **Chapter 3:** The new SVS-EFIE formulation followed by the \mathcal{H} -matrix acceleration to the case of 3-D composite dielectric objects made of arbitrary number of piece-wise homogeneous dielectric regions is discussed. The computational complexity of the proposed solver is derived.
- **Chapter 4:** The new formulation of the SVS-EFIE is developed for the electromagnetic analysis of the 3-D general composite structures of metallic and homogeneous dielectric made of multiple regions as well as its \mathcal{H} -matrix acceleration of MoM solution.
- **Chapter 5:** The new formulation of the SVS-EFIE and its acceleration using \mathcal{H} -matrix is developed for the case of multi-region composite dielectric objects situated in the layered medium.

-
- **Chapter 6:** In order to extend the application of the proposed \mathcal{H} -matrix framework in chapter 4 and 5 to the case of HO solution of scattering and radiation problems, a new fast direct error-controlled solver based on the \mathcal{H} -matrix acceleration of the HO-LCN discretization of the MFIE is developed and discussed in detail.

2

\mathcal{H} -Matrix Arithmetic for Fast Direct and Iterative Method of Moment Solution of Surface-Volume-Surface EFIE for 3-D Radiation Problems

©2018 PIERS B. Reprinted, with permission, from *Reza Gholami, Jamiu Mojolagbe, Anton Menshov, Farhad Sheikh Hosseini Lori, and Vladimir Okhmatovski, Progress In Electromagnetics Research B, Dec. 2018.*

2.1 Abstract

Hierarchical (\mathcal{H})-matrix based fast direct and iterative algorithms are presented for acceleration of the method of moments (MoM) solution of the surface-volume-surface electric field integral equation (SVS-EFIE) formulated for scattering and radiation problems on homogeneous dielectric objects. As the SVS-EFIE features the product of the integral operator mapping the tangential equivalent electric current on the surface of the scatterer to the volume polarization current and the integral operator

mapping the volume polarization current to the tangential component of the scattered electric field, its MoM discretization produces the product of non-square matrices. Formation of the non-square \mathcal{H} -matrices for the MoM discretized integral operators is described. The algorithms for arithmetics pertinent to the product of the non-square \mathcal{H} -matrices are explained. The memory and CPU time complexity scaling of the required \mathcal{H} -matrix operations are analyzed in detail and verified numerically. The numerical validation of the proposed algorithm is provided for both the low-loss dielectric objects as well as for the high-loss biological tissues found in the bioelectromagnetics (BioEM) applications. The numerical experiments demonstrate a significant reduction of memory usage and a considerable speedup for CPU time compared to naïve MoM, thus, enabling solution of the large-scale scattering and radiation problems with the SVS-EFIE.

2.2 Introduction

Electromagnetic field interactions with the biological tissues occur in many natural and staged scenarios ranging from involuntary human body exposures to the natural and man-made sources of RF and microwave radiation [48] to the near field radiation of the mobile [49], wearable and implanted antennas [50] or biomedical imaging systems [1]. Understanding, prediction, and control of such interactions is becoming of paramount importance in the design of the novel body mounted communication systems [3] and sensor networks [51], setting up the Internet-of-Things connected home and office spaces [52], development of smart antennas for 5G systems [4], and many other practical applications [2].

The limiting capabilities of the non-invasive experimental techniques for studies of field-to-body interactions motivate development of computational methods [7] for accurate virtual prototyping of such phenomenon. Due to significant inhomogeneity of the biological tissues, the methods of computational electromagnetics (CEM) based on the direct discretization of the Maxwell Equations such as Finite-Difference Time-Domain (FDTD) [8] and discretization of the wave equations such as the Finite Element Method (FEM) [9] have become the most popular approaches for bioelectro-

magnetics (BioEM) analysis with various commercial tools available [53, 54]. While FDTD and FEM offer great versatility and simplicity in implementation and parallelization, they are plagued by fundamental limitations of error accumulation when propagation of wave phenomena over electrically large distances is analyzed [15] and necessity to discretize the space outside the regions of interest [9]. Integral equations (IEs) of CEM discretized with Method of Moments (MoM) [10] establish computational frameworks free of these disadvantages. The discretization of the IEs, however, results in the dense matrix equations which require development of sophisticated fast algorithms [15] in order to reduce the CPU time and memory complexity associated with their solution. The detailed comparisons in terms of the achieved accuracy and used computational resources between the differential and integral equations based approaches in application to solution of the BioEM problems can be found in [55].

The development of fast algorithms aiding iterative solutions of the dense matrix equations [25, 26] which result from the discretization of the IEs has reached a certain maturity [15] with Multi-Level-Fast-Multipole-Method (MLFMM) [16–19], FFT-based methods [20–22], and Adaptive Cross Approximation (ACA) [23, 24] methods dominating the field. The grand challenge in use of the fast iterative algorithms though is in development of appropriate preconditioning schemes which ensure sufficiently rapid convergence under conditions of multiscale discretization, high disparity in the material properties, and broad range of frequencies. To date development of such preconditioning schemes has been met with only partial success and remains a rather 'black art' than science [56].

The recent efforts in circumventing this grand challenge posed by the lack of robustness in the iterative schemes for the solution of the dense matrix equations has been in the two areas. First, is the construction of well-conditioned IE formulations and their appropriate discretization schemes [57–61]. Second, is the development of the fast methods for direct solution of the dense matrix equations [27–34]. The non-iterative nature of the latter allows them to remain largely insensitive to the deterioration of the IEs conditioning stemming from the multiscaling and other factors and, hence, provide robust computational schemes under conditions where traditional iterative schemes fail.

In this work, we develop a hierarchical (\mathcal{H})-matrix [27, 36, 62] based method of moments (MoM) frameworks for solution of the surface-volume-surface electric field integral equation (SVS-EFIE) which we recently introduced for analysis of the scattering problems on dielectric objects [13, 37, 38, 63]. The SVS-EFIE is a class of Single-Source Surface Integral Equations (SSSIE) [46, 64] which reduces the number of unknowns by half compared to the traditional surface integral-equation formulations [65, 66]. It features only one product of electric-field type integral operators and allows for a mixed potential formulation free of hyper-singular integrals under MoM discretization. These benefits of the SVS-EFIE come at an extra cost of computing field translations from the scatterer surface to its volume and then from its volume back to the surface. In the bio-electromagnetics (BioEM) applications, computation of the field throughout the volume of the lossy body tissues is typically required for determining of the specific absorption rate, depth of field penetration, and localization of the high field concentration areas making SVS-EFIE particularly suitable [63] for solution of such problems. Due to field translation to the volume of the object of interest, discretization of both surface and volume field quantities takes place in the SVS-EFIE. As such, the memory requirements and computational complexity of dense matrix operations and storage for naïve MoM solution of the SVS-EFIE become prohibitive for tackling of practically important problems. To reduce the computational and memory costs, \mathcal{H} -matrix based fast direct and iterative solvers are developed in this work to accelerate MoM solution of the SVS-EFIE for 3-D scattering and radiation problems on dielectric objects.

2.3 Formulations and Equations of SVS-EFIE and Its MoM Solution

In our previous work [13, 63], we introduced a new type of a SSSIE by combining the ideas of the traditional volume equivalence principle and the theory of the SSIEs. The SVS-EFIE formulation for 3-D scattering problem is given by (2.1), where \mathbf{r} is an observation location on the scatterer boundary ∂V , \mathbf{r}' is the position-vector

of the total electric field inside the scatterer, and complex relative permittivity ϵ is $\epsilon = \varepsilon + \sigma/(i\omega\varepsilon_0)$. In 2.1, $\hat{\mathbf{t}}$ is the tangential vector to the scatterer surface ∂V and ω is the cyclic frequency.

$$i\omega\mu_0\hat{\mathbf{t}} \cdot \left(- \oint_{\partial V} \overline{\overline{G}}_\epsilon(\mathbf{r}, \mathbf{r}'') \cdot \mathbf{J}(\mathbf{r}'') ds'' + k_0^2 (\epsilon - 1) \int_V \overline{\overline{G}}_0(\mathbf{r}, \mathbf{r}') \cdot \oint_{\partial V} \overline{\overline{G}}_\epsilon(\mathbf{r}', \mathbf{r}'') \cdot \mathbf{J}(\mathbf{r}'') ds'' dv' \right) = \hat{\mathbf{t}} \cdot \mathbf{E}^{\text{inc}}(\mathbf{r}), \quad \mathbf{r} \in \partial V. \quad (2.1)$$

It is convenient to express (2.1) in the integral-operator form

$$- \underbrace{\left(\mathcal{T}_{\epsilon, \nabla\Phi}^{\partial V, \partial V} + \mathcal{T}_{\epsilon, A}^{\partial V, \partial V} \right)}_{\mathcal{T}_\epsilon^{\partial V, \partial V}} \circ \mathbf{J} + \underbrace{\left(\mathcal{T}_{0, \nabla\varphi}^{\partial V, V} + \mathcal{T}_{0, a}^{\partial V, V} \right)}_{\mathcal{T}_0^{\partial V, V}} \circ \underbrace{\left(\mathcal{T}_{\epsilon, \nabla\Phi}^{V, \partial V} + \mathcal{T}_{\epsilon, A}^{V, \partial V} \right)}_{\mathcal{T}_\epsilon^{V, \partial V}} \circ \mathbf{J} = \hat{\mathbf{t}} \cdot \mathbf{E}^{\text{inc}}, \quad (2.2)$$

where $\mathcal{T}_\epsilon^{\partial V, \partial V}$, $\mathcal{T}_0^{\partial V, V}$, and $\mathcal{T}_\epsilon^{V, \partial V}$ are surface-to-surface, volume-to-surface, and surface-to-volume operators, respectively. Operators $\mathcal{T}_\epsilon^{\partial V, \partial V}$, $\mathcal{T}_0^{\partial V, V}$, and $\mathcal{T}_\epsilon^{V, \partial V}$ in (2.2) are composed as a sum of two integral operators corresponding to the scalar and vector potentials and are defined as follows:

$$\left(-P \left\{ \begin{array}{c} P \\ \mathbf{Z}_\epsilon^{\partial V, \partial V} \end{array} \right\} + \begin{array}{c} 3N \\ \mathbf{Z}_0^{\partial V, V} \cdot \Gamma^{-1} \end{array} \right) \cdot \begin{array}{c} P \\ \mathbf{Z}_\epsilon^{V, \partial V} \\ 3N \end{array} \cdot \begin{array}{c} I \\ \mathcal{V} \end{array} = \mathcal{V}$$

Figure 2.1: System of linear equations structure resulting from MoM discretization of the SVS-EFIE (2.1). Here, P is the number of RWG basis functions on the boundary ∂V and N is the number of tetrahedron elements in the volume V .

$$\mathcal{T}_{\epsilon, \Phi}^{\partial V, \partial V} \circ \mathbf{J} = \frac{i\omega\mu_0}{k_\epsilon^2} \oint_{\partial V} G_\epsilon(\mathbf{r}, \mathbf{r}'') \nabla_s'' \cdot \mathbf{J}(\mathbf{r}'') ds'', \quad (2.3)$$

$$\mathcal{T}_{\epsilon, A}^{\partial V, \partial V} \circ \mathbf{J} = i\omega\mu_0 \hat{\mathbf{t}} \cdot \oint_{\partial V} G_\epsilon(\mathbf{r}, \mathbf{r}'') \mathbf{J}(\mathbf{r}'') ds'', \quad (2.4)$$

$$\mathcal{T}_{\epsilon, \nabla \Phi}^{V, \partial V} \circ \mathbf{J} = \frac{i\omega\mu_0}{k_\epsilon^2} \oint_{\partial V} \nabla' G_\epsilon(\mathbf{r}', \mathbf{r}'') \nabla_s'' \cdot \mathbf{J}(\mathbf{r}'') ds'', \quad (2.5)$$

$$\mathcal{T}_{\epsilon, A}^{V, \partial V} \circ \mathbf{J} = i\omega\mu_0 \oint_{\partial V} G_\epsilon(\mathbf{r}', \mathbf{r}'') \mathbf{J}(\mathbf{r}'') ds'', \quad (2.6)$$

$$\mathcal{T}_{0, \varphi}^{\partial V, V} \circ \mathbf{j} = \frac{1}{k_0^2} \int_V \nabla G_0(\mathbf{r}, \mathbf{r}') \cdot \mathbf{j}(\mathbf{r}') dv', \quad (2.7)$$

$$\mathcal{T}_{0, a}^{\partial V, V} \circ \mathbf{j} = \hat{\mathbf{t}} \cdot \int_V G_0(\mathbf{r}, \mathbf{r}') \mathbf{j}(\mathbf{r}') dv', \quad (2.8)$$

$$\mathbf{r} \in \partial V, \quad \mathbf{r}' \in V,$$

where $\mathbf{j} = k_0^2(\epsilon - 1)\mathbf{E}$ is polarization current density defined inside the object and $\nabla_s \cdot$ denotes surface divergence. Also, in (2.2) $\mathcal{T}_{\epsilon, \nabla \Phi}^{\partial V, \partial V} = \hat{\mathbf{t}} \cdot \nabla \mathcal{T}_{\epsilon, \Phi}^{\partial V, \partial V}$ and $\mathcal{T}_{0, \nabla \varphi}^{\partial V, V} = \hat{\mathbf{t}} \cdot \nabla \mathcal{T}_{0, \varphi}^{\partial V, V}$.

In order to solve SVS-EFIE (2.1) with MoM, the volume of the scatterer V is discretized with a 3-D mesh consisting of N tetrahedron elements and its surface ∂V is discretized with a 2-D mesh consisting of M triangle elements. Discretization of the

unknown tangential weighting function \mathbf{J} defined on the boundary ∂V is performed over P Rao-Wilton-Glisson (RWG) basis functions [67] as

$$\mathbf{J}(\mathbf{r}'') \cong \sum_{m''=1}^P I_{m''} \mathbf{t}_{m''}(\mathbf{r}''). \quad (2.9)$$

Following the standard MoM procedure (described in detail in [13]), the SVS-EFIE is reduced to the set of linear algebraic equations with respect to the unknown coefficients vector I in the expansion of the unknown surface weighting function in (2.9). The MoM matrix equation structure is shown in Fig 2.1.

The surface-to-surface impedance matrix $\mathbf{Z}_\epsilon^{\partial V, \partial V}$ corresponding to the operator $\mathcal{T}_\epsilon^{\partial V, \partial V}$ is a $P \times P$ square matrix since the surface ∂V serves as support for both the domain and range of $\mathcal{T}_\epsilon^{\partial V, \partial V}$. The x , y , and z components of $\mathbf{Z}_0^{\partial V, V}$, translating the volume polarization current to the tangential component of the scattered electric field and $\mathbf{Z}_\epsilon^{V, \partial V}$ translating the unknown tangential weighting source function to the total field inside the scatterer are handled separately and result in $P \times 3N$ and $3N \times P$ sized matrices. These matrices have rectangular structure since their continuous counterparts have different range and domain supports: ∂V and V for $\mathcal{T}_0^{\partial V, V}$ and V and ∂V for $\mathcal{T}_\epsilon^{V, \partial V}$, respectively. In Fig. 2.1, Γ is the Gram matrix with elements of $\Gamma_{n, n'} = V_n$, if $n = n'$ and zero, otherwise, $n = 1, \dots, N$. Here, V_n is the volume of the n th tetrahedron element.

2.4 \mathcal{H} -Matrix Acceleration of MoM Solution

Blocks of the MoM matrices corresponding to far interactions can be compressed using Adaptive Cross Approximation (ACA) [23, 24] or other low-rank factorization methods [68, 69] allowing for significant reduction of storage requirements and fast arithmetic in \mathcal{H} -matrix format, including \mathcal{H} -LU decomposition and matrix-vector product (MVP) for the fast direct and fast iterative solution of the SVS-EFIE, respectively. Since the SVS-EFIE (2.2) involves a product of integral operators with range and domain supports being different, the \mathcal{H} -matrix based MoM solution of

the SVS-EFIE (2.1) requires operations with rectangular \mathcal{H} -matrices and separate hierarchical interaction trees as discussed in the following subsections.

2.4.1 Multilevel Geometry Partitioning

The \mathcal{H} -matrix based MoM algorithm starts with a multilevel partitioning of discretized domains. In this work, we use geometric based bisection [27] that performs well for relatively uniform meshes. Since two different domains ∂V and V are discretized, two separate cluster trees are created: binary tree T_S for the test functions and binary tree T_V for the basis functions (Fig. 2.2). To construct a surface cluster tree T_S , we start from the full index set of RWG basis/testing functions $S_1^{(0)}$ (the superscript represents the level and the subscript represents the ID of the set within the level). Next, we determine the bounding box for this set and partition it in half along the largest dimension to form disjoint children clusters $S_1^{(1)}$ and $S_2^{(1)}$. The partitioning process is repeated recursively until the number of basis/testing functions becomes less than the predetermined leafsize n_{\min} parameter which controls the depth of the cluster tree. The leafsize n_{\min} is usually chosen empirically and it is problem/hardware dependent. The cluster tree for the volume domain T_V is constructed similarly to T_S with the piece-wise basis/testing functions on the tetrahedron elements being partitioned as opposed to the RWGs. As depicted in Fig. 2.2, both surface and volume basis/testing functions are hierarchically divided into an L -level tree of clusters. In the subsequent discussion, the level ℓ relative of the cluster $S^{(j)}$ at the j th level is denoted as $R_\ell(S^{(j)})$.*

*Terminology: Relatives of a cluster at all levels ℓ higher than its own level j (i.e. $\ell < j$) are called *ancestors*. For example, for cluster $S_1^{(2)}$ in Fig. 2.2, its relative $R_0(S_1^{(2)})$ at level 0 is $S_1^{(0)}$, e.g. $R_0(S_1^{(2)}) = S_1^{(0)}$. Similarly, level 1 relative $R_1(S_1^{(2)})$ of $S_1^{(2)}$ is $S_1^{(1)}$. Relatives of a cluster at its own level (i.e. $\ell = j$) $R_2(S_1^{(2)}) = \{S_1^{(2)}, S_2^{(2)}\}$ are the cluster itself and its *sibling* $R_2(S_1^{(2)}) = S_2^{(2)}$. Also, relatives of a cluster at levels ℓ lower than its own level (i.e. $\ell > j$) are called *descendants*, e.g. $R_3(S_1^{(2)}) = \{S_1^{(3)}, S_2^{(3)}\}$.

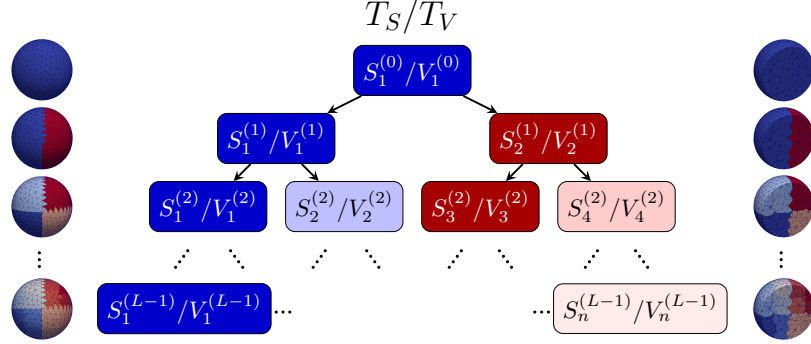


Figure 2.2: Hierarchical partitioning of RWG basis/testing functions for surface mesh and piece-wise basis/testing functions for volume mesh into an L -level hierarchy of clusters. T_S and T_V represent surface and volume cluster trees, respectively.

2.4.2 \mathcal{H} -Matrix Structure for the SVS-EFIE Operators

To approximate the impedance matrices of the MoM discretized SVS-EFIE integral operators, the hierarchical matrix structure for each impedance matrix is constructed. The process starts by taking the root elements of the cluster trees corresponding to the range (observer) and domain (source) of the MoM discretized integral operator. The distance between the source and observer, as well as the size of the individual clusters are calculated, and their interaction is classified as admissible or inadmissible according to the following criterion [62]

$$\min\{\text{diam}(\mathcal{B}_{\text{obs}}), \text{diam}(\mathcal{B}_{\text{src}})\} \leq \eta \text{dist}(\mathcal{B}_{\text{obs}}, \mathcal{B}_{\text{src}}) \quad (2.10)$$

where \mathcal{B}_{obs} and \mathcal{B}_{src} are the bounding boxes of the observer and source clusters, respectively, $\text{diam}(\cdot)$ and $\text{dist}(\cdot, \cdot)$ denote the Euclidean diameter and minimum distance between these bounding boxes. In (2.10), parameter η is a positive real number that controls the amount of admissible blocks and accuracy of the solver. The interactions between the test/basis functions in the clusters are considered admissible (corresponding matrix block is rank-deficient), if the distance between the bounding boxes is sufficiently large (2.10). Otherwise, the interactions at this level are classified as inadmissible and interactions between all the children of both the source and ob-

server clusters are examined on admissibility recursively until the leaf level is reached. To demonstrate the described process, the construction of \mathcal{H} -matrix structure for the volume-to-surface operator $\mathbf{Z}_0^{\partial V, V}$ of SVS-EFIE is visualized in Fig. 2.3. Here, the spheroid model [55] is chosen as an example, and four-level surface and volume cluster trees for its test and basis functions are constructed. As demonstrated in Fig. 2.3, to construct an \mathcal{H} -matrix structure for $\mathbf{Z}_0^{\partial V, V}$, T_S is chosen as the observer tree T_{obs} and T_V is chosen as the source tree T_{src} . The process starts from the interaction between the whole set of surface testing functions $S_1^{(0)}$ and volume basis functions $V_1^{(0)}$ and continues recursively by applying admissibility criterion (2.10).

To solve the SVS-EFIE, \mathcal{H} -matrix structures have to be constructed for each of the three operators (Fig. 2.1):

- $\mathbf{Z}_\epsilon^{\partial V, \partial V}$: T_S is chosen for both source T_{src} and observer T_{obs} trees. Therefore, as shown in Fig. 2.4, the corresponding surface-to-surface square \mathcal{H} -matrix arising from $T_{S \times S}$ interaction tree has the total size of $P \times P$.
- $\mathbf{Z}_0^{\partial V, V}$: For volume-to-surface interactions, $T_{\text{src}} = T_V$ and $T_{\text{obs}} = T_S$. The corresponding rectangular \mathcal{H} -matrix arising from $T_{S \times V}$ interaction tree is shown in Fig. 2.4 and has the total size of $P \times 3N$.
- $\mathbf{Z}_\epsilon^{V, \partial V}$: For surface-to-volume interactions, $T_{\text{src}} = T_S$ and $T_{\text{obs}} = T_V$. Therefore, as shown in Fig. 2.4, the volume-to-surface rectangular \mathcal{H} -matrix arising from $T_{V \times S}$ interaction tree has the total size of $3N \times P$.

2.4.3 Filling \mathcal{H} -Matrices of the SVS-EFIE Operators

Fig. 2.4 depicts the constructed \mathcal{H} -matrices, where red blocks represent inadmissible blocks that will be stored without any approximation in a full-matrix (\mathcal{F}) format. For the green blocks corresponding to admissible interactions, ACA algorithm [23] is being used to obtain the blocks in a compressed low-rank (\mathcal{R}) format:

$$\underbrace{\mathcal{R}}_{m \times n, k(\tau_{\text{ACA}})} = \underbrace{A}_{m \times k(\tau_{\text{ACA}})} \times \underbrace{B^H}_{n \times k(\tau_{\text{ACA}})} \quad (2.11)$$

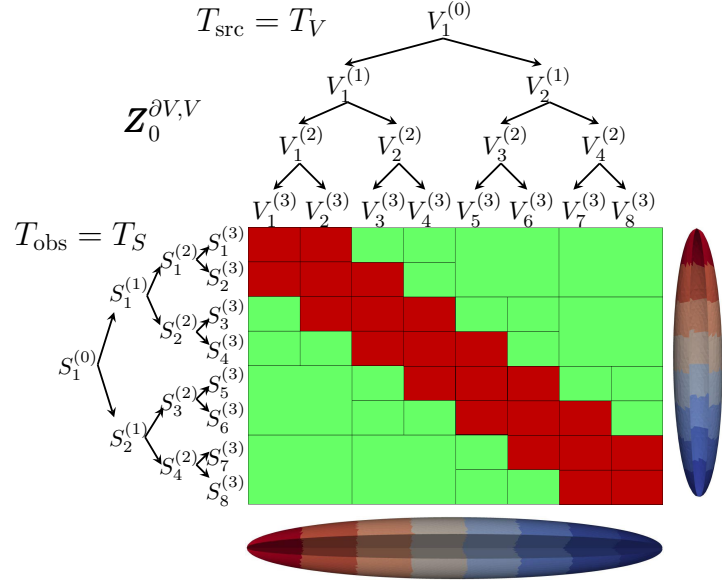


Figure 2.3: \mathcal{H} -matrix representation of the volume-to-surface MoM impedance matrix $\mathbf{Z}_0^{\partial V, V}$ arising from $T_{S \times V}$ interaction tree. The structure is constructed using an spheroid model with its surface tree T_S as observer tree and volume tree T_V as source tree with tree depth $L = 3$. Red blocks represent inadmissible blocks and green blocks represent admissible blocks.

where m and n are the row and column sizes of the block and $k(\tau_{ACA})$ is the revealed rank with the accuracy of the approximation controlled by the ACA truncation threshold τ_{ACA} . The complexity of the ACA is linearly proportional to the size of the block and revealed rank $k(\tau_{ACA})$ [23].

2.5 \mathcal{H} -Matrix Fast Iterative and Direct Solutions

After \mathcal{H} -matrix approximations are constructed for each discretized integral operator entering SVS-EFIE, the resultant system of linear algebraic equations

$$(\mathbf{Z}_\epsilon^{\partial V, \partial V} \oplus \mathbf{Z}_0^{\partial V, V} \otimes \mathbf{Z}_\epsilon^{V, \partial V}) \cdot \mathbf{I} = \mathcal{V}, \quad (2.12)$$

has to be solved, \otimes and \oplus being the operations of formatted multiplication and addition described later in this section. In this paper, we consider both \mathcal{H} -GMRES

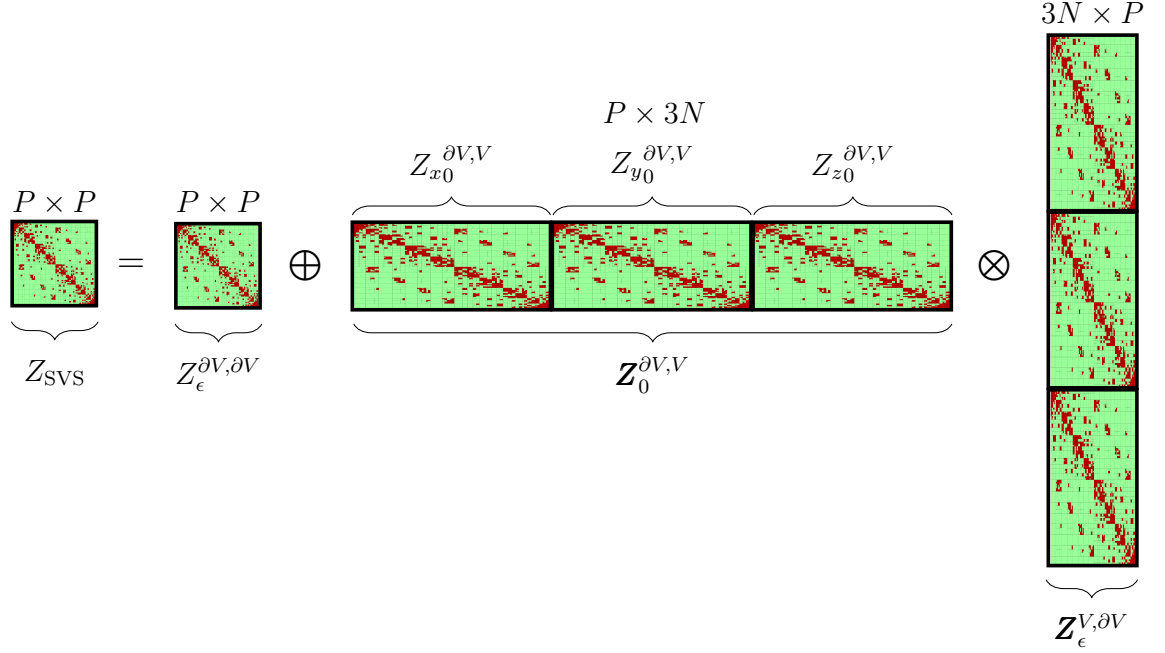


Figure 2.4: Assembly of Z_{SVS} MoM \mathcal{H} -matrix from the individual \mathcal{H} -matrices of SVS-EFIE operators: $Z_{\epsilon}^{\partial V, \partial V}$ arising from $T_{S \times S}$ interaction tree, $Z_0^{\partial V, V}$ arising from $T_{S \times V}$, and $Z_{\epsilon}^{V, \partial V}$ arising from $T_{V \times S}$ via formatted multiplication and addition (2.14) required by a \mathcal{H} -LU based direct solution of the SVS-EFIE.

iterative and \mathcal{H} -LU direct solution approaches. To solve the system using iterative \mathcal{H} -GMRES method, at each iteration the MVPs $Z_{\text{SVS}} \otimes I$ are performed via formatted multiplication $i = Z_{\epsilon}^{V, \partial V} \otimes I$ followed by formatted multiplication $Z_0^{\partial V, V} \otimes i$ and its addition to the result of the formatted multiplication $Z_{\epsilon}^{\partial V, \partial V} \otimes I$, as follows:

$$Z_{\text{SVS}} \cdot I = Z_{\epsilon}^{\partial V, \partial V} \cdot I + Z_0^{\partial V, V} \otimes Z_{\epsilon}^{V, \partial V} \cdot I. \quad (2.13)$$

In contrast to the iterative method, the construction of the Z_{SVS} combining all three approximated integral operators entering the SVS-EFIE is required to solve the system directly. After the final Z_{SVS} MoM \mathcal{H} -matrix is assembled as (Fig. 2.4)

$$Z_{\text{SVS}} = Z_{\epsilon}^{\partial V, \partial V} \oplus Z_0^{\partial V, V} \otimes Z_{\epsilon}^{V, \partial V}, \quad (2.14)$$

\mathcal{H} -LU decomposition followed by \mathcal{H} -back-substitution are applied in order to solve the system of linear equations using the \mathcal{H} -matrix arithmetic [62]. To elaborate, let's consider how resultant $P \times P$ \mathcal{H} -matrix Z_{SVS} is formed through combining the \mathcal{H} -matrices for the individual SVS-EFIE operators using approximate \mathcal{H} -arithmetic (Fig. 2.4).

The key steps of constructing Z_{SVS} are given in Algorithms 1 and 2. The procedure starts from a call to a recursive function $MulAdd(Z_\epsilon^{\partial V, \partial V}, \mathbf{Z}_0^{\partial V, V}, \mathbf{Z}_\epsilon^{V, \partial V}, \partial V, \partial V, V)$ (see line 1 in Algorithm 1) with SVS-EFIE \mathcal{H} -matrices, where $\partial V \in T_S$ and $V \in T_V$ are the root-level clusters in Fig. 2.2. This function performs recursive block matrix-matrix multiplication of $\mathbf{Z}_0^{\partial V, V}$ and $\mathbf{Z}_\epsilon^{V, \partial V}$ and adds it to $Z_\epsilon^{\partial V, \partial V}$ in order to form the resultant Z_{SVS} .

As long as all input matrices for this function are in \mathcal{H} -format, the function calls itself for the corresponding sub-blocks (line 8, Algorithm 1). However, if at a certain level a block $r_1 \times r_2$ of $Z_\epsilon^{\partial V, \partial V}$ ($Z_\epsilon^{\partial V, \partial V}|_{r_1 \times r_2}$) is in \mathcal{R} -format (i.e. it is a leaf), while the other function arguments $\mathbf{Z}_0^{\partial V, V}|_{r_1 \times s}$ and $\mathbf{Z}_\epsilon^{V, \partial V}|_{s \times r_2}$ are still in \mathcal{H} -format, the function $MulAdd(\dots)$ calls itself only with the required part $Z_\epsilon^{\partial V, \partial V}|_{r_i \times r_j}$ (corresponding to $(r_i \times r_j)$ child of $(r_1 \times r_2)$) of $Z_\epsilon^{\partial V, \partial V}|_{r_1 \times r_2}$ in \mathcal{R} -format that is returned through $GetPart\mathcal{R}(\dots)$ function (line 10, Algorithm 1). Subsequently, the child $Z_\epsilon^{\partial V, \partial V}|_{r_i \times r_j}$ of $Z_\epsilon^{\partial V, \partial V}|_{r_1 \times r_2}$ will be overwritten by the matrix $Z_\epsilon^{\partial V, \partial V}|_{r_i \times r_j}$ (line 12, Algorithm 1) resulting from the recursive call to multiplication and addition function $MulAdd(\dots)$ (line 11, Algorithm 1).

If $Z_\epsilon^{\partial V, \partial V}|_{r_1 \times r_2} \in \mathcal{F}$ (lines 17–28, Algorithm 1), the resultant matrix of $\mathbf{Z}_0^{\partial V, V}|_{r_1 \times s} \otimes \mathbf{Z}_\epsilon^{V, \partial V}|_{s \times r_2}$ has to be stored in \mathcal{F} -format. Hence, a naïve multiplication and addition can be performed (line 28, Algorithm 1) after conversion of the arguments $\mathbf{Z}_0^{\partial V, V}|_{r_1 \times s}$ and $\mathbf{Z}_\epsilon^{V, \partial V}|_{s \times r_2}$ to the \mathcal{F} -format (see lines 19, 21, 24, 26 in Algorithm 1). The recursive function $\mathcal{H}\text{-Approx}\mathcal{F}(M \leftarrow M''')$ is depicted in Fig. 2.5(a) for an example of an \mathcal{H} -matrix with depth $L = 2$. Here, \mathcal{H} -matrix M''' is converted to a block M in \mathcal{F} -format by converting \mathcal{R} -blocks to \mathcal{F} ($M'' \leftarrow M'''$) and coarsening the structure in the next two recursive steps ($M \leftarrow M' \leftarrow M''$).

If $Z_\epsilon^{\partial V, \partial V}|_{r_1 \times r_2}$ is in \mathcal{H} - or \mathcal{R} -format, and the leaf level is reached for any of $\mathbf{Z}_0^{\partial V, V}|_{r_1 \times s}$ or $\mathbf{Z}_\epsilon^{V, \partial V}|_{s \times r_2}$ (lines 29–30, Algorithm 1), their product will be computed

Algorithm 1 Multiplication and addition of \mathcal{H} -matrices

Inputs: matrices $Z_\epsilon^{\partial V, \partial V}|_{r_1 \times r_2}$, $Z_0^{\partial V, V}|_{r_1 \times s}$, and $Z_\epsilon^{V, \partial V}|_{s \times r_2}$, clusters $r_1, r_2 \in \partial V$ and $s \in V$.

Output: $Z_{\text{SVS}} = Z_\epsilon^{\partial V, \partial V} \oplus (Z_0^{\partial V, V} \otimes Z_\epsilon^{V, \partial V})$

```

1: MulAdd( $Z_\epsilon^{\partial V, \partial V}|_{\partial V \times \partial V}$ ,  $Z_0^{\partial V, V}|_{\partial V \times V}$ ,  $Z_\epsilon^{V, \partial V}|_{V \times \partial V}$ ,  $\partial V$ ,  $\partial V$ ,  $V$ )
2: function MulAdd( $Z_\epsilon^{\partial V, \partial V}|_{r_1 \times r_2}$ ,  $Z_0^{\partial V, V}|_{r_1 \times s}$ ,  $Z_\epsilon^{V, \partial V}|_{s \times r_2}$ ,  $r_1$ ,  $r_2$ ,  $s$ )
3: if ( $Z_\epsilon^{\partial V, \partial V}|_{r_1 \times r_2} \in \{\mathcal{H} \text{ or } \mathcal{R}\}$ ) and ( $Z_0^{\partial V, V}|_{r_1 \times s} \in \mathcal{H}$ ) and ( $Z_\epsilon^{V, \partial V}|_{s \times r_2} \in \mathcal{H}$ ) then
4:   for all  $r_i$  children of  $r_1$  do
5:     for all  $r_j$  children of  $r_2$  do
6:       for all  $s_k$  children of  $s$  do
7:         if  $Z_\epsilon^{\partial V, \partial V}|_{r_1 \times r_2} \in \mathcal{H}$  then
8:           MulAdd( $Z_\epsilon^{\partial V, \partial V}|_{r_i \times r_j}$ ,  $Z_0^{\partial V, V}|_{r_i \times s_k}$ ,
                   $Z_\epsilon^{V, \partial V}|_{s_k \times r_j}$ ,  $r_i$ ,  $r_j$ ,  $s_k$ )
9:         else if  $Z_\epsilon^{\partial V, \partial V}|_{r_1 \times r_2} \in \mathcal{R}$  then
10:           $Z'_\epsilon{}^{\partial V, \partial V}|_{r_i \times r_j} = \text{GetPartR}(Z_\epsilon^{\partial V, \partial V}|_{r_1 \times r_2})$ 
              { GetPartR returns a part of matrix  $Z_\epsilon^{\partial V, \partial V}$  in  $\mathcal{R}$ -format corresponding
              to  $r_i \times r_j$  child of  $r_1 \times r_2$  }
11:          MulAdd( $Z'_\epsilon{}^{\partial V, \partial V}|_{r_i \times r_j}$ ,  $Z_0^{\partial V, V}|_{r_i \times s_k}$ ,
                   $Z_\epsilon^{V, \partial V}|_{s_k \times r_j}$ ,  $r_i$ ,  $r_j$ ,  $s_k$ )
12:          UpdatePartR( $Z_\epsilon^{\partial V, \partial V}|_{r_i \times r_j}$ ,  $Z'_\epsilon{}^{\partial V, \partial V}|_{r_i \times r_j}$ )
              { UpdatePartR rewrites part of matrix  $Z_\epsilon^{\partial V, \partial V}$  corresponding to  $r_i \times r_j$ 
              with  $Z'_\epsilon{}^{\partial V, \partial V}$  }
13:         end if
14:       end for
15:     end for
16:   end for
17: else if  $Z_\epsilon^{\partial V, \partial V}|_{r_1 \times r_2} \in \mathcal{F}$  then
18:   if  $Z_0^{\partial V, V}|_{r_1 \times s} \in \mathcal{H}$  then
19:      $\mathcal{H}\text{-Approx}\mathcal{F}(\mathcal{F} \leftarrow Z_0^{\partial V, V}|_{r_1 \times s})$  {Fig. 2.5(a)}
20:   else if  $Z_0^{\partial V, V}|_{r_1 \times s} \in \mathcal{R}$  then
21:     convert  $Z_0^{\partial V, V}|_{r_1 \times s}$  to  $\mathcal{F}$ 
22:   end if
23:   if  $Z_\epsilon^{V, \partial V}|_{s \times r_2} \in \mathcal{H}$  then
24:      $\mathcal{H}\text{-Approx}\mathcal{F}(\mathcal{F} \leftarrow Z_\epsilon^{V, \partial V}|_{s \times r_2})$ 
25:   else if  $Z_\epsilon^{V, \partial V}|_{s \times r_2} \in \mathcal{R}$  then
26:     convert  $Z_\epsilon^{V, \partial V}|_{s \times r_2}$  to  $\mathcal{F}$ 
27:   end if
28:    $Z_\epsilon^{\partial V, \partial V}|_{r_1 \times r_2} + = Z_0^{\partial V, V}|_{r_1 \times s} \times Z_\epsilon^{V, \partial V}|_{s \times r_2}$  {naïve}
29: else if ( $Z_\epsilon^{\partial V, \partial V}|_{r_1 \times r_2} \in \{\mathcal{H} \text{ or } \mathcal{R}\}$ ) and ( $Z_0^{\partial V, V}|_{r_1 \times s} \notin \mathcal{H}$  or  $Z_\epsilon^{V, \partial V}|_{s \times r_2} \notin \mathcal{H}$ ) then
30:   FmtMulAdd( $Z_\epsilon^{\partial V, \partial V}|_{r_1 \times r_2}$ ,  $Z_0^{\partial V, V}|_{r_1 \times s}$ ,  $Z_\epsilon^{V, \partial V}|_{s \times r_2}$ ,  $r_1$ ,  $r_2$ ,  $s$ )
31: end if
32: return

```

Algorithm 2 Formatted multiplication (at leaves) and addition

Inputs: matrices $Z_\epsilon^{\partial V, \partial V}|_{r_1 \times r_2}$, $Z_0^{\partial V, V}|_{r_1 \times s}$, and $Z_\epsilon^{V, \partial V}|_{s \times r_2}$, clusters $r_1, r_2 \in T_S$ and $s \in T_V$.

Output: $Z_\epsilon^{\partial V, \partial V}|_{r_1 \times r_2} = Z_\epsilon^{\partial V, \partial V}|_{r_1 \times r_2} \oplus (Z_0^{\partial V, V}|_{r_1 \times s} \otimes Z_\epsilon^{V, \partial V}|_{s \times r_2})$

Require: ($Z_\epsilon^{\partial V, \partial V}|_{r_1 \times r_2} \in \{\mathcal{H} \text{ or } \mathcal{R}\}$) and ($Z_0^{\partial V, V}|_{r_1 \times s} \notin \mathcal{H}$ or $Z_\epsilon^{V, \partial V}|_{s \times r_2} \notin \mathcal{H}$)

- 1: **function** *FmtMulAdd*($Z_\epsilon^{\partial V, \partial V}|_{r_1 \times r_2}$, $Z_0^{\partial V, V}|_{r_1 \times s}$, $Z_\epsilon^{V, \partial V}|_{s \times r_2}$, r_1 , r_2 , s)
- FORMATTED MULTIPLICATION:
- 2: **if** ($Z_0^{\partial V, V}|_{r_1 \times s} \in \mathcal{R}$) or ($Z_\epsilon^{V, \partial V}|_{s \times r_2} \in \mathcal{R}$) **then** {the result of multiplication $Z_\epsilon^{\partial V, \partial V}|_{r_1 \times r_2}$ is stored as \mathcal{R} }
- 3: **if** $Z_0^{\partial V, V}|_{r_1 \times s} \in \mathcal{H}$ **then**
- 4: $Z_\epsilon^{\partial V, \partial V}|_{r_1 \times r_2} = \mathcal{H}mul\mathcal{R}(Z_0^{\partial V, V}|_{r_1 \times s}, Z_\epsilon^{V, \partial V}|_{s \times r_2})$ {Fig. 2.6}
- 5: **else if** $Z_\epsilon^{V, \partial V}|_{s \times r_2} \in \mathcal{H}$ **then**
- 6: $Z_\epsilon^{\partial V, \partial V}|_{r_1 \times r_2} = \mathcal{R}mul\mathcal{H}(Z_0^{\partial V, V}|_{r_1 \times s}, Z_\epsilon^{V, \partial V}|_{s \times r_2})$ {Fig. 2.6}
- 7: **else**
- 8: $Z_\epsilon^{\partial V, \partial V}|_{r_1 \times r_2} = Z_0^{\partial V, V}|_{r_1 \times s} \cdot Z_\epsilon^{V, \partial V}|_{s \times r_2}$
- 9: **end if**
- 10: **else if** ($Z_0^{\partial V, V}|_{r_1 \times s} \in \mathcal{F}$) or ($Z_\epsilon^{V, \partial V}|_{s \times r_2} \in \mathcal{F}$) **then** { $Z_\epsilon^{\partial V, \partial V}|_{r_1 \times r_2}$ is stored as \mathcal{F} }
- 11: **if** $Z_0^{\partial V, V}|_{r_1 \times s} \in \mathcal{H}$ **then**
- 12: $\mathcal{H}\text{-Approx}\mathcal{F}(\mathcal{F} \leftarrow Z_0^{\partial V, V}|_{r_1 \times s})$ {Fig. 2.5 (a)}
- 13: **end if**
- 14: **if** $Z_\epsilon^{V, \partial V}|_{s \times r_2} \in \mathcal{H}$ **then**
- 15: $\mathcal{H}\text{-Approx}\mathcal{F}(\mathcal{F} \leftarrow Z_\epsilon^{V, \partial V}|_{s \times r_2})$ {Fig. 2.5 (a)}
- 16: **end if**
- 17: $Z_\epsilon^{\partial V, \partial V}|_{r_1 \times r_2} = Z_0^{\partial V, V}|_{r_1 \times s} \cdot Z_\epsilon^{V, \partial V}|_{s \times r_2}$
- 18: **end if**
- FORMATTED ADDITION:
- 19: **if** ($Z_\epsilon^{\partial V, \partial V}|_{r_1 \times r_2} \in \mathcal{H}$) and ($Z_\epsilon^{\partial V, \partial V}|_{r_1 \times r_2} \in \mathcal{F}$) **then**
- 20: $\mathcal{H}\text{-Approx}\mathcal{F}(Z_\epsilon^{\partial V, \partial V}|_{r_1 \times r_2} \rightarrow Z_\epsilon^{\partial V, \partial V}|_{r_1 \times r_2})$
 {Fig. 2.5 (a)}
- 21: **else if** ($Z_\epsilon^{\partial V, \partial V}|_{r_1 \times r_2} \in \mathcal{H}$) and ($Z_\epsilon^{\partial V, \partial V}|_{r_1 \times r_2} \in \mathcal{R}$) **then**
- 22: $\mathcal{H}\text{-Approx}\mathcal{R}(Z_\epsilon^{\partial V, \partial V}|_{r_1 \times r_2} \rightarrow Z_\epsilon^{\partial V, \partial V}|_{r_1 \times r_2})$ {Fig. 2.5 (b)}
- 23: **end if**
- 24: **if** $Z_\epsilon^{\partial V, \partial V}|_{r_1 \times r_2} \in \mathcal{H}$ **then**
- 25: $Trun_{k'' \leftarrow k+k'}^{\mathcal{H}+\mathcal{H}}(Z_\epsilon^{\partial V, \partial V}|_{r_1 \times r_2}, Z_\epsilon^{\partial V, \partial V}|_{r_1 \times r_2})$
 {Fig. 2.7 (b)}
- 26: **else** { $Z_\epsilon^{\partial V, \partial V}|_{r_1 \times r_2} \in \mathcal{R}$ }
- 27: **if** $Z_\epsilon^{\partial V, \partial V}|_{r_1 \times r_2} \in \mathcal{F}$ **then**
- 28: convert $Z_\epsilon^{\partial V, \partial V}|_{r_1 \times r_2}$ to \mathcal{R}
- 29: **end if**
- 30: $Trun_{k'' \leftarrow k+k'}^{\mathcal{R}+\mathcal{R}}(Z_\epsilon^{\partial V, \partial V}|_{r_1 \times r_2}, Z_\epsilon^{\partial V, \partial V}|_{r_1 \times r_2})$ {Fig. 2.7 (a)}
- 31: **end if**
- 32: **return** $Z_\epsilon^{\partial V, \partial V}|_{r_1 \times r_2}$

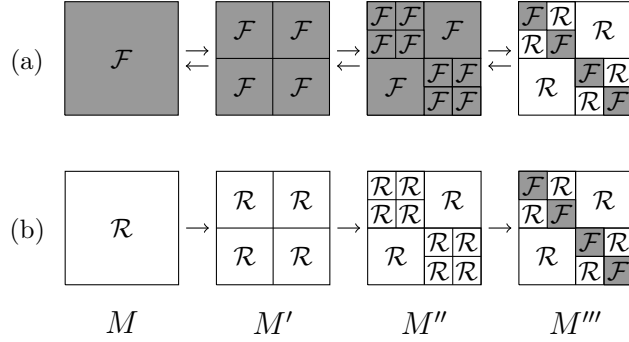


Figure 2.5: (a) Recursive function $\mathcal{H}\text{-Approx}\mathcal{F}(M \rightarrow M''')$ converting an \mathcal{F} -block M to an \mathcal{H} -matrix M''' . This procedure can also be implemented in the opposite order as $\mathcal{F}\text{-Approx}\mathcal{H}(M''' \rightarrow M)$. (b) Recursive function $\mathcal{H}\text{-Approx}\mathcal{R}(M \rightarrow M''')$ converting an \mathcal{R} block M to an \mathcal{H} -matrix M''' . If \mathcal{H} -matrix M''' has depth of L , then L -step recursion (e.g. $M \rightarrow M''$) and one final step (e.g. $M'' \rightarrow M'''$) are needed for both cases (a) and (b). Here, to simplify the depiction, the depth of M''' is considered to be $L = 2$ which leads to 3 steps conversion.

and stored as \mathcal{R} or \mathcal{F} . Here (line 30, Algorithm 1), the function $FmtMulAdd$ (see Algorithm 2) performing formatted multiplication (at leaves) and addition [62] is called:

- If any of $\mathbf{Z}_0^{\partial V, V}|_{r_1 \times s}$ or $\mathbf{Z}_\epsilon^{V, \partial V}|_{s \times r_2} \in \mathcal{R}$ (lines 2–9, Algorithm 2), the result of the multiplication is stored as \mathcal{R} . Hence, if $\mathbf{Z}_0^{\partial V, V}|_{r_1 \times s}$ is \mathcal{H} (line 3, Algorithm 2), recursive function $\mathcal{H}mul\mathcal{R}(\dots)$ depicted in Fig. 2.6 is called to perform $\mathcal{H} \otimes \mathcal{R}$ and store the result as \mathcal{R} (line 4, Algorithm 2). Otherwise (lines 5–6, Algorithm 2), recursive function $\mathcal{R}mul\mathcal{H}(\dots)$ is called to perform $\mathcal{R} \otimes \mathcal{H}$ that is similar to $\mathcal{H}mul\mathcal{R}(\dots)$ in Fig. 2.6. As it is shown in Fig. 2.6, these two functions include the truncation step $Trun_{k'' \leftarrow k+k'}^{\mathcal{R}+\mathcal{R}}(\dots)$ which is depicted in Fig. 2.7(a). This operation can be performed by truncating the singular values of the matrix block stored in an \mathcal{R} -format (2.11) that can be done fast using reduced singular value decomposition (rSVD) [70, 7.1.1].
- If neither $\mathbf{Z}_0^{\partial V, V}|_{r_1 \times s}$ nor $\mathbf{Z}_\epsilon^{V, \partial V}|_{s \times r_2}$ are in \mathcal{R} -format (i.e. one of them is in \mathcal{F} -format), the multiplication result matrix $\mathbf{Z}'_\epsilon^{\partial V, \partial V}|_{r_1 \times r_2}$ has to be stored in \mathcal{F} -format (lines 10–18, Algorithm 2). Hence, for any of $\mathbf{Z}_0^{\partial V, V}|_{r_1 \times s}$ or $\mathbf{Z}_\epsilon^{V, \partial V}|_{s \times r_2}$

in \mathcal{H} -format, they will be converted to the \mathcal{F} using $\mathcal{H}\text{-Approx}\mathcal{F}(M \leftarrow M''')$ in Fig. 2.5(a) and then naïve multiplication is performed on the two \mathcal{F} -blocks.

As it is shown in Algorithm 2, after formatted multiplication the formatted addition is performed. Before adding the multiplication result matrix $Z'_\epsilon{}^{\partial V, \partial V}|_{r_1 \times r_2}$ to the matrix of $Z_\epsilon{}^{\partial V, \partial V}|_{r_1 \times r_2}$, the format of $Z_\epsilon{}^{\partial V, \partial V}|_{r_1 \times r_2}$ is checked (lines 19–31, Algorithm 2):

- If $Z_\epsilon{}^{\partial V, \partial V}|_{r_1 \times r_2} \in \mathcal{H}$ the structure of $Z'_\epsilon{}^{\partial V, \partial V}|_{r_1 \times r_2}$, which is in either \mathcal{F} or \mathcal{R} format, is converted to the hierarchical structure of $Z_\epsilon{}^{\partial V, \partial V}$ using $\mathcal{H}\text{-Approx}\mathcal{F}(M \rightarrow M''')$ or $\mathcal{H}\text{-Approx}\mathcal{R}(M \rightarrow M''')$ in Fig. 2.5, respectively (lines 20 and 22, Algorithm 2). After matching the structures, we add these two \mathcal{H} -matrices and then compress the new created \mathcal{H} -matrix using $\text{Trun}_{k'' \leftarrow k+k'}^{\mathcal{H}+\mathcal{H}}(\dots)$ function (line 25, Algorithm 2). As shown in Fig. 2.7(b), this recursive function adds two \mathcal{H} -matrices and then re-compresses \mathcal{R} -blocks from rank $k+k'$ to rank k'' using rSVD [70, 7.1.1] based on the predefined \mathcal{H} -arithmetic tolerance $\tau_{\mathcal{H}}$ in the new \mathcal{H} -matrix.
- If $Z_\epsilon{}^{\partial V, \partial V}|_{r_1 \times r_2} \in \mathcal{R}$, the structure of $Z'_\epsilon{}^{\partial V, \partial V}|_{r_1 \times r_2}$ is converted to \mathcal{R} when it is in \mathcal{F} -format (line 28, Algorithm 2). Then, two \mathcal{R} -blocks of $Z_\epsilon{}^{\partial V, \partial V}|_{r_1 \times r_2}$ and $Z'_\epsilon{}^{\partial V, \partial V}|_{r_1 \times r_2}$ are added and compressed through $\text{Trun}_{k'' \leftarrow k+k'}^{\mathcal{R}+\mathcal{R}}(\dots)$ function with \mathcal{H} -arithmetic tolerance $\tau_{\mathcal{H}}$ in Fig. 2.7(a) (line 30, Algorithm 2).

$$\begin{aligned}
 & \boxed{\mathcal{R}^M} \otimes \begin{array}{|c|c|} \hline \mathcal{F}_{11} & \mathcal{R}_{12} \\ \hline \mathcal{R}_{21} & \mathcal{F}_{22} \\ \hline \end{array} = \begin{array}{|c|c|} \hline \mathcal{R}_{11}^{M'} & \mathcal{R}_{12}^{M'} \\ \hline \mathcal{R}_{21}^{M'} & \mathcal{R}_{22}^{M'} \\ \hline \end{array} \otimes \begin{array}{|c|c|} \hline \mathcal{F}_{11} & \mathcal{R}_{12} \\ \hline \mathcal{R}_{21} & \mathcal{F}_{22} \\ \hline \end{array} = \\
 & \begin{array}{|c|c|} \hline \text{Trun}^{\mathcal{R}+\mathcal{R}}(\mathcal{R}_{11}^M \mathcal{F}_{11} + \mathcal{R}_{12}^M \mathcal{R}_{21}) & \text{Trun}^{\mathcal{R}+\mathcal{R}}(\mathcal{R}_{11}^M \mathcal{R}_{12} + \mathcal{R}_{12}^M \mathcal{F}_{22}) \\ \hline \text{Trun}^{\mathcal{R}+\mathcal{R}}(\mathcal{R}_{21}^M \mathcal{F}_{11} + \mathcal{R}_{22}^M \mathcal{R}_{21}) & \text{Trun}^{\mathcal{R}+\mathcal{R}}(\mathcal{R}_{21}^M \mathcal{R}_{12} + \mathcal{R}_{22}^M \mathcal{F}_{22}) \\ \hline \end{array} = \\
 & \begin{array}{|c|c|} \hline \mathcal{R}_{11}^{M'} & \mathcal{R}_{12}^{M'} \\ \hline \mathcal{R}_{21}^{M'} & \mathcal{R}_{22}^{M'} \\ \hline \end{array} = \boxed{\mathcal{R}^{M'}}
 \end{aligned}$$

Figure 2.6: Recursive function $\mathcal{R}mul\mathcal{H}(\mathcal{R}, \mathcal{H})$ performing formatted multiplication of \mathcal{R} - and \mathcal{H} -blocks and storing the result in \mathcal{R} -format. The recursive function $\mathcal{H}mul\mathcal{R}(\mathcal{H}, \mathcal{R})$ is defined similarly with an opposite order of operations. Here, to simplify the depiction, the depth of \mathcal{H} -matrix is considered to be $L = 1$. In general, \mathcal{H} -blocks of various depths occur.

2.6 Memory and Computational Complexity Analysis for \mathcal{H} -matrix SVS-EFIE

To derive the expressions for computational complexity and storage requirements, we define the sparsity constant [62] $C_{\text{sp}}^{S \times V}$ for a given interaction tree $T_{S \times V}$, as

$$\begin{aligned}
 C_{\text{sp}}^{S \times V} := \max \left\{ \overbrace{\max_{\substack{r_1 \in T_S, \\ \ell=0, \dots, L}} \#\{s \in T_V : r_1 \times s \in \mathcal{L}(T_{S \times V}, \ell)\}}^{(a)}, \right. \\
 \left. \overbrace{\max_{\substack{s \in T_V, \\ \ell=0, \dots, L}} \#\{r_1 \in T_S : r_1 \times s \in \mathcal{L}(T_{S \times V}, \ell)\}}^{(b)} \right\} \quad (2.15)
 \end{aligned}$$

where the term (a) in (2.15) is the maximum number of interaction blocks $r_1 \times s$ at the leaf level associated with an observer cluster $r_1 \in T_S$ and the term (b) in (2.15) is the maximum number of interaction blocks $r_1 \times s$ at the leaf level associated with a source cluster $s \in T_V$ among all levels $\ell = 0, \dots, L$ of interaction tree $T_{S \times V}$. Here, $\mathcal{L}(T_{S \times V}, \ell)$ is the set of leaves at the ℓ th level and L is the number of levels of $T_{S \times V}$. The largest of these two counts is the sparsity constant $C_{\text{sp}}^{S \times V}$ of $T_{S \times V}$.

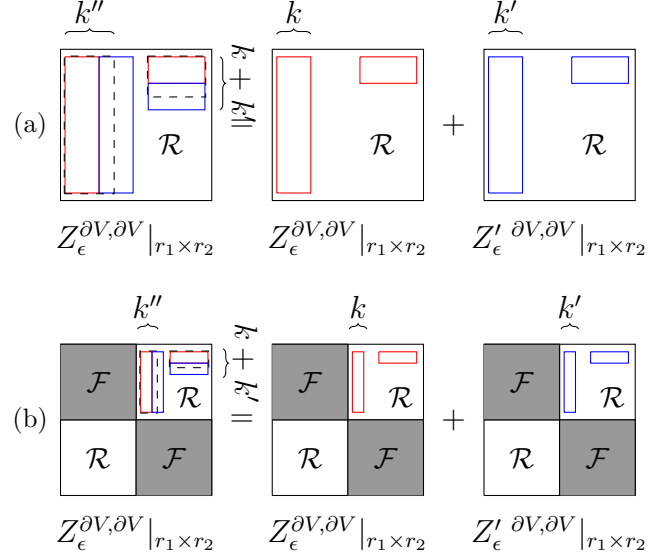


Figure 2.7: Procedures to re-compress the addition of two matrices. a) Function $Trun_{k'' \leftarrow k+k'}^{\mathcal{R}+\mathcal{R}}(\dots)$ for addition and truncation of two matrices in \mathcal{R} -format. b) Recursive function $Trun_{k'' \leftarrow k+k'}^{\mathcal{H}+\mathcal{H}}(\dots)$ for addition and truncation of two \mathcal{H} -matrices. Again, to simplify the depiction, the depth of \mathcal{H} -matrices in (b) is considered to be $L = 1$. The resultant compressed blocks with revealed rank k'' are represented as dashed blocks.

As an example, for the \mathcal{H} -matrix structure in Fig. 2.3 the number of interaction blocks $r_1 \times s$ associated with the observer cluster $r_1 = S_1^{(3)}$ at level 3 is:

$$\#\{s \in T_V : S_1^{(3)} \times s \in \mathcal{L}(T_{S \times V}, 3)\} = \#\{S_1^{(3)} \times \{V_1^{(3)}, V_2^{(3)}, V_3^{(3)}, V_4^{(3)}\}\} = 4. \quad (2.16)$$

Also, at the same level $\ell = 3$, the number of interaction blocks $r_1 \times s$ associated with the observer cluster $r_1 = S_3^{(3)}$ is:

$$\#\{s \in T_V : S_3^{(3)} \times s \in \mathcal{L}(T_{S \times V}, 3)\} = \#\{S_3^{(3)} \times \{V_1^{(3)}, V_2^{(3)}, V_3^{(3)}, V_4^{(3)}, V_5^{(3)}, V_6^{(3)}\}\} = 6. \quad (2.17)$$

After computing this counts for all observer clusters $r_1 \in T_S$ in each level, the maximum number of these counts among all four levels of this \mathcal{H} -matrix is 6 for the term

(a) in (2.15). Analogously, for term (b) in (2.15), this maximum number among all source clusters $s \in T_V$ in each level of the \mathcal{H} -matrix is 6. So, the sparsity constant $C_{\text{sp}}^{S \times V}$ for \mathcal{H} -matrix in Fig. 2.3 is maximum between the two counts (a) and (b) in (2.15), which is 6.

Since in the interaction tree $T_{V \times S}$ the domain and range are merely switched compared to the interaction tree $T_{S \times V}$, its sparsity constant is:

$$C_{\text{sp}}^{V \times S} = C_{\text{sp}}^{S \times V} = C_{\text{sp}}. \quad (2.18)$$

To simplify the notation, $\mathcal{M}(\cdot)$ will be used for asymptotic memory requirement in \mathcal{H} -matrix format, while $\mathcal{M}^{\mathcal{R}}(\cdot)$ and $\mathcal{M}^{\mathcal{F}}(\cdot)$ for the memory required by all \mathcal{R} - and \mathcal{F} -blocks, respectively.

2.6.0.1 Memory Complexity for SVS-EFIE \mathcal{H} -matrices

The memory usage to store volume-to-surface $\mathbf{Z}_0^{\partial V, V}$ and surface-to-volume $\mathbf{Z}_\epsilon^{V, \partial V}$ discretized operators can be derived analogously to the ones for the square \mathcal{H} -matrix [27, 62].

To compute the storage for the rectangular \mathcal{H} -matrix $\mathbf{Z}_0^{\partial V, V}$ of the size $P \times 3N$, the storage of \mathcal{R} - and \mathcal{F} -blocks is analyzed, separately. Since all \mathcal{F} -blocks exist only at the leaf level and the number of them scales linearly with the size of the matrix [62], the storage $\mathcal{M}^{\mathcal{F}}$ is estimated as $\mathcal{O}(n_{\min}^2(N + P))$, $n_{\min} \times n_{\min}$ being the size of the full leaf blocks.

On the other hand, rank deficient b th \mathcal{R} -block of size $m(\ell) \times n(\ell)$ at the ℓ th level is stored as AB^H (2.11), where matrix A is of size $m(\ell) \times k_b^{\partial V, V}$ and matrix B^H is of size $k_b^{\partial V, V} \times n(\ell)$. Therefore, its storage is $k_b^{\partial V, V}(m(\ell) + n(\ell))$. Since, there are at most $2^\ell C_{\text{sp}}$ interaction blocks at the ℓ th level in case of bisection based partitioning and considering sparsity constant definition (2.15), the complexity to store all \mathcal{R} -blocks for $\mathbf{Z}_0^{\partial V, V}$ can be approximated as

$$\mathcal{M}^{\mathcal{R}} \left(\mathbf{Z}_0^{\partial V, V} \right) \leq \sum_{\ell=0}^{L_S} 2^\ell C_{\text{sp}} k_{\max}^{\partial V, V} m(\ell) + \sum_{\ell=0}^{L_V} 2^\ell C_{\text{sp}} k_{\max}^{\partial V, V} n(\ell), \quad (2.19)$$

where L_S is the number of levels in T_S and L_V the number of levels in T_V for the $\mathbf{Z}_0^{\partial V, V}$ interaction tree $T_{S \times V}$, $b = 1, \dots, N^{\mathcal{R}}$, and $k_{\max}^{\partial V, V}$ is the maximum rank revealed (e.g., by ACA) among all $N^{\mathcal{R}}$ \mathcal{R} -blocks of $\mathbf{Z}_0^{\partial V, V}$. Here, we assume $k_{\max}^{\partial V, V}$ to only weakly increase across the levels; hence, implying quasi-dynamic simulation scenarios, in which the structure does not exceed several wavelengths in size. Since, $m(\ell) = P/2^\ell$ and $n(\ell) = 3N/2^\ell$ are the sizes of the row and the column of each \mathcal{R} -block at the ℓ th level, respectively, and $L_S = \mathcal{O}(\log P)$ and $L_V = \mathcal{O}(\log N)$, (2.19) is simplified to

$$\begin{aligned} \mathcal{M}^{\mathcal{R}}(\mathbf{Z}_0^{\partial V, V}) &\leq C_{\text{sp}} k_{\max}^{\partial V, V} \left(P \sum_{\ell=0}^{L_S} 1 + 3N \sum_{\ell=0}^{L_V} 1 \right) \\ &= \mathcal{O}(k_{\max}^{\partial V, V} P \log P) + \mathcal{O}(k_{\max}^{\partial V, V} N \log N). \end{aligned} \quad (2.20)$$

Therefore, the storage $\mathcal{M}(\mathbf{Z}_0^{\partial V, V})$ is dominated by the storage of its \mathcal{R} -blocks in (2.20)

$$\begin{aligned} \mathcal{M}(\mathbf{Z}_0^{\partial V, V}) &= \mathcal{M}^{\mathcal{R}}(\mathbf{Z}_0^{\partial V, V}) + \mathcal{M}^{\mathcal{F}}(\mathbf{Z}_0^{\partial V, V}) \\ &= \mathcal{O}(k_{\max}^{\partial V, V} (P \log P + N \log N)) + \mathcal{O}(n_{\min}^2 (N + P)) \\ &= \mathcal{O}(k_{\max}^{\partial V, V} P \log P) + \mathcal{O}(k_{\max}^{\partial V, V} N \log N), \end{aligned} \quad (2.21)$$

where for simplicity $k_{\max}^{\partial V, V}$ is assumed to be of $\mathcal{O}(n_{\min})$. Note, since the \mathcal{H} -matrix structure of $\mathbf{Z}_\epsilon^{V, \partial V}$ is a transpose of $\mathbf{Z}_0^{\partial V, V}$, asymptotically its storage is the same

$$\mathcal{M}(\mathbf{Z}_\epsilon^{V, \partial V}) = \mathcal{O}(k_{\max}^{V, \partial V} P \log P) + \mathcal{O}(k_{\max}^{V, \partial V} N \log N). \quad (2.22)$$

For $P \times P$ matrix $Z_\epsilon^{\partial V, \partial V}$, the expression for the memory requirement can be derived by simplifying (2.21) for a square \mathcal{H} -matrix case:

$$\mathcal{M}(Z_\epsilon^{\partial V, \partial V}) = \mathcal{O}(k_{\max}^{\partial V, \partial V} P \log P), \quad (2.23)$$

where $k_{\max}^{\partial V, \partial V}$ is the maximum rank revealed (e.g. by ACA) among all \mathcal{R} -blocks of $\mathbf{Z}_\epsilon^{\partial V, \partial V}$.

2.6.0.2 Computational Complexity of \mathcal{H} -GMRES Based Iterative Solver

The number of operations \mathcal{N}_{MVP} (complexity) of the MVP for an \mathcal{H} -matrix can be bounded by the memory required to store the \mathcal{H} -matrix itself [27, Lemma 2.5]

$$\mathcal{N}_{\text{MVP}}(Z) \leq \mathcal{M}(Z), \quad Z \in \{Z_\epsilon^{\partial V, \partial V}, \mathbf{Z}_\epsilon^{V, \partial V}, \mathbf{Z}_0^{\partial V, V}\}. \quad (2.24)$$

Therefore, the computational complexity for \mathcal{H} -GMRES based solver for SVS-EFIE is composed of three MVPs with the corresponding discretized integral operators:

$$\begin{aligned} \mathcal{N}_{\mathcal{H}\text{-GMRES}} &= N_{\text{it}} \left(\mathcal{N}_{\text{MVP}}(\mathbf{Z}_\epsilon^{V, \partial V}) + \mathcal{N}_{\text{MVP}}(\mathbf{Z}_0^{\partial V, V}) + \mathcal{N}_{\text{MVP}}(Z_\epsilon^{\partial V, \partial V}) \right) \\ &= N_{\text{it}} (\mathcal{O}(k_{\max} P \log P) + \mathcal{O}(k_{\max} N \log N)), \end{aligned} \quad (2.25)$$

where N_{it} is the number of iterations required for GMRES to converge to a prescribed tolerance.

2.6.0.3 Computational Complexity of \mathcal{H} -LU Based Direct Solver

As discussed in Section 2.5, \mathcal{H} -LU based direct solver has three steps, the setup of \mathcal{H} -matrix Z_{SVS} involving formatted multiplication and addition of \mathcal{H} -matrices $Z_\epsilon^{\partial V, \partial V} \oplus \mathbf{Z}_0^{\partial V, V} \otimes \mathbf{Z}_\epsilon^{V, \partial V}$, \mathcal{H} -LU decomposition, and backsubstitution. Below, we estimate computational complexity of these steps.

Formatted Multiplication $\mathbf{Z}_0^{\partial V, V} \otimes \mathbf{Z}_\epsilon^{V, \partial V}$ As shown in (2.14), the complexity to setup Z_{SVS} can be estimated through formatted multiplication and addition of \mathcal{H} -matrices. To simplify the analysis, at first the truncation functions $\text{Trun}_{k'' \leftarrow k+k'}^{\mathcal{H}+\mathcal{H}}(\dots)$ and $\text{Trun}_{k'' \leftarrow k+k'}^{\mathcal{R}+\mathcal{R}}(\dots)$ in Algorithm 2 will be considered as a simple copying of the data without any re-compression, so $k'' = k + k'$ in Fig. 2.7. For this scenario, the formatted multiplication of two sub-blocks $\mathbf{Z}_0^{\partial V, V}|_{r_1 \times s} \otimes \mathbf{Z}_\epsilon^{V, \partial V}|_{s \times r_2}$ in Algorithm 1, line 30 (see also lines 4 and 6 of Algorithm 2) becomes the exact multiplication $\mathbf{Z}_0^{\partial V, V}|_{r_1 \times s} \times \mathbf{Z}_\epsilon^{V, \partial V}|_{s \times r_2}$ in \mathcal{H} -matrix format.

So, in Algorithm 2, each leaf block $r_1 \times r_2$ at the j th level resulting from the

multiplication $\mathbf{Z}_0^{\partial V, V}|_{r_1 \times s} \times \mathbf{Z}_\epsilon^{V, \partial V}|_{s \times r_2}$ is performed with

$$(\mathbf{Z}_0^{\partial V, V}|_{r_1 \times s} \times \mathbf{Z}_\epsilon^{V, \partial V}|_{s \times r_2})|_{r_1 \times r_2} = \sum_{\ell=0}^{\iota} \left(\sum_{s \in \mathcal{U}(r_1 \times r_2, \ell)} \hat{\mathbf{Z}}_0^{\partial V, V}|_{r_1 \times s} \times \hat{\mathbf{Z}}_\epsilon^{V, \partial V}|_{s \times r_2} \right), \quad (2.26)$$

where $\iota \in [0, L]$ which L is the depth of \mathcal{H} -matrices $\mathbf{Z}_0^{\partial V, V}$ and $\mathbf{Z}_\epsilon^{V, \partial V}$. Also,

$$\begin{aligned} \mathcal{U}(r_1 \times r_2, \ell) = \left\{ s \in T_V^{(\ell)} : \{R_\ell(r_1) \times s \in T_{S \times V} \text{ and } s \times R_\ell(r_2) \in \mathcal{L}(T_{V \times S})\} \right. \\ \left. \text{or } \{R_\ell(r_1) \times s \in \mathcal{L}(T_{S \times V}) \text{ and } s \times R_\ell(r_2) \in T_{V \times S}\} \right\}, \end{aligned} \quad (2.27)$$

and

$$V = \bigcup_{\ell=0, \dots, L} \bigcup_{s \in \mathcal{U}(r_1 \times r_2, \ell)} s. \quad (2.28)$$

In (2.27), $R_\ell(r_1)$ is the relative of cluster r_1 (ancestor ($\ell < j$), self ($\ell = j$), or descendant ($\ell > j$)) at ℓ th level and $\mathcal{L}(T_{V \times S})$ is a leaf of the $T_{V \times S}$ interaction tree. Hence, in (2.26) sub-block $\hat{\mathbf{Z}}_0^{\partial V, V}|_{r_1 \times s}$, or sub-block $\hat{\mathbf{Z}}_\epsilon^{V, \partial V}|_{s \times r_2}$, or both are in the leaf level of the corresponding interaction tree and are stored as \mathcal{R} - or \mathcal{F} -blocks.

Since \mathcal{F} -blocks have the size of at most $n_{\min} \times n_{\min}$, \mathcal{H} -matrix-matrix product with them requires n_{\min} MVPs, while the exact \mathcal{H} -matrix-matrix product with an \mathcal{R} -block involves k MVPs. Therefore, to compute $\mathbf{Z}_0^{\partial V, V}|_{r_1 \times s} \times \mathbf{Z}_\epsilon^{V, \partial V}|_{s \times r_2}$ in (2.26) at any level ℓ will require at most $\max(k_{\max}, n_{\min})$ MVPs, where k_{\max} is the maximum rank revealed for $\mathbf{Z}_0^{\partial V, V}$ and $\mathbf{Z}_\epsilon^{V, \partial V}$. Without loss of generality if $k_{\max} \geq n_{\min}$, the complexity \mathcal{N} to compute the product of sub-blocks $\mathbf{Z}_0^{\partial V, V}|_{r_1 \times s}$ and $\mathbf{Z}_\epsilon^{V, \partial V}|_{s \times r_2}$ can be estimated as

$$\begin{aligned} \mathcal{N} \left(\mathbf{Z}_0^{\partial V, V}|_{r_1 \times s \in \mathcal{L}(T_{S \times V}, \ell)} \times \mathbf{Z}_\epsilon^{V, \partial V}|_{s \times r_2 \in (T_{V \times S}, \ell)} \right) \\ \leq k_{\max}^{\partial V, V} \mathcal{N}_{\text{MVP}}(\mathbf{Z}_\epsilon^{V, \partial V}|_{s \times r_2 \in (T_{V \times S}, \ell)}) \\ \stackrel{(2.24)}{\leq} k_{\max}^{\partial V, V} \mathcal{M}(\mathbf{Z}_\epsilon^{V, \partial V}|_{s \times r_2 \in (T_{V \times S}, \ell)}), \quad k_{\max}^{\partial V, V} \geq n_{\min}. \end{aligned} \quad (2.29)$$

Similarly,

$$\begin{aligned} \mathcal{N} \left(\mathbf{Z}_0^{\partial V, V} \Big|_{r_1 \times s \in (T_{S \times V}, \ell)} \times \mathbf{Z}_\epsilon^{V, \partial V} \Big|_{s \times r_2 \in \mathcal{L}(T_{V \times S}, \ell)} \right) \\ \leq k_{\max}^{V, \partial V} \mathcal{M}(\mathbf{Z}_0^{\partial V, V} \Big|_{r_1 \times s \in (T_{S \times V}, \ell)}), \quad k_{\max}^{V, \partial V} \geq n_{\min}. \end{aligned} \quad (2.30)$$

The overall complexity to multiply $\mathbf{Z}_0^{\partial V, V}$ and $\mathbf{Z}_\epsilon^{V, \partial V}$ can be calculated by analyzing the interaction tree $T_{S \times V} \times T_{V \times S} = T_{S \times S}$ resulting from the multiplication. By considering all resultant leaf blocks $r_1 \times r_2 \in \mathcal{L}(T_{S \times S}, j)$ at the j th level of (2.26), $j = 1, \dots, L_S$, the complexity estimate is

$$\mathcal{N}(\mathbf{Z}_0^{\partial V, V} \times \mathbf{Z}_\epsilon^{V, \partial V}) \leq \sum_{j=0}^{L_S} \sum_{r_1 \times r_2 \in \mathcal{L}(T_{S \times S}, j)} \times \sum_{\ell=0}^L \sum_{s \in \mathcal{U}(r_1 \times r_2, \ell)} \mathcal{N} \left(\hat{\mathbf{Z}}_0^{\partial V, V} \Big|_{r_1 \times s} \times \hat{\mathbf{Z}}_\epsilon^{V, \partial V} \Big|_{s \times r_2} \right), \quad (2.31)$$

where L is the depth of \mathcal{H} -matrices $\mathbf{Z}_0^{\partial V, V}$ and $\mathbf{Z}_\epsilon^{V, \partial V}$. By substituting (2.29) and (2.30) into (2.31), it can be written as:

$$\begin{aligned} \mathcal{N}(\mathbf{Z}_0^{\partial V, V} \times \mathbf{Z}_\epsilon^{V, \partial V}) \\ \leq \sum_{j=0}^{L_S} \sum_{r_1 \times r_2 \in \mathcal{L}(T_{S \times S}, j)} \sum_{\ell=0}^L \sum_{s \in \mathcal{U}(r_1 \times r_2, \ell)} \left(k_{\max}^{V, \partial V} \mathcal{M}(\mathbf{Z}_0^{\partial V, V} \Big|_{r_1 \times s}) + k_{\max}^{\partial V, V} \mathcal{M}(\mathbf{Z}_\epsilon^{V, \partial V} \Big|_{s \times r_2}) \right). \end{aligned} \quad (2.32)$$

Considering the definition (2.28) for the union of all the volume clusters s contributing to formation of the destination block $r_1 \times r_2$ the operation count $\sum_{\ell=0}^L \sum_{s \in \mathcal{U}(r_1 \times r_2, \ell)} (k_{\max}^{V, \partial V} \mathcal{M}(\mathbf{Z}_0^{\partial V, V} \Big|_{r_1 \times s}) + k_{\max}^{\partial V, V} \mathcal{M}(\mathbf{Z}_\epsilon^{V, \partial V} \Big|_{s \times r_2}))$ in the summation over the volume clusters s in (2.32) can be simplified by considering the root cluster V containing all volume basis/testing functions, yielding

$$\mathcal{N}(\mathbf{Z}_0^{\partial V, V} \times \mathbf{Z}_\epsilon^{V, \partial V}) \leq \sum_{j=0}^{L_S} \sum_{r_1 \times r_2 \in \mathcal{L}(T_{S \times S}, j)} \left(k_{\max}^{V, \partial V} \mathcal{M}(\mathbf{Z}_0^{\partial V, V} \Big|_{r_1 \times V}) + k_{\max}^{\partial V, V} \mathcal{M}(\mathbf{Z}_\epsilon^{V, \partial V} \Big|_{V \times r_2}) \right). \quad (2.33)$$

On the other hand, for each level j , the total number of leaf blocks $r_1 \times r_2 \in \mathcal{L}(T_{S \times S}, j)$ in the resultant interaction tree $T_{S \times S}$ is bounded by $2^j C_{\text{sp}}^{S \times S}$ in case of bisection based partitioning and considering sparsity constant definition (2.15). Here,

2^j is the total number of observer clusters r_1 or source clusters r_2 at the j th level of interaction tree $T_{S \times S}$. Therefore, in (2.33) the number of operations (estimated via memory use) in summations $\sum_{r_1 \times r_2 \in \mathcal{L}(T_{S \times S}, j)} \mathcal{M}(\mathbf{Z}_0^{\partial V, V}|_{r_1 \times V})$ and $\sum_{r_1 \times r_2 \in \mathcal{L}(T_{S \times S}, j)} \mathcal{M}(\mathbf{Z}_\epsilon^{V, \partial V}|_{V \times r_2})$ required for computation of the resultant leaf clusters $r_1 \times r_2$ at level j can be replaced by the operation count $C_{\text{sp}}^{S \times S}(\mathcal{M}(\mathbf{Z}_0^{\partial V, V}|_{\partial V \times V}) + \mathcal{M}(\mathbf{Z}_\epsilon^{V, \partial V}|_{\partial V \times V}))$ over the root cluster ∂V containing all the surface RWG basis/testing functions. So, (2.33) can be rewritten as:

$$\mathcal{N}(\mathbf{Z}_0^{\partial V, V} \times \mathbf{Z}_\epsilon^{V, \partial V}) \leq \sum_{j=0}^{L_S} C_{\text{sp}}^{S \times S} \left(k_{\text{max}}^{V, \partial V} \mathcal{M}(\mathbf{Z}_0^{\partial V, V}|_{\partial V \times V}) + k_{\text{max}}^{\partial V, V} \mathcal{M}(\mathbf{Z}_\epsilon^{V, \partial V}|_{V \times \partial V}) \right). \quad (2.34)$$

Here, $\mathcal{M}(\mathbf{Z}_0^{\partial V, V}|_{\partial V \times V})$ and $\mathcal{M}(\mathbf{Z}_\epsilon^{V, \partial V}|_{V \times \partial V})$ can simply be replaced by $\mathcal{M}(\mathbf{Z}_0^{\partial V, V})$ and $\mathcal{M}(\mathbf{Z}_\epsilon^{V, \partial V})$ denoting the memory use for storage of the \mathcal{H} -matrices $\mathbf{Z}_0^{\partial V, V}$ and $\mathbf{Z}_\epsilon^{V, \partial V}$, respectively. Then, by recalling that the depth of the surface tree is $L_S = \mathcal{O}(\log P)$ and introducing the maximum rank k_{max} for blocks of either $\mathbf{Z}_0^{\partial V, V}$ or $\mathbf{Z}_\epsilon^{V, \partial V}$ (i.e. $k_{\text{max}} = \max(k_{\text{max}}^{\partial V, V}, k_{\text{max}}^{V, \partial V})$), (2.34) becomes

$$\mathcal{N}(\mathbf{Z}_0^{\partial V, V} \times \mathbf{Z}_\epsilon^{V, \partial V}) \leq L_S C_{\text{sp}}^{S \times S} k_{\text{max}} \left(\mathcal{M}(\mathbf{Z}_\epsilon^{V, \partial V}) + \mathcal{M}(\mathbf{Z}_0^{\partial V, V}) \right). \quad (2.35)$$

Recalling the estimates for memory use (2.21) and (2.22) we finally get the estimate for operation count in the *exact* multiplication of the \mathcal{H} -matrices

$$\mathcal{N}(\mathbf{Z}_0^{\partial V, V} \times \mathbf{Z}_\epsilon^{V, \partial V}) = \mathcal{O}(k_{\text{max}}^2 P \log^2 P) + \mathcal{O}(k_{\text{max}}^2 N \log N \log P). \quad (2.36)$$

Note, that the *formatted* multiplication $\mathbf{Z}_0^{\partial V, V} \otimes \mathbf{Z}_\epsilon^{V, \partial V}$ requires the truncation based on the prescribed \mathcal{H} -arithmetic tolerance $\tau_{\mathcal{H}}$ of small singular values resulting from addition of the \mathcal{R} -blocks. For that, the rSVD with the complexity of $\mathcal{O}(n(\ell) + m(\ell))k^2 + \mathcal{O}(k^3)$ [70, 7.1.1] is used throughout the Algorithm 2 leaving the complexity estimate (2.36) correct for the formatted multiplication as well (i.e. $\mathcal{N}(\mathbf{Z}_0^{\partial V, V} \times \mathbf{Z}_\epsilon^{V, \partial V}) \simeq \mathcal{N}(\mathbf{Z}_0^{\partial V, V} \otimes \mathbf{Z}_\epsilon^{V, \partial V})$) provided k_{max} is relatively small compared to P and N and can be considered to be independent of them.

Formatted Addition $\mathbf{Z}_\epsilon^{\partial V, \partial V} \oplus (\mathbf{Z}_0^{\partial V, V} \otimes \mathbf{Z}_\epsilon^{V, \partial V})$ Next, the complexity of the formatted addition of two \mathcal{H} -matrices of the size $P \times P$ required to form Z_{SVS} by adding $Z_\epsilon^{\partial V, \partial V}$ and the result of $\mathbf{Z}_0^{\partial V, V} \otimes \mathbf{Z}_\epsilon^{V, \partial V}$ in (2.14) has to be considered. For formatted addition of the square \mathcal{H} -matrices, the estimate for number of operations is $O(k_{\max}^2 P \log P) + O(k_{\max}^3 P)$ [62]. The total complexity for setting up the Z_{SVS} is composed of the complexity of the formatted multiplication (2.36) and the formatted addition as

$$\mathcal{N}(Z_{\text{SVS}}) = \mathcal{O}(k_{\max}^2 P \log^2 P) + \mathcal{O}(k_{\max}^2 N \log N \log P) + \mathcal{O}(k_{\max}^3 P). \quad (2.37)$$

One can see that for the problems of electrically moderate sizes with bounded rank, the complexity for setting up the Z_{SVS} is dominated by the complexity of the formatted multiplication (2.36).

\mathcal{H} -LU Decomposition and Back Substitution To solve the matrix equations, \mathcal{H} -LU decomposition and back substitution are applied to Z_{SVS} . Since Z_{SVS} is a square \mathcal{H} -matrix of the size $P \times P$, the time complexity for the \mathcal{H} -LU decomposition and back substitution are $\mathcal{O}(k_{\max}^3 P \log^2 P)$ and $\mathcal{O}(k_{\max}^3 P \log P)$, respectively [62].

2.7 Numerical Results

To validate the accuracy of the \mathcal{H} -matrix SVS-EFIE solver, we performed comparison of its numerical solutions against the analytic Mie series [71] and the results obtained using FEKO commercial solver [72] for several scattering problems. The performance of the SVS-EFIE solver for the timing and memory requirements is shown to corroborate the asymptotic complexities derived in Section 2.6. In all the numerical results, we considered the tolerance for \mathcal{H} -matrix compression $\tau_{\mathcal{H}}$ to be the same as the truncation tolerance of the ACA algorithm τ_{ACA} . So, for brevity $\tau = \tau_{\text{ACA}} = \tau_{\mathcal{H}}$ is used throughout Section 2.7. The optimal values of the admissibility criterion η and leafsize n_{\min} are usually problem dependent and chosen empirically. The \mathcal{H} -matrix parameters in the paper are the optimized values for $\eta = \{1, 2, 3, 4, 5\}$

and $n_{\min} = \{8, 16, 32, 64\}$ sets in all numerical examples. It was observed that all combination of these parameters are working well for the proposed solver. However, to balance between memory use and CPU time we run the numerical example for different parameters and empirically find that $\eta = 4$ and $n_{\min} = 16$ provide better time and memory performance for certain numerical examples of this paper.

2.7.1 Dielectric Sphere

In the first example, we consider scattering on a dielectric sphere of radius $R = 0.1$ m and relative dielectric permittivity $\epsilon = 1.5$ excited by a radial dipole with the dipole moment $I\ell = 1[\text{A} \cdot \text{m}]$.

To demonstrate the behavior of the error in \mathcal{H} -matrix accelerated MoM solution of SVS-EFIE and its reduction with the decrease of ACA truncation threshold τ , we consider dielectric sphere excitation by a z -directed electric dipole at 3 GHz situated above the north pole of the sphere 0.4 m away from the origin. The behavior of the average relative error (δ) of both \mathcal{H} -matrix accelerated MoM solution and direct MoM solution of the SVS-EFIE [13] with respect to the Mie series solution is depicted as a function of τ in Fig. 2.8 for three different mesh densities, $h = \lambda/10, \lambda/20$, and $\lambda/30$, h being the characteristic size of mesh elements. The results demonstrate that \mathcal{H} -matrix accelerated MoM solution with $\tau \leq 10^{-3}$ does not produce any substantial increase in accuracy compared to the direct MoM solution. On the other hand, the compression ratio (CR) of the overall MoM memory use in SVS-EFIE is shown for different τ in Table 2.1, where

$$\text{CR} = \left(1 - \frac{\text{Mem. } \mathcal{H}\text{-matrix SVS-EFIE}}{\text{Mem. direct MoM SVS-EFIE [13]}} \right) \times 100\%. \quad (2.38)$$

From Fig. 2.8 and Table 2.1 it can be seen that the proposed solver has a good compression for $\tau = 10^{-3}$ with an acceptable error level. So, the ACA truncation threshold is set to $\tau = 10^{-3}$ for the other examples of this paper.

To analyze the \mathcal{H} -matrix acceleration performance for MoM solution with large number of degrees of freedom (DoF), we examine the memory usage by the \mathcal{H} -Matrices

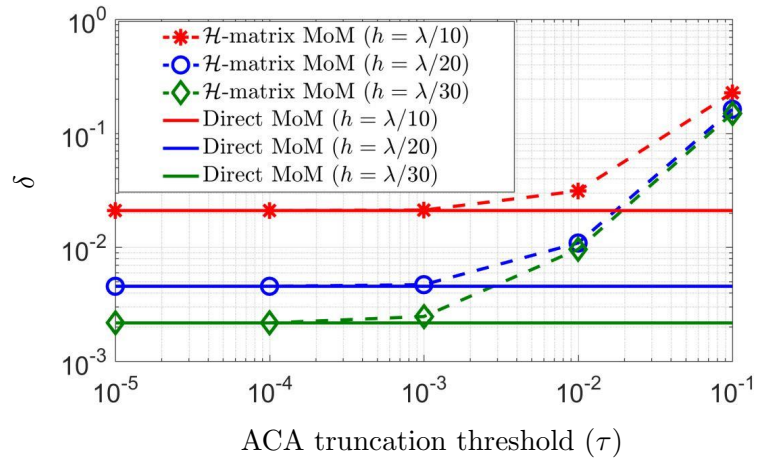


Figure 2.8: Average relative error δ of both \mathcal{H} -matrix accelerated MoM solution for dielectric sphere excitation problem with different mesh densities ($h = \lambda/10, \lambda/20$, and $\lambda/30$) with respect to the Mie series solution as a function of ACA truncation tolerance τ . The error in the direct MoM solution of SVS-EFIE [13] is shown for reference.

Table 2.1: Memory compression ratio (5.12) for the \mathcal{H} -matrix accelerated MoM solution of the SVS-EFIE for the dielectric sphere excitation problem with different mesh densities ($h = \lambda/10, \lambda/20$, and $\lambda/30$).

τ	$CR \%$ ($h = \lambda/10$)	$CR \%$ ($h = \lambda/20$)	$CR \%$ ($h = \lambda/30$)
10^{-1}	62	87	93
10^{-2}	48	82	90
10^{-3}	31	75	86
10^{-4}	7	55	80
10^{-5}	0	20	63

and CPU time used for pertinent \mathcal{H} -matrix operations in comparison with those in the naïve MoM solution [13].

For the first study, to show the complexity behavior of the proposed solver in the range of frequency we consider the dielectric sphere benchmark with a constant mesh density $h = \lambda/10$ over the frequency range from 4 GHz to 10 GHz. In Fig. 2.9(a), the memory usage for $Z_\epsilon^{\partial V, \partial V}$ is demonstrated as a function of number of RWG basis functions P . Its \mathcal{H} -matrix MoM scaling behaves as $\mathcal{O}(P \log P)$ confirming the theoretical estimates (2.23). In addition, the memory requirement of $Z_0^{\partial V, V}$ and $Z_\epsilon^{V, \partial V}$ is also depicted in Fig. 2.9(b) with respect to the total number of surface and volume DoFs $X = 3N + P$. It can be seen that the numerically observed memory scaling of $\mathcal{O}(N \log N) + \mathcal{O}(P \log P)$ for \mathcal{H} -matrix MoM confirms the theoretical estimates (2.21) and (2.22).

Next, in Fig. 2.9(c) and (d), the time required to fill the compressed \mathcal{H} -matrices is plotted. Fig. 2.9(c) shows the time to fill $Z_\epsilon^{\partial V, \partial V}$ that behaves as $\mathcal{O}(P \log P)$ for \mathcal{H} -matrix solver. Also, the CPU time to fill $Z_0^{\partial V, V}$ and $Z_\epsilon^{V, \partial V}$ is plotted as a function of total number of surface and volume DoFs $X = 3N + P$ in Fig. 2.9(d). One can observe fill time complexities of $\mathcal{O}(N \log N) + \mathcal{O}(P \log P)$ which is of the same order as the memory use complexity (2.21) and (2.22). In addition, the set up time for creating Z_{SVS} as a part of the \mathcal{H} -LU direct method is depicted in Fig. 2.10(a) with the complexity of $\mathcal{O}(N \log N \log P) + \mathcal{O}(P \log^2 P)$ which confirms the theoretical analysis (2.37). The time complexities for \mathcal{H} -LU decomposition and back-substitution are also plotted in Fig. 2.10(b) with scaling of $\mathcal{O}(P \log^2 P)$ and $\mathcal{O}(P \log P)$, respectively [62].

For the same scattering problem, the computational time using \mathcal{H} -GMRES iterative method is plotted in Fig. 2.10(c). In the first study, the number of iterations is fixed to $N_{\text{it}} = 1000$ and the time is plotted in blue triangles as a function of number of DoFs leading to $N_{\text{it}}(\mathcal{O}(N \log N) + \mathcal{O}(P \log P))$ scaling. In the second study, to show the convergence behavior of \mathcal{H} -GMRES iterative SVS-EFIE, the iterative solver tolerance is set to 10^{-6} and the solution time is depicted in red crosses in the same figure.

In this study, the dielectric sphere having $\epsilon = 1.5$ has a relatively small electrical

radius ranging from $D = 3.2\lambda$ to $D = 8\lambda$ in the considered frequency range from 4 GHz to 10 GHz. Therefore, the maximum rank will be approximately constant for all \mathcal{H} -matrices [69] in the entire frequency range. It can be seen from Fig. 2.9 (a)–(f) that the memory requirement and CPU time scale according to the constant rank assumption.

In the next study, to analyze the performance of the proposed fast solver for a system with large number of DoF we fix the frequency at 3 GHz and then increase the number of DoF up to 1 M by increasing the number of meshes. The electrical size of the object is $D = 2.4\lambda$ in this case. The complexity behavior of both \mathcal{H} -matrix and naïve MoM SVS-EFIE are depicted in Fig. 2.11 and Fig. 2.12 with excellent agreement for memory and time scaling behaviors.

2.7.2 Dielectric NASA Almond

In order to show the behaviour of SVS-EFIE solution for a non-smooth geometry featuring a sharp corner, we consider an accelerated MoM solution for the analysis of a dipole radiation near NASA almond [73] target at 3 GHz. The target has a relative permittivity $\epsilon = 12$ and a size of 0.252 m, 0.0976 m, and 0.0325 m along x , y , and z axes, respectively. The model is excited by the electric dipole directed along the short axis of the almond (z axis in Fig. 2.13) and situated on the long axis (x axis in Fig. 2.13) 0.8528 m away from almond's tip. The electric dipole moment is $I\ell = 1[\text{A} \cdot \text{m}]$. In this example, the number of triangles in the MoM discretization on the boundary ∂V is $M = 11,994$, the number of edges is $P = 17,991$, and the number of tetrahedrons in the volume V is $N = 191,440$ which leads to 592,311 number of volumetric and surface DoFs. Distribution of the magnitude of the total electric field using accelerated SVS-EFIE is depicted in Fig. 2.13. In order to validate the \mathcal{H} -matrix MoM solution of SVS-EFIE, MoM solution via surface equivalence principle (SEP) for the same radiation problem is obtained using FEKO commercial software [72]. The magnitude of the total electric field along the x and y axes of the almond are depicted in the same Fig. 2.13 for both the \mathcal{H} -matrix based MoM solution of SVS-EFIE and MoM solution from FEKO with an observed good agreement between the two.

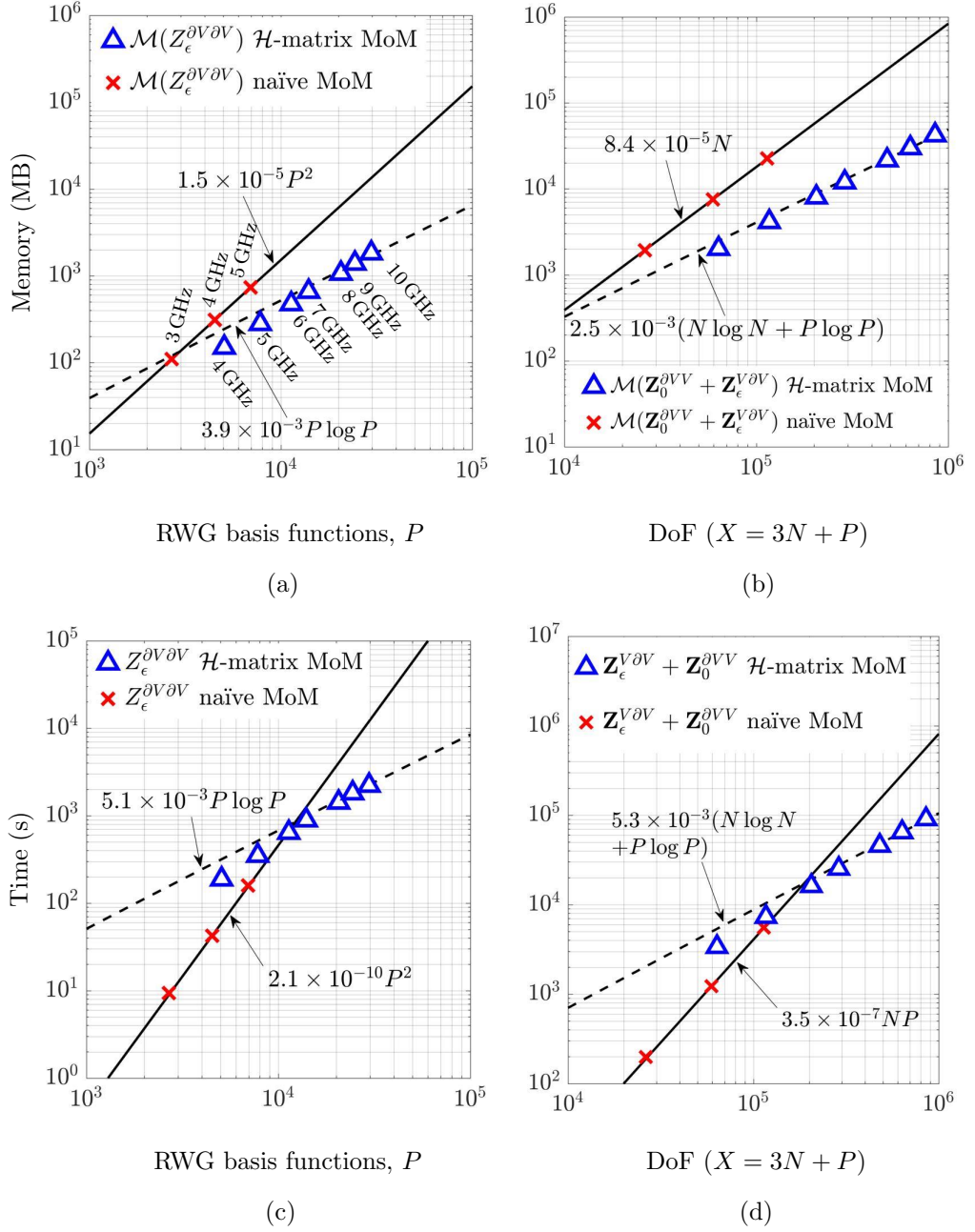


Figure 2.9: Scaling behavior of both \mathcal{H} -matrix (dashed lines) and naïve (solid lines) MoM SVS-EFIE for the dielectric sphere with mesh density $h = \lambda/10$ across the frequency range from 4 GHz to 10 GHz. (a) Memory for $Z_\epsilon^{\partial V, \partial V}$. (b) Memory for $Z_0^{\partial V, V} + Z_\epsilon^{\partial V, \partial V}$. (c) Set up time for $Z_\epsilon^{\partial V, \partial V}$. (d) Set up time for $Z_0^{\partial V, V}$ and $Z_\epsilon^{\partial V, \partial V}$.

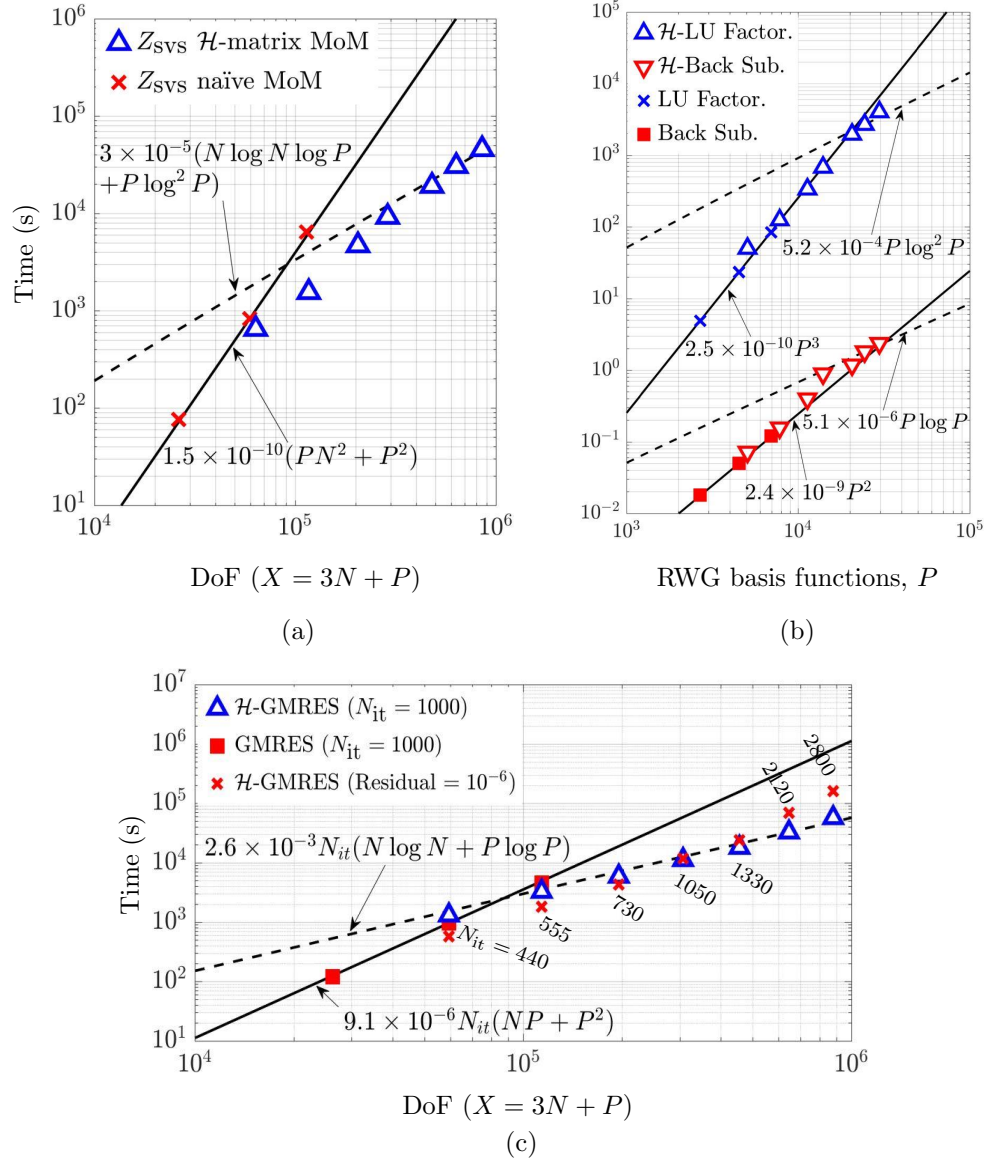


Figure 2.10: Scaling behavior of both \mathcal{H} -matrix (dashed lines) and naïve (solid lines) MoM SVS-EFIE for the dielectric sphere with mesh density $h = \lambda/10$ across the frequency range from 4 GHz to 10 GHz. (a) Set up time for Z_{SVS} as a part of \mathcal{H} -LU-based direct solver. (b) Solution time for \mathcal{H} -LU-based direct method (\mathcal{H} -LU factorization and back substitution) (c) Solution time for \mathcal{H} -GMRES-based iterative method (fixed $N_{\text{it}} = 1000$ and fixed residual 10^{-6} cases).

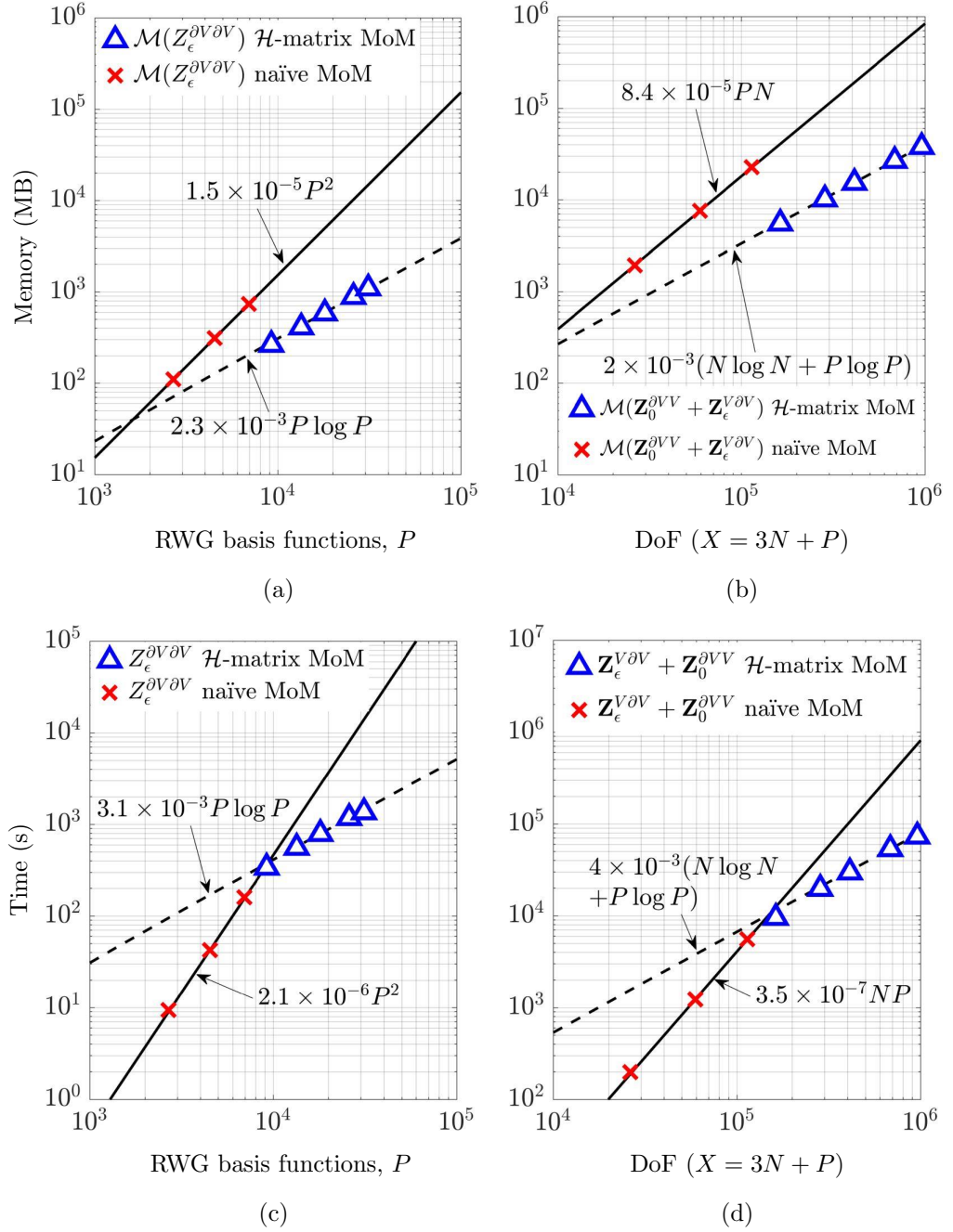


Figure 2.11: Scaling behavior of both \mathcal{H} -matrix (dashed lines) and naive (solid lines) MoM SVS-EFIE for the dielectric sphere with relative permittivity of $\epsilon = 1.5$ at 3 GHz. (a) Memory for $Z_\epsilon^{\partial V, \partial V}$. (b) Memory for $Z_0^{\partial V, V} + Z_\epsilon^{V, \partial V}$. (c) Set up time for $Z_\epsilon^{\partial V, \partial V}$. (d) Set up time for $Z_0^{\partial V, V}$ and $Z_\epsilon^{V, \partial V}$.

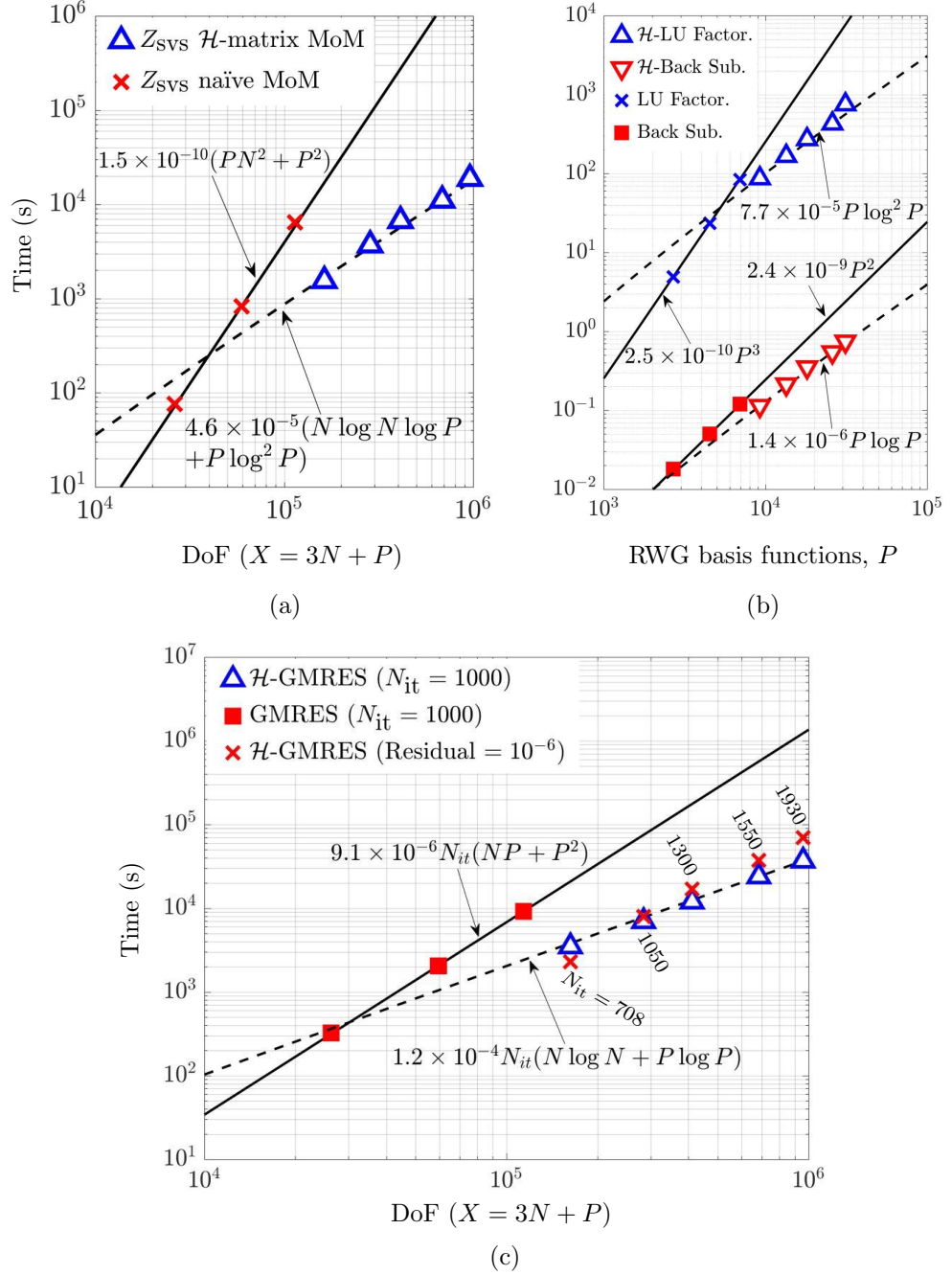


Figure 2.12: Scaling behavior of both \mathcal{H} -matrix (dashed lines) and naïve (solid lines) MoM SVS-EFIE for the dielectric sphere with relative permittivity of $\epsilon = 1.5$ at 3 GHz. (a) Set up time for Z_{SVS} as a part of \mathcal{H} -LU-based direct solver. (b) Solution time for \mathcal{H} -LU-based direct method (\mathcal{H} -LU factorization and back substitution) (c) Solution time for \mathcal{H} -GMRES-based iterative method (fixed $N_{it} = 1000$ and fixed residual 10^{-6} cases).

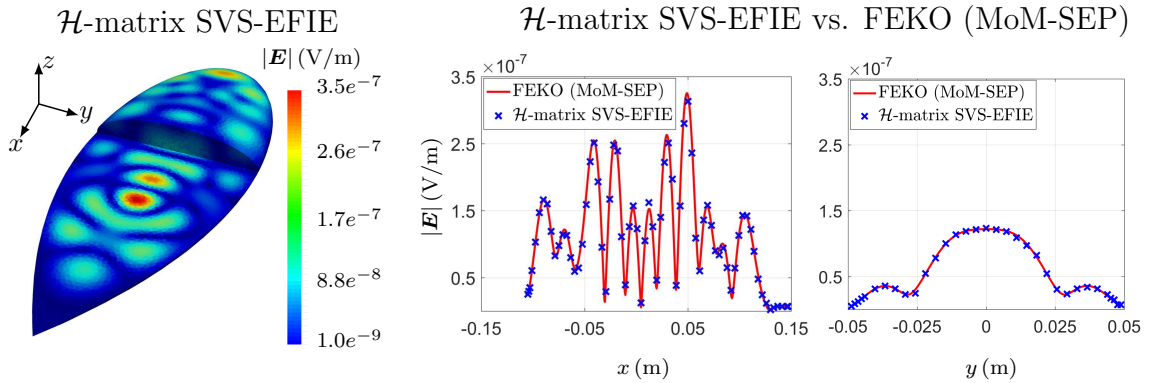


Figure 2.13: Magnitude of the total electric field at 3 GHz inside the dielectric NASA almond model with the relative dielectric permittivity $\epsilon = 12$. A 3-D representation of the total electric field obtained from \mathcal{H} -matrix SVS-EFIE is in the left plot. The distribution of the magnitude of the total electric field along the x and y axes for the \mathcal{H} -matrix SVS-EFIE and FEKO solutions are shown in the right plots.

2.7.3 Austin Benchmark Suite for Computational Bioelectromagnetics

Another example considers the scattering problems on a human head sized sphere and a human body sized spheroid from Austin Benchmark Suite [55]. Both models are filled with a tissue-equivalent homogeneous material [74] with frequency dependent relative dielectric permittivity and conductivity as listed in Table 2.2. The sphere has a radius of $R = 0.108$ m and the spheroid model has minor and major axes of 0.344 m, and 1.76 m, respectively, with its major axis aligned with the z -axis. The scattering problem is solved at three frequencies in the UHF band: 402 MHz, 900 MHz, and 2.45 GHz.

Table 2.2: Values of tissue-equivalent material relative dielectric permittivity and conductivity [74].

402 MHz		900 MHz		2.45 GHz	
ϵ_r	σ	ϵ_r	σ	ϵ_r	σ
44.7	0.87	41.5	0.97	39.2	1.80

2.7.3.1 Homogeneous Human Head-Sized Sphere

The model is excited by the same dipole used for dielectric sphere example in Section 2.7.1 that is situated above the north pole of the sphere 0.4 m away from the origin. Distribution of the computed field is depicted in Fig. 2.14 at 900 MHz and 2.45 GHz. In this example, the number of triangles in the MoM discretization on the boundary ∂V is $M = 17,262$, the number of edges is $P = 25,893$, and the number of tetrahedrons in the volume V is $N = 263,309$ that leads to total 815,820 number of DoFs. The numerical solutions of the radiation problem obtained using the proposed method at 900 MHz and 2.45 GHz are shown in Fig. 2.14 (a) and (b), respectively. The relative error between the \mathcal{H} -matrix SVS-EFIE solution and the Mie series solution is depicted in Fig. 2.14 (c) and (d) for 900 MHz and 2.45 GHz, respectively. The average relative error in the solution at 900 MHz is below 0.006 with a standard deviation of 0.002. Also, the solution of the same problem at 2.45 GHz has an average error of 0.049 with a standard deviation of 0.018.

2.7.3.2 Homogeneous Human Body-Sized Spheroid

The spheroid model is excited by a uniform z -polarized plane-wave traveling in the $+x$ -direction. In this example, the number of triangles in the MoM discretization on the boundary ∂V is $M = 15,804$, the number of edges is $P = 23,706$, and the number of tetrahedrons in the volume V is $N = 206,431$ which leads to 642,999 number of DoFs. Distribution of the magnitude of the total electric field using \mathcal{H} -matrix accelerated MoM solution of SVS-EFIE is depicted in Fig. 2.15 for 402 MHz and 900 MHz. The magnitude of the total electric field along the x and z axes are also depicted in the same Fig. 2.15 for the case of \mathcal{H} -matrix based MoM solution of SVS-EFIE and FEKO's MoM solution with an observed good agreement between the two.

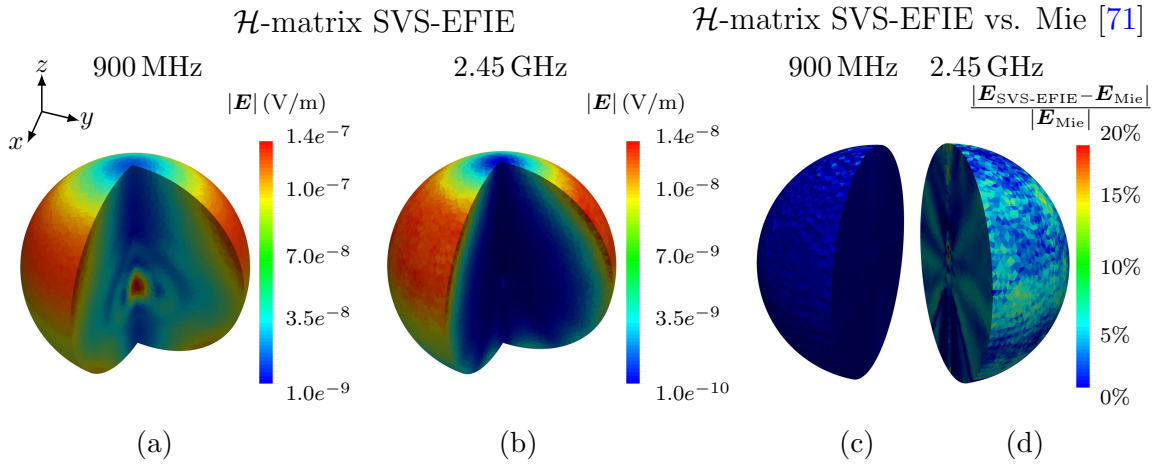


Figure 2.14: Magnitude of the total electric field inside the human head-sized sphere produced by a z -directed electric dipole situated at $x' = 0$ m, $y' = 0$ m, $z' = 0.4$ m obtained by the \mathcal{H} -matrix solver at (a) 900 MHz (b) 2.45 GHz. The relative error distribution with respect to the Mie series solution is shown in (c) and (d).

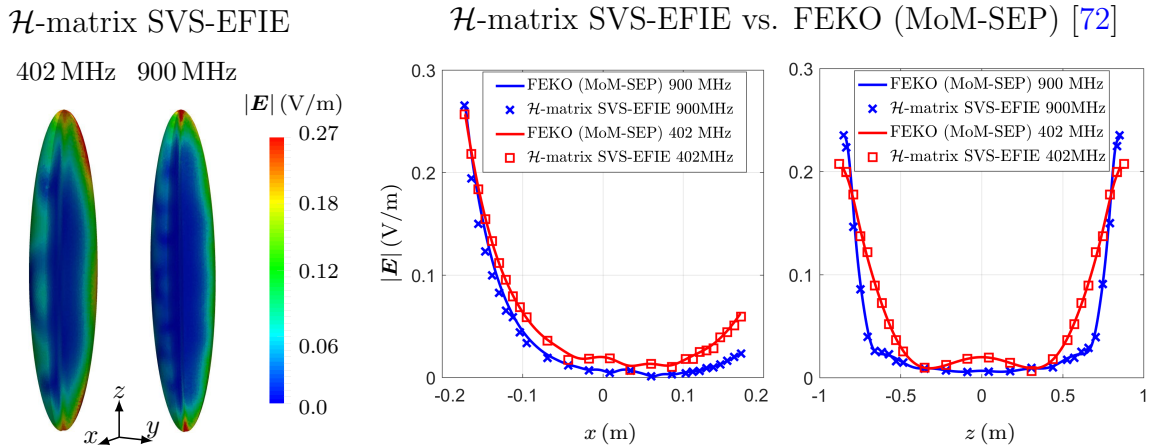


Figure 2.15: Magnitude of the total electric field inside the human body-sized spheroid produced by a uniform \hat{z} -polarized plane-wave traveling in the $+x$ direction at 402 MHz and 900 MHz obtained by the \mathcal{H} -matrix SVS-EFIE. The distribution of the magnitude of total electric field along the x and z axes for \mathcal{H} -matrix SVS-EFIE and FEKO solutions are shown in the right.

2.8 Conclusion

An \mathcal{H} -matrix based direct and iterative algorithms are developed for the fast MoM solution of the SVS-EFIE. The new computational framework allows for the iterative solution of 3-D scattering and radiation problems on homogeneous non-magnetic dielectrics with $O(N \log N) + O(P \log P)$ CPU time and memory complexity and their direct solution with $O(N \log N \log P) + O(P \log^2 P)$ CPU time and $O(N \log N) + O(P \log P)$ memory complexity for problems of moderate electrical size, N being the number of tetrahedrons in the volume and P being the number of surface unknowns produced by the MoM discretization. The \mathcal{H} -matrix arithmetics used to form and operate with the rectangular matrices produced by the MoM discretization of SVS-EFIE is described in detail, as well as the associated computational and memory complexity estimates. The proposed accelerated method is shown to provide an efficient compression of the MoM impedance matrix which leads to significant reduction of the memory usage and the CPU time. Solution of the 3-D scattering problems of moderate electrical sizes which feature large number of associated degrees of freedom is demonstrated for both the dielectrics with low loss levels and the biological tissues exhibiting substantial loss. The method is particularly effective for the solution of scattering and radiation problems in BioEM which require computation of the fields throughout the volume of the objects.

3

\mathcal{H} -Matrix Accelerated Solution of Surface-Volume-Surface EFIE for Fast Analysis of Scattering on Composite Dielectric Objects

©2019 IEEE. Reprinted, with permission, from *Reza Gholami, Anton Menshov, and Vladimir Okhmatovski, IEEE Journal on Multiscale and Multiphysics Computational Techniques, May 2019.*

3.1 Abstract

An efficient fast direct algorithm based on the hierarchical (\mathcal{H})-matrices is presented for solution of the radiation and scattering problems on piece-wise homogeneous dielectric objects using method of moments (MoM) discretization of the surface-volume-surface electric field integral equation (SVS-EFIE). The SVS-EFIE for the composite objects introduces independent surface electric current density on the boundary of each region. Therefore, different from the traditional Poggio-Miller-Chang-Harrington-Wu-Tsai (PMCHWT) formulation, in the SVS-EFIE the scatterer regions can be meshed independently according to their local properties which im-

proves the flexibility and efficiency of the proposed method. It also makes the proposed algorithms appropriate for analysis of both multiscale and large-scale composite structures. The numerical results from the proposed fast method are provided for the high-loss biological tissues from bio-electromagnetics (BioEM) applications and agree well with the analytical Mie series solution and commercial software. The CPU time and memory cost of the required \mathcal{H} -matrix operations is analyzed in detail and verified through several numerical experiments. The new computational framework allows for fast direct solution of 3-D radiation and scattering problems of moderate electrical size with $O(P^\alpha \log^2 P)$ CPU time and $O(P^\alpha \log P)$ memory complexity, P being the number of surface unknowns produced by the MoM discretization, and $1 \leq \alpha \leq 1.5$ being a geometry dependent parameter.

3.2 Introduction

Solution of the scattering problems on composite homogeneous dielectric objects plays important role in analysis of field interactions with the biological tissues [2, 3, 49, 55] and other applied problems. Since biological tissues contain inhomogeneous and/or anisotropic materials the Finite Element Method (FEM) [9] have become the most popular approach for solution of scattering and radiation problems in BioEM. Although the FEM is able to solve such problems, its is plagued by fundamental limitation of error accumulation when solving large-scale problems, it requires discretization of the volume of both the scatterer and the surrounding space, and depends on accurate enforcement of the absorbing boundary condition truncating the mesh [15].

Alternatively, such scattering and radiation problems on composite dielectric objects can be solved using integral equations (IE) and their discretization with method of moments (MoM). Traditional surface IE (SIE) formulations require two unknown surface current densities [12] on the boundary of each region of the the composite object. They also need sophisticated handling of the MoM discretization at the material junctions, and require complicated meshing which is consistent with MoM discretization requirement at the boundaries of the regions. In our previous

works [13, 35, 37, 38, 63], we proposed a new type of single-source integral equation known as surface-volume-surface electric field integral equation (SVS-EFIE) which requires only a single surface current density on the boundary of each region to uniquely represent the field inside of it. In the SVS-EFIE formulation for composite objects [38], independent fictitious electric surface current density is introduced at the boundary of each dielectric region to produce the field throughout its volume. Due to independence of the sought surface current densities on the boundaries of the regions, the respective surface and volume meshes in different regions can be different. This property of SVS-EFIE eliminates the difficulties associated with representation of the surface current densities at material junctions featured in the traditional SIEs [41] and allows to generate non-conformal meshes according to the respective material properties of distinct regions. It makes the proposed computational framework particularly suitable for the electromagnetic analysis of scattering from multiscale composite objects. Independent discretization of distinct regions of the object also improves the flexibility and efficiency of fast iterative [18, 22] and direct [28, 30, 31, 62] algorithms used for acceleration of the pertinent MoM solution as it enables construction of the more balanced trees in the pertinent matrix-implicit data structures.

The major challenge in the use of iterative algorithms is that they typically produce a poorly conditioned matrix equation for the objects with high contrasts and/or multiscale discretization such as featured in the BioEM applications. It can cause slow convergence in the iterative matrix solver or make it fail to converge. Even though the convergence problems can be alleviated using adequate preconditioning, construction of effective preconditioners often drastically increases the memory and CPU time due to operations required for its inversion [56]. The complexity of operations and memory use related to preconditioning often far exceed those of the fast iterative algorithm itself. Fast direct algorithms can effectively resolve the problem. In this paper, we propose such fast direct solution framework which is largely insensitive to the poor conditioning of the MoM matrix equation which may arise due to multiscale discretization and/or large disparity in the material parameters. In our previous work [35], we developed a fast direct method using hierarchical (\mathcal{H})-matrix [27, 36] for acceleration of the MoM solution of the SVS-EFIE for homogeneous dielectric

objects. In this work, we generalize the formulation to the case of piece-wise homogeneous dielectric regions. This algorithm can be used to accelerate matrix-matrix multiplications, LU-decomposition, and back-substitution within a framework of the fast direct solver for composite dielectric structures with arbitrary number of regions. Construction of the block- \mathcal{H} -matrices pertinent to the MoM discretization of the composite SVS-EFIE [38] is described in detail in this paper. The \mathcal{H} -matrix accelerated SVS-EFIE is shown to produce accurate results using only a fraction of the resources needed by the conventional MoM both in terms of memory and total CPU time. The proposed fast direct solution framework is also particularly advantageous for solution of the problems in which the field computation throughout the volume of the penetrable multi-region object is of interest. This is typically the case in BioEM applications requiring the knowledge of the fields distribution throughout the volume of the tissues in order to determine the specific absorption rate (SAR) [75–77].

3.3 Synopsis of SVS-EFIE for 3-D Composite Scatterers and Its MoM Solution

In [38], we introduced a new type of a single source surface integral equation (SSSIE) by combining the ideas of the traditional volume equivalence principle [71] and the theory of the SSIEs [46]. To derive the new SVS-EFIE formulation, let's consider scattering problem of a 3-D piece-wise homogeneous non-magnetic dielectric composite object with volumes V_1 and V_2 bounded by ∂V_1 and ∂V_2 . The object is situated in free-space with permittivity ϵ_0 radiated and excited by an incident field E^{inc} . Complex relative permittivity of regions with volume V_1 and V_2 are represented as ϵ_1 and ϵ_2 , respectively (Fig. 3.1(a)).

Consider the volume equivalence principle [71] (Fig. 3.1(b)) written for the electric

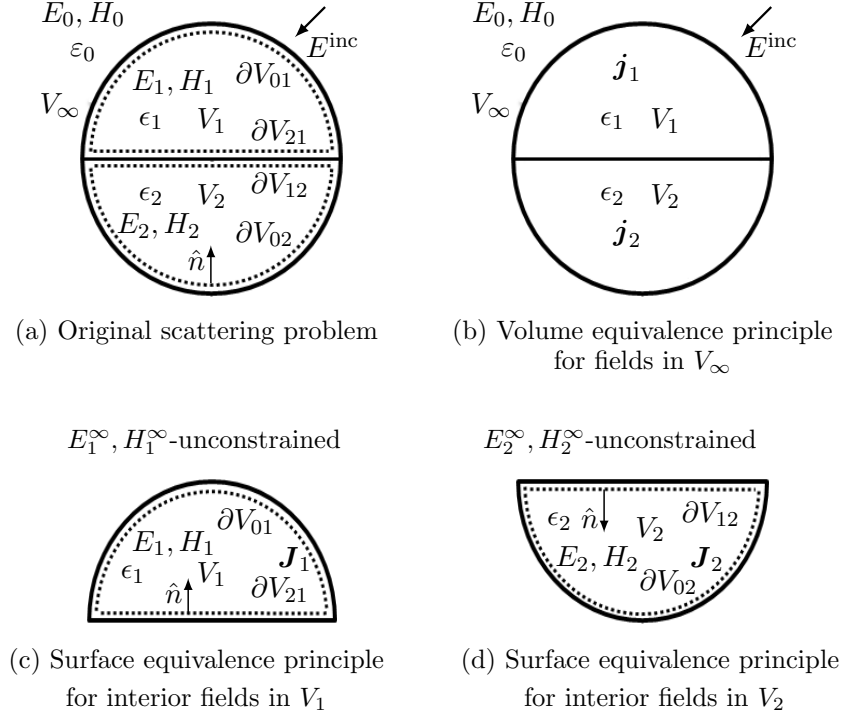


Figure 3.1: To derivation of SVS-EFIE in the scattering problem of 3-D composite dielectric object excited by incident field E^{inc} . (a) Original scattering problem of a two-region composite scatterer with volumes V_1 and V_2 bounded by surfaces $\partial V_1 = \partial V_{01} + \partial V_{21}$ and $\partial V_2 = \partial V_{02} + \partial V_{12}$, and situated in free-space background medium with permittivity ϵ_0 . Complex relative permittivity of volume V_1 and V_2 are ϵ_1 and ϵ_2 , respectively. (b) Volume equivalence principle to generate the true fields E_0, H_0 in V_∞ by volume polarization currents \mathbf{j}_1 and \mathbf{j}_2 . (c) Generalized surface equivalence principle interior to V_1 with single fictitious electric surface current density \mathbf{J}_1 producing true fields E_1, H_1 in V_1 and unconstrained field E_1^∞ outside V_1 . (d) Generalized surface equivalence principle interior to V_2 with single fictitious electric surface current density \mathbf{J}_2 producing true fields E_2, H_2 in V_2 and unconstrained field E_2^∞ outside V_2 .

field \mathbf{E} outside the scatterer

$$\begin{aligned} \mathbf{E}(\mathbf{r}) = & \mathbf{E}^{\text{inc}}(\mathbf{r}) + \int_{V_1} \overline{\overline{G}}_{e0}(\mathbf{r}, \mathbf{r}') \cdot \mathbf{j}_1(\mathbf{r}') dv' \\ & + \int_{V_2} \overline{\overline{G}}_{e0}(\mathbf{r}, \mathbf{r}') \cdot \mathbf{j}_2(\mathbf{r}') dv', \quad \mathbf{r} \in V_\infty \end{aligned} \quad (3.1)$$

where \mathbf{r} and \mathbf{r}' are being the observation and source locations. Also, $\overline{\overline{G}}_{e0}(\mathbf{r}, \mathbf{r}') = (k_0^{-2} \nabla \nabla + \overline{\overline{I}}) e^{-ik_0 |\mathbf{r} - \mathbf{r}'|} / (4\pi |\mathbf{r} - \mathbf{r}'|)$ is the 3-D dyadic Green's function of free-space with k_0 being wave number. In (3.1), $\mathbf{j}_m(\mathbf{r}) = k_0^2 [\epsilon_m(\mathbf{r}) - 1] \mathbf{E}_m(\mathbf{r})$ is the polarization current density inside volume V_m with complex relative permittivity $\epsilon_m = \epsilon_m + \sigma_m / (i\omega \epsilon_0)$ (here $m = 1, 2$).

Using the interior to V_1 single source surface equivalence principle (Fig. 3.1(c)), the total electric field $\mathbf{E}_1(\mathbf{r})$ inside V_1 can be written as

$$\mathbf{E}_1(\mathbf{r}) = -i\omega\mu_0 \oint_{\partial V_1} \overline{\overline{G}}_{ee1}(\mathbf{r}, \mathbf{r}') \cdot \mathbf{J}_1(\mathbf{r}') ds', \quad \mathbf{r} \in V_1 \setminus \partial V_1 \quad (3.2)$$

which involves only the equivalent fictitious surface electric current density \mathbf{J}_1 on the boundary ∂V_1 . In (3.2), $\mathbf{J}_1 = \hat{n} \times [\mathbf{H}_1 - \mathbf{H}_1^\infty]$ is the fictitious electric current defined on the boundary ∂V_1 equal to the difference of the tangential component of the true magnetic field \mathbf{H}_1 inside V_1 and unconstrained magnetic field \mathbf{H}_1^∞ outside V_1 . Also, $\overline{\overline{G}}_{ee1}(\mathbf{r}, \mathbf{r}') = (k_{\epsilon_1}^{-2} \nabla \nabla + \overline{\overline{I}}) e^{-ik_{\epsilon_1} |\mathbf{r} - \mathbf{r}'|} / (4\pi |\mathbf{r} - \mathbf{r}'|)$ is the electric field dyadic Green's function of homogeneous medium with permittivity ϵ_1 and wavenumber $k_{\epsilon_1} = k_0 \sqrt{\epsilon_1}$ and ω is the cyclic frequency.

Similarly, using the interior to V_2 single source surface equivalence principle (Fig.3.1(d)), the total electric field $\mathbf{E}_1(\mathbf{r})$ inside V_2 can be written as

$$\mathbf{E}_2(\mathbf{r}) = -i\omega\mu_0 \oint_{\partial V_2} \overline{\overline{G}}_{ee2}(\mathbf{r}, \mathbf{r}') \cdot \mathbf{J}_2(\mathbf{r}') ds', \quad \mathbf{r} \in V_2 \setminus \partial V_2 \quad (3.3)$$

where $\mathbf{J}_2 = \hat{n} \times [\mathbf{H}_2 - \mathbf{H}_2^\infty]$ is the fictitious electric current defined on the boundary ∂V_2 equal to the difference of the tangential component of the true magnetic field

\mathbf{H}_2 inside V_2 and unconstrained magnetic field \mathbf{H}_2^∞ outside V_2 and $\overline{\overline{G}}_{ee_2}(\mathbf{r}, \mathbf{r}') = (k_{e_2}^{-2} \nabla \nabla + \overline{\overline{I}}) e^{-ik_{e_2} |\mathbf{r} - \mathbf{r}'|} / (4\pi |\mathbf{r} - \mathbf{r}'|)$ is the electric field dyadic Green's function of homogeneous medium with permittivity ϵ_2 and wavenumber $k_{e_2} = k_0 \sqrt{\epsilon_2}$.

Substitution of (3.2) and (3.3) into (3.1) followed by the restriction of the observation point to the boundaries ∂V_1 and ∂V_2 from inside the scatterer yields two coupled formulations (SVS-EFIEs)

$$\begin{aligned} \hat{\mathbf{t}}_\ell \cdot \mathbf{E}^{\text{inc}}(\mathbf{r}) &= i\omega\mu_0 \hat{\mathbf{t}}_\ell \cdot \left(- \oint_{\partial V_\ell} \overline{\overline{G}}_{ee_\ell}(\mathbf{r}, \mathbf{r}'') \cdot \mathbf{J}_\ell(\mathbf{r}'') ds'' \right. \\ &+ (\epsilon_1 - 1) \cdot k_0^2 \int_{V_1} \overline{\overline{G}}_{e0}(\mathbf{r}, \mathbf{r}') \cdot \oint_{\partial V_1} \overline{\overline{G}}_{ee_1}(\mathbf{r}', \mathbf{r}'') \cdot \mathbf{J}_1(\mathbf{r}'') ds'' dv' \\ &\left. + (\epsilon_2 - 1) \cdot k_0^2 \int_{V_2} \overline{\overline{G}}_{e0}(\mathbf{r}, \mathbf{r}') \cdot \oint_{\partial V_2} \overline{\overline{G}}_{ee_2}(\mathbf{r}', \mathbf{r}'') \cdot \mathbf{J}_2(\mathbf{r}'') ds'' dv' \right), \end{aligned} \quad (3.4)$$

$$\mathbf{r} \in \partial V_\ell, \quad \ell = 1, 2$$

where ℓ specifies the index of the observation boundary (here are ∂V_1 and ∂V_2) and $\hat{\mathbf{t}}_\ell$ is the tangential vector to the ℓ th boundar ∂V_ℓ . The integral operator representation of (3.4) is

$$\begin{aligned} \hat{\mathbf{t}}_\ell \cdot \mathbf{E}^{\text{inc}}(\mathbf{r}) &= - \overline{\overline{\mathcal{T}}}_{\epsilon_\ell}^{\partial V_\ell, \partial V_\ell} \circ \mathbf{J}_\ell + \\ &\sum_{m=1}^2 (\epsilon_m - 1) \left(\overline{\overline{\mathcal{T}}}_0^{\partial V_\ell, V_m} \circ \overline{\overline{\mathcal{T}}}_{\epsilon_m}^{V_m, \partial V_m} \right) \circ \mathbf{J}_m, \quad \ell = 1, 2 \end{aligned} \quad (3.5)$$

where $\overline{\overline{\mathcal{T}}}_{\epsilon_\ell}^{\partial V_\ell, \partial V_\ell}$ is integral operator mapping surface current \mathbf{J}_ℓ on boundary ∂V_ℓ to tangential field $\hat{\mathbf{t}}_\ell \cdot \mathbf{E}_\ell$ on the same boundary ∂V_ℓ [13] and known as surface-to-surface operator and is composed of scalar and vector potentials operators,

$$\overline{\overline{\mathcal{T}}}_{\epsilon_\ell}^{\partial V_\ell, \partial V_\ell} = \mathcal{T}_{\epsilon_\ell, \nabla \Phi}^{\partial V_\ell, \partial V_\ell} + \mathcal{T}_{\epsilon_\ell, A}^{\partial V_\ell, \partial V_\ell} \quad (3.6)$$

where

$$\mathcal{T}_{\epsilon_\ell, \Phi}^{\partial V_\ell, \partial V_\ell} \circ \mathbf{J}_\ell = \frac{i\omega\mu_0}{k_{\epsilon_\ell}^2} \oint_{\partial V_\ell} G_{\epsilon_\ell}(\mathbf{r}, \mathbf{r}'') \nabla_s'' \cdot \mathbf{J}_\ell(\mathbf{r}'') ds'' \quad (3.7)$$

$$\mathcal{T}_{\epsilon_\ell, A}^{\partial V_\ell, \partial V_\ell} \circ \mathbf{J}_\ell = i\omega\mu_0 \hat{\mathbf{t}}_\ell \cdot \oint_{\partial V_\ell} G_{\epsilon_\ell}(\mathbf{r}, \mathbf{r}'') \mathbf{J}_\ell(\mathbf{r}'') ds''. \quad (3.8)$$

In (3.6), $\mathcal{T}_{\epsilon_\ell, \nabla\Phi}^{\partial V_\ell, \partial V_\ell} = \hat{\mathbf{t}}_\ell \cdot \nabla \mathcal{T}_{\epsilon_\ell, \Phi}^{\partial V_\ell, \partial V_\ell}$ and $\mathbf{r} \in \partial V_\ell$.

In the new SVS-EFIE formulation (3.5) for the composite dielectric scatterer, $\overline{\overline{\mathcal{T}}}_0^{\partial V_\ell, V_m}$ is volume-to-surface operator which translating the polarization current \mathbf{j}_m inside V_m to the tangential scattered electric field on the boundary ∂V_ℓ , establishes coupling of the electric fields in different regions of the composite scatterer. Also, $\overline{\overline{\mathcal{T}}}_\epsilon^{V_m, \partial V_m}$ is surface-to-volume operator and map the tangential surface current \mathbf{J}_m on boundary ∂V_m to the tangential component of the total electric field on the same boundary ∂V_m . These operators are defined as follows:

$$\overline{\overline{\mathcal{T}}}_0^{\partial V_\ell, V_m} = \mathcal{T}_{0, \nabla\Phi}^{\partial V_\ell, V_m} + \mathcal{T}_{0, a}^{\partial V_\ell, V_m} \quad (3.9)$$

and

$$\overline{\overline{\mathcal{T}}}_{\epsilon_m}^{V_m, \partial V_m} = \mathcal{T}_{\epsilon_m, \nabla\Phi}^{V_m, \partial V_m} + \mathcal{T}_{\epsilon_m, A}^{V_m, \partial V_m} \quad (3.10)$$

where

$$\mathcal{T}_{0, \varphi}^{\partial V_\ell, V_m} \circ \mathbf{j}_m = \frac{1}{k_0^2} \int_{V_m} \nabla G_0(\mathbf{r}, \mathbf{r}') \cdot \mathbf{j}_m(\mathbf{r}') dv' \quad (3.11)$$

$$\mathcal{T}_{0, a}^{\partial V_\ell, V_m} \circ \mathbf{j}_m = \hat{\mathbf{t}}_\ell \cdot \int_{V_m} G_0(\mathbf{r}, \mathbf{r}') \mathbf{j}_m(\mathbf{r}') dv' \quad (3.12)$$

$$\mathcal{T}_{\epsilon_m, \nabla\Phi}^{V_m, \partial V_m} \circ \mathbf{J}_m = \frac{i\omega\mu_0}{k_{\epsilon_m}^2} \oint_{\partial V_m} \nabla' G_{\epsilon_m}(\mathbf{r}', \mathbf{r}'') \nabla_s'' \cdot \mathbf{J}_m(\mathbf{r}'') ds'' \quad (3.13)$$

$$\mathcal{T}_{\epsilon_m, A}^{V_m, \partial V_m} \circ \mathbf{J}_m = i\omega\mu_0 \oint_{\partial V_m} G_{\epsilon_m}(\mathbf{r}', \mathbf{r}'') \mathbf{J}_m(\mathbf{r}'') ds'', \quad (3.14)$$

$$\mathbf{r} \in \partial V_\ell, \quad \mathbf{r}' \in V_m.$$

In (3.9), $\mathcal{T}_{0,\nabla\varphi}^{\partial V_\ell, V_m} = \hat{\mathbf{t}}_\ell \cdot \nabla \mathcal{T}_{0,\varphi}^{\partial V_\ell, V_m}$.

Generalization of the new SVS-EFIE formulation for scattering problem of non-magnetic dielectric objects consisting of \mathcal{L} regions ($\mathcal{L} = 2$ in Fig. 3.1) follows from (3.4) in a straightforward manner and can be written as

$$i\omega\mu_0\hat{\mathbf{t}}_\ell \cdot \left(- \oint_{\partial V_\ell} \bar{\bar{\mathbf{G}}}_{ee_\ell}(\mathbf{r}, \mathbf{r}'') \cdot \mathbf{J}_\ell(\mathbf{r}'') ds'' + k_0^2 \sum_{m=1}^{\mathcal{L}} (\epsilon_m - 1) \int_{V_m} \bar{\bar{\mathbf{G}}}_0(\mathbf{r}, \mathbf{r}') \cdot \oint_{\partial V_m} \bar{\bar{\mathbf{G}}}_{ee_m}(\mathbf{r}', \mathbf{r}'') \cdot \mathbf{J}_m(\mathbf{r}'') ds'' dv' \right) = \hat{\mathbf{t}}_\ell \cdot \mathbf{E}^{\text{inc}}(\mathbf{r}),$$

$$\ell = 1, 2, \dots, \mathcal{L}, \quad m = 1, 2, \dots, \mathcal{L}, \quad \mathbf{r} \in \partial V_\ell \quad (3.15)$$

where \mathbf{r} is an observation location on the scatterer boundary ∂V_ℓ , $\ell = 1, 2, \dots, \mathcal{L}$ specifies the index of the observation surface object, and \mathbf{r}' is the source location on the boundary ∂V_m or inside V_m with $m = 1, 2, \dots, \mathcal{L}$ specifying the index of the corresponding source region (surface or volume).

We can express (3.15) in the integral-operator form [38]

$$- \underbrace{\left(\mathcal{T}_{\epsilon_\ell, \nabla\Phi}^{\partial V_\ell, \partial V_\ell} + \mathcal{T}_{\epsilon_\ell, A}^{\partial V_\ell, \partial V_\ell} \right)}_{\mathcal{T}_{\epsilon_\ell}^{\partial V_\ell, \partial V_\ell}} \circ \mathbf{J}_\ell + \sum_{m=1}^{\mathcal{L}} (\epsilon_m - 1) \underbrace{\left(\mathcal{T}_{0, \nabla\varphi}^{\partial V_\ell, V_m} + \mathcal{T}_{0, a}^{\partial V_\ell, V_m} \right)}_{\mathcal{T}_0^{\partial V_\ell, V_m}} \circ \underbrace{\left(\mathcal{T}_{\epsilon_m, \nabla\Phi}^{V_m, \partial V_m} + \mathcal{T}_{\epsilon_m, A}^{V_m, \partial V_m} \right)}_{\mathcal{T}_{\epsilon_m}^{V_m, \partial V_m}} \circ \mathbf{J}_m = \hat{\mathbf{t}}_\ell \cdot \mathbf{E}^{\text{inc}}. \quad (3.16)$$

In order to solve SVS-EFIE (3.15) with MoM (described in detail in [13]), discretization of both the surface (with M triangles) and the volume (with N tetrahedrons) of the scatterer is required. The MoM discretization of SVS-EFIE reduces it to the following set of linear algebraic equations with respect to the vector of unknown

scalar coefficients I in the expansion of the unknown surface weighting function

$$\left(Z_{\epsilon_\ell}^{\partial V_\ell, \partial V_\ell} + \sum_{m=1}^{\mathcal{L}} Z_0^{\partial V_\ell, V_m} \cdot Z_{\epsilon_m}^{V_m, \partial V_m} \right) \cdot I = \mathcal{V}, \quad (3.17)$$

$$\ell = 1, 2, \dots, \mathcal{L}, \quad m = 1, 2, \dots, \mathcal{L}, \quad \mathbf{r} \in \partial V_\ell.$$

Hence, for the two region scatterer in Fig. 3.1 the vector of unknown scalar coefficients I_1 and I_2 corresponding to ∂V_1 and ∂V_2 and (3.17) can be written as follows:

$$\left(\begin{bmatrix} Z_{\epsilon_1}^{\partial V_1, \partial V_1} & 0 \\ 0 & Z_{\epsilon_2}^{\partial V_2, \partial V_2} \end{bmatrix} + \begin{bmatrix} Z_0^{\partial V_1, V_1} & Z_0^{\partial V_1, V_2} \\ Z_0^{\partial V_2, V_1} & Z_0^{\partial V_2, V_2} \end{bmatrix} \times \begin{bmatrix} Z_{\epsilon_1}^{V_1, \partial V_1} & 0 \\ 0 & Z_{\epsilon_2}^{V_2, \partial V_2} \end{bmatrix} \right) \begin{bmatrix} I_1 \\ I_2 \end{bmatrix} = \begin{bmatrix} \mathcal{V}_1 \\ \mathcal{V}_2 \end{bmatrix}. \quad (3.18)$$

To reduce computational and memory complexities of the MoM solution, in this paper we propose its acceleration using the framework of the \mathcal{H} -matrices. The proposed scheme features formatted multiplication of rectangular \mathcal{H} -matrices, formatted addition of the squared \mathcal{H} -matrices, and \mathcal{H} -LU decomposition of the resultant block matrix [36].

3.4 \mathcal{H} -Matrix Based Fast Direct MoM Solution of SVS-EFIE for 3-D Composite Scatterer

The idea of \mathcal{H} -matrix is that the MoM matrix is decomposed into sub-blocks each representing the interaction between a pair of observers (obs) and sources (src). Then, for each well-separated pair, the corresponding block $Z_{\text{obs} \times \text{src}}$ is expected to be low-rank (\mathcal{R}) and is approximated in the $Z_{\text{obs} \times \text{src}} \approx A_{\text{obs} \times k} \cdot B_{\text{src} \times k}^H = \mathcal{R}_{\text{obs} \times \text{src}}$ form, k being the rank. The accuracy of this approximation is dependent on the low-rank factorization strategy, such as Singular Value Decomposition (SVD) [78], Adaptive Cross Approximation (ACA) [23, 24], and grid-based algorithms such as HCA [36] and others [69].

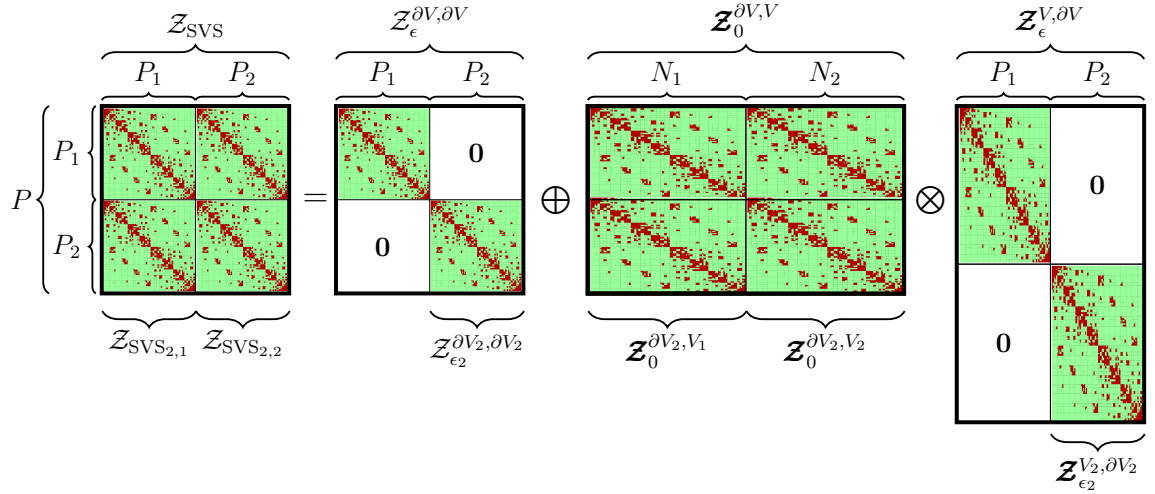


Figure 3.2: Assembly of \mathcal{Z}_{SVS} MoM \mathcal{H} -matrix for composite scatterer featuring two regions from the individual \mathcal{H} -matrices of SVS-EFIE operators: $\mathcal{Z}_{\epsilon}^{\partial V, \partial V}$, $\mathcal{Z}_0^{\partial V, V}$, and $\mathcal{Z}_{\epsilon}^{V, \partial V}$ via formatted multiplication and addition (3.22) required by \mathcal{H} -LU based direct solution of the SVS-EFIE. Admissible blocks (green) corresponding to far interactions and inadmissible blocks (red) corresponding to near interactions. The number of RWG basis functions on the boundaries ∂V_1 and ∂V_2 are P_1 and P_2 , respectively, with $P = P_1 + P_2$ being the total number of RWG basis functions. The number of tetrahedron elements in the volumes V_1 and V_2 are N_1 and N_2 , respectively, with $N = N_1 + N_2$ being the total number of tetrahedrons discretizing the object volume $V_1 + V_2$ (Fig. 3.1).

3.4.1 Geometry Partitioning and Construction of \mathcal{H} -matrix

At first, \mathcal{H} -matrix based MoM solver hierarchically divides the structure of interest into sub-domains [36]. In the case of the SVS-EFIE for a composite scatterer, both surface ∂V_ℓ and volume V_ℓ domains are discretized for each region ℓ . Hence, two separate cluster trees (T_{S_ℓ} for surface domain and T_{V_ℓ} for volume domain) are required. As an example, for a two-region composite object in Fig. 3.1) a set of cluster trees $\{T_{S_1}, T_{V_1}, T_{S_2}, T_{V_2}\}$ is required.

To construct a cluster tree T_{S_ℓ} for the surface domain of region ℓ , we start from the root cluster containing the full index set of Rao-Wilton-Glisson (RWG) [67] basis/testing functions $\mathcal{I}_{S_\ell} = \{1, 2, \dots, P_\ell\}$ (P_ℓ being the number of RWG of region ℓ)

and then geometrically bisect its bounding box into two subsets. The bisectioning continues recursively until the number of RWG basis/testing functions in each cluster becomes less than the leafsize n_{\min} , which is a predefined parameter to control the depth of the cluster tree. The cluster tree T_{V_ℓ} for the volume domain V_ℓ is constructed similarly to T_{S_ℓ} and start with the root cluster $\mathcal{I}_{V_\ell} = \{1, 2, \dots, N_\ell\}$ containing the full index set of the piece-wise basis/testing functions on the tetrahedrons as opposed to the RWGs.

Next, matrix of each of the MoM discretized integral operators (3.16) (surface-to-surface, surface-to-volume, and volume-to-surface) is approximated using \mathcal{H} -matrices. Each \mathcal{H} -matrix is built from two cluster trees corresponding to the observer (range) and source (domain) of the MoM discretized integral operator. To construct the \mathcal{H} -matrix for integral operators, we start by taking the root elements (test/basis functions) of the appropriate cluster trees. If the interactions between the test/basis functions in the clusters meets an admissibility criterion as

$$\min\{\text{diam}(\mathcal{B}_{\text{obs}}), \text{diam}(\mathcal{B}_{\text{src}})\} \leq \eta \text{dist}(\mathcal{B}_{\text{obs}}, \mathcal{B}_{\text{src}}) \quad (3.19)$$

then the interaction blocks are considered admissible and ACA algorithm or another compression scheme is used to represent them in a compressed $\mathcal{R}_{\text{obs} \times \text{src}}$ format. In (3.19), \mathcal{B}_{obs} and \mathcal{B}_{src} represent the bounding box of the observer and the source clusters, respectively, $\text{diam}(\cdot)$ and $\text{dist}(\cdot, \cdot)$ denote the Euclidean diameter and minimum distance between these bounding boxes. Also, positive real parameter η (i.e. $\eta \in \mathbb{R}^+$) controls the number of admissible blocks. However, the near interaction at this level are inadmissible and we examine the interactions between all the children of both the source and observer clusters using admissibility criterion (3.19) recursively until the leaf level is reached. Inadmissible blocks will be computed by using naïve MoM [38] and stored in full matrix (\mathcal{F}) representation.

To construct the required impedance \mathcal{H} -matrices of SVS-EFIE operators (3.16) arising from the appropriate observer and source cluster trees, we have:

- $\mathcal{Z}_{\epsilon_\ell}^{\partial V_\ell, \partial V_\ell}$ arising from $T_{S_\ell \times S_\ell}$ interaction tree: For each region ℓ , $\mathcal{Z}_{\epsilon_\ell}^{\partial V_\ell, \partial V_\ell}$ is represented as surface-to-surface MoM impedance \mathcal{H} -matrix corresponding to the

operator $\mathcal{T}_{\epsilon_\ell}^{\partial V_\ell, \partial V_\ell}$. Therefore, T_{S_ℓ} is chosen for both source and observer trees of $\mathcal{Z}_{\epsilon_\ell}^{\partial V_\ell, \partial V_\ell}$ with the size $P_\ell \times P_\ell$. (for the case of two-region composite scatterer we have two \mathcal{H} -matrices $\mathcal{Z}_{\epsilon_1}^{\partial V_1, \partial V_1}$ and $\mathcal{Z}_{\epsilon_2}^{\partial V_2, \partial V_2}$).

- $\mathcal{Z}_0^{\partial V_\ell, V_m}$ arising from $T_{S_\ell \times V_m}$ interaction tree: $\mathcal{Z}_0^{\partial V_\ell, V_m}$ is represented as volume-to-surface MoM impedance \mathcal{H} -matrix for observer region ℓ and source region m and corresponding to the operator $\mathcal{T}_0^{\partial V_\ell, V_m}$. Therefore, T_{S_ℓ} is chosen for observer tree and T_{V_m} is chosen for source tree of $\mathcal{Z}_0^{\partial V_\ell, V_m}$ \mathcal{H} -matrix with rectangular structure as shown in Fig. 3.2 and has the size of $P_\ell \times N_m$. (for two-region composite scatterer we have four volume-to-surface \mathcal{H} -matrices $\mathcal{Z}_0^{\partial V_1, V_1}$, $\mathcal{Z}_0^{\partial V_1, V_2}$, $\mathcal{Z}_0^{\partial V_2, V_1}$, and $\mathcal{Z}_0^{\partial V_2, V_2}$).
- $\mathcal{Z}_{\epsilon_m}^{V_m, \partial V_m}$ arising from $T_{V_m \times S_m}$ interaction tree: $\mathcal{Z}_{\epsilon_m}^{V_m, \partial V_m}$ is represented as surface-to-volume MoM impedance \mathcal{H} -matrix for source region m . Hence, T_{V_m} is chosen for observer tree and T_{S_m} is chosen for source tree. The corresponding rectangular \mathcal{H} -matrix is shown in Fig. 3.2 and has the size of $N_m \times P_m$ for region m . (for two-region scatterer we have two surface-to-volume \mathcal{H} -matrices $\mathcal{Z}_{\epsilon_1}^{V_1, \partial V_1}$ and $\mathcal{Z}_{\epsilon_2}^{V_2, \partial V_2}$).

3.4.2 Assembling of Final \mathcal{Z}_{SVS} MoM \mathcal{H} -matrix

After \mathcal{H} -matrix approximations are constructed for each discretized integral operator in (3.16), the resultant system of linear algebraic equations

$$(\mathcal{Z}_\epsilon^{\partial V, \partial V} \oplus \mathcal{Z}_0^{\partial V, V} \cdot \mathcal{Z}_\epsilon^{V, \partial V}) \cdot I = \mathcal{Z}_{\text{SVS}} \cdot I = \mathcal{V} \quad (3.20)$$

has to be solved. In (3.20), I is the vector of unknown current expansion coefficient in MoM discretization of SVS-EFIE contains P elements, P being the total number of RWG basis functions on the surface of the composite scatterer. Also, \otimes and \oplus being the operations of formatted multiplication and addition [27, 35]. In this paper, we consider \mathcal{H} -LU direct solution approach. Hence, the construction of the final MoM \mathcal{H} -matrix \mathcal{Z}_{SVS} in (3.20) combining all three approximated integral operators is required. To demonstrate the described process, MoM discretization of SVS-EFIEs

for a two-region scatterer yields an structure shown in Fig. 3.2. To construct the final MoM \mathcal{H} -matrix \mathcal{Z}_{SVS} in Fig. 3.2 we have

$$\mathcal{Z}_{\text{SVS}} = \begin{bmatrix} \mathcal{Z}_{\text{SVS}_{1,1}} & \mathcal{Z}_{\text{SVS}_{1,2}} \\ \mathcal{Z}_{\text{SVS}_{2,1}} & \mathcal{Z}_{\text{SVS}_{2,2}} \end{bmatrix} = \begin{bmatrix} \mathcal{Z}_{\epsilon_1}^{\partial V_1, \partial V_1} & 0 \\ 0 & \mathcal{Z}_{\epsilon_2}^{\partial V_2, \partial V_2} \end{bmatrix} \oplus \begin{bmatrix} \mathcal{Z}_0^{\partial V_1, V_1} & \mathcal{Z}_0^{\partial V_1, V_2} \\ \mathcal{Z}_0^{\partial V_2, V_1} & \mathcal{Z}_0^{\partial V_2, V_2} \end{bmatrix} \otimes \begin{bmatrix} \mathcal{Z}_{\epsilon_1}^{V_1, \partial V_1} & 0 \\ 0 & \mathcal{Z}_{\epsilon_2}^{V_2, \partial V_2} \end{bmatrix} \quad (3.21)$$

where each \mathcal{H} -matrix of $\mathcal{Z}_{\text{SVS}_{\ell,m}}$ (here, $\ell = 1, 2$ and $m = 1, 2$) of final \mathcal{Z}_{SVS} is calculated individually as

$$\mathcal{Z}_{\text{SVS}_{\ell,m}} = \mathcal{Z}_{\epsilon_\ell}^{\partial V_\ell, \partial V_m} \oplus \mathcal{Z}_0^{\partial V_\ell, V_m} \otimes \mathcal{Z}_{\epsilon_m}^{V_m, \partial V_m}. \quad (3.22)$$

In the general case, the total of \mathcal{L}^2 \mathcal{H} -matrix blocks of $\mathcal{Z}_{\text{SVS}_{\ell,m}}$ must be constructed. Detailed implementation of formatted multiplication and addition (3.22) the reader can find in [35].

3.4.3 Direct Solution Using Block \mathcal{H} -LU Decomposition

After assembling of all individual \mathcal{H} -matrices entering \mathcal{Z}_{SVS} , block \mathcal{H} -LU decomposition followed by block \mathcal{H} -substitutions (composed of \mathcal{H} -LowerTriSolver and \mathcal{H} -UpperTriSolver) are applied to \mathcal{Z}_{SVS} in order to solve the system. The block \mathcal{H} -LU decomposition of \mathcal{Z}_{SVS} for the two-region scatterer can be computed as

$$\mathcal{Z}_{\text{SVS}} = \begin{bmatrix} \mathcal{Z}_{\text{SVS}_{1,1}} & \mathcal{Z}_{\text{SVS}_{1,2}} \\ \mathcal{Z}_{\text{SVS}_{2,1}} & \mathcal{Z}_{\text{SVS}_{2,2}} \end{bmatrix} = \begin{bmatrix} L_{1,1} & \\ & L_{2,2} \end{bmatrix} \cdot \begin{bmatrix} U_{1,1} & U_{1,2} \\ & U_{2,2} \end{bmatrix} = L \cdot U. \quad (3.23)$$

The key steps of block \mathcal{H} -LU decomposition is given in Algorithm 3. The procedure starts from a call to function *BlockH-LU(...)* with final \mathcal{Z}_{SVS} and \mathcal{L} as the number of regions of the composite scatterer. In Algorithm 3, function *MulAdd(...)* performs recursive formatted matrix-matrix multiplication of \mathcal{H} -matrices $L_{\ell,\ell'}$ and $U_{\ell',m}$ and adds it to $\mathcal{Z}_{\text{SVS}_{\ell,m}}$ as

$$\mathcal{Z}_{\text{SVS}_{\ell,m}} = \mathcal{Z}_{\text{SVS}_{\ell,m}} \oplus (-L_{\ell,\ell'} \otimes U_{\ell',m}). \quad (3.24)$$

Also, function \mathcal{H} -*LowerTriSolver*(...) acts as a lower triangular solver $L_{\ell,\ell} \cdot U_{\ell,m} = \mathcal{Z}_{\text{SVS}_{\ell,m}}$ to find $U_{\ell,m}$ with $\mathcal{Z}_{\text{SVS}_{\ell,m}}$ as a given RHS-matrix and $L_{\ell,\ell}$ as a given lower triangular \mathcal{H} -matrix. Similarly, function \mathcal{H} -*UpperTriSolver*(...) acts as an upper triangular solver $L_{\ell,m} \cdot U_{m,m} = \mathcal{Z}_{\text{SVS}_{\ell,m}}$ to find $L_{\ell,m}$ with $\mathcal{Z}_{\text{SVS}_{\ell,m}}$ as a given RHS-matrix and $U_{m,m}$ as a given upper triangular \mathcal{H} -matrix. Also, function \mathcal{H} -*LU*(...) is a recursive function to perform \mathcal{H} -LU decomposition for \mathcal{H} -matrices on the main diagonal of \mathcal{Z}_{SVS} [36].

Algorithm 3 Block \mathcal{H} -LU Decomposition

Inputs: \mathcal{Z}_{SVS} and \mathcal{L}

Output: L, U

```

1: BlockH-LU( $\mathcal{Z}_{\text{SVS}}, \mathcal{L}$ )
2: function BlockH-LU( $\mathcal{Z}_{\text{SVS}}, \mathcal{L}$ )
3: for  $\ell = 1, 2, \dots, \mathcal{L}$  do
4:   for  $m = 1, 2, \dots, \mathcal{L}$  do
5:     if  $m > \ell$  then
6:       for  $\ell' = 1, 2, \dots, \ell - 1$  do
7:         MulAdd( $\mathcal{Z}_{\text{SVS}_{\ell,m}}, L_{\ell,\ell'}, U_{\ell',m}$ ) {see (3.24)}
8:       end for
9:        $U_{\ell,m} = \mathcal{H}$ -LowerTriSolver( $L_{\ell,\ell}, \mathcal{Z}_{\text{SVS}_{\ell,m}}$ )
10:    else if  $m < \ell$  then
11:      for  $m' = 1, 2, \dots, m - 1$  do
12:        MulAdd( $\mathcal{Z}_{\text{SVS}_{\ell,m}}, L_{\ell,m'}, U_{m',m}$ )
13:      end for
14:       $L_{\ell,m} = \mathcal{H}$ -UpperTriSolver( $U_{m,m}, \mathcal{Z}_{\text{SVS}_{\ell,m}}$ )
15:    else  $\{\ell = m\}$ 
16:      for  $\ell' = 1, 2, \dots, \ell - 1$  do
17:        MulAdd( $\mathcal{Z}_{\text{SVS}_{\ell,m}}, L_{\ell,\ell'}, U_{\ell',m}$ )
18:      end for
19:       $\mathcal{H}$ -LU( $\mathcal{Z}_{\text{SVS}_{\ell,m}}$ )
20:    end if
21:  end for
22: end for
23: return  $L, U$ 

```

3.4.4 Forward and Backward Substitutions

After calculation of L and U \mathcal{H} -matrices, next we find the vector of unknowns I in (3.20). For a two-region composite scatterer we have

$$\begin{bmatrix} L_{1,1} & \\ L_{2,1} & L_{2,2} \end{bmatrix} \cdot \begin{bmatrix} U_{1,1} & U_{1,2} \\ & U_{2,2} \end{bmatrix} \cdot \begin{bmatrix} I_1 \\ I_2 \end{bmatrix} = \begin{bmatrix} \mathcal{V}_1 \\ \mathcal{V}_2 \end{bmatrix} \quad (3.25)$$

where I_1 and I_2 are the vector of unknowns corresponding to ∂V_1 and ∂V_2 in Fig. 3.1. In order to solve (3.25), first, the procedure of block \mathcal{H} -LowerTriSolver solver

$$L \cdot \mathcal{W} = \begin{bmatrix} L_{1,1} & \\ L_{2,1} & L_{2,2} \end{bmatrix} \cdot \begin{bmatrix} \mathcal{W}_1 \\ \mathcal{W}_2 \end{bmatrix} = \begin{bmatrix} \mathcal{V}_1 \\ \mathcal{V}_2 \end{bmatrix} \quad (3.26)$$

is performed to find \mathcal{W}_1 and \mathcal{W}_2 . Next, these solutions are considered as the RHS in

$$U \cdot I = \begin{bmatrix} U_{1,1} & U_{1,2} \\ & U_{2,2} \end{bmatrix} \cdot \begin{bmatrix} I_1 \\ I_2 \end{bmatrix} = \begin{bmatrix} \mathcal{W}_1 \\ \mathcal{W}_2 \end{bmatrix} \quad (3.27)$$

to solve for the vector of unknowns I via block \mathcal{H} -UpperTriSolver.

3.5 Computational Complexity of \mathcal{H} -Matrix SVS-EFIE for 3-D Composite Scatterer (3.15)

Without loss of generality, to simplify the derivation of the memory usage and computational complexity of \mathcal{H} -matrix SVS-EFIE solver for composite scatterers, we assume the equal number of surface and volume mesh elements for each region such as $P_1 = P_2 = \dots = P_{\mathcal{L}} = P/\mathcal{L}$ and $N_1 = N_2 = \dots = N_{\mathcal{L}} = N/\mathcal{L}$, P being the total number of RWG functions and N being the total number of tetrahedrons among all \mathcal{L} regions.

3.5.1 Memory Complexity for a Composite Scatterer Consisting of \mathcal{L} Regions

The required memory to store $P \times P$ \mathcal{H} -matrix $\mathcal{Z}_\epsilon^{\partial V, \partial V}$ for a single-region scatterer is $\mathcal{O}(k_{\max}^{\partial V, \partial V} P \log P)$ [36] where P is the total number of RWG basis/testing functions on the surface of the scatterer and $k_{\max}^{\partial V, \partial V}$ is the maximum rank revealed among all \mathcal{R} -blocks of $\mathcal{Z}_\epsilon^{\partial V, \partial V}$. However, for the case of \mathcal{L} -region composite scatterer we need to store \mathcal{L} \mathcal{H} -matrices $\mathcal{Z}_{\epsilon_\ell}^{\partial V_\ell, \partial V_\ell}$ (as shown in Fig. 3.2), ℓ being the index of the region. So, the complexity of general surface-to-surface \mathcal{H} -matrix can be estimated as

$$\begin{aligned} \mathcal{M}(\mathcal{Z}_\epsilon^{\partial V, \partial V}) &= \sum_{\ell=1}^{\mathcal{L}} \mathcal{O}(k_{\max}^{\partial V_\ell, \partial V_\ell} P_\ell \log P_\ell) \\ &\stackrel{P_\ell = P/\mathcal{L}}{=} \mathcal{L} \mathcal{O}(k_{\max}^{\partial V, \partial V} \frac{P}{\mathcal{L}} \log \frac{P}{\mathcal{L}}) = \mathcal{O}(k_{\max}^{\partial V, \partial V} P \log \frac{P}{\mathcal{L}}) \end{aligned} \quad (3.28)$$

where $\mathcal{M}(\cdot)$ is asymptotic memory requirement.

The memory requirement of $\mathcal{Z}_0^{\partial V, V}$ (of the size $P \times N$) and $\mathcal{Z}_\epsilon^{V, \partial V}$ (of the size $N \times P$) for a single-region scatterer is $\mathcal{O}(k_{\max}^{\partial V, V} P \log P) + \mathcal{O}(k_{\max}^{\partial V, V} N \log N)$ and $\mathcal{O}(k_{\max}^{V, \partial V} P \log P) + \mathcal{O}(k_{\max}^{V, \partial V} N \log N)$ [27], N is the total number of tetrahedrons inside the volume of the scatterer. Also, $k_{\max}^{\partial V, V}$ and $k_{\max}^{V, \partial V}$ are the maximum ranks revealed among all \mathcal{R} -blocks of $\mathcal{Z}_0^{\partial V, V}$ and $\mathcal{Z}_\epsilon^{V, \partial V}$, respectively. The complexity of volume-to-surface \mathcal{H} -matrix for the case of \mathcal{L} -region composite scatterer can be estimated as

$$\mathcal{M}(\mathcal{Z}_0^{\partial V, V}) = \sum_{\ell=1}^{\mathcal{L}} \sum_{m=1}^{\mathcal{L}} \left(\mathcal{O}(k_{\max}^{\partial V_\ell, V_m} P_\ell \log P_\ell) + \mathcal{O}(k_{\max}^{\partial V_\ell, V_m} N_m \log N_m) \right). \quad (3.29)$$

Considering $P_\ell = P/\mathcal{L}$ and $N_m = N/\mathcal{L}$, (3.29) is simplified to

$$\begin{aligned} \mathcal{M}(\mathcal{Z}_0^{\partial V, V}) &= \mathcal{L}^2 \left(\mathcal{O}(k_{\max}^{\partial V, V} \frac{P}{\mathcal{L}} \log \frac{P}{\mathcal{L}}) + \mathcal{O}(k_{\max}^{\partial V, V} \frac{N}{\mathcal{L}} \log \frac{N}{\mathcal{L}}) \right) \\ &= \mathcal{O}(k_{\max}^{\partial V, V} \mathcal{L} P \log \frac{P}{\mathcal{L}}) + \mathcal{O}(k_{\max}^{\partial V, V} \mathcal{L} N \log \frac{N}{\mathcal{L}}) \end{aligned} \quad (3.30)$$

where $k_{\max}^{\partial V, V}$ is the maximum rank revealed among all \mathcal{R} -blocks of matrix $\mathcal{Z}_0^{\partial V, V}$. Similarly, the complexity of surface-to-volume \mathcal{H} -matrix for the case of \mathcal{L} -region composite

scatterer can be estimated as (we need to store \mathcal{L} \mathcal{H} -matrices $\mathbf{Z}_\epsilon^{V_m, \partial V_m}$)

$$\begin{aligned} \mathcal{M}(\mathbf{Z}_\epsilon^{V, \partial V}) &= \sum_{m=1}^{\mathcal{L}} \left(\mathcal{O}(k_{\max}^{V_m, \partial V_m} P_m \log P_m) + \mathcal{O}(k_{\max}^{V_m, \partial V_m} N_m \log N_m) \right) \\ &= \mathcal{O}(k_{\max}^{V, \partial V} P \log \frac{P}{\mathcal{L}}) + \mathcal{O}(k_{\max}^{V, \partial V} N \log \frac{N}{\mathcal{L}}). \end{aligned} \quad (3.31)$$

Therefore, the total memory requirement of the proposed solver is composed of the memory of \mathcal{H} -matrices corresponding to the SVS-EFIE operators and can be approximated as

$$\begin{aligned} \mathcal{M}(\mathcal{H}\text{-matrix SVS-EFIE}) &= \mathcal{M}(\mathbf{Z}_\epsilon^{\partial V, \partial V}) + \mathcal{M}(\mathbf{Z}_0^{\partial V, V}) + \mathcal{M}(\mathbf{Z}_\epsilon^{V, \partial V}) \\ &= \mathcal{O}(k_{\max} \mathcal{L} P \log \frac{P}{\mathcal{L}}) + \mathcal{O}(k_{\max} \mathcal{L} N \log \frac{N}{\mathcal{L}}) \end{aligned} \quad (3.32)$$

where k_{\max} is the maximum rank revealed among all \mathcal{R} -blocks of \mathcal{H} -matrices entering the SVS-EFIE. For a general multi-region 3-D scatterer, the number of tetrahedrons in the volume is related to P as the number of surface degrees of freedom as $N = P^\alpha$ ($1 < \alpha < 1.5$). Hence, (3.32) can be written as a function of P as

$$\mathcal{M}(\mathcal{H}\text{-matrix SVS-EFIE}) = \mathcal{O} \left((k_{\max} \mathcal{L} P^\alpha \log \frac{P}{\mathcal{L}}) \right). \quad (3.33)$$

3.5.2 Computational Complexity of \mathcal{H} -LU Based Direct Solver

As discussed in Section 3.4, \mathcal{H} -LU based direct solver for SVS-EFIE starts with assembling of the final \mathcal{Z}_{SVS} followed by block \mathcal{H} -LU decomposition and block \mathcal{H} -substitutions. The computational complexity to create \mathcal{Z}_{SVS} via formatted multiplication and addition (3.20) for a single-region scatterer is $\mathcal{O}(k_{\max}^2 P \log^2 P) + \mathcal{O}(k_{\max}^2 N \log N \log P)$ [27] ($k_{\max} = \max(k_{\max}^{\partial V, V}, k_{\max}^{V, \partial V})$). As shown in Section 3.4.2, for the case of \mathcal{L} -region composite scatterer we need to compute \mathcal{L}^2 \mathcal{H} -matrices $\mathcal{Z}_{\text{SVS}_{\ell, m}}$ (3.22). The computational complexity \mathcal{N} for setting up \mathcal{Z}_{SVS} in Fig. 3.2

is estimated as

$$\begin{aligned} \mathcal{N}(\mathcal{Z}_{\text{SVS}}) &= \mathcal{L}^2 \left(\mathcal{O}\left(k_{\max}^2 \frac{P}{\mathcal{L}} \log^2 \frac{P}{\mathcal{L}}\right) + \mathcal{O}\left(k_{\max}^2 \frac{N}{\mathcal{L}} \log \frac{N}{\mathcal{L}} \log \frac{P}{\mathcal{L}}\right) \right) \\ &= \mathcal{O}\left(k_{\max}^2 \mathcal{L} P \log^2 \frac{P}{\mathcal{L}}\right) + \mathcal{O}\left(k_{\max}^2 \mathcal{L} N \log \frac{N}{\mathcal{L}} \log \frac{P}{\mathcal{L}}\right). \end{aligned} \quad (3.34)$$

Next, \mathcal{H} -LU decomposition and \mathcal{H} -substitution (composed of \mathcal{H} -forward and \mathcal{H} -backward) can be performed with $\mathcal{O}(k_{\max}^2 P \log^2 P)$ and $\mathcal{O}(k_{\max}^2 P \log P)$, respectively, for a single-region scatterer with \mathcal{Z}_{SVS} of the size $P \times P$ [27]. Complexity of block \mathcal{H} -LU decomposition in Algorithm 3 is dominated by the complexity of $f(\mathcal{L}) = \mathcal{L} \cdot (\mathcal{L} - 1) \cdot (2\mathcal{L} - 1)/6$ *MulAdd*(...) operations and complexity of \mathcal{L} (blocks on diagonal) \mathcal{H} -LU(...) operations. So, we can write

$$\begin{aligned} \mathcal{N}(\text{Block } \mathcal{H}\text{-LU}) &\approx \mathcal{L}(\mathcal{N}(\mathcal{H}\text{-LU})) + f(\mathcal{L})(\mathcal{N}(\text{MulAdd})) \\ &= \mathcal{L}(\mathcal{O}(k_{\max}^2 \frac{P}{\mathcal{L}} \log^2 \frac{P}{\mathcal{L}})) + f(\mathcal{L})(\mathcal{O}(k_{\max}^2 \frac{P}{\mathcal{L}} \log^2 \frac{P}{\mathcal{L}})) \\ &\stackrel{f(\mathcal{L})=\mathcal{O}(\mathcal{L}^3)}{=} \mathcal{O}(k_{\max}^2 \mathcal{L}^2 P \log^2 \frac{P}{\mathcal{L}}). \end{aligned} \quad (3.35)$$

Therefore, the computational complexity of the direct solve is composed of the computational complexity of three steps (Creation of final \mathcal{Z}_{SVS} , \mathcal{H} -LowerTriSolver and \mathcal{H} -UpperTriSolver) and can be approximated as

$$\begin{aligned} \mathcal{N}(\mathcal{H}\text{-matrix SVS-EFIE}) &= \mathcal{N}(\mathcal{Z}_{\text{SVS}}) + \mathcal{N}(\text{Block } \mathcal{H}\text{-LU}) \\ &= \mathcal{O}(k_{\max}^2 \mathcal{L}^2 P \log^2 \frac{P}{\mathcal{L}}) + \mathcal{O}(k_{\max}^2 \mathcal{L} N \log \frac{N}{\mathcal{L}} \log \frac{P}{\mathcal{L}}). \end{aligned} \quad (3.36)$$

Hence, for a general multi-region 3-D scatterer with $N = P^\alpha$ (3.36) can be written as a function of P as $\mathcal{O}(k_{\max}^2 \mathcal{L}^2 P^\alpha \log^2 \frac{P}{\mathcal{L}})$.

Computational complexity and memory of the SVS-EFIE is given in Table 3.1 and it is compared to that of PMCHWT solution [11] for both naïve MoM and \mathcal{H} -matrix accelerated MoM. The complexity is formulated as a function of number of unknowns on the surface P with the assumption that the volume is discretized with $N = P^\alpha$ ($1 < \alpha < 1.5$) elements.

Table 3.1: Computational complexity comparison for the proposed solver and PM-CHWT [11] equations for the case of $N = P^\alpha$ ($1 < \alpha < 1.5$) and fixed number of regions \mathcal{L} .

	SVS-EFIE	PMCHWT
Matrix Fill		
Naïve MoM	$\mathcal{O}(P^{1+\alpha})$	$\mathcal{O}(P^2)$
\mathcal{H} -matrix MoM	$\mathcal{O}(P^\alpha \log P)$	$\mathcal{O}(P \log P)$
Direct Solve		
Naïve LU	$\mathcal{O}(P^{2+\alpha})$	$\mathcal{O}(P^3)$
\mathcal{H} -matrix LU	$\mathcal{O}(P^\alpha \log^2 P)$	$\mathcal{O}(P \log^2 P)$
Calculating the E-field Inside Volume		
Naïve MoM	$\mathcal{O}(P^{1+\alpha})$	$\mathcal{O}(P^{1+\alpha})$
\mathcal{H} -matrix MoM	$\mathcal{O}(P^\alpha \log P)$	$\mathcal{O}(P^\alpha \log P)$
Required Memory with Calculation of the E-field Inside Volume		
Naïve MoM	$\mathcal{O}(P^{1+\alpha})$	$\mathcal{O}(P^{1+\alpha})$
\mathcal{H} -matrix MoM	$\mathcal{O}(P^\alpha \log P)$	$\mathcal{O}(P^\alpha \log P)$

3.6 Numerical Results

In order to validate the accuracy of the proposed solver, the scattering problems of electric dipole radiation near a piece-wise homogeneous human head-sized sphere [55] and a homogeneous human head model are tested. The results are compared with analytic Mie series [71] and FEKO commercial simulator [72]. The \mathcal{H} -matrix parameters are chosen empirically and are $\eta = 4$ and $n_{\min} = 16$ for the numerical examples of this paper. Also, we considered the tolerance for formatted multiplication and addition algorithm $\tau_{\mathcal{H}}$ to be the same as the truncation tolerance of the ACA algorithm τ_{ACA} which is set to $\tau_{\text{ACA}} = 10^{-3}$. The numerical results are obtained using a single Intel Xeon X5650 processor running at 2.66 GHz.

3.6.1 Three Piece-wise Homogeneous Head-Sized Spheres

For the first example, we consider a human head-sized sphere composed with three layers (from outer to inner): 4 mm fat, 8 mm bone, and 92 mm brain as shown

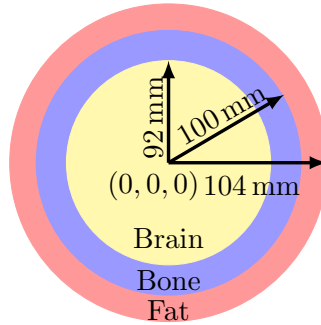


Figure 3.3: The geometry of the three piece-wise homogeneous human head-sized spheres

in Fig. 3.3. The model is centered at the origin and is excited by a radial electric dipole with moment $I \cdot \ell = 1$ [A · m] at frequency of 402 MHz which is situated at $(0, 0, 1)$ m. The frequency-dependent relative dielectric permittivity and conductivity of the layers are: $\varepsilon = 5.6$ and $\sigma = 0.04$ S/m for fat, $\varepsilon = 9.4$ and $\sigma = 0.06$ S/m for bone, and $\varepsilon = 49.7$ and $\sigma = 0.59$ S/m for brain [74]. The model has average electrical size of $2.14\lambda_e$.

Distribution of the computed field obtained by the \mathcal{H} -matrix SVS-EFIE is depicted in Fig. 3.4 (a). The layered sphere volumes are discretized with (from outer to inner): $N_1 = 24,929$, $N_2 = 40,690$, and $N_3 = 235,730$ tetrahedrons, which leads to total number of tetrahedrons $N = 301,349$. Surfaces are discretized with $P_1 = 23,838$, $P_2 = 37,839$, and $P_3 = 26,658$ RWG functions, resulting in $P = 88,335$ as the total number of RWG basis functions. This discretization corresponds to 15 mesh elements per wavelength inside the most inner sphere. To evaluate the error behaviour of the solver, the solution is obtained using Mie series. Distribution of the relative error in total field of the proposed solver with respect to the Mie series solution is shown in Fig. 3.4 (b) with the average relative error of 0.05 and standard deviation of 0.04.

To analyze the performance of the solver, we examine the memory usage and CPU time for this radiation problem using both naïve and fast MoM solution by increasing the number of mesh elements. Memory requirements are depicted in Fig. 3.5 (a) with respect to the number of surface unknowns P with the assumption that the volume is discretized with about $N = P^{1.1}$ ($\alpha = 1.1$) elements and, hence, complexities scaling

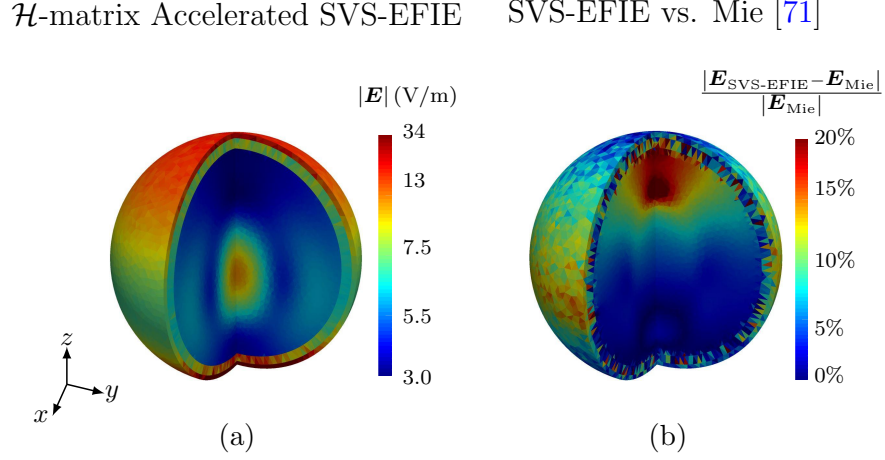


Figure 3.4: (a) Magnitude of the total electric field inside the three piece-wise human head-sized spheres produced by a z -directed electric dipole computed by the proposed solver (3.15) at 402 MHz. (b) The distribution of the relative error in total electric field with respect to the Mie series analytical solution.

close to $\mathcal{O}(P^{1.1} \log P)$ (3.32). Next, the CPU time to set up is computed and depicted in Fig. 3.5 (b) with complexities close to $\mathcal{O}(P^{1.1} \log P)$ which is of the same order as the memory use complexity in (3.32). Also, the direct solution time is plotted in Fig. 3.5 (c) with scaling of $\mathcal{O}(P^{1.1} \log^2 P)$ similar to the theoretical analysis (3.36). The computational time for solving the matrix equation is including of creation of final \mathcal{Z}_{SVS} , block \mathcal{H} -LU decomposition, and block \mathcal{H} -substitutions as described in Section 3.4.3.

Also, the time and memory consumption for the solution of this scattering problem is given in Table 3.2 for the \mathcal{H} -matrix accelerated SVS-EFIE and PMCHWT solutions. In addition, the compression ratio (CR) of the memory usage for \mathcal{H} -matrix accelerated SVS-EFIE solution is calculated as

$$\text{CR} = \left(1 - \frac{\text{Mem. } \mathcal{H}\text{-matrix SVS-EFIE}}{\text{Mem. naïve MoM SVS-EFIE [13]}} \right) \times 100\%. \quad (3.37)$$

The CR is 94% for the scattering problem of the three human head-sized 3-layer sphere model.

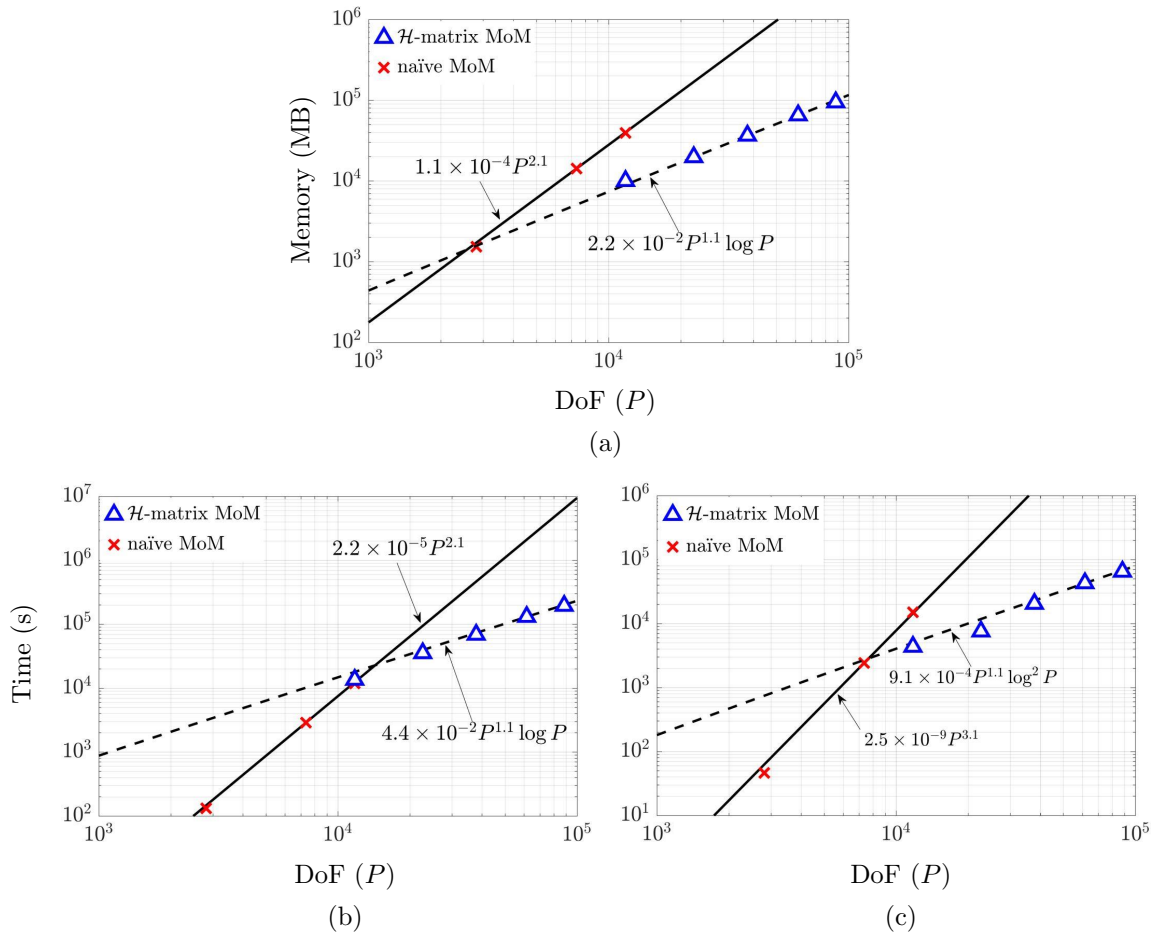


Figure 3.5: Scaling behavior of both \mathcal{H} -matrix (dashed lines) and naive (solid lines) MoM discretization of SVS-EFIE for the radiation problem of the three piece-wise spheres at 402 MHz varying number of mesh elements. (a) Memory. (b) Fill time (time to construct the MoM matrices of the SVS-EFIE). (c) Solution time (including of creation of final \mathcal{Z}_{SVS} , block \mathcal{H} -LU decomposition, and block \mathcal{H} -substitutions).

Table 3.2: Time and memory for the \mathcal{H} -matrix accelerated MoM solutions of both SVS-EFIE and PMCHWT [11] for the radiation problem of the three piecewise homogeneous head-sized sphere model at 402 MHz.

Three-layer sphere with 88,335 RWGs and 310,349 tetrahedrons		
	SVS-EFIE ($\tau_{ACA}=10^{-3}$)	PMCHWT ($\tau_{ACA}=10^{-3}$)
Fill Time	54 hrs	8 hrs
Solve Time	18 hrs	61 hrs
Field in Volume	63 s	16 hrs
Total Time	72 hrs	85 hrs
Memory	94 GB	78 GB

3.6.2 Homogeneous Human Head Model

In the second example, we consider the radiation problems on a homogeneous human head with a tissue-equivalent material [74] having permittivity of $\varepsilon = 41.5$ and conductivity of $\sigma = 0.97$ S/m at 900 MHz and permittivity of $\varepsilon = 39.2$ and conductivity of $\sigma = 1.5$ S/m at 2.45 GHz. The model has a size of 0.1 m, 0.15 m, and 0.2 m along x , y , and z axes, respectively, which leads to the electrical size of $2\lambda_\epsilon$, $3\lambda_\epsilon$, and $4.1\lambda_\epsilon$ at 900 MHz and $5.2\lambda_\epsilon$, $7.8\lambda_\epsilon$, and $10.5\lambda_\epsilon$ at 2.45 GHz. The model is centered at the origin and excited by the electric dipole with moment $I \cdot \ell = 1$ [A · m] directed along the $+z$ axis and situated at (0.065, 0.03, 0.1) m (0.015 m away from the left ear).

The distribution of the magnitude of the total electric field computed via proposed \mathcal{H} -matrix acceleration of MoM solution of the SVS-EFIE is shown in Fig. 3.6. The number of triangles in MoM discretization on the surface of the head is 31,848 with 363,618 tetrahedrons discretizing the \mathbf{E} field in the volume. Such surface discretization produces 47,772 RWG basis functions which corresponds to 20 and 8 mesh elements per wavelength for 900 MHz and 2.45 GHz, respectively. The solution for the same problem is obtained using FEKO. The magnitude of the total electric field along the x , y , and z axes inside the model is depicted in Fig. 3.7 for both proposed solver and FEKO with an good agreement between the two. The maximum revealed rank in the pertinent \mathcal{H} -matrices at 900MHz is $k_{\max} = 30$. It grows to $k_{\max} = 54$

at 2.45GHz. Despite k_{\max} growing significantly from 30 to 54, the compression ratio (CR) decreased only slightly from 96.3% at 900MHz to 95.7% at 2.45GHz, thus justifying \mathcal{H} -matrix accelerated SVS-EFIE maintaining efficiency for the problems of resonant electrical sizes.

Next, the memory usage and CPU time performance of \mathcal{H} -matrix accelerated SVS-EFIE solution at 2.45 GHz is depicted in Fig. 3.8 and compared to its predicted scaling under the assumption that the volume is discretized with approximately $N = P^{1.2}$ ($\alpha = 1.2$) elements. The memory requirement is depicted in Fig. 3.8 (a) with respect to the number of surface unknowns P with complexities close to $\mathcal{O}(P^{1.2} \log P)$ (3.32). Also, set up time is depicted in Fig. 3.8 (b) with complexities close to $\mathcal{O}(P^{1.2} \log P)$ for proposed fast direct solver. The solution time using direct method is plotted in Fig. 3.8 (c) with scaling of $\mathcal{O}(P^{1.2} \log^2 P)$ which is of the same order as the scaling predicted by the theoretical analysis (3.36) with $\alpha = 1.2$.

Table 3.3: Time and memory for the \mathcal{H} -matrix accelerated MoM solutions of both SVS-EFIE and PMCHWT [11] for the radiation problem of the homogeneous head at 2.45 GHz.

Homogeneous head with 47,772 RWGs and 363,618 tetrahedrons		
	SVS-EFIE ($\tau_{ACA}=10^{-3}$)	PMCHWT ($\tau_{ACA}=10^{-3}$)
Fill Time	38 hrs	5 hrs
Solve Time	13 hrs	3 hrs
Field in Volume	39 s	41 hrs
Total Time	51 hrs	49 hrs
Memory	68 GB	89 GB

For comparison, computational time and memory used in the solutions of the scattering problem on the homogeneous head is given in Table 3.3 for \mathcal{H} -matrix accelerated SVS-EFIE and \mathcal{H} -matrix accelerated PMCHWT formulations.

3.7 Conclusion

The \mathcal{H} -matrix based fast direct algorithm is proposed for acceleration of the MoM solution of the SVS-EFIE formulated for electromagnetic analysis of 3-D radiation

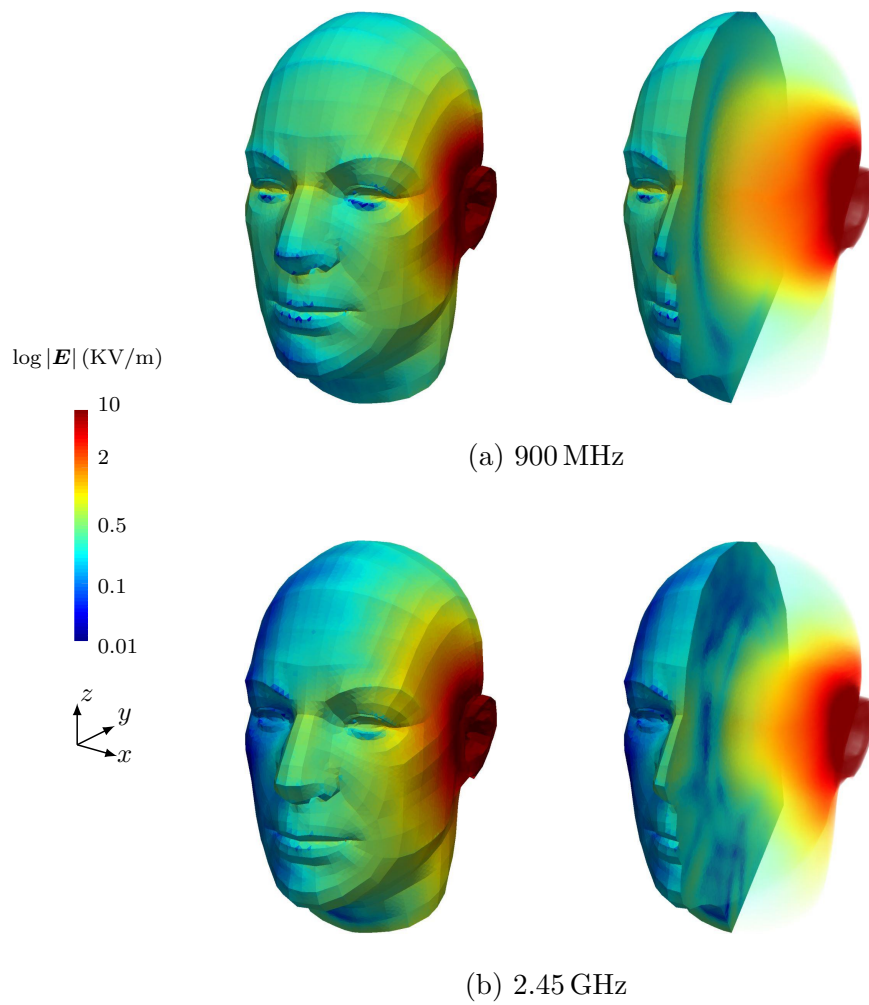


Figure 3.6: A 3-D representation of the magnitude of the total electric field inside the homogeneous human head model produced by a z -directed electric dipole situated at $x' = 0.065$ m, $y' = 0.03$ m, and $z' = 0.1$ m obtained by the proposed solver.

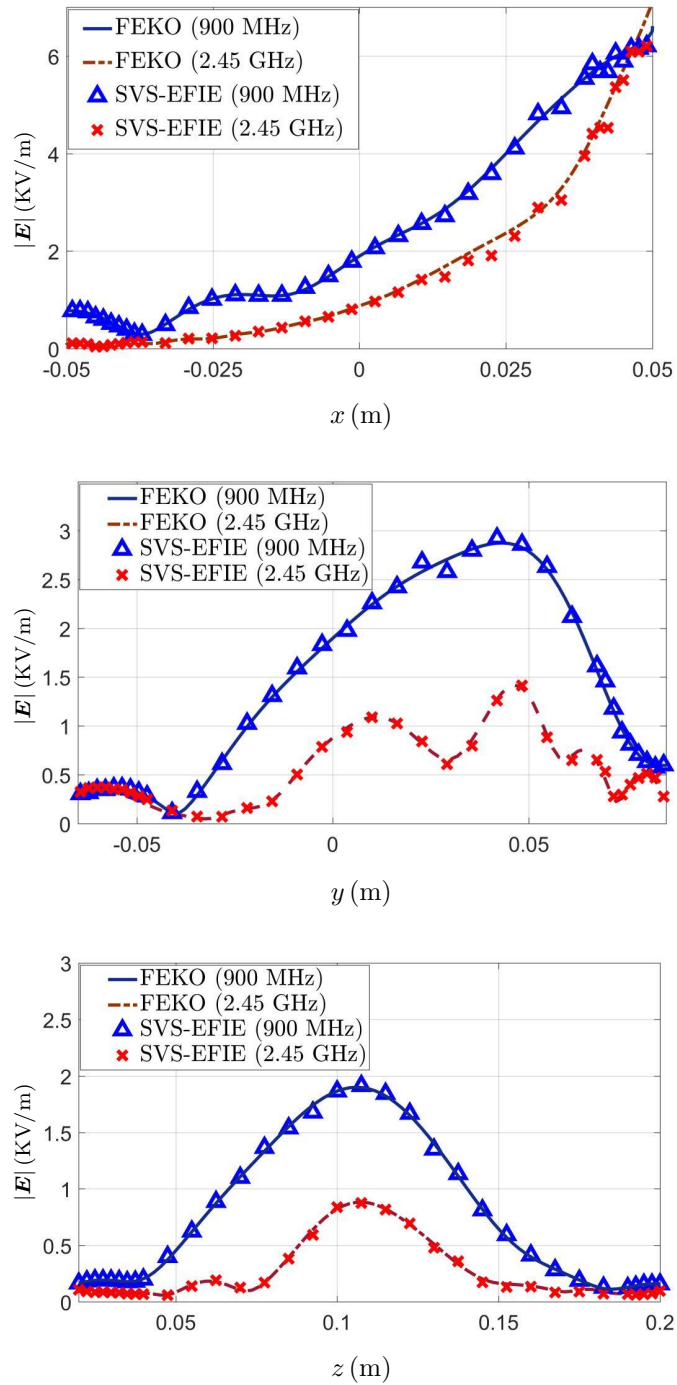


Figure 3.7: Magnitude of the total electric field inside the homogeneous human head model with observation lines along x , y , and z axis obtained by the proposed solver and FEKO at 900 MHz and 2.45 GHz .

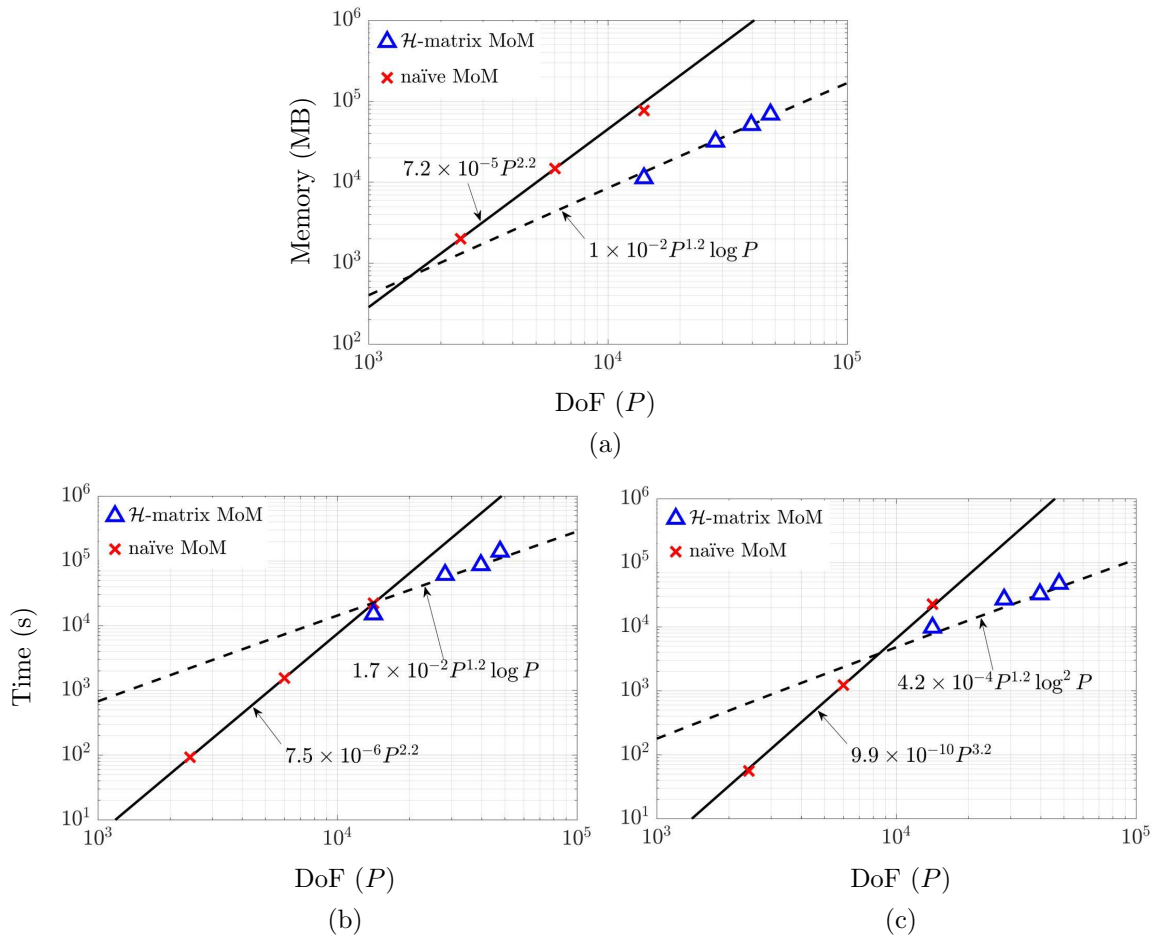


Figure 3.8: Scaling behavior of both \mathcal{H} -matrix (dashed lines) and conventional (solid lines) MoM discretization of SVS-EFIE for the radiation problem of homogeneous human head at 2.45 GHz varying number of mesh elements. (a) Memory. (b) Fill time (time to construct the MoM matrices of the SVS-EFIE). (c) Solution time (including of creation of final \mathcal{Z}_{SVS} , block \mathcal{H} -LU decomposition, and block \mathcal{H} -substitutions).

problems on composite dielectric objects featuring large number of associated degrees of freedom. In comparison to the traditional integral equation formulations for the dielectric composite scatterer, in the SVS-EFIE the meshes on the common boundaries, junctions, and different regions can be independent. It makes SVS-EFIE formulation more favorable for solution of multiscale problems when fast \mathcal{H} -matrix based algorithm is constructed. The procedures of the solution with the appropriate \mathcal{H} -matrix arithmetics for the case of piece-wise homogeneous dielectric region is presented. The numerical results confirm the efficiency of the new algorithm and demonstrate significant reduction of the memory usage and the CPU time in solution of large-scale radiation problems in BioEM.

4

**Surface-Volume-Surface EFIE
Formulation for Fast Direct
Solution of Scattering Problem on
General 3-D Composite
Metal-Dielectric Objects**

©2019 IEEE. Reprinted, with permission, from *Reza Gholami and Vladimir Okhmatovski, IEEE Transaction on Antennas and Propagation, to be published.*

Abstract

A new formulation of the Surface-Volume-Surface Electric Field Integral Equation (SVS-EFIE) combined with the regular EFIE is introduced for the electromagnetic analysis of the 3-D general composite structures of impenetrable metal and penetrable homogeneous dielectric objects. The proposed method introduces independent surface electric current densities on the boundary of each region which brings the benefit of the independent discretization of the regions according to their respective material properties and straightforward handling of the material junctions. This makes the algorithm more efficient and flexible for analysis of multiscale and large-scale composite structures in comparison with the traditional Poggio-Miller-Chang-Harrington-Wu-Tsai (PMCHWT) integral equation combined with the EFIE. The method of moment (MoM) solution of the new formulation is accelerated by the hierarchical (\mathcal{H})-matrix framework. Numerical results are given to validate the new formulation. Also, the \mathcal{H} -matrix acceleration of MoM solution of the new combined EFIE and SVS-EFIE formulation is shown to produce accurate results using only the small fraction of memory and total CPU time needed by conventional MoM.

4.1 Introduction

Electromagnetic analysis of the composite metal-dielectric objects plays important role in antenna design, remote sensing, radar applications, and other areas. The method of moments (MoM) solution of the pertinent integral equations is a popular method for the analysis of such structures due to localization of the unknown field quantities to the boundaries of the object, accurate description of propagation over electrically large distances inherent to the integral equation formulations, and exact enforcement of the radiation condition. In our previous work we introduced a new single source integral equation for the analysis of homogeneous dielectric objects [13, 37] and composite objects [38] featuring multiple adjacent dielectric regions. The new surface-volume-surface electric field integral equation (SVS-EFIE) requires only a single unknown on the boundary of each region while the traditional surface integral equation (SIE) requires two unknowns to reproduce the field throughout each region of a composite dielectric object [12, 79, 80].

In this paper, we extend the previous formulation [38] for the composite piece-wise homogeneous dielectric objects to the case of composite structures consisting of multiple impenetrable metal and piece-wise homogeneous penetrable dielectric regions. In the new formulation enforcement of the traditional surface electric field integral equation (S-EFIE) on the surfaces of the metals and the SVS-EFIE on the penetrable regions establishes a new set of coupled integral equations which we term SVS-S-EFIE. While on the metal regions this electric surface current density is equal to the tangential component of the magnetic field $\hat{n} \times \mathbf{H}$, the electric surface current densities on the boundaries of the homogeneous dielectric regions are fictitious functions which are equal to the jump of the tangential component of the true magnetic field inside the region and unconstrained magnetic field outside the region. Hence, on the common boundaries between two dielectric regions two independent fictitious electric surface current densities are introduced. Similarly, on the common boundaries between the metal and dielectric regions two independent surface electric current densities are introduced also. However, while on the surface of the metal the electric current density has a clear physical meaning of $\hat{n} \times \mathbf{H}$, the surface current densities

on the boundaries of the dielectric regions are fictitious [11, 46].

In the new formulation applied to the piece-wise scatterer, due to independence of the current densities on the boundaries of the regions, the surface and volume meshes can be generated independently for different regions. This feature eliminates the complications associated with representation of the surface currents at material junctions encountered in traditional SIEs [41, 42]. Therefore, SVS-S-EFIE allows to generate non-conformal meshes based on the material properties of individual regions. It reduces the number of required degrees of freedom (DoF) in discretization of the surface currents in the proposed SVS-S-EFIE formulation compared to the traditional SIEs making it more suitable for solution of scattering and radiation problems on composite dielectric and perfect electrically conducting (PEC) objects featuring multiscaling in either the material parameters (high disparity in permittivity and/or conductivity) and/or discretization densities.

Discretization of the integral equation often produces a poorly conditioned matrix equation especially when non-smooth objects with sharp edges, multiscale discretizations, and/or high disparity in the material properties are involved [56, 81]. In addition, solution of such problems become prohibitively expensive in terms of required CPU time and memory when number of DoFs involved in MoM discretization is large. To address these issues, in this work, we also introduce a hierarchical (\mathcal{H})-matrix [36, 62] based fast direct algorithm for fast MoM solution of the proposed new integral equation. The non-iterative nature of the developed \mathcal{H} -matrix direct algorithm allows the SVS-S-EFIE to remain largely insensitive to the deterioration of the integral equations conditioning and, hence, provide robust computational frameworks under conditions where iterative fast solution methods [18, 21] fail. The accuracy and efficiency of the new fast direct solver are studied on various examples and demonstrated in this paper.

4.2 Problem Formulation

Consider the time-harmonic incident field \mathbf{E}^{inc} with frequency ω in a piece-wise homogeneous medium divided into two non-magnetic dielectrics and a PEC domain

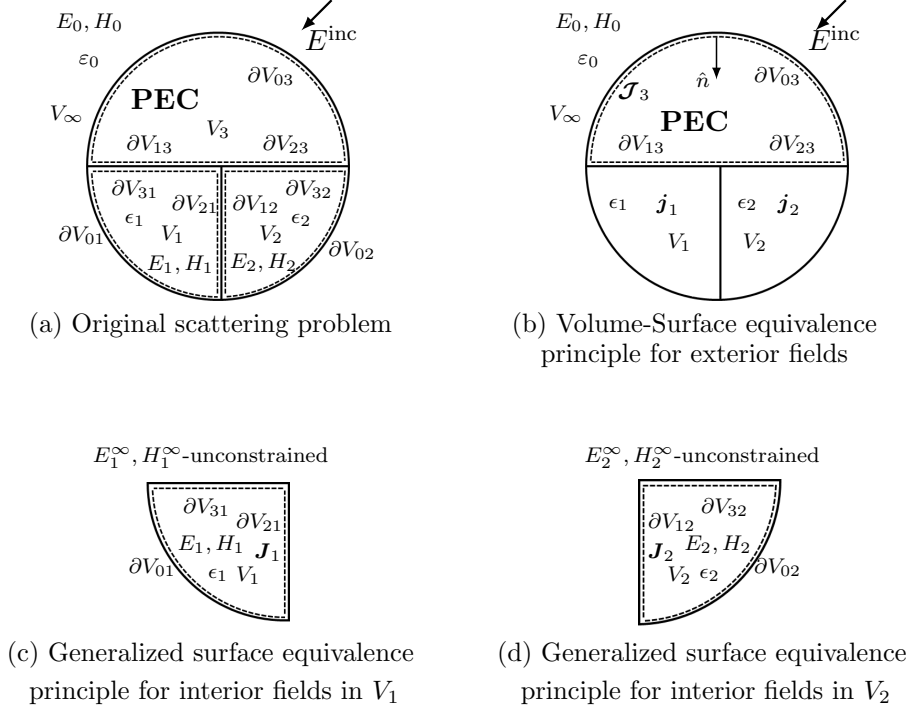


Figure 4.1: (a) Derivation of SVS-S-EFIE for the scattering problem of a 3-D composite metal-dielectric object excited by E^{inc} for a three-region scatterer with volumes V_1 , V_2 , and V_3 bounded by surfaces $\partial V_1 = \partial V_{01} + \partial V_{21} + \partial V_{31}$, $\partial V_2 = \partial V_{02} + \partial V_{12} + \partial V_{32}$, and $\partial V_3 = \partial V_{03} + \partial V_{13} + \partial V_{23}$. The composite object situated in free-space background medium. The dielectric regions V_1 and V_2 have complex relative permittivities of ϵ_1 and ϵ_2 , respectively, and V_3 being PEC. The original scattering problem is decomposed to: (b) exterior volume-surface equivalence problem (true fields E_0 , H_0 in V_∞ produced by volume polarization currents \mathbf{j}_1 and \mathbf{j}_2 and surface equivalence current \mathcal{J}_3), (c) interior to V_1 generalized surface equivalence problem with single fictitious electric surface current density \mathbf{J}_1 producing true field in V_1 and unconstrained field E_1^∞ outside V_1 , and (d) interior to V_2 generalized surface equivalence problem with single fictitious electric surface current density \mathbf{J}_2 producing true field in V_2 and unconstrained field E_2^∞ outside V_2 .

with volumes V_1 , V_2 , and V_3 situated in free-space with permittivity ε_0 (Fig. 4.1a). Using the volume-surface equivalence principle [71] (Fig. 4.1b), the electric field \mathbf{E} inside the penetrable scatterer can be written as

$$\begin{aligned} \mathbf{E}(\mathbf{r}) = & \mathbf{E}^{\text{inc}}(\mathbf{r}) + \int_{V_1} \overline{\overline{G}}_{e0}(\mathbf{r}, \mathbf{r}') \cdot \mathbf{j}_1(\mathbf{r}') dv' \\ & + \int_{V_2} \overline{\overline{G}}_{e0}(\mathbf{r}, \mathbf{r}') \cdot \mathbf{j}_2(\mathbf{r}') dv' \\ & + \oint_{\partial V_3} \overline{\overline{G}}_{e0}(\mathbf{r}, \mathbf{r}') \cdot \mathcal{J}_3(\mathbf{r}') ds', \quad \mathbf{r} \in V_1, V_2 \end{aligned} \quad (4.1)$$

where $\overline{\overline{G}}_{e0}(\mathbf{r}, \mathbf{r}') = (k_0^{-2} \nabla \nabla + \overline{\overline{I}}) e^{-ik_0 |\mathbf{r} - \mathbf{r}'|} / (4\pi |\mathbf{r} - \mathbf{r}'|)$ is the 3-D dyadic Green's functions of free-space with k_0 being wave number of free space and $\mathbf{j}_m(\mathbf{r}) = k_0^2 [\epsilon_m(\mathbf{r}) - 1] \mathbf{E}_m(\mathbf{r})$ is the polarization current density inside volume V_m with complex relative permittivity $\epsilon_m = \varepsilon_m + \sigma_m / (i\omega \varepsilon_0)$, $m = 1, 2$. Time factor $e^{-i\omega t}$ is suppressed throughout the paper. The equivalent true surface electric current density impressed on surface $\partial V_3 = \partial V_{03} + \partial V_{13} + \partial V_{23}$ of PEC region is represented as \mathcal{J}_3 .

Equivalence principle and enforcement of vanishing tangential electric field on the surface of the PEC region (Fig. 4.1b) yields

$$\begin{aligned} -\hat{\mathbf{t}}_3 \cdot \mathbf{E}^{\text{inc}}(\mathbf{r}) = & \hat{\mathbf{t}}_3 \cdot \int_{V_1} \overline{\overline{G}}_{e0}(\mathbf{r}, \mathbf{r}') \cdot \mathbf{j}_1(\mathbf{r}') dv' \\ & + \hat{\mathbf{t}}_3 \cdot \int_{V_2} \overline{\overline{G}}_{e0}(\mathbf{r}, \mathbf{r}') \cdot \mathbf{j}_2(\mathbf{r}') dv' \\ & + \hat{\mathbf{t}}_3 \cdot \oint_{\partial V_3} \overline{\overline{G}}_{e0}(\mathbf{r}, \mathbf{r}') \cdot \mathcal{J}_3(\mathbf{r}') ds', \quad \mathbf{r} \in \partial V_3 \end{aligned} \quad (4.2)$$

where $\hat{\mathbf{t}}_3$ is the tangential vector to the surface ∂V_3 .

For the penetrable dielectric region V_1 , the total electric field $\mathbf{E}_1(\mathbf{r})$ inside the object itself can be written as a superposition of elementary waves $\overline{\overline{G}}_{e0}(\mathbf{r}, \mathbf{r}')$ emanating

from object boundary $\partial V_1 = \partial V_{01} + \partial V_{21} + \partial V_{31}$ [14, 46], as (Fig. 4.1c)

$$\mathbf{E}_1(\mathbf{r}) = -i\omega\mu_0 \oint_{\partial V_1} \overline{\overline{G}}_{e\epsilon_1}(\mathbf{r}, \mathbf{r}') \cdot \mathbf{J}_1(\mathbf{r}') ds', \quad \mathbf{r} \in V_1 \setminus \partial V_1 \quad (4.3)$$

where $\overline{\overline{G}}_{e\epsilon_1}(\mathbf{r}, \mathbf{r}') = (k_{\epsilon_1}^{-2} \nabla \nabla + \overline{\overline{I}}) e^{-ik_{\epsilon_1} |\mathbf{r} - \mathbf{r}'|} / (4\pi |\mathbf{r} - \mathbf{r}'|)$ is the electric field 3-D dyadic Green's function of homogeneous medium with permittivity ϵ_1 and $k_{\epsilon_1} = k_0 \sqrt{\epsilon_1}$ being its wavenumber. The equivalence fictitious electric surface current density \mathbf{J}_1 defines the discontinuity between the tangential component of the true magnetic field \mathbf{H}_1 inside the dielectric region and unconstrained magnetic field \mathbf{H}_1^∞ outside it. The contribution from the fictitious magnetic surface current density can be taken with an arbitrary weight including zero [46]. Similarly, the total electric field inside the penetrable dielectric region with volume V_2 can be represented as (Fig. 4.1d)

$$\mathbf{E}_2(\mathbf{r}) = -i\omega\mu_0 \oint_{\partial V_2} \overline{\overline{G}}_{e\epsilon_2}(\mathbf{r}, \mathbf{r}') \cdot \mathbf{J}_2(\mathbf{r}') ds', \quad \mathbf{r} \in V_2 \setminus \partial V_2 \quad (4.4)$$

where $\overline{\overline{G}}_{e\epsilon_2}(\mathbf{r}, \mathbf{r}') = (k_{\epsilon_2}^{-2} \nabla \nabla + \overline{\overline{I}}) e^{-ik_{\epsilon_2} |\mathbf{r} - \mathbf{r}'|} / (4\pi |\mathbf{r} - \mathbf{r}'|)$ is the electric field 3-D dyadic Green's function of homogeneous medium with permittivity ϵ_2 and $k_{\epsilon_2} = k_0 \sqrt{\epsilon_2}$ being its wavenumber. Also, \mathbf{J}_2 is the equivalence fictitious electric surface current density defined on ∂V_2 .

Substitution of (4.3) and (4.4) into (4.1) followed by the restriction of the observation point to the boundaries ∂V_1 and ∂V_2 produces two coupled integral equations

$$\begin{aligned} \hat{\mathbf{t}}_1 \cdot \mathbf{E}^{\text{inc}}(\mathbf{r}) = & i\omega\mu_0 \hat{\mathbf{t}}_1 \cdot \left(- \oint_{\partial V_1} \overline{\overline{G}}_{e\epsilon_1}(\mathbf{r}, \mathbf{r}'') \cdot \mathbf{J}_1(\mathbf{r}'') ds'' \right. \\ & + (\epsilon_1 - 1) \cdot k_0^2 \int_{V_1} \overline{\overline{G}}_{e0}(\mathbf{r}, \mathbf{r}') \cdot \oint_{\partial V_1} \overline{\overline{G}}_{e\epsilon_1}(\mathbf{r}', \mathbf{r}'') \cdot \mathbf{J}_1(\mathbf{r}'') ds'' dv' \\ & + (\epsilon_2 - 1) \cdot k_0^2 \int_{V_2} \overline{\overline{G}}_{e0}(\mathbf{r}, \mathbf{r}') \cdot \oint_{\partial V_2} \overline{\overline{G}}_{e\epsilon_2}(\mathbf{r}', \mathbf{r}'') \cdot \mathbf{J}_2(\mathbf{r}'') ds'' dv' \\ & \left. - \oint_{\partial V_3} \overline{\overline{G}}_{e0}(\mathbf{r}, \mathbf{r}'') \cdot \mathcal{J}_3(\mathbf{r}'') ds'' \right), \quad \mathbf{r} \in \partial V_1 \end{aligned} \quad (4.5)$$

and

$$\begin{aligned}
\hat{\mathbf{t}}_2 \cdot \mathbf{E}^{\text{inc}}(\mathbf{r}) = & i\omega\mu_0\hat{\mathbf{t}}_2 \cdot \left(- \oint_{\partial V_2} \overline{\overline{G}}_{e\epsilon_2}(\mathbf{r}, \mathbf{r}'') \cdot \mathbf{J}_2(\mathbf{r}'') ds'' \right. \\
& + (\epsilon_1 - 1) \cdot k_0^2 \int_{V_1} \overline{\overline{G}}_{e0}(\mathbf{r}, \mathbf{r}') \cdot \oint_{\partial V_1} \overline{\overline{G}}_{e\epsilon_1}(\mathbf{r}', \mathbf{r}'') \cdot \mathbf{J}_1(\mathbf{r}'') ds'' dv' \\
& + (\epsilon_2 - 1) \cdot k_0^2 \int_{V_2} \overline{\overline{G}}_{e0}(\mathbf{r}, \mathbf{r}') \cdot \oint_{\partial V_2} \overline{\overline{G}}_{e\epsilon_2}(\mathbf{r}', \mathbf{r}'') \cdot \mathbf{J}_2(\mathbf{r}'') ds'' dv' \\
& \left. - \oint_{\partial V_3} \overline{\overline{G}}_{e0}(\mathbf{r}, \mathbf{r}'') \cdot \mathcal{J}_3(\mathbf{r}'') ds'' \right), \quad \mathbf{r} \in \partial V_2
\end{aligned} \tag{4.6}$$

where $\hat{\mathbf{t}}_m$ is the tangential vector to the surface ∂V_m , $m = 1, 2$. Also, substitution of (4.3) and (4.4) into (4.2) followed by the restriction of the observation point to the PEC region boundary ∂V_3 produces the third coupled integral equation

$$\begin{aligned}
\hat{\mathbf{t}}_3 \cdot \mathbf{E}^{\text{inc}}(\mathbf{r}) = & i\omega\mu_0\hat{\mathbf{t}}_3 \cdot \left((\epsilon_1 - 1) \cdot k_0^2 \int_{V_1} \overline{\overline{G}}_{e0}(\mathbf{r}, \mathbf{r}') \cdot \right. \\
& \oint_{\partial V_1} \overline{\overline{G}}_{e\epsilon_1}(\mathbf{r}', \mathbf{r}'') \cdot \mathbf{J}_1(\mathbf{r}'') ds'' dv' + (\epsilon_2 - 1) \cdot k_0^2 \int_{V_2} \overline{\overline{G}}_{e0}(\mathbf{r}, \mathbf{r}') \cdot \\
& \left. \oint_{\partial V_2} \overline{\overline{G}}_{e\epsilon_2}(\mathbf{r}', \mathbf{r}'') \cdot \mathbf{J}_2(\mathbf{r}'') ds'' dv' - \oint_{\partial V_3} \overline{\overline{G}}_{e0}(\mathbf{r}, \mathbf{r}'') \cdot \mathcal{J}_3(\mathbf{r}'') ds'' \right), \quad \mathbf{r} \in \partial V_3.
\end{aligned} \tag{4.7}$$

The new formulations (4.5)-(4.7) can be expressed in the integral operators form [13]. Hence, (4.5) and (4.6) can be written as

$$\begin{aligned}
\hat{\mathbf{t}}_\ell \cdot \mathbf{E}^{\text{inc}}(\mathbf{r}) = & - \overline{\overline{T}}_{\epsilon_\ell}^{\partial V_\ell, \partial V_\ell} \circ \mathbf{J}_\ell \\
& + \sum_{m=1}^2 (\epsilon_m - 1) \cdot k_0^2 \overline{\overline{T}}_0^{\partial V_\ell, V_m} \circ \overline{\overline{T}}_{\epsilon_m}^{V_m, \partial V_m} \circ \mathbf{J}_m \\
& - \overline{\overline{T}}_0^{\partial V_\ell, \partial V_3} \circ \mathcal{J}_3, \quad \mathbf{r} \in \partial V_\ell, \quad \ell = 1, 2.
\end{aligned} \tag{4.8}$$

Also, the integral operator form of (4.7) is

$$\begin{aligned} \hat{\mathbf{t}}_3 \cdot \mathbf{E}^{\text{inc}}(\mathbf{r}) = & \sum_{m=1}^2 (\epsilon_m - 1) \cdot k_0^2 \overline{\overline{\mathcal{T}}}_0^{\partial V_3, V_m} \circ \overline{\overline{\mathcal{T}}}_{\epsilon_m}^{V_m, \partial V_m} \circ \mathbf{J}_m \\ & - \overline{\overline{\mathcal{T}}}_0^{\partial V_3, \partial V_3} \circ \mathcal{J}_3, \quad \mathbf{r} \in \partial V_3 \end{aligned} \quad (4.9)$$

where $\mathcal{T}_{\epsilon/0}^{\partial V, \partial V}$, $\mathcal{T}_0^{\partial V, V}$, and $\mathcal{T}_\epsilon^{V, \partial V}$ are surface-to-surface, volume-to-surface, and surface-to-volume operators, respectively, in the set of SVS-S-EFIE (4.8) and (4.9). These operators are composed as a sum of two integral operators corresponding to the scalar and vector potentials as detailed in [13].

For the sake of clarity, we have derived the new formulation considering only three-region metal-dielectric composite scatterer as shown in Fig. 4.1(a). However, it can be generalized for a composite scatterer consisting of \mathcal{R}_1 dielectric regions and \mathcal{R}_2 PEC regions with junctions follows from (4.8) and (4.9) in a straightforward manner and can be written as

$$\begin{aligned} \hat{\mathbf{t}}_\ell \cdot \mathbf{E}^{\text{inc}}(\mathbf{r}) = & -\overline{\overline{\mathcal{T}}}_{\epsilon_\ell}^{\partial V_\ell, \partial V_\ell} \circ \mathbf{J}_\ell + k_0^2 \\ & \sum_{m=1}^{\mathcal{R}_1} (\epsilon_m - 1) \overline{\overline{\mathcal{T}}}_0^{\partial V_\ell, V_m} \circ \overline{\overline{\mathcal{T}}}_{\epsilon_m}^{V_m, \partial V_m} \circ \mathbf{J}_m - \sum_{n=\mathcal{R}_1+1}^{\mathcal{R}_1+\mathcal{R}_2} \overline{\overline{\mathcal{T}}}_0^{\partial V_\ell, \partial V_n} \circ \mathcal{J}_n \end{aligned} \quad (4.10)$$

and

$$\begin{aligned} \hat{\mathbf{t}}_{\ell'} \cdot \mathbf{E}^{\text{inc}}(\mathbf{r}) = & k_0^2 \\ & \sum_{m=1}^{\mathcal{R}_1} (\epsilon_m - 1) \overline{\overline{\mathcal{T}}}_0^{\partial V_{\ell'}, V_m} \circ \overline{\overline{\mathcal{T}}}_{\epsilon_m}^{V_m, \partial V_m} \circ \mathbf{J}_m - \sum_{n=\mathcal{R}_1+1}^{\mathcal{R}_1+\mathcal{R}_2} \overline{\overline{\mathcal{T}}}_0^{\partial V_{\ell'}, \partial V_n} \circ \mathcal{J}_n \end{aligned} \quad (4.11)$$

where $\ell = 1, \dots, \mathcal{R}_1$ and $\ell' = \mathcal{R}_1 + 1, \dots, \mathcal{R}_1 + \mathcal{R}_2$ are the indices of observation boundary ∂V_ℓ of \mathcal{R}_1 dielectric regions and $\partial V_{\ell'}$ of \mathcal{R}_2 PEC regions, respectively. In addition, the source regions are denoted by $m = 1, \dots, \mathcal{R}_1$ for dielectric regions and by $n = \mathcal{R}_1 + 1, \dots, \mathcal{R}_1 + \mathcal{R}_2$ for PEC regions.

In order to solve SVS-S-EFIE (4.10) and (4.11) with MoM (detailed in [13]), discretization of surface is required for both dielectric and PEC regions. Also, discretization of volume is required for the dielectric regions. Here, discretization of

$$\begin{array}{c}
\begin{array}{c}
\overbrace{\begin{array}{ccc}
P_1 & P_2 & P_3 \\
\overline{\overline{\mathcal{T}}}_{\epsilon_1}^{\partial V_1, \partial V_1} & \mathbf{0} & \overline{\overline{\mathcal{T}}}_0^{\partial V_1, \partial V_3} \\
\mathbf{0} & \overline{\overline{\mathcal{T}}}_{\epsilon_2}^{\partial V_2, \partial V_2} & \overline{\overline{\mathcal{T}}}_0^{\partial V_2, \partial V_3} \\
\mathbf{0} & \mathbf{0} & \overline{\overline{\mathcal{T}}}_0^{\partial V_3, \partial V_3}
\end{array}}^{Z_{\epsilon/0}^{\partial V, \partial V}} \\
- \\
\end{array}
+
\begin{array}{c}
\overbrace{\begin{array}{cc}
N_1 & N_2 \\
\overline{\overline{\mathcal{T}}}_0^{\partial V_1, V_1} & \overline{\overline{\mathcal{T}}}_0^{\partial V_1, V_2} \\
\overline{\overline{\mathcal{T}}}_0^{\partial V_2, V_1} & \overline{\overline{\mathcal{T}}}_0^{\partial V_2, V_2} \\
\overline{\overline{\mathcal{T}}}_0^{\partial V_3, V_1} & \overline{\overline{\mathcal{T}}}_0^{\partial V_3, V_2}
\end{array}}^{Z_0^{\partial V, V}} \\
+ \\
\end{array}
\bullet
\begin{array}{c}
\overbrace{\begin{array}{ccc}
P_1 & P_2 & P_3 \\
\overline{\overline{\mathcal{T}}}_{\epsilon_1}^{V_1, \partial V_1} & \mathbf{0} & \mathbf{0} \\
\mathbf{0} & \overline{\overline{\mathcal{T}}}_{\epsilon_2}^{V_2, \partial V_2} & \mathbf{0}
\end{array}}^{Z_{\epsilon}^{V, \partial V}} \\
\left. \begin{array}{l}
\phantom{\overline{\overline{\mathcal{T}}}_{\epsilon_1}^{V_1, \partial V_1}} \\
\phantom{\overline{\overline{\mathcal{T}}}_{\epsilon_2}^{V_2, \partial V_2}}
\end{array} \right\} \begin{array}{l} N_1 \\ N_2 \end{array}
\end{array}
\end{array}$$

Figure 4.2: System of matrix equations resulting from MoM discretization of the SVS-S-EFIE (formulations (4.8) and (4.9)) for a composite metal-dielectric scatterer of Fig. 4.1(a). The number of RWG functions on the boundaries ∂V_1 , ∂V_2 , and ∂V_3 are P_1 , P_2 and P_3 , respectively, with $P = P_1 + P_2 + P_3$ being the total number of RWG basis functions. The number of tetrahedron elements in the dielectrics with volumes V_1 and V_2 are N_1 and N_2 , respectively. The vectors of unknowns and RHS are not appeared in the system of matrix equations.

the unknown surface currents is performed over P Rao-Wilton-Glisson (RWG) basis functions. Also, the volumes are discretized with N tetrahedrons. For the case of a general three-region metal-dielectric scatterer (Fig. 4.1(a)) SVS-S-EFIE yields a system of linear equations with respect to the unknown coefficients vector \mathbf{I} in the expansion of the unknown surface currents in (4.10) and (4.11). The MoM matrix structure is shown in Fig. 4.2, P being the total number of RWG basis functions on the surfaces and N_1 and N_2 being the number of tetrahedrons in the dielectric regions with volumes V_1 and V_2 , respectively. In Fig. 4.2, MoM impedance matrices $Z_{\epsilon/0}^{\partial V, \partial V}$, $Z_0^{\partial V, V}$, and $Z_{\epsilon}^{V, \partial V}$ are corresponding to the operators $\overline{\overline{\mathcal{T}}}_{\epsilon/0}^{\partial V, \partial V}$, $\overline{\overline{\mathcal{T}}}_0^{\partial V, V}$, and $\overline{\overline{\mathcal{T}}}_{\epsilon}^{V, \partial V}$, respectively.

4.3 \mathcal{H} -matrix-Based Direct Solution

When the number of DoF P and N become large, the conventional direct MoM solution [13, 38] requires large amount of memory and prolonged CPU times to solve

the radiation and scattering problems of interest. To accelerate the MoM solution of the proposed SVS-S-EFIE formulation we adopt \mathcal{H} -matrix [36] framework. It enables fast evaluation of the pertinent matrix-matrix multiplications, LU decomposition, and back-substitution required for construction of direct solver for the case of general piece-wise homogeneous metal-dielectric composite structures with arbitrary number of regions.

The algorithm begins with clustering of the basis and testing functions discretizing surface and volumetric field distributions in each regions based on the geometrical information [35]. Next, each of the pertinent discretized integral operator (surface-to-surface, surface-to-volume, and volume-to-surface) is represented in \mathcal{H} -matrix format and their interaction sets are classified as admissible (far interactions) or inadmissible (near interactions) according to the admissibility condition [35]. In this work, the adaptive cross approximation (ACA) algorithm [24] is used to obtain the admissible blocks in a compressed low-rank form. Inadmissible blocks are computed by using conventional MoM and stored in full matrix representation. To demonstrate the above process, the \mathcal{H} -matrix representation of the proposed matrix equation yields a structure shown in Fig. 4.3 with \otimes and \oplus being the operations of formatted multiplication and addition. In Fig. 4.3, the surface-to-surface impedance matrix $\mathcal{Z}_{\epsilon/0}^{\partial V, \partial V}$ is corresponding to the operator $\overline{\overline{\mathcal{T}}}_{\epsilon/0}^{\partial V, \partial V}$. Also, $\mathcal{Z}_0^{\partial V, V}$ and $\mathcal{Z}_\epsilon^{V, \partial V}$ are corresponding to the operators $\overline{\overline{\mathcal{T}}}_0^{\partial V, V}$ and $\overline{\overline{\mathcal{T}}}_\epsilon^{V, \partial V}$, respectively.

After \mathcal{H} -matrix approximations are constructed for each discretized integral operator, the resultant system of linear algebraic equations

$$(\mathcal{Z}_{\epsilon/0}^{\partial V, \partial V} \oplus \mathcal{Z}_0^{\partial V, V} \otimes \mathcal{Z}_\epsilon^{V, \partial V}) \cdot I = \mathcal{Z}_{\text{SVS}} \cdot I = \mathcal{V} \quad (4.12)$$

has to be solved. Hence, to solve (4.12) with direct method, the final MoM \mathcal{H} -matrix \mathcal{Z}_{SVS} demonstrated in Fig. 4.3 must be first constructed using formatted multiplica-

tion and addition [35]

$$\begin{aligned}
\mathcal{Z}_{\text{SVS}} &= \begin{bmatrix} \mathcal{Z}_{\text{SVS}_{1,1}} & \mathcal{Z}_{\text{SVS}_{1,2}} & \mathcal{Z}_{\text{SVS}_{1,3}} \\ \mathcal{Z}_{\text{SVS}_{2,1}} & \mathcal{Z}_{\text{SVS}_{2,2}} & \mathcal{Z}_{\text{SVS}_{2,3}} \\ \mathcal{Z}_{\text{SVS}_{3,1}} & \mathcal{Z}_{\text{SVS}_{3,2}} & \mathcal{Z}_{\text{SVS}_{3,3}} \end{bmatrix} \\
&= \begin{bmatrix} \mathcal{Z}_{\epsilon_1}^{\partial V_1, \partial V_1} & 0 & \mathcal{Z}_0^{\partial V_1, \partial V_3} \\ 0 & \mathcal{Z}_{\epsilon_2}^{\partial V_2, \partial V_2} & \mathcal{Z}_0^{\partial V_2, \partial V_3} \\ 0 & 0 & \mathcal{Z}_0^{\partial V_3, \partial V_3} \end{bmatrix} \oplus \begin{bmatrix} \mathcal{Z}_0^{\partial V_1, V_1} & \mathcal{Z}_0^{\partial V_1, V_2} \\ \mathcal{Z}_0^{\partial V_2, V_1} & \mathcal{Z}_0^{\partial V_2, V_2} \\ \mathcal{Z}_0^{\partial V_3, V_1} & \mathcal{Z}_0^{\partial V_3, V_2} \end{bmatrix} \otimes \begin{bmatrix} \mathcal{Z}_{\epsilon_1}^{V_1, \partial V_1} & 0 & 0 \\ 0 & \mathcal{Z}_{\epsilon_1}^{V_2, \partial V_2} & 0 \end{bmatrix}
\end{aligned} \tag{4.13}$$

where each sub- \mathcal{H} -matrix $\mathcal{Z}_{\text{SVS}_{\ell,m}}$ (here, $\ell = 1, 2, 3$ and $m = 1, 2, 3$) is calculated individually as

$$\mathcal{Z}_{\text{SVS}_{\ell,m}} = \mathcal{Z}_{\epsilon_\ell/0}^{\partial V_\ell, \partial V_m} \oplus \mathcal{Z}_0^{\partial V_\ell, V_m} \otimes \mathcal{Z}_{\epsilon_m}^{V_m, \partial V_m}. \tag{4.14}$$

Next, block \mathcal{H} -LU decomposition followed by block \mathcal{H} -substitutions is applied to the final MoM \mathcal{H} -matrix \mathcal{Z}_{SVS} to solve (4.12). Detailed implementation of block \mathcal{H} -LU the reader can find in [39].

The computational complexity and memory of the SVS-S-EFIE is given in Table 4.1 and it is compared to that of PMCHWT solution [11] for both naïve MoM and \mathcal{H} -matrix accelerated MoM. The complexity is formulated as a function of number of unknowns on the surfaces P with the assumption that the volume is discretized with $N = P^\alpha$ ($1 < \alpha < 1.5$) elements for a general multi-region 3-D scatterer [13, 35].

4.4 Numerical Results

In this section the proposed method is validated numerically. We consider the problems of electric dipole radiation near 3-D composite objects such as multilayer sphere and bifurcated sphere. The results are compared with analytic Mie series [71] and FEKO commercial simulator [72]. The \mathcal{H} -matrix parameters are chosen empirically and set to the following values. The admissibility coefficient is $\eta = 4$, the leaf-size is $n_{\min} = 32$, and the truncation tolerance of the ACA algorithm is $\tau_{\text{ACA}} = 10^{-3}$. The numerical results are obtained on a single core of the Intel Xeon X5650 processor

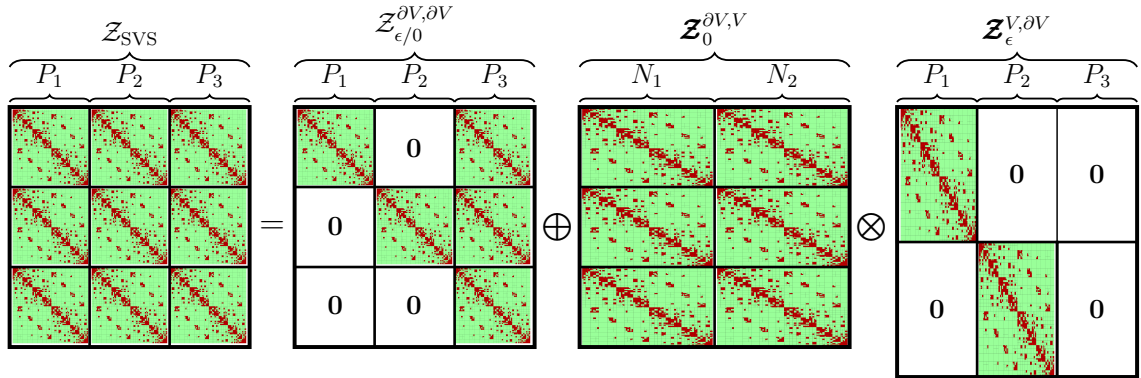


Figure 4.3: Assembly of \mathcal{Z}_{SVS} MoM \mathcal{H} -matrix for composite metal-dielectric scatterer featuring three regions (Fig. 4.1(a)). The \mathcal{Z}_{SVS} \mathcal{H} -matrix computed from the individual \mathcal{H} -matrices operators $\mathcal{Z}_{\epsilon/0}^{\partial V, \partial V}$, $\mathcal{Z}_0^{\partial V, V}$, and $\mathcal{Z}_\epsilon^{V, \partial V}$ via formatted multiplication and addition required by \mathcal{H} -LU based direct solution. Green blocks are corresponding to the far interactions and red blocks are corresponding to the near interactions. The number of RWG basis functions on the boundaries ∂V_1 , ∂V_2 , and ∂V_2 are P_1 , P_2 , and P_3 , respectively. The number of tetrahedron elements in the volumes V_1 and V_2 are N_1 and N_2 .

running at 2.66 GHz.

4.4.1 Multilayer sphere

To demonstrate the proposed formulation for the solution of a piece-wise metal-dielectric multilayer sphere model, we conducted two experiments. First, we consider the model with one dielectric region formed by the outer layer having relative electric permittivity of $\epsilon_1 = 3.0$ and the PEC region formed by the inner sphere as shown in Fig. 4.4(a). The model is centered at the origin with inner radius of 0.92 m and the outer radius of 0.1 m. The sphere is excited by a radial electric dipole with moment $I \cdot \ell = 1 [\text{A} \cdot \text{m}]$ situated at $(0, 0, 0.4)$ m. The frequency of analysis is 1.5 GHz. In order to show flexibility of meshing in the proposed solver, each region is discretized separately with mesh sizes $h_1 = 0.003$ m and $h_2 = 0.005$ m for dielectric and PEC regions, respectively. This discretization produces $M_1 = 44,378$ triangles for dielectric boundary and $M_2 = 16,366$ triangles for PEC boundary which leads to total number

Table 4.1: Computational complexity comparison for the SVS-S-EFIE and PM-CHWT [11] equations for the case of $N = P^\alpha$ ($1 < \alpha < 1.5$) and fixed number of penetrable regions \mathcal{R}_1 and PEC regions \mathcal{R}_2 for both naïve and \mathcal{H} -matrix accelerated MoM.

	SVS-S-EFIE	PMCHWT
Matrix Fill		
Naïve MoM	$\mathcal{O}(P^{1+\alpha})$	$\mathcal{O}(P^2)$
\mathcal{H} -matrix MoM	$\mathcal{O}(P^\alpha \log P)$	$\mathcal{O}(P \log P)$
Direct Solve		
Naïve LU	$\mathcal{O}(P^{2+\alpha})$	$\mathcal{O}(P^3)$
\mathcal{H} -matrix LU	$\mathcal{O}(P^\alpha \log^2 P)$	$\mathcal{O}(P \log^2 P)$
Calculating the E-field Inside Volume		
Naïve MoM	$\mathcal{O}(P^{1+\alpha})$	$\mathcal{O}(P^{1+\alpha})$
\mathcal{H} -matrix MoM	$\mathcal{O}(P^\alpha \log P)$	$\mathcal{O}(P^\alpha \log P)$
Required Memory with Calculation of the E-field Inside Volume		
Naïve MoM	$\mathcal{O}(P^{1+\alpha})$	$\mathcal{O}(P^{1+\alpha})$
\mathcal{H} -matrix MoM	$\mathcal{O}(P^\alpha \log P)$	$\mathcal{O}(P^\alpha \log P)$

of RWG basis functions $P = 91,116$. The volume of the dielectric region is also discretized with $N_1 = 102,763$ tetrahedrons. The distribution of the magnitude of the total electric field inside the dielectric region computed by the \mathcal{H} -matrix accelerated SVS-S-EFIE is demonstrated in Fig. 4.4(a). The relative error in total electric field computed with the proposed solver with respect to the analytic Mie series solution is shown in Fig. 4.4(b). The \mathcal{H} -matrix accelerated SVS-S-EFIE is seen to match closely with the analytic Mie series solution with average relative error of 0.015 and standard deviation in relative error of 0.012.

Second, we consider the same model with one extra dielectric region formed the outer layer with radius of 0.104 m. The outer dielectric layer has relative electric permittivity of $\epsilon_1 = 3.0$ and the inner dielectric layer has relative electric permittivity of $\epsilon_2 = 1.5$ as shown in Fig. 4.4(c). The model is excited by the same dipole with operating frequency of 1.5 GHz. In Fig. 4.4(c), the magnitude of \mathbf{E} -field inside the dielectric regions computed by the \mathcal{H} -matrix accelerated SVS-S-EFIE is demonstrated.

The relative error in the solution of the electric field compared against the analytic Mie series solution is shown in the Fig. 4.4(d). The proposed accelerated solver produces average relative error of 0.038 and standard deviation in relative error of 0.037 in the computed \mathbf{E} -field compared with the Mie series solution. The non-conformal discretization used to simulate the three-region model is also depicted in Fig. 4.4(e). Each region is discretized separately with mesh sizes $h_1 = 0.035$ m, $h_2 = 0.055$ m, and $h_3 = 0.0075$ m for outer dielectric, inner dielectric, and PEC regions, respectively. This discretization produces (from outer to inner): $N_1 = 30,485$ and $N_2 = 77,670$ tetrahedrons and their surfaces are discretized with $P_1 = 74,484$, $P_2 = 29,154$. The surface of PEC region is also discretized with $P_3 = 6,966$ RWG functions, resulting in $P = 110,604$ as the total number of RWG functions for the composite three-region multilayer sphere model.

Next, in order to examine the complexity performance of the proposed \mathcal{H} -matrix accelerated SVS-S-EFIE, we choose the radiation problem of three-region metal-dielectric multilayer sphere model and increase the number of discretized elements. In Fig. 4.5, we show the memory requirement and CPU time used as a function of the number of the surface unknowns P . In this model, the volume is discretized with about $N = P$ ($\alpha = 1$ in Table 4.1) elements. In Fig. 4.5(a), memory requirements is depicted and Its \mathcal{H} -matrix MoM scaling behaves as $\mathcal{O}(P \log P)$ confirming the theoretical estimates in Table 4.1. The computational time to fill the pertinent \mathcal{H} -matrix operations is plotted in Fig. 4.5(b) with scaling of $\mathcal{O}(P \log P)$. Also, the CPU time to solve the matrix equation using the block \mathcal{H} -LU algorithm including of creation of final \mathcal{Z}_{SVS} , block \mathcal{H} -LU decomposition, and block \mathcal{H} -substitutions [39] is plotted in Fig. 4.5(c) with scaling of $\mathcal{O}(P \log^2 P)$ which closely matches theoretically predicted scaling detailed in [39].

4.4.2 Bifurcated sphere

In the third example, we consider the dipole excitation problem for a bifurcated sphere centered at the origin and made of a PEC hemisphere and a homogeneous dielectric hemisphere (consider the model shown in Fig. 4.1(a) with $\epsilon_1 = \epsilon_2$). The

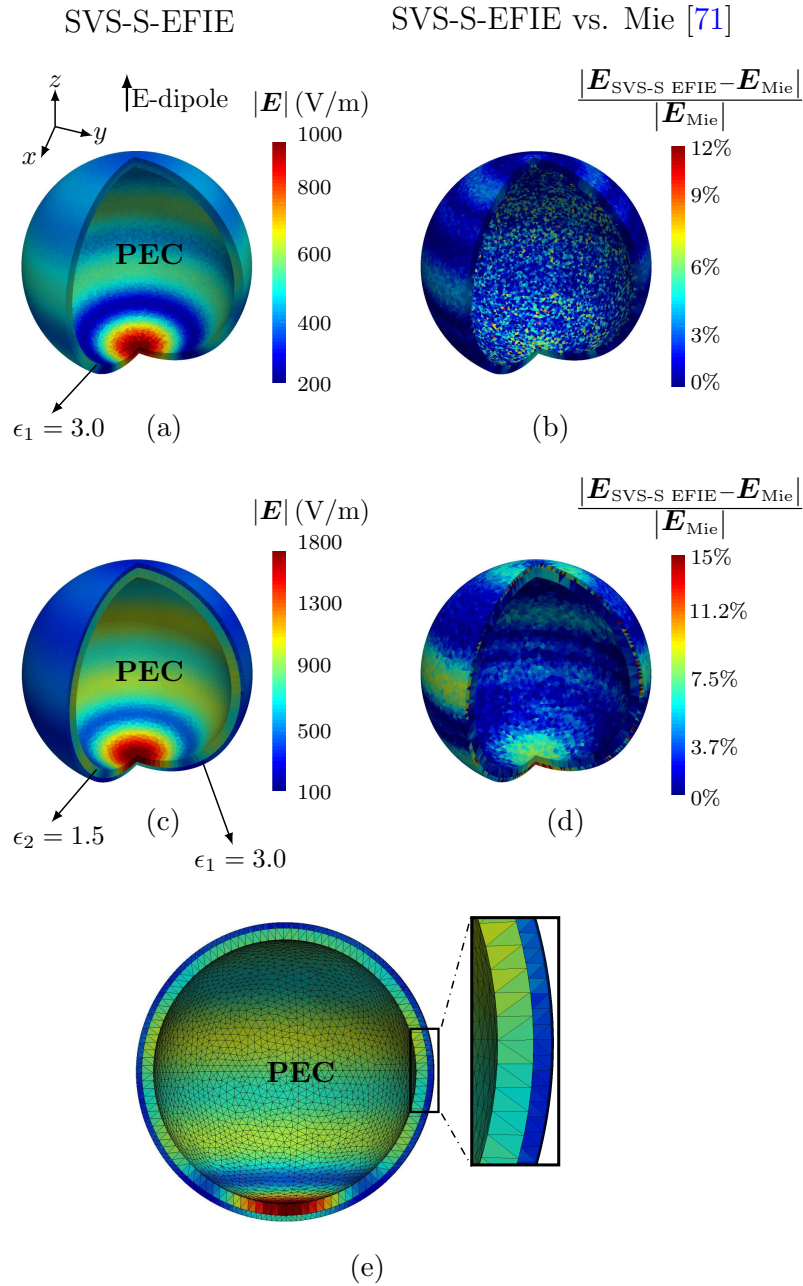


Figure 4.4: (a) Magnitude of \mathbf{E} -field in the dielectric region of the two-region composite metal-dielectric multilayer sphere model obtained by the \mathcal{H} -matrix accelerated of the SVS-S-EFIE. (b) Relative error in the solution of the two-region model compared against Mie series. (c) Magnitude of \mathbf{E} -field in the dielectric region of the three-region composite metal-dielectric multilayer sphere model obtained by the \mathcal{H} -matrix accelerated of the SVS-S-EFIE. (d) Relative error in the solution of the three-region model compared against Mie series. (e) Non-conformal mesh representation of the three-region composite metal-dielectric multilayer sphere model.

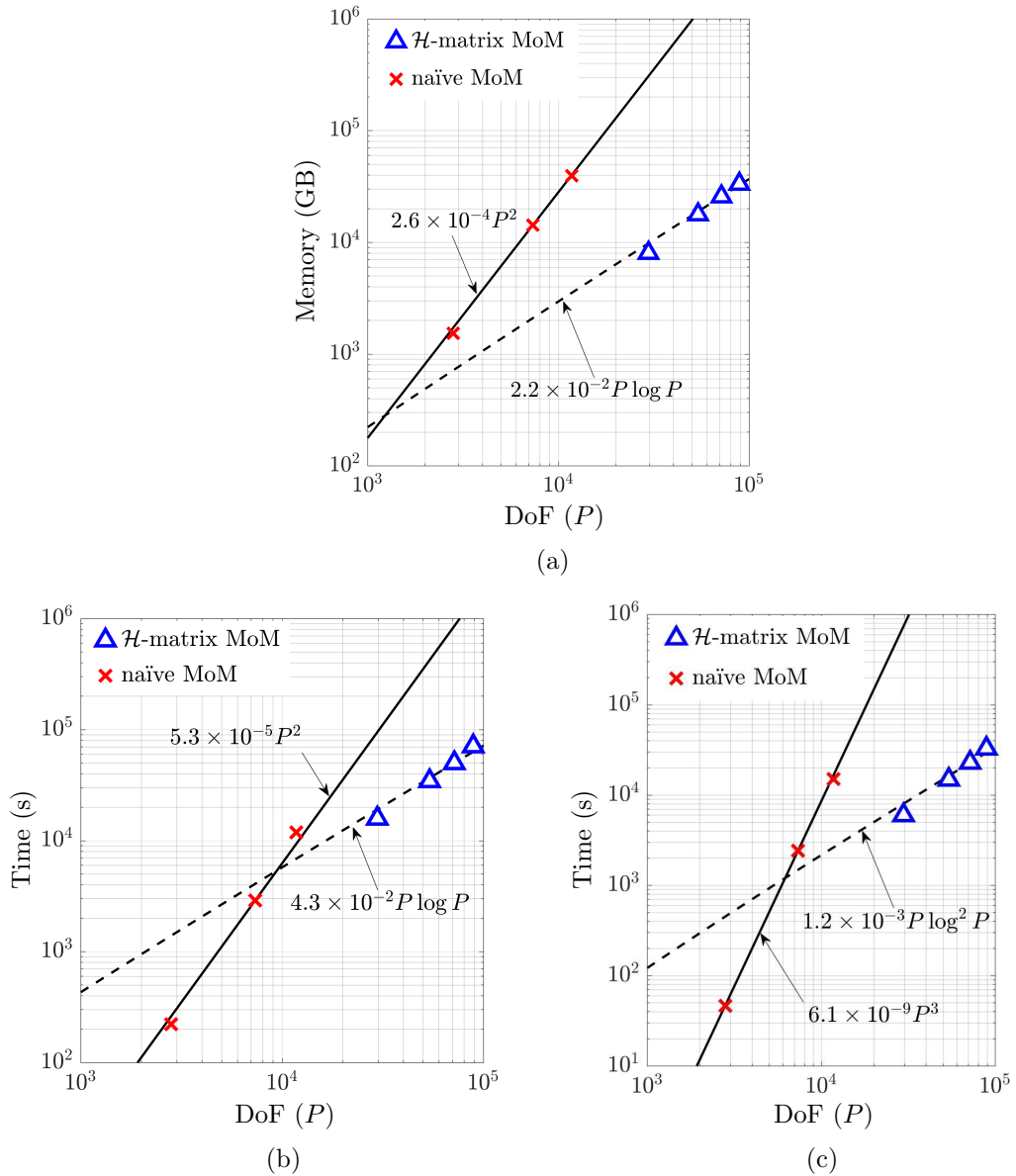


Figure 4.5: Scaling behavior of both \mathcal{H} -matrix (dashed lines) and naïve (solid lines) MoM discretization of SVS-S-EFIE for the radiation problem of the three-region multilayer sphere model. (a) Memory. (b) Fill time (time to construct the MoM matrices of the SVS-S-EFIE). (c) Solution time (including of creation of final \mathcal{Z}_{SVS} , block \mathcal{H} -LU decomposition, and block \mathcal{H} -substitutions).

operation frequency of the dipole is 3 GHz. The dipole is situated at $(0, 0, 0.4)$ m. Each hemisphere has the radius of 0.1 m and the dielectric region has relative per-

mittivity $\epsilon_1 = \epsilon_2 = 3$. The distribution of the magnitude of the total electric field inside the dielectric region computed using the \mathcal{H} -matrix accelerated SVS-S-EFIE is shown in Fig. 4.6(a). Each region is discretized separately with a uniform mesh of size $h_1 = 0.004$ m and $h_2 = 0.006$ m for dielectric and PEC regions, respectively. In the figure, part of the surface between the boundary is magnified for better visibility of the uniform mesh structure. Also, the mesh structure of the model is depicted in Fig. 4.6(b) to show the non-conformal behaviour of the mesh in material junction with emphasize on the flexibility of the proposed SVS-S-EFIE. For this model, the number of triangles in MoM discretization is $M_1 = 14,778$ and $M_2 = 6,924$ for the dielectric and PEC boundaries which leads to the total number of RWG functions being $P = 32,553$. The dielectric region is also discretized with $N_1 = 131,266$ tetrahedrons. In order to validate the proposed solver, solution of the same radiation problem is obtained using FEKO and the magnitude of the electric field along the x axis is shown in Fig. 4.6(c). From FEKO solution in Fig. 4.6(c), one can observe singular behavior of the electric field near the material junction (e.g. $x = -0.1$ m and $x = 0.1$ m). Therefore, in order to reconstruct the electric field near this region by the SVS-S-EFIE accurately, multiscale meshing is used. Namely, the mesh near the material junction is refined. The size of the mesh near the junction is selected as $1/10$ of the uniform mesh size and is equal to 0.0004 m. The distribution of the electric field computed inside the dielectric is demonstrated in Fig. 4.6(d). One can see that the SVS-S-EFIE solution on the multiscale mesh accurately reconstructs the field singularity near the edge. The refined mesh structure on the surface of the dielectric region is shown in Fig. 4.6(d). Also, the discretized model is depicted in Fig. 4.6(e) to show the multiscale mesh structure of both dielectric and PEC regions. For the structure with refined mesh, the total number of triangles is increased to $M = 29,380$. It leads to the total number of RWG functions equal to $P = 88,140$. The number of tetrahedrons in multiscale volumetric mesh refined near the edge is also increased and features $N_1 = 155,775$ elements.

The complexity scaling of both \mathcal{H} -matrix accelerated and naïve MoM solutions of the SVS-S-EFIE for the bifurcated sphere with both regular and multiscale mesh models are depicted in Fig. 4.7 and Fig. 4.8, respectively. The complexity scaling

Memory requirements are depicted in Fig. 4.7(a) and Fig. 4.8(a) with respect to the number of surface unknowns P . In the bifurcated sphere model, the volume is discretized with about $N = P^{1.3}$ ($\alpha = 1.3$) and $N = P^{1.2}$ ($\alpha = 1.2$) elements for regular and multiscale mesh structures, respectively. The complexity of \mathcal{H} -matrix accelerated MoM validated to scale close to $\mathcal{O}(P^\alpha \log P)$. The numerical results demonstrate a significant reduction of memory usage compared to the direct MoM solution. The time required to fill the matrices is depicted in Fig. 4.7(b) and Fig. 4.8(b) with complexities close to $\mathcal{O}(P^\alpha \log P)$ for the fast solver. Also, the computational time to solve the matrix equation using the fast direct method is plotted in Fig. 4.7(c) and Fig. 4.8(c) with scaling of $\mathcal{O}(P^\alpha \log^2 P)$ which closely matches theoretically predicted scaling in Table 4.1.

4.5 Conclusion

A novel single source integral equation formulation is proposed for electromagnetic analysis of the 3-D composite objects with metallic and dielectric regions. In comparison to the traditional EFIE-PMCHWT formulation, the new method requires only a single unknown on the boundaries between scatterer and the background medium, while two independent sets of unknown surface currents are required at the common boundaries between the regions. Therefore, the meshes can be independent between the common boundaries. Consequently, the proposed method can be efficient when combining with the fast algorithms specifically for multiscale problems. Therefore, solution of the SVS-S-EFIE is accelerated by the \mathcal{H} -matrix direct based method and the numerical examples show that the new method provides the similar precision for the field calculations against the analytical Mie series solution and commercial solver.

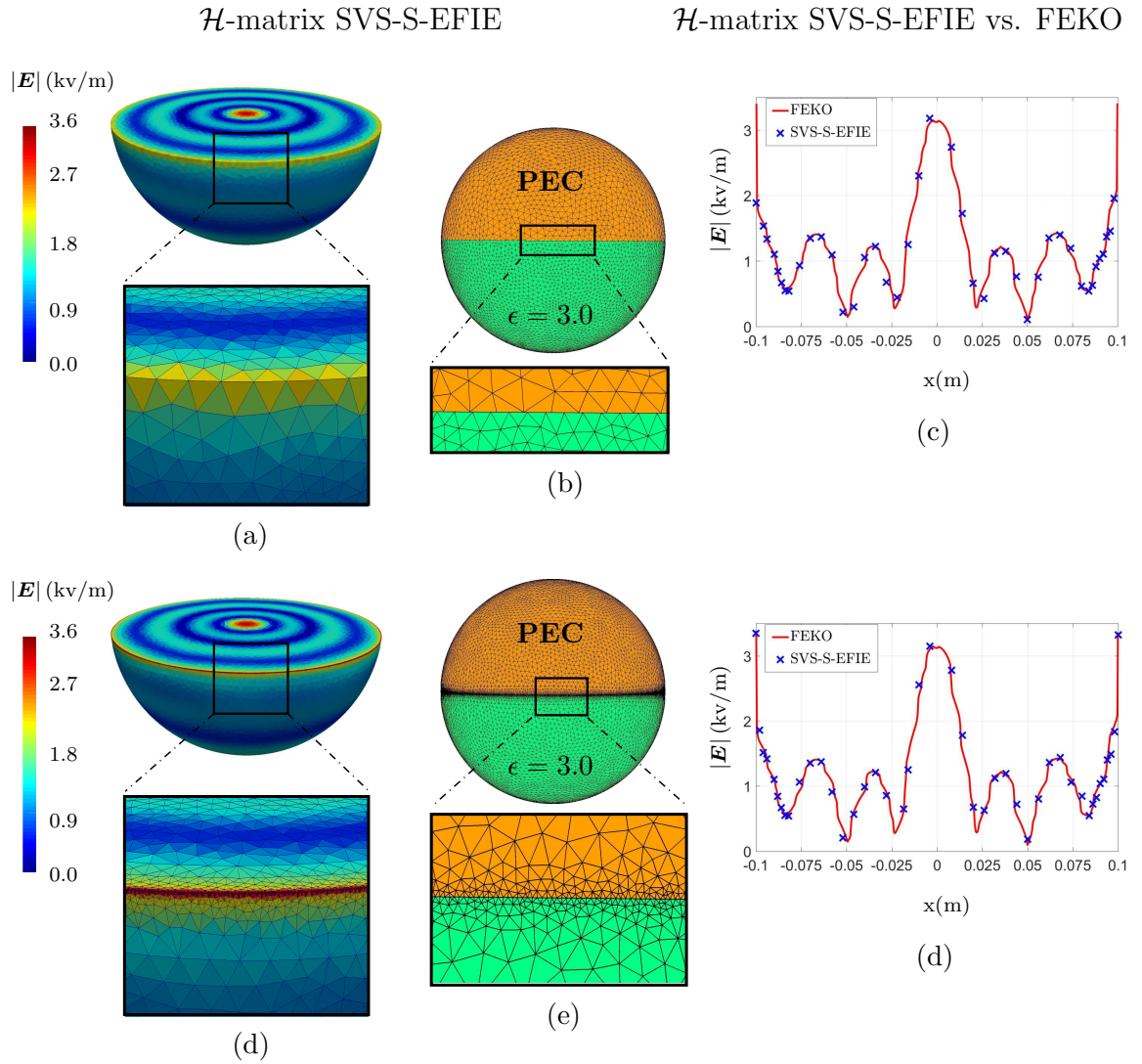


Figure 4.6: (a) A 3-D representation of the magnitude of \mathbf{E} -field inside the dielectric region of a composite metal-dielectric bifurcated sphere discretized with uniform mesh using the \mathcal{H} -matrix accelerated SVS-S-EFIE. (b) Non-conformal mesh representation of the model with uniform discretization of dielectric and PEC regions. (c) Magnitude of \mathbf{E} -field along x axis obtained by the proposed solver and FEKO for the uniform mesh model. (d) The 3-D representation of magnitude of \mathbf{E} -field inside the dielectric region of the multiscale mesh model using the proposed solver. (e) Non-conformal mesh representation of the model with multiscale discretization of the dielectric region. (f) Magnitude of the total electric field along x axis after mesh refinement compared against the FEKO.

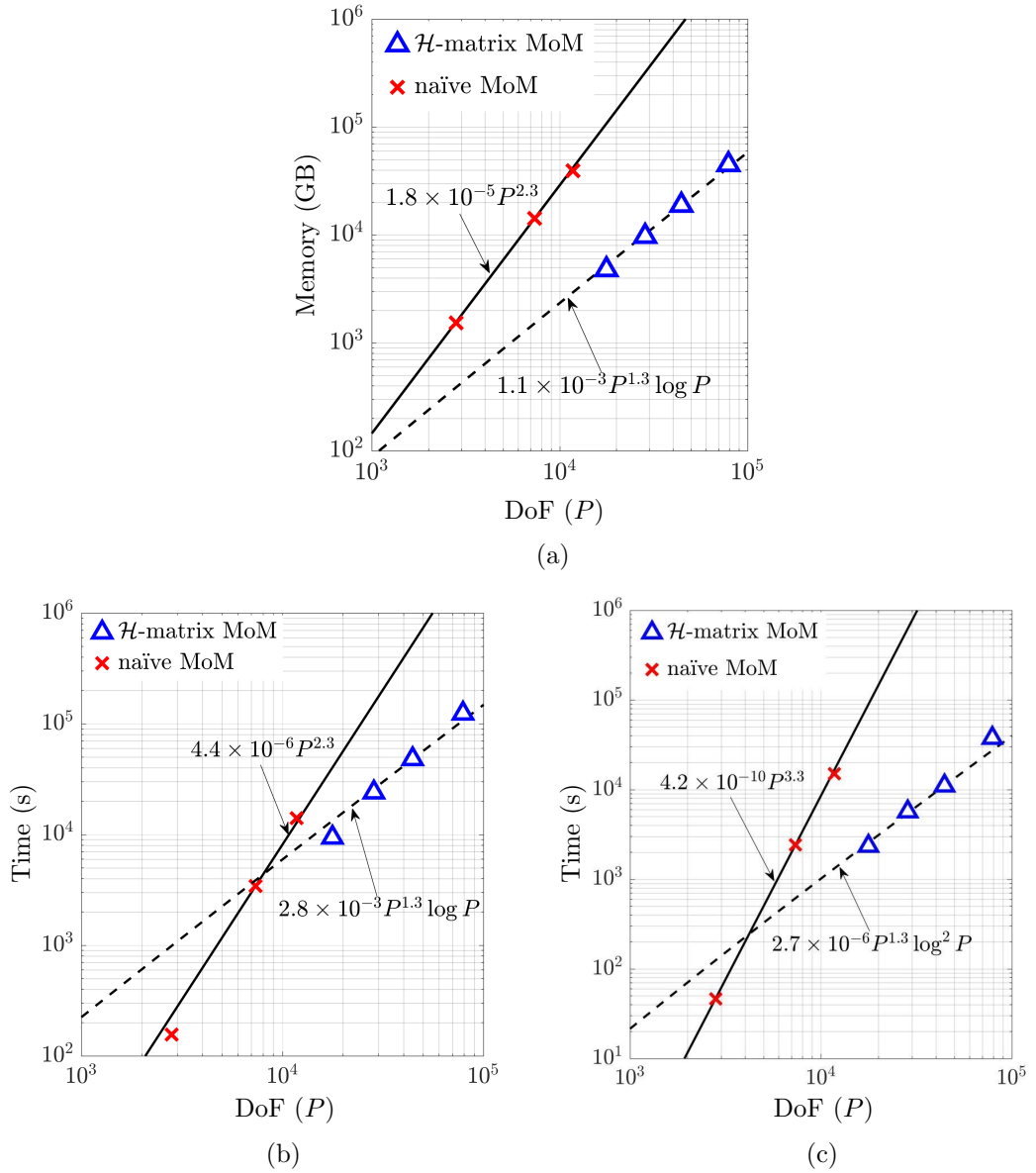


Figure 4.7: Scaling behavior of both \mathcal{H} -matrix (dashed lines) and naive (solid lines) MoM discretization of SVS-S-EFIE for the radiation problem of bifurcated sphere with regular mesh model. (a) Memory. (b) Fill time (time to construct the MoM matrices of the SVS-S-EFIE). (c) Solution time (including of creation of final \mathcal{Z}_{SVS} , block \mathcal{H} -LU decomposition, and block \mathcal{H} -substitutions).

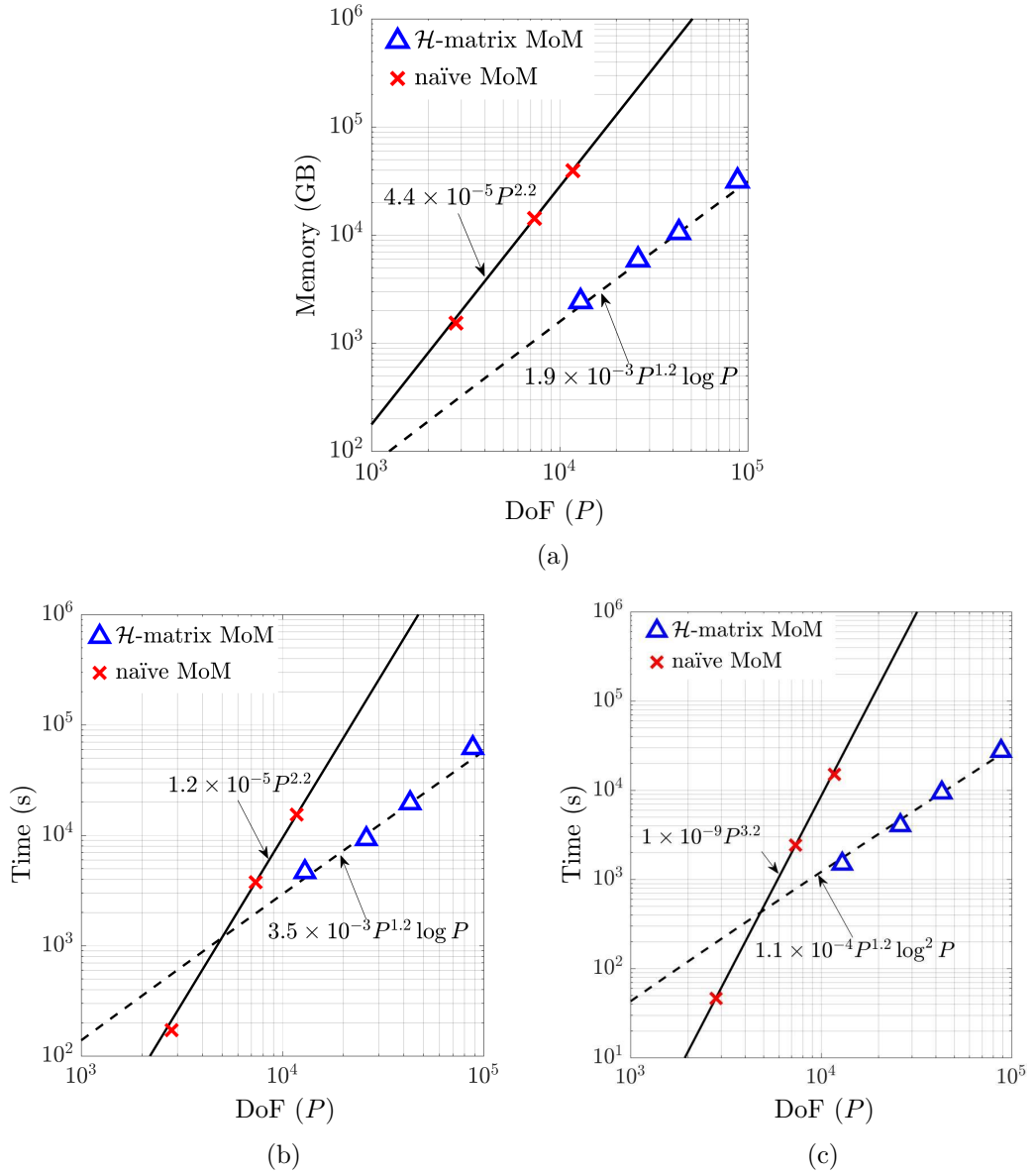


Figure 4.8: Scaling behavior of both \mathcal{H} -matrix (dashed lines) and naive (solid lines) MoM discretization of SVS-S-EFIE for the radiation problem of bifurcated sphere with multiscale mesh model. (a) Memory. (b) Fill time (time to construct the MoM matrices of the SVS-S-EFIE). (c) Solution time (including of creation of final \mathcal{Z}_{SVS} , block \mathcal{H} -LU decomposition, and block \mathcal{H} -substitutions).

5

Surface-Volume-Surface EFIE for Electromagnetic Analysis of 3-D Composite Dielectric Objects in Multilayered Media

©2019 IEEE. Reprinted, with permission, from *Reza Gholami, Shucheng Zheng, and Vladimir Okhmatovski, IEEE Journal on Multiscale and Multiphysics Computational Techniques, Under Review.*

5.1 Abstract

The Surface-Volume-Surface Electric Field Integral Equation (SVS-EFIE) is generalized for the case of scattering and radiation problems on the composite non-magnetic dielectric objects situated in planar non-magnetic layered medium. The piece-wise homogeneous regions of the scatterer can be arbitrarily positioned with respect to the layers of stratification. The SVS-EFIE being a class of single source integral equations (SSIE) is formed by restricting the surface single source electric field representation in each distinct region of the scatterer through the Volume-EFIE (V-EFIE) enforced on the boundary of that region for only the tangential component

of the total field. As a result, the SVS-EFIE utilizes only the electric field dyadic Green's functions. This allows for its cast into the mixed-potential form using classical Michalski-Zheng's formulation and Method of Moments (MoM) discretization featuring easily computable integrals with singularities no stronger than $1/R$, R being the distance from the source to the observation point in such integrals. The matrices of MoM discretization are represented in hierarchical form (as \mathcal{H} -matrices) enabling solution of the scattering problems in multilayered media with $O(N^\alpha \log N)$ CPU time and memory complexities, where α is a geometry dependent constant ranging from 1 to 1.5 depending on the shape of the scatterer. While the MoM surface and volume meshes discretizing the regions of the scatterer are constructed to ensure that no mesh element crosses interfaces between the layers, the clusters of both the surface and volume elements in their respective recursive partitionings in the process of \mathcal{H} -matrix construction are allowed to span multiple layers of the medium. Upon computation of the layered medium Green's function kernels with the Discrete Complex Image Method (DCIM) allowing clusters of elements to cross dielectric interfaces between the layers is shown to preserve compressibility of the corresponding \mathcal{H} -matrix blocks.

5.2 Introduction

Analysis of electromagnetic fields in the presence of general objects situated in multilayered media has been of significant interest and topic of intensive research over several decades [71, 82]. This interest is fuelled by a broad variety of applications in both science and engineering ranging from nanotechnology to geoscience, in which such analysis plays a critical role. Scattering of light on quantum dots deposited in photonic crystal slabs [83], signal propagation on high-speed interconnects [84], transient analysis of power installations and their grounding systems [85], and scattering on undergrounds reservoirs of oil and gas [86] are just few such applications.

Analysis techniques based on direct solution of the differential equations of electromagnetics such as Finite Element Method (FEM) [9] and Finite-Difference Method (FDM) [8] and based on solution of the integral equations [11] exist for field problems in multilayered media. While the FEM and FD techniques offer great flexibility

in handling complex geometries and material properties of the objects and result in sparse matrix equations, they struggle with handling thin layers, accumulation of error when structures span electrically large areas, large number of involved degrees of freedom due to the need to discretize both layers and the objects, and perturbation of the sought fields due to truncation of the mesh. The integral equation formulations are free from the above issues. However, they result in dense matrix equations which call for use of sophisticated fast algorithms to afford solution of practically interesting problems. They are also limited in their ability to handle complex materials featuring anisotropy and inhomogeneities. Despite these limitations the integral equation methods have been the methods of choice for analyzing the fields in the layered media. The primary reason for this is the ability of the integral equations to decompose the problem into the problem of finding the field of point source in the presence of the layers (a.k.a. the Green's function [45]) and the problem of finding unknown fields in the object itself.

Analogously with the integral equations formulated for the penetrable objects situated in free space, the integral equations for the objects situated in multilayered media can be stated with respect to the distribution of unknown fields in the objects' volume (volume integral equations, VIEs [71, 87]), with respect to the tangential components of the electric and magnetic field on the object's boundary (traditional surface integral equations, SIEs [12, 66, 88, 89]), or with respect to a single unknown vector function defined on the object's surface and acting as the weighting function for the waves emanating from its points (single source surface integral equations, SSSIEs [46, 47, 59, 90, 91]). The SSSIE have the least degrees of freedom upon MoM discretization out of the three classes of equations. They also offer simple handling of the material junctions unlike the SIEs. They have found only limited use, however, due to the large number of involved integral operators and their notably more complicated MoM discretization than VIEs or SIEs due to the presence of integral operator products.

In our previous work [13, 37–39] we introduced a new SSIE based on constraining of the single source integral field representations with the volume equivalence principle as opposed to their constraining with the surface equivalence principle as it was

done in SSSIEs. The resultant SVS-EFIE produced fewer integral operator products, allowed for simple discretization of the fields at the material junctions [38, 39], and featured only electric field dyadic Green's functions enabling its mixed-potential formulation in the presence of multilayered media [37]. The mixed-potential formulation of the SVS-EFIE with multilayered media dyadic Green's function formulated for homogeneous dielectric scatterers utilized Michalski-Zheng's formulation previously used for solution of scattering problems on metal objects embedded in the layers. This allowed for easy retrofitting of the MoM codes developed for metal cases to the case of penetrable objects without any need to define new MoM interactions or dyadic Green's function components in the presence of the multilayered media [37].

In this work we generalize multilayered medium formulation of the SVS-EFIE previously developed for the case of single region homogeneous scatterers for the case of multi-region composite scatterers situated in the layered medium. The new SVS-EFIE is obtained through combination of its previous composite formulation for multi-region scatterers situated in free space [38, 39] and its mixed-potential formulation for homogeneous single-region scatterers situated in multilayered media [37]. The new formulation allows for analysis of the electromagnetic fields in composite multi-region objects with arbitrary orientation of the regions with respect to the layers of the dielectric medium.

In order to enable field analysis in the practical problems, previously developed acceleration scheme for MoM solution of the SVS-EFIE for composite objects based on \mathcal{H} -matrices [39] is extended to the case of multi-region objects in multilayered medium. It is shown that while the MoM mesh elements discretizing the surfaces and volumes of each region must not cross dielectric interfaces between the layers of the medium, the clusters in the hierarchical grouping of the elements taking place in the process of \mathcal{H} -matrix formation can span multiple layers and still produce highly compressible blocks in the \mathcal{H} -matrix. Such compressibility of the \mathcal{H} -matrix blocks was confirmed when the components of the dyadic Green's function of the multilayered medium used in the pertinent MoM interactions based on the Michalski-Zheng's mixed potential formulation were computed using DCIM [92, 93].

This paper is an expanded version of a conference paper presented at IEEE MTT-

S NEMO 2019, Cambridge, MA [94]. The proposed formulation is validated through numerical solution of a variety of scattering problems on multi-region objects situated in multilayered medium and their comparisons with the field computed using commercial MoM layered medium solver from Altair's FEKO software [72].

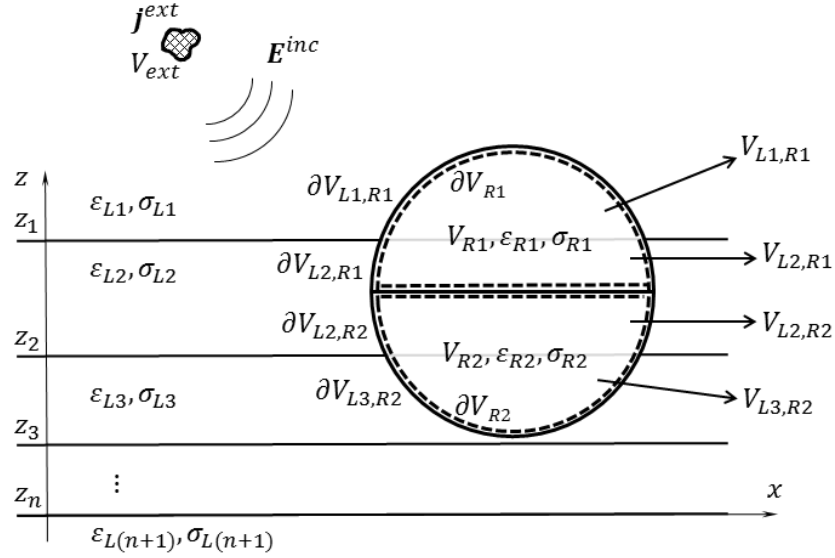


Figure 5.1: Radiation problem of extraneous currents \mathbf{j}^{ext} producing incident field \mathbf{E}^{inc} , which scatters on a 3-D composite dielectric object consisting of two regions with volumes V_{R1} and V_{R2} bounded by surfaces ∂V_{R1} and ∂V_{R2} , and having complex relative permittivities $\epsilon_{R1} = \epsilon_{R1} + \sigma_{R1}/(\omega\epsilon_0)$ and $\epsilon_{R2} = \epsilon_{R2} + \sigma_{R2}/(\omega\epsilon_0)$, respectively. The composite object is situated in general $(n + 1)$ -layer non-magnetic planar layered medium. The partial volumes $V_{L1,R1}$ and $V_{L2,R1}$ forming first region of the object V_{R1} and the partial surfaces $\partial V_{L1,R1}$ and $\partial V_{L2,R1}$ forming first region surface ∂V_{R1} denote parts of the first region confined to the first and second layers, respectively. Similarly, partial volumes $V_{L2,R2}$ and $V_{L3,R2}$ forming the second region of the object V_{R2} and the partial surfaces $\partial V_{L2,R2}$ and $\partial V_{L3,R2}$ forming the second region surface ∂V_{R2} denote parts of the objects confined to the second and third layers, respectively.

5.3 SVS-EFIE Formulation for Composite Dielectric Objects in Layered Media

Consider the scattering problem of a composite dielectric object consisting of two non-magnetic dielectric regions $R1$ and $R2$ with volumes V_{R1} and V_{R2} (subscript R is denoting region) situated in $(n + 1)$ -layer non-magnetic layered medium (Fig. 5.1). Using the volume equivalence principle [71], the time-harmonic electric field \mathbf{E}^p inside the p th layer can be written as

$$\begin{aligned} \mathbf{E}^p(\mathbf{r}) &= \mathbf{E}_p^{\text{inc}}(\mathbf{r}) \\ &+ k_0^2 \sum_{p'=1}^{n+1} (\epsilon_{R1} - \epsilon_{Lp'}) \int_{V_{Lp',R1}} \overline{\mathbf{G}}_{eb}^{pp'}(\mathbf{r}, \mathbf{r}') \cdot \mathbf{E}_{R1}^{p'}(\mathbf{r}') dv' \\ &+ k_0^2 \sum_{p'=1}^{n+1} (\epsilon_{R2} - \epsilon_{Lp'}) \int_{V_{Lp',R2}} \overline{\mathbf{G}}_{eb}^{pp'}(\mathbf{r}, \mathbf{r}') \cdot \mathbf{E}_{R2}^{p'}(\mathbf{r}') dv', \end{aligned} \quad (5.1)$$

$$\mathbf{r} \in V_{R1}, V_{R2}$$

where $\mathbf{E}_{R1}^{p'}$ is the electric field inside the volumes $V_{Lp',R1}$ (subscript L is denoting the layer) of the region $R1$ of the composite object situated in the p' th layer, $p' = 1, \dots, n + 1$. In (5.1), $\overline{\mathbf{G}}_{eb}^{pp'}$ is the multilayered media electric field dyadic Green's function

$$\overline{\mathbf{G}}_{eb}^{pp'}(\mathbf{r}, \mathbf{r}') = \overline{\mathbf{G}}_A^{pp'}(\mathbf{r}, \mathbf{r}') + \frac{1}{k_0^2 \epsilon_{Lp}} \nabla \nabla \cdot \overline{\mathbf{G}}_A^{pp'}(\mathbf{r}, \mathbf{r}') \quad (5.2)$$

and $\overline{\mathbf{G}}_A^{pp'}$ is the multilayered media magnetic vector potential dyadic Green's function [82]

$$\overline{\mathbf{G}}_A^{pp'} = (\hat{\mathbf{x}}\hat{\mathbf{x}} + \hat{\mathbf{y}}\hat{\mathbf{y}})G_{xx}^{pp'} + \hat{\mathbf{z}}\hat{\mathbf{x}}G_{zx}^{pp'} + \hat{\mathbf{z}}\hat{\mathbf{y}}G_{zy}^{pp'} + \hat{\mathbf{z}}\hat{\mathbf{z}}G_{zz}^{pp'} \quad (5.3)$$

with $k_0 = \omega\sqrt{\epsilon_0\mu_0}$ being the wave number of free space. The complex relative permittivity of the composite object regions is $\epsilon_{Rm} = \epsilon_{Rm} + \sigma_{Rm}/(i\omega\epsilon_0)$ with region index m ($m = 1, 2$). Also, the complex relative permittivity of the p th layer of the medium

is $\epsilon_{Lp} = \epsilon_{Lp} + \sigma_{Lp}/(\iota\omega\epsilon_0)$, $p = 1, \dots, n + 1$. The incident field $\mathbf{E}_p^{\text{inc}}$ in p th layer of the multilayered medium produced in the absence of the scatterer by the extraneous currents \mathbf{j}^{ext} confined to volume V^{ext} is defined as

$$\mathbf{E}_p^{\text{inc}}(\mathbf{r}) = -\iota\omega\mu_0 \sum_{p'=1}^{n+1} \int_{V^{\text{ext}}} \overline{\mathbf{G}}_{eb}^{pp'}(\mathbf{r}, \mathbf{r}') \cdot \mathbf{j}_{p'}^{\text{ext}}(\mathbf{r}') dv'. \quad (5.4)$$

Time factor $e^{-\iota\omega t}$ is suppressed throughout the paper.

The total electric field \mathbf{E}_{R1}^p inside the partial volume $V_{Lp,R1}$ of the dielectric region $R1$ can be written as a superposition of elementary waves $\overline{\mathbf{G}}_{e\epsilon_{R1}}(\mathbf{r}, \mathbf{r}')$ emanating from object boundary (a.k.a. single-source field representation) [14, 46], as

$$\mathbf{E}_{R1}^p(\mathbf{r}) = -\iota\omega\mu_0 \oint_{\partial V_{Lp,R1}} \overline{\mathbf{G}}_{e\epsilon_{R1}}(\mathbf{r}, \mathbf{r}') \cdot \mathbf{J}_1(\mathbf{r}') ds', \quad (5.5)$$

$$\mathbf{r} \in V_{Lp,R1} \setminus \partial V_{Lp,R1}$$

where $\overline{\mathbf{G}}_{e\epsilon_{R1}}(\mathbf{r}, \mathbf{r}') = (k_{\epsilon_{R1}}^{-2} \nabla \nabla + \overline{\mathbf{I}}) e^{-ik_{\epsilon_{R1}} |\mathbf{r} - \mathbf{r}'|} / (4\pi |\mathbf{r} - \mathbf{r}'|)$ is the electric field dyadic Green's function of homogeneous medium with permittivity ϵ_{R1} and $k_{\epsilon_{R1}} = k_0 \sqrt{\epsilon_{R1}}$ being its wavenumber. In (5.5), $\overline{\mathbf{I}}$ is the identity dyadic and \mathbf{J}_1 is the equivalent fictitious electric surface current density equal to the difference between the tangential component of the true magnetic field \mathbf{H}_{R1} inside the region $R1$ and undefined magnetic field \mathbf{H}_{R1}^{∞} outside of it, i.e. $\mathbf{J}_1 = \hat{\mathbf{n}}_1 \times [\mathbf{H}_{R1} - \mathbf{H}_{R1}^{\infty}]$. Similarly, the single source representation of the electric field \mathbf{E}_{R2}^p inside the partial volume $V_{Lp,R2}$ of the dielectric region $R2$ can be represented as (Fig. 5.1)

$$\mathbf{E}_{R2}^p(\mathbf{r}) = -\iota\omega\mu_0 \oint_{\partial V_{Lp,R2}} \overline{\mathbf{G}}_{e\epsilon_{R2}}(\mathbf{r}, \mathbf{r}') \cdot \mathbf{J}_2(\mathbf{r}') ds', \quad (5.6)$$

$$\mathbf{r} \in V_{Lp,R2} \setminus \partial V_{Lp,R2}$$

where $\mathbf{J}_2 = \hat{\mathbf{n}}_2 \times [\mathbf{H}_{R2} - \mathbf{H}_{R2}^{\infty}]$ is the fictitious electric surface current density defined on ∂V_2 .

The single-source field representations in (5.5) and (5.6) can be constrained through

their substitution into (5.1) and restriction of the observation point to the boundaries ∂V_{R1} and ∂V_{R2} while considering only tangential components of the electric field. This produces the following two coupled integral equations for the tangential component of the total electric field at the the boundaries ∂V_{R1} and ∂V_{R2}

$$\begin{aligned}
 & -\omega\mu_0\hat{\mathbf{t}}_1(\mathbf{r}) \cdot \oint_{\partial V_{Lp,R1}} \overline{\mathbf{G}}_{e\epsilon_{R1}}(\mathbf{r}, \mathbf{r}'') \cdot \mathbf{J}_1(\mathbf{r}'') ds'' \\
 & + \omega\mu_0 k_0^2 \sum_{p'=1}^{n+1} (\epsilon_{R1} - \epsilon_{Lp'}) \hat{\mathbf{t}}_1(\mathbf{r}) \cdot \int_{V_{Lp',R1}} \overline{\mathbf{G}}_{eb}^{pp'}(\mathbf{r}, \mathbf{r}') \\
 & \cdot \oint_{\partial V_{R1}} \overline{\mathbf{G}}_{e\epsilon_{R1}}(\mathbf{r}', \mathbf{r}'') \cdot \mathbf{J}_1(\mathbf{r}'') ds'' dv' \\
 & + \omega\mu_0 k_0^2 \sum_{p'=1}^{n+1} (\epsilon_{R2} - \epsilon_{Lp'}) \hat{\mathbf{t}}_1(\mathbf{r}) \cdot \int_{V_{Lp',R2}} \overline{\mathbf{G}}_{eb}^{pp'}(\mathbf{r}, \mathbf{r}') \\
 & \cdot \oint_{\partial V_{R2}} \overline{\mathbf{G}}_{e\epsilon_{R2}}(\mathbf{r}', \mathbf{r}'') \cdot \mathbf{J}_2(\mathbf{r}'') ds'' dv' \\
 & = \hat{\mathbf{t}}_1(\mathbf{r}) \cdot \mathbf{E}_p^{\text{inc}}(\mathbf{r}), \quad \mathbf{r} \in \partial V_{Lp,R1}
 \end{aligned} \tag{5.7}$$

and

$$\begin{aligned}
 & -\omega\mu_0\hat{\mathbf{t}}_2(\mathbf{r}) \cdot \oint_{\partial V_{Lp,R2}} \overline{\mathbf{G}}_{e\epsilon_{R2}}(\mathbf{r}, \mathbf{r}'') \cdot \mathbf{J}_2(\mathbf{r}'') ds'' \\
 & + \omega\mu_0 k_0^2 \sum_{p'=1}^{n+1} (\epsilon_{R1} - \epsilon_{Lp'}) \hat{\mathbf{t}}_2(\mathbf{r}) \cdot \int_{V_{Lp',R1}} \overline{\mathbf{G}}_{eb}^{pp'}(\mathbf{r}, \mathbf{r}') \\
 & \cdot \oint_{\partial V_{R1}} \overline{\mathbf{G}}_{e\epsilon_{R1}}(\mathbf{r}', \mathbf{r}'') \cdot \mathbf{J}_1(\mathbf{r}'') ds'' dv' \\
 & + \omega\mu_0 k_0^2 \sum_{p'=1}^{n+1} (\epsilon_{R2} - \epsilon_{Lp'}) \hat{\mathbf{t}}_2(\mathbf{r}) \cdot \int_{V_{Lp',R2}} \overline{\mathbf{G}}_{eb}^{pp'}(\mathbf{r}, \mathbf{r}') \\
 & \cdot \oint_{\partial V_{R2}} \overline{\mathbf{G}}_{e\epsilon_{R2}}(\mathbf{r}', \mathbf{r}'') \cdot \mathbf{J}_2(\mathbf{r}'') ds'' dv' \\
 & = \hat{\mathbf{t}}_2(\mathbf{r}) \cdot \mathbf{E}_p^{\text{inc}}(\mathbf{r}), \quad \mathbf{r} \in \partial V_{Lp,R2}
 \end{aligned} \tag{5.8}$$

$$\begin{array}{c}
 \begin{array}{|c|c|}
 \hline
 \overbrace{I_{R1} \quad I_{R2}}^I \\
 \hline
 \overline{\overline{\mathcal{T}}}_{\epsilon_{R1}}^{\partial V_{R1}, \partial V_{R1}} & \mathbf{0} \\
 \hline
 \mathbf{0} & \overline{\overline{\mathcal{T}}}_{\epsilon_{R2}}^{\partial V_{R2}, \partial V_{R2}} \\
 \hline
 \underbrace{\hspace{10em}}_{\mathbf{Z}_\epsilon^{\partial V, \partial V}}
 \end{array}
 +
 \begin{array}{|c|c|c|c|}
 \hline
 \overbrace{N_{L1,R1} \quad N_{L2,R1} \quad N_{L2,R2} \quad N_{L3,R2}}^{N_{R1} \quad N_{R2}} \\
 \hline
 \alpha_{1,1} \overline{\overline{\mathcal{T}}}_{p1}^{\partial V_{R1}, V_{L1,R1}} & \alpha_{1,2} \overline{\overline{\mathcal{T}}}_{p2}^{\partial V_{R1}, V_{L2,R1}} & \alpha_{2,2} \overline{\overline{\mathcal{T}}}_{p2}^{\partial V_{R1}, V_{L2,R2}} & \alpha_{2,3} \overline{\overline{\mathcal{T}}}_{p3}^{\partial V_{R1}, V_{L3,R2}} \\
 \hline
 \alpha_{1,1} \overline{\overline{\mathcal{T}}}_{p1}^{\partial V_{R2}, V_{L1,R1}} & \alpha_{1,2} \overline{\overline{\mathcal{T}}}_{p2}^{\partial V_{R2}, V_{L2,R1}} & \alpha_{2,2} \overline{\overline{\mathcal{T}}}_{p2}^{\partial V_{R2}, V_{L2,R2}} & \alpha_{2,3} \overline{\overline{\mathcal{T}}}_{p3}^{\partial V_{R2}, V_{L3,R2}} \\
 \hline
 \underbrace{\hspace{10em}}_{\mathbf{Z}_p^{\partial V, V}}
 \end{array}
 \cdot
 \begin{array}{|c|c|}
 \hline
 \overbrace{I_{R1} \quad I_{R2}}^I \\
 \hline
 \overline{\overline{\mathcal{T}}}_{\epsilon_{R1}}^{V_{L1,R1}, \partial V_{R1}} & \mathbf{0} \\
 \hline
 \overline{\overline{\mathcal{T}}}_{\epsilon_{R1}}^{V_{L2,R1}, \partial V_{R1}} & \mathbf{0} \\
 \hline
 \mathbf{0} & \overline{\overline{\mathcal{T}}}_{\epsilon_{R2}}^{V_{L2,R2}, \partial V_{R2}} \\
 \hline
 \mathbf{0} & \overline{\overline{\mathcal{T}}}_{\epsilon_{R2}}^{V_{L3,R2}, \partial V_{R2}} \\
 \hline
 \underbrace{\hspace{10em}}_{\mathbf{Z}_\epsilon^{V, \partial V}}
 \end{array}
 \end{array}$$

Figure 5.2: Matrix structure resulting from MoM discretization of the SVS-EFIE formulation (5.9) for a generic two-region composite dielectric objects situated in layered media Fig. 5.1. The number of RWG functions on the boundaries ∂V_{R1} and ∂V_{R2} are I_{R1} and I_{R2} , respectively, with $I = I_{R1} + I_{R2}$ being the total number of RWG basis functions. The number of tetrahedron elements in the dielectrics with volumes V_{R1} and V_{R2} are N_{R1} and N_{R2} , respectively. The total number of tetrahedron elements in the models is $N = N_{R1} + N_{R2}$. Also, $N_{L1,R1}$ and $N_{L2,R1}$ are the number of tetrahedrons of parts of the region $R1$ confined to the first and second layers, respectively. Similarly, $N_{L2,R2}$ and $N_{L3,R2}$ are the number of tetrahedrons of parts of the region $R2$ confined to the second and third layers, respectively, with $N_{R2} = N_{L2,R2} + N_{L3,R2}$. Coefficients $\alpha_{m,p'}$ in the MoM matrix corresponding to the volume-to-surface operator are equal to $k_0^2(\epsilon_{Rm} - \epsilon_{Lp'})$ (see formulation (5.9)).

where index $p = 1, \dots, n+1$ denotes observation layer index, $\hat{\mathbf{t}}_m$ is the tangential vector to the surface ∂V_m , $m = 1, 2$. Note that even though the index p of the observation layer runs from 1 to $n+1$, the equations (5.7) and (5.8) are only enforced in the layers containing parts of the object regions $V_{Lp,R1}$ and $V_{Lp,R2}$. The new formulations (5.7) and (5.8) are two coupled SVS-EFIEs for two-region composite dielectric objects in layered media with respect to two unknown functions \mathbf{J}_1 and \mathbf{J}_2 .

The above SVS-EFIE formulation can be generalized for a composite scatterer consisting of arbitrary number of dielectric regions in a straightforward manner. Coupled

equations (5.7) and (5.8) can be expressed in a concise form by introducing notations for integral operators, as follows:

$$\begin{aligned}
 & -\overline{\overline{\mathcal{T}}}_{\epsilon_{R\ell}}^{\partial V_{R\ell}, \partial V_{R\ell}} \circ \mathbf{J}_\ell + k_0^2 \sum_{m=1}^2 \sum_{p'=1}^{n+1} (\epsilon_{Rm} - \epsilon_{Lp'}) \overline{\overline{\mathcal{T}}}_{pp'}^{\partial V_{R\ell}, V_{Lp'}, Rm} \\
 & \circ \overline{\overline{\mathcal{T}}}_{\epsilon_{R\ell}}^{V_{Rm}, \partial V_{Rm}} \circ \mathbf{J}_m = \hat{\mathbf{t}}_\ell \cdot \mathbf{E}_p^{\text{inc}}(\mathbf{r}), \quad \mathbf{r} \in \partial V_{R\ell}, \quad \ell = 1, 2
 \end{aligned} \tag{5.9}$$

where operators $\overline{\overline{\mathcal{T}}}_{\epsilon}^{\partial V, \partial V}$, $\overline{\overline{\mathcal{T}}}_{pp'}^{\partial V, V}$, and $\overline{\overline{\mathcal{T}}}_{\epsilon}^{V, \partial V}$ are known as surface-to-surface, volume-to-surface, and surface-to-volume, respectively, and are composed as a sum of two integral operators corresponding to the scalar and vector potentials as detailed in [13, 37].

The MoM discretization of the integral operators in (5.9) is described in detail in [37]. For the case of two-region dielectric composite object (Fig. 5.1) the MoM discretization of SVS-EFIE yields a system of linear equations with structure shown in Fig. 5.2 with I_{R1} and I_{R2} being the number of Rao-Wilton-Glisson (RWG) basis functions defined on the surface of the region $R1$ and $R2$, respectively. In the matrix equation in Fig. 5.2, N_{R1} and N_{R2} are the number of tetrahedrons in the volumes V_{R1} and V_{R2} , respectively. The MoM impedance matrices $Z_{\epsilon}^{\partial V, \partial V}$, $\mathbf{Z}_p^{\partial V, V}$, and $\mathbf{Z}_{\epsilon}^{V, \partial V}$ correspond to the operators $\overline{\overline{\mathcal{T}}}_{\epsilon}^{\partial V, \partial V}$, $\overline{\overline{\mathcal{T}}}_p^{\partial V, V}$, and $\overline{\overline{\mathcal{T}}}_{\epsilon}^{V, \partial V}$, respectively. The MoM matrix structure in Fig. 5.2 reflects on the discretization strategy for the composite dielectric objects, which does not allow the surface and volume mesh elements to cross dielectric interfaces between the layers of the background medium.

5.4 \mathcal{H} -matrix-Based Fast Direct MoM Solution of the Proposed SVS-EFIE

The strategy for \mathcal{H} -matrix acceleration of MoM solution of the SVS-EFIE for composite objects was developed in [35, 39]. It was observed that blocks of MoM matrix corresponding to well-separated clusters of the basis and test functions situated in multilayered medium remain well compressible whether they straddle multiple lay-

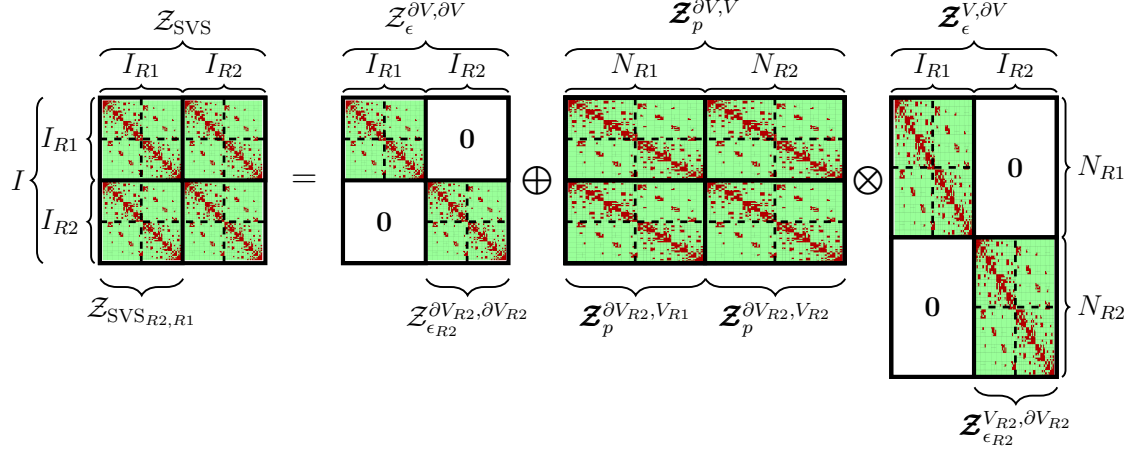


Figure 5.3: \mathcal{H} -matrix structure of the MoM discretization of the proposed solver for a generic two-region composite dielectric objects situated in layered media of Fig. 5.1. Green blocks represent the admissible blocks, which are compressed using ACA algorithm. The red blocks represent the inadmissible blocks. Creation of the final \mathcal{Z}_{SVS} MoM \mathcal{H} -matrix using formatted multiplication and addition [39] is required for fast block \mathcal{H} -LU based direct solution of the matrix equation. Symbols \otimes and \oplus denote operations of formatted multiplication and addition. Dashed lines represent the pertinent \mathcal{H} -matrix blocks for clustering of the regions corresponding to the strategy honouring the structure of the layers of the medium. In such strategy the clusters of elements are not allowed to straddle the dielectric interfaces of the layers. However, in this work we adopt the strategy of mesh elements clustering such that groups of elements are formed regardless of the structure of the layers of the medium (i.e. the clusters can straddle the interfaces between the layers) as it is done in the case of composite scatterers situated in free space [39]. The actual \mathcal{H} -matrix blocks introduced according to the clustering strategy adopted in this work are represented with solid lines.

ers or not. Such compressibility is observed when ACA tolerance is set to be above the error level associated with the error occurring during numerical evaluation of the layered medium Green's function values, interpolation from them, and in quadrature based evaluation of MoM reaction integrals. Numerical experiments supporting this observation were conducted on MoM matrix blocks of RWG test and basis functions interacting via layered medium Green's function computed with DCIM [92], and stored in the databases covering required intervals over z , z' , and ρ coordinates

of the cylindrical system [95]. Values of the Green's function components required by MoM integrals are interpolated from the precomputed database values using 3D linear interpolation [96] from the values for predefined z , z' , and ρ samples. Due to compressibility of the MoM matrix blocks corresponding to the clusters straddling multiple layers of the medium, the strategy for creation of the \mathcal{H} -matrices for composite objects in layered medium is the same as for those located in free space [39]. Namely, the RWG basis/testing functions defined on the surface of the regions and the piecewise basis/testing functions on the tetrahedrons inside the volume of the regions are partitioned into separate multi-level cluster trees regardless of their structure with respect to the structure of the layers of the medium. Alternative clustering strategy considering the structure of layers in the process of forming the blocks of the surface and volume cluster trees can be introduced instead. In this case, clusters are created strictly to be confined to the individual layers with straddling of the clusters across layers prohibited. Though viable, such strategy increases the number of clusters and, hence, sophistication of the algorithm. Through various numerical experiments it was observed that the \mathcal{H} -matrix blocks preserve their compressibility regardless of whether the clusters straddle dielectric interfaces or not. For that reason the simple clustering strategy disregarding dielectric interfaces is adopted. Hence, for the case of two region composite object in Fig. 5.1, two sets of cluster trees $\{T_{\partial V_{R1}}, T_{V_{R1}}\}$ and $\{T_{\partial V_{R2}}, T_{V_{R2}}\}$ are generated for regions $R1$ and $R2$ without consideration of the layered medium, respectively. Here, $T_{\partial V}$ and T_V denote the surface and volume cluster trees. As an example, to create the surface cluster tree $T_{\partial V_{R1}}$ the full index set of RWG basis/testing functions $\mathcal{I}_{\partial V_{R1}} = \{1, 2, \dots, I_{R1}\}$ (I_{R1} being the total number of RWG functions of region $R1$) is bisectioned recursively until the number of degrees of freedom (DoF) in each cluster of the tree becomes less than the predefined \mathcal{H} -matrix parameter *leafsize* n_{\min} . The volume cluster tree $T_{V_{R1}}$ is created through recursive bisection of the full piecewise basis/testing functions set $\mathcal{I}_{V_{R1}} = \{1, 2, \dots, N_{R1}\}$, where N_{R1} is the total number of tetrahedrons inside the region $R1$. The *leafsize* parameter n_{\min} controlling the number of basis functions in the leaf level can be different for surface and volume cluster trees.

After construction of the cluster trees, approximation of the MoM matrices re-

sulting from discretization of the integral operators in Fig. 5.2 with \mathcal{H} -matrices is performed. After choosing the appropriate observer and source cluster trees for a particular integral operator, we classify the interactions between their clusters into admissible and inadmissible. The process is started with taking the root clusters of the trees and checking, if their interactions meet the following criteria

$$\min\{\text{diam}(\mathcal{B}_{\text{obs}}), \text{diam}(\mathcal{B}_{\text{src}})\} \leq \eta \text{dist}(\mathcal{B}_{\text{obs}}, \mathcal{B}_{\text{src}}). \quad (5.10)$$

The checking continues recursively down the source and observer cluster trees level by level. If condition (5.10) is met for a given source and observer clusters, their corresponding interaction block in \mathcal{H} -matrix is considered admissible. Otherwise, the \mathcal{H} -matrix block is inadmissible. In (5.10), $\text{diam}(\cdot)$ and $\text{dist}(\cdot, \cdot)$ denote the Euclidean diameter and minimum distance between the observer bounding box \mathcal{B}_{obs} and the source bounding box \mathcal{B}_{src} , respectively. Also, η is the predefined positive real parameter controlling how far the source and observer blocks have to be before they may be considered admissible.

The admissible blocks are rank deficient and stored in compressed form, which can be obtained efficiently using the adaptive cross approximation (ACA) [23, 24], the hybrid cross-approximation (HCA) [36], [69], or naively using the singular value decomposition (SVD) [78]. In this work the ACA algorithm is used.

Inadmissible blocks are computed directly with the conventional MoM and stored as full matrices. The \mathcal{H} -matrix structure corresponding to matrix of the conventional MoM (Fig. 5.2) is shown in Fig. 5.3. In Fig. 5.3, \mathcal{H} -matrices $\mathcal{Z}_\epsilon^{\partial V, \partial V}$, $\mathcal{Z}_p^{\partial V, V}$, and $\mathcal{Z}_\epsilon^{V, \partial V}$ correspond to MoM matrices $Z_\epsilon^{\partial V, \partial V}$, $Z_p^{\partial V, V}$, and $Z_\epsilon^{V, \partial V}$, respectively. The structure of the \mathcal{H} -matrix in Fig. 5.1 reflects on the adopted strategy for creation of the cluster tree, which disregards the structure of the layered medium. Specifically, the matrix blocks corresponding to the groups of sources and observers confined to individual layers are outlined with dashed lines, while the solid lines in Fig. 5.3 outline the actual computed \mathcal{H} -matrix blocks.

To enable fast direct solution of the proposed SVS-EFIE using \mathcal{H} -LU decomposition and back-substitution, the final \mathcal{H} -matrix \mathcal{Z}_{SVS} must be constructed using

formatted multiplication and addition first as (Fig. 5.3)

$$\begin{aligned} \mathcal{Z}_{\text{SVS}} &= \begin{bmatrix} \mathcal{Z}_{\text{SVS}_{R1,R1}} & \mathcal{Z}_{\text{SVS}_{R1,R2}} \\ \mathcal{Z}_{\text{SVS}_{R2,R1}} & \mathcal{Z}_{\text{SVS}_{R2,R2}} \end{bmatrix} = \begin{bmatrix} \mathcal{Z}_{\epsilon_{R2}}^{\partial V_{R1}, \partial V_{R1}} & 0 \\ 0 & \mathcal{Z}_{\epsilon_{R2}}^{\partial V_{R2}, \partial V_{R2}} \end{bmatrix} \\ &\oplus \begin{bmatrix} \mathcal{Z}_p^{\partial V_{R1}, V_{R1}} & \mathcal{Z}_p^{\partial V_{R1}, V_{R2}} \\ \mathcal{Z}_p^{\partial V_{R2}, V_{R1}} & \mathcal{Z}_p^{\partial V_{R2}, V_{R2}} \end{bmatrix} \otimes \begin{bmatrix} \mathcal{Z}_{\epsilon_{R1}}^{V_{R1}, \partial V_{R1}} & 0 \\ 0 & \mathcal{Z}_{\epsilon_{R2}}^{V_{R2}, \partial V_{R2}} \end{bmatrix}. \end{aligned} \quad (5.11)$$

Next, block \mathcal{H} -LU decomposition of the \mathcal{H} -matrix \mathcal{Z}_{SVS} is performed and the sought vector of current expansion coefficients in MoM discretization is computed via back-substitution. Detailed implementation of the block \mathcal{H} -LU algorithm for \mathcal{H} -matrix of the SVS-EFIE formulation for the composite dielectric objects in free space is described in [39]). Due to the fact that clusters of basis and test functions can straddle multiple layers, the \mathcal{H} -LU decomposition in the proposed SVS-EFIE formulation for multi-region objects situated in multi-layered medium remains unchanged.

The memory and time complexity of the proposed method is studied in the numerical results section.

5.5 Numerical Results

In order to validate the proposed new SVS-EFIE formulation for composite dielectric objects in layered medium, we solved the dipole radiation problems in the presence of different composite objects and compared solutions with the FEKO commercial MoM layered media solver. The \mathcal{H} -matrix parameters are chosen empirically to provide optimal performance for the chosen numerical examples. These values are $\eta = \{3, 4, 5\}$ and $n_{\min} = \{16, 32, 64\}$. The numerical experiments in [35, 39] demonstrated that \mathcal{H} -matrix accelerated low-order MoM solution of the SVS-EFIE does not produce any substantial increase in overall accuracy of the solutions in comparison to the direct MoM solver, when the truncation tolerance τ of the ACA algorithm is taken below 10^{-3} . This is because the error of MoM discretization and its pertinent operations produce the error above the levels set by $\tau = 10^{-3}$. For that reason, the truncation tolerances of the ACA algorithm below $\tau = 10^{-3}$ level are not considered

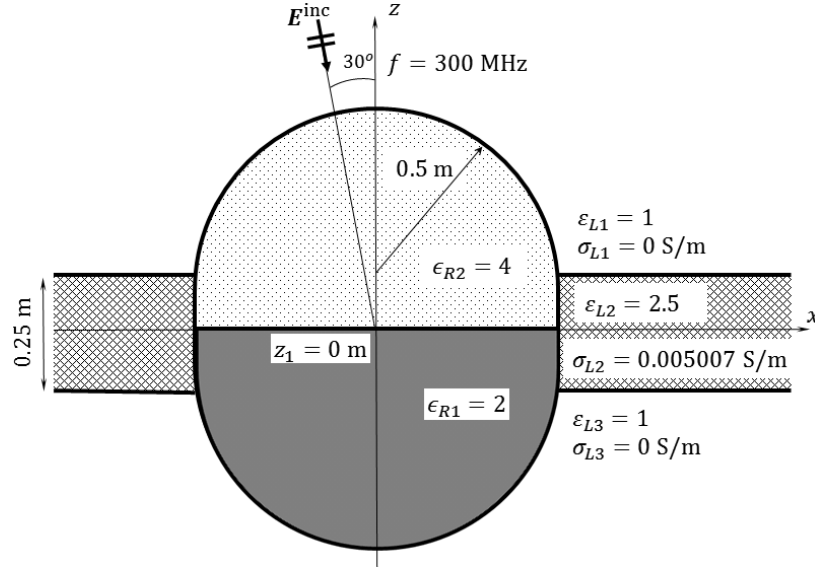


Figure 5.4: Depiction of a composite dielectric bifurcated capsule with 0.5 m radius and 0.25 m height is embedded in the three layer medium. Complex relative permittivity of the objects are $\epsilon_{R1} = 2$ and $\epsilon_{R2} = 4$. The model is excited by a electric dipole.

in this work. The truncation tolerance of the ACA algorithm is $\tau = 10^{-3}$. All numerical results presented in this section are obtained using a single Intel Xeon X5650 Processor running with a single core at 2.66 GHz.

5.5.1 Dielectric Bifurcated Capsule

For the first example, we consider a scattering problem on a lossless dielectric two-region capsule with the relative permittivity of the top and bottom regions equal to $\epsilon_{R2} = 4$ and $\epsilon_{R1} = 2$, respectively. The model is centered at the origin with radius of the spherical caps being 0.5 m and vertical displacement of the spherical caps centers from the origin being 0.125 m and buried in the three layer medium shown in Fig. 5.4. The top and bottom layers are made of air. The middle layer has relative permittivity of 2.5 and conductivity 0.005007 S/m. The incident field is produced by a electric dipole with moment $I \cdot \ell = 1 [\text{A} \cdot \text{m}]$, which operates at 300 MHz. The dipole orientation is $\hat{\mathbf{I}} = 0.866\hat{\mathbf{x}} + 0.5\hat{\mathbf{z}}$. It is located in the far zone at $\mathcal{R} = 10^6\lambda_0$,

λ_0 being the wavelength of the free space, $\theta = 30^\circ$, $\phi = 180^\circ$ in spherical coordinates originated at the center of the bifurcated capsule.

The magnitude of the total electric field inside the bifurcated capsule computed via the proposed solver is shown in Fig. 5.5. The surface and volume of each region of the object are discretized with the meshes having the same characteristic length resulting in $I = 24,087$ RWG functions and $N = 118,326$ tetrahedrons, respectively. The proposed formulation is validated using the Altair's FEKO MoM layered medium solver by computing the magnitude of the total electric field. The field is sampled on the observation lines, which are collinear with x -, y -, and z -axis and go through the object's volume as $(-0.45 \leq x \leq 0.45, y = 0.0, z = -0.325)$ m, $(x = 0.0, -0.45 \leq y \leq 0.45, z = -0.325)$ m and $(x = 0.0, y = 0.0, -0.625 \leq z \leq 0.625)$ m. The magnitude of the electric field along the observation lines is plotted in Fig. 5.5 for both the proposed SVS-EFIE formulation and FEKO's layered medium solver. Faster variation in standing wave pattern in the upper region of the capsule is observed along z -axis due to its higher electrical size than in its lower region. The discontinuity at $z = 0$ is observed in the magnitude of the electric field due to discontinuity in the permittivity of the regions. In order to present the impact of the layered media on the field distribution, the radiation problem of the same bifurcated capsule model is solved in free space using the SVS-EFIE [39] and FEKO's MoM solver. The results for solution of the radiation problem in free space are depicted in Fig. 5.5.

Next, the complexity performance of the proposed solver is examined for both \mathcal{H} -matrix accelerated and naïve MoM solution of the proposed SVS-EFIE solution for the bifurcated capsule model. In Fig. 5.6, memory requirements and CPU time complexity are depicted with respect to the number of surface unknowns I . In the capsule model, the number of tetrahedrons is discretized with $N = I^{1.1}$ ($\alpha = 1.1$). As shown in Fig. 5.6, the complexity of the \mathcal{H} -matrix accelerated MoM solution of the layered medium SVS-EFIE closely matches theoretically predicted scaling of the \mathcal{H} -matrix accelerated MoM solution of the free space SVS-EFIE in [39] with memory complexity close to $\mathcal{O}(I^\alpha \log I)$, matrix fill time complexity of $\mathcal{O}(I^\alpha \log I)$, and solution time complexity of $\mathcal{O}(I^\alpha \log^2 I)$.

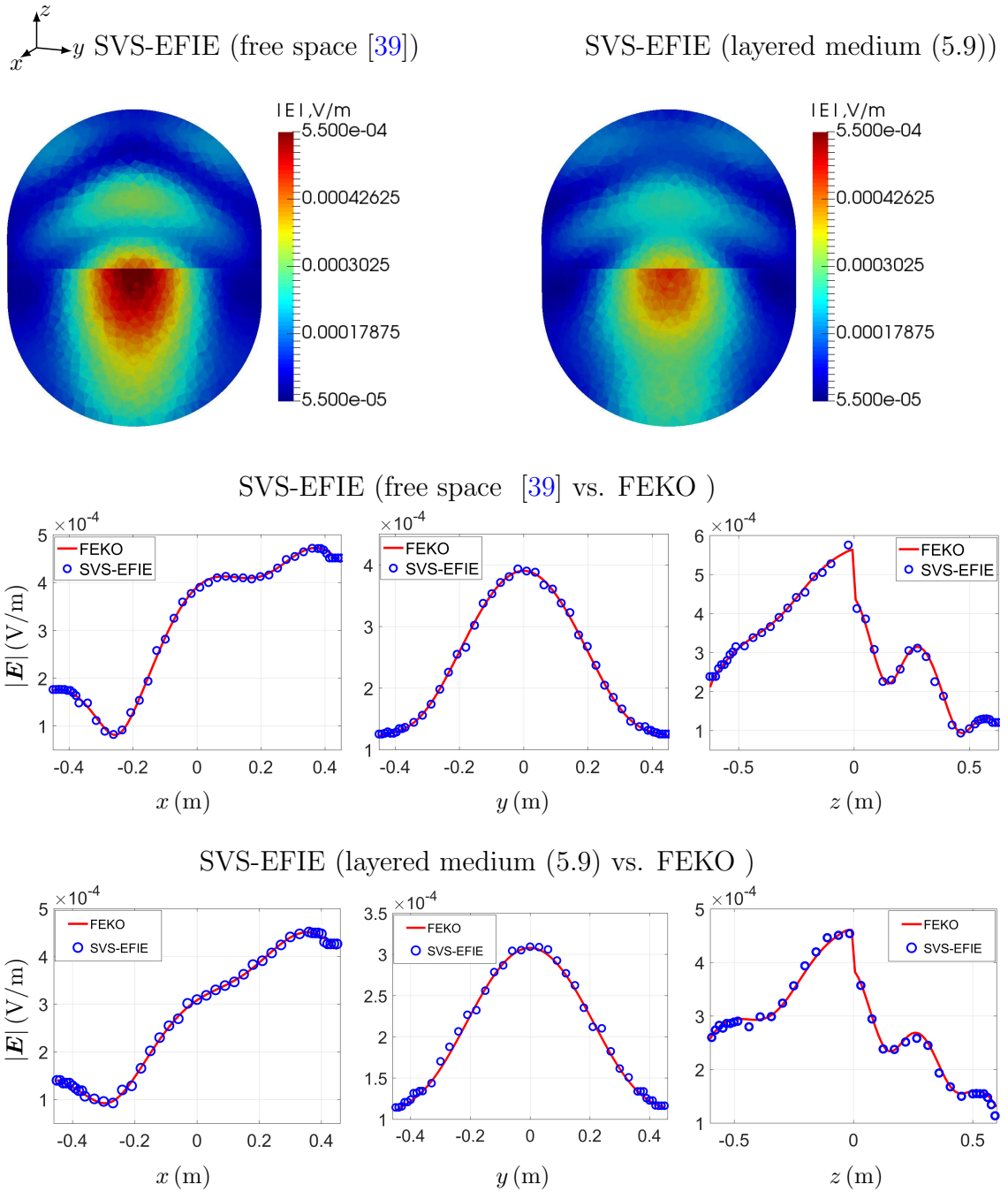


Figure 5.5: Magnitude of the total electric field inside the dielectric bifurcated capsule for object in free space (top) and object buried in the layered media (bottom) for the problem in Fig. 5.4. The field distribution inside the object obtained by the free space SVS-EFIE formulation [39] and SVS-EFIE layered media formulation (5.9) are shown in the left. Also, the fields inside the object with observation lines at $(-0.45 \leq x \leq 0.45, y = 0.0, z = -0.325)$ m, $(x = 0.0, -0.45 \leq y \leq 0.45, z = -0.325)$ m and $(x = 0.0, y = 0.0, -0.0625 \leq z \leq 0.0625)$ m obtained by the SVS-EFIE and FEKO are shown in the right for comparison.

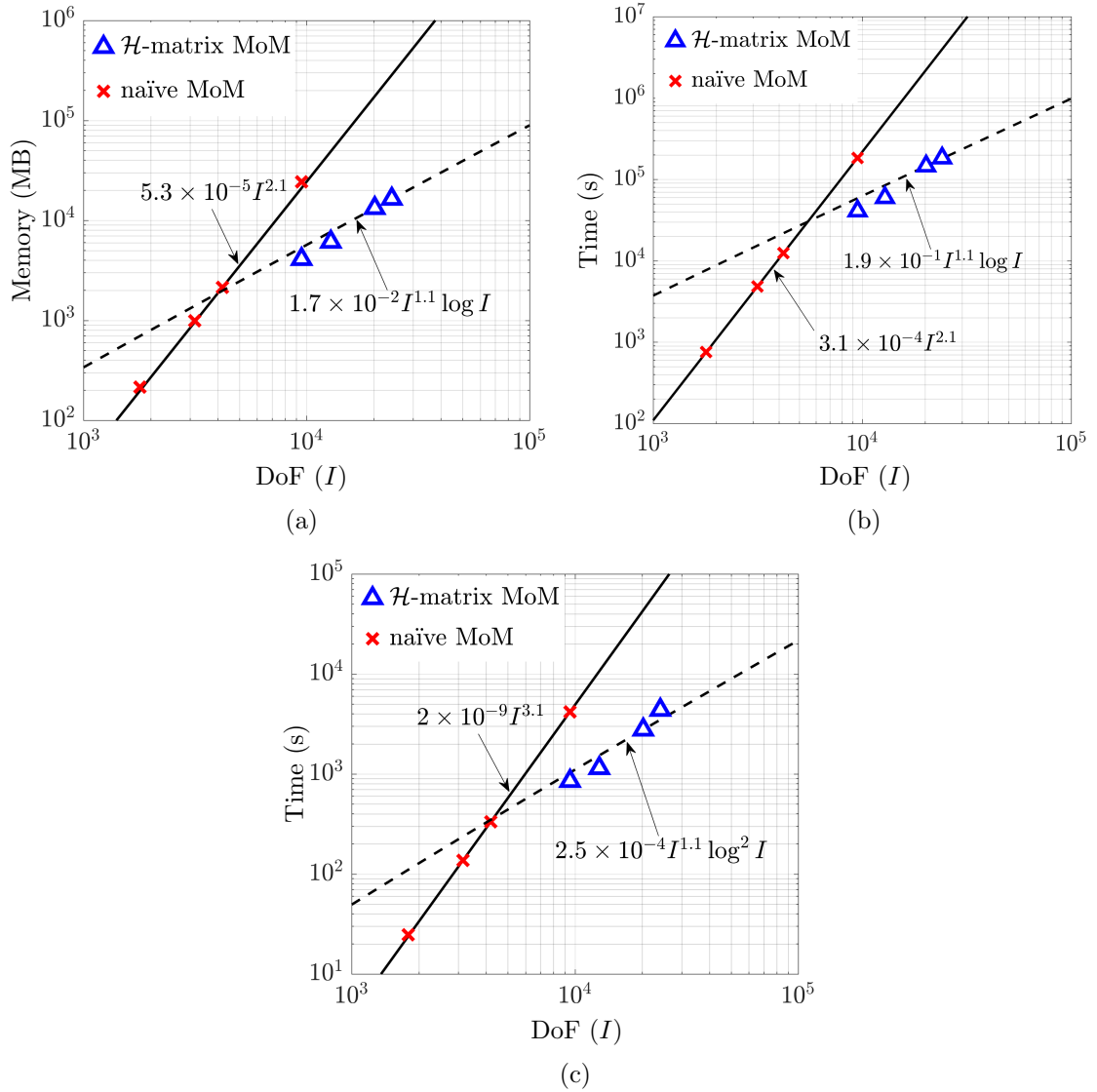


Figure 5.6: Memory cost and CPU time complexity of both \mathcal{H} -matrix (dashed lines) and naïve (solid lines) MoM discretization of SVS-EFIE for the scattering problem of the bifurcated capsule model buried in layered medium. (a) Memory. (b) Fill time. (c) Direct solve time (including of creation of final \mathcal{Z}_{SVS} , block \mathcal{H} -LU decomposition, and block \mathcal{H} -substitution).

5.5.2 Dielectric Coated Sphere

In the second example, we consider lossless two-layer spherical layered medium embedded into three-layer planar layered medium. The coated sphere has 0.15 m

radius of the inner layer, 0.25 m radius of the outer layer, and is centered at the origin. The inner sphere has relative permittivity $\epsilon_{R1} = 5$ and the outer shell has relative permittivity $\epsilon_{R2} = 3$. As shown in Fig. 5.7, the model is buried into a three-layer planar medium with top layer made of air, middle layer with 0.4 m thickness and relative permittivity and conductivity of $\epsilon_{L2} = 4.0$ and $\sigma_{L2} = 0.01$ S/m, and bottom layer with relative permittivity and conductivity of $\epsilon_{L3} = 10.0$ and $\sigma_{L3} = 0.01$ S/m. The model is excited by the electric dipole of the same orientation and location as the dipole in the first numerical example. The surface and volume of each spherical region of the object are discretized with the meshes having the same characteristic length of triangle and tetrahedral elements resulting in $I = 29,022$ and $N = 107,485$ RWG functions and tetrahedrons, respectively. The Green's function components of the coated sphere problem at $\rho = 0.035$ m and $\rho = 0.69$ m from four databases [95] used to compute the Green's function components K_{xx}^A , K_{xz}^A , K_{yz}^A , K_{zz}^A and K_ϕ (detailed in [37], [95]) are depicted in Fig 5.8. The magnitude of the total electric field along the x , y , and z axes inside the object obtained using the proposed SVS-EFIE formulation and FEKO is depicted in Fig. 5.9. In order to show the impact on the field distribution from the layered media, the radiation problem for the same coated sphere in free space is solved. The field distribution is obtained by the SVS-EFIE free space formulation in [39] and depicted in Fig. 5.9. The field computed using FEKO MoM solver is provided for reference.

The memory usage and CPU time performance of the \mathcal{H} -matrix accelerated SVS-EFIE solution for the coated sphere model buried in the layered medium is depicted in Fig. 5.10 with respect to the number of surface unknowns I and compared to its predicted scaling under assumption of $N = I^{1.1}$ ($\alpha = 1.1$).

5.5.3 Rough Surface of Composite Snow Sea-Ice Model

In the third example, we consider the scattering problem on the rough surface of the snow (region 1) covered sea-ice (region 2), which forms a piece-wise homogeneous composite object in multilayered medium. The model is positioned above the layer of the sea-ice (layer 2) and the layer of the sea water (layer 3) as shown in Fig. 5.11.

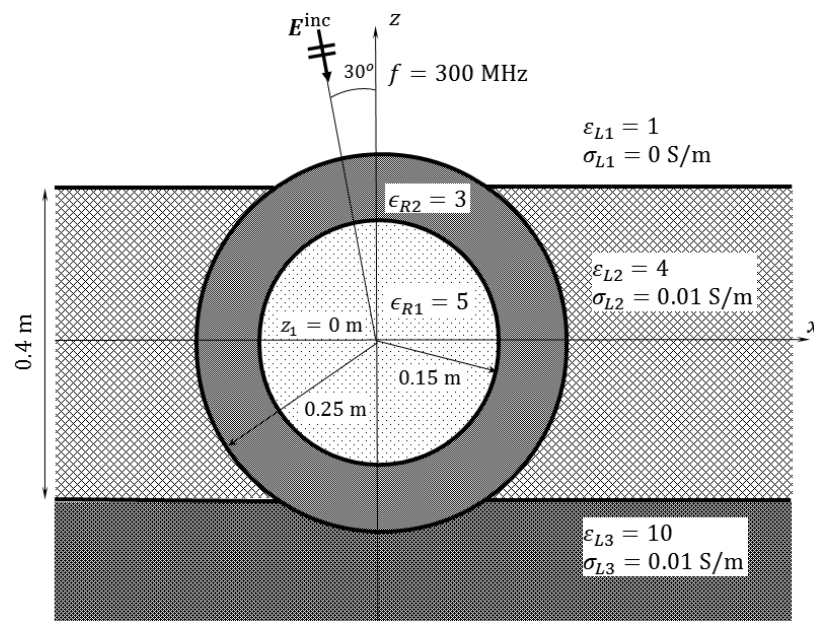


Figure 5.7: Depiction of a coated sphere with inner radius of 0.15 m and outer radius of 0.25 m embedded in three layer medium. Complex relative permittivity of the regions are $\epsilon_{R1} = 5$ and $\epsilon_{R2} = 3$ for inner and outer spheres, respectively. The model is excited by electric dipole located in far zone.

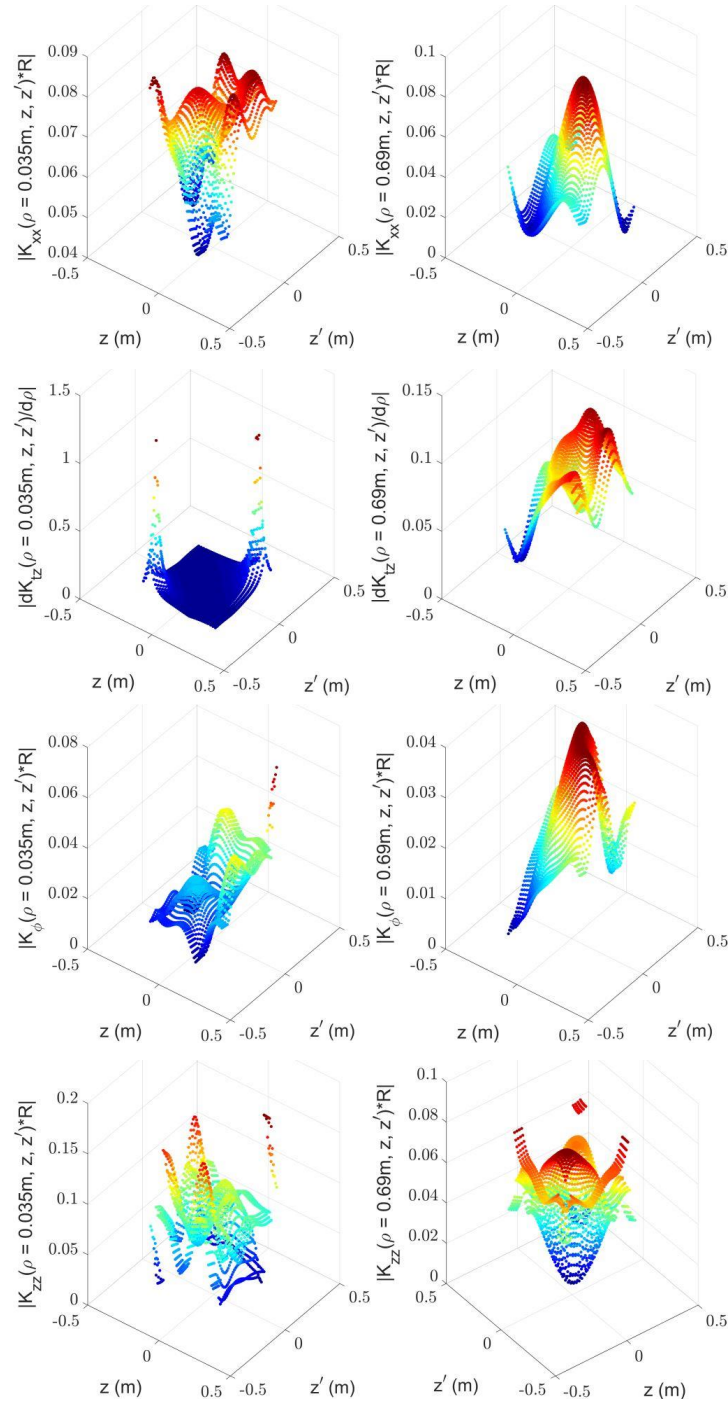


Figure 5.8: Visualization of the Green's function component in mixed-potential Michalski-Zheng's formulation used in MoM solution of SVS-EFIE at 300MHz for 2-layer sphere buried in 3-layer medium (Fig. 5.7). The Green's function data at $\rho = 0.035\text{ m}$ and $\rho = 0.69\text{ m}$ from four databases used to compute the Green's function components K_{xx}^A , K_{xz}^A , K_{yz}^A , K_{zz}^A and K_ϕ , where K_{xz}^A can be evaluated as $\iota \cos(\phi) \partial K_{tz} / \partial \rho$, and K_{yz}^A can be evaluated as $\iota \sin(\phi) \partial K_{tz} / \partial \rho$.

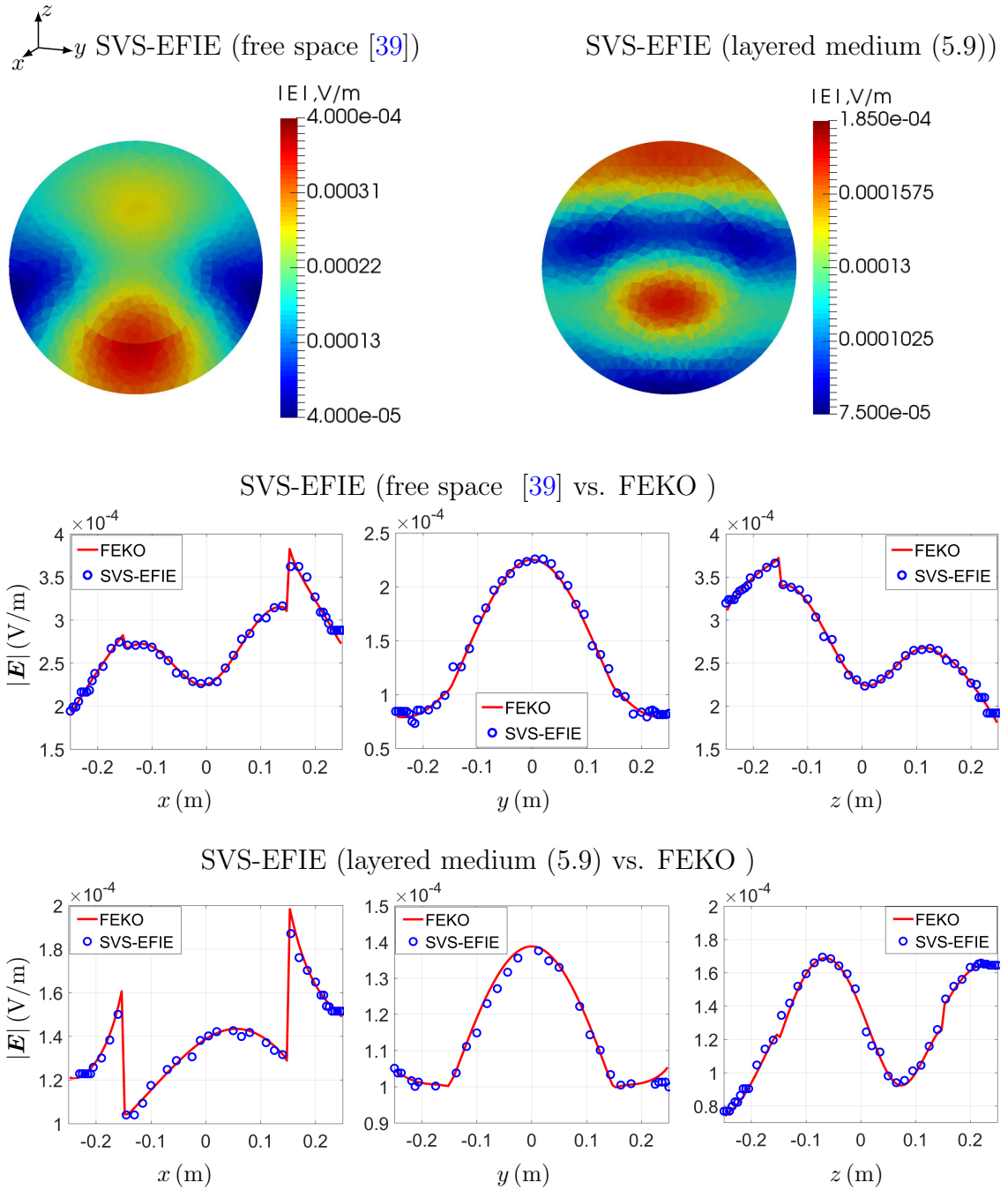


Figure 5.9: Magnitude of the total electric field inside the dielectric coated sphere situated in free space (top) and situated in the layered media (bottom) for the problem in Fig. 5.7 at 300MHz. The field distribution inside the object obtained by the free space SVS-EFIE formulation [39] and SVS-EFIE layered media formulation (5.9) is shown in the left. Also, the fields inside the object with observation lines along x , y , and z axis obtained by the SVS-EFIE and FEKO are shown in the right for comparison.

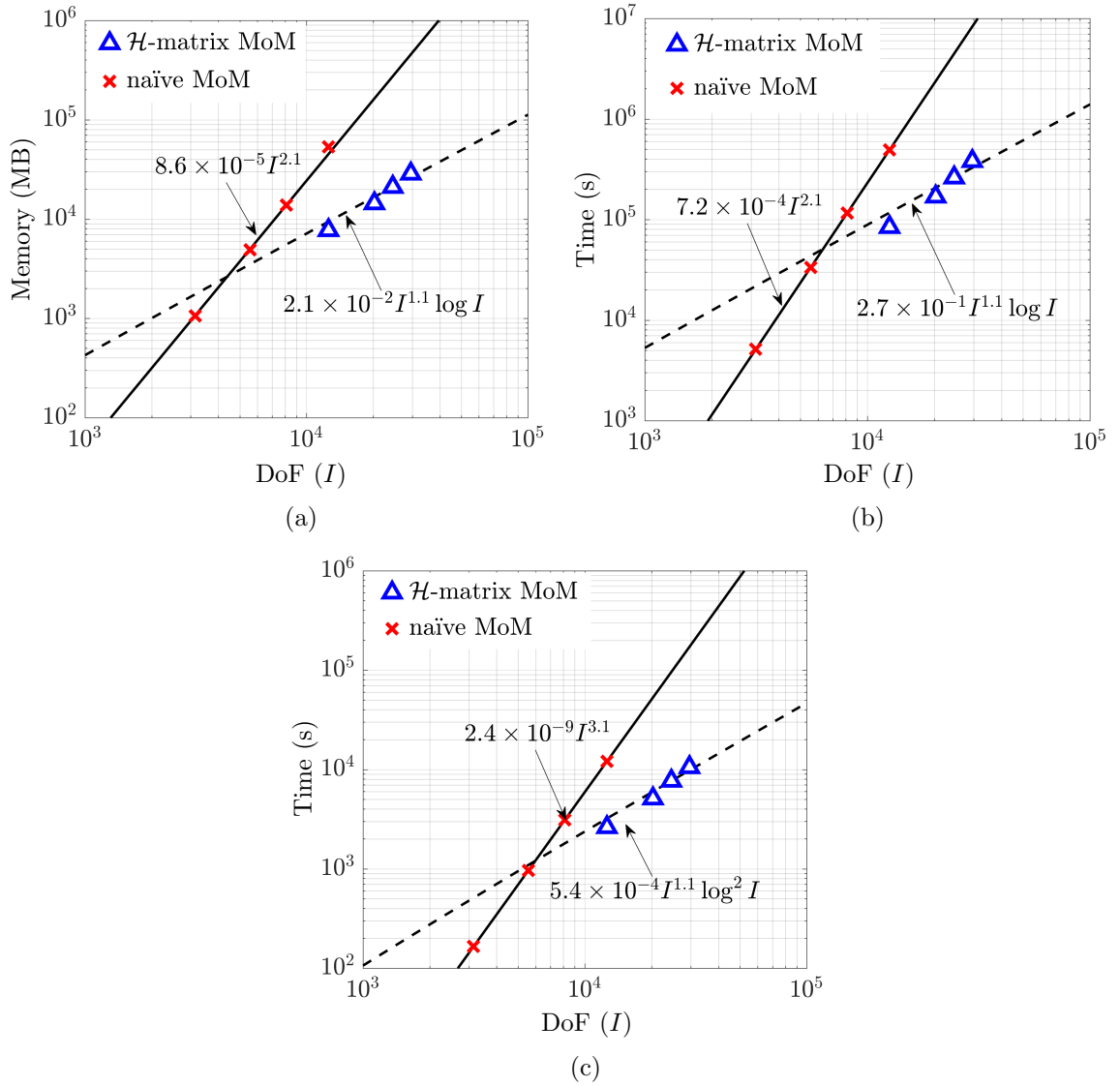


Figure 5.10: Memory cost and CPU time complexity of both \mathcal{H} -matrix (dashed lines) and naïve (solid lines) MoM discretization of SVS-EFIE for the scattering problem of the coated sphere model buried in layered medium. (a) Memory. (b) Fill time. (c) Direct solve time (including of creation of final \mathcal{Z}_{SVS} , block \mathcal{H} -LU decomposition, and block \mathcal{H} -substitution).

The top layer (layer 1) is considered to be air. The rough surface of the snow layer is modeled as region 1 of composite object and has relative permittivity $\epsilon_{R1} = 1.5$. The random surface is generated on top of a slab with 0.005 m thickness and lateral dimensions of 17 cm \times 17 cm. The sea-ice region of the object has a thickness of

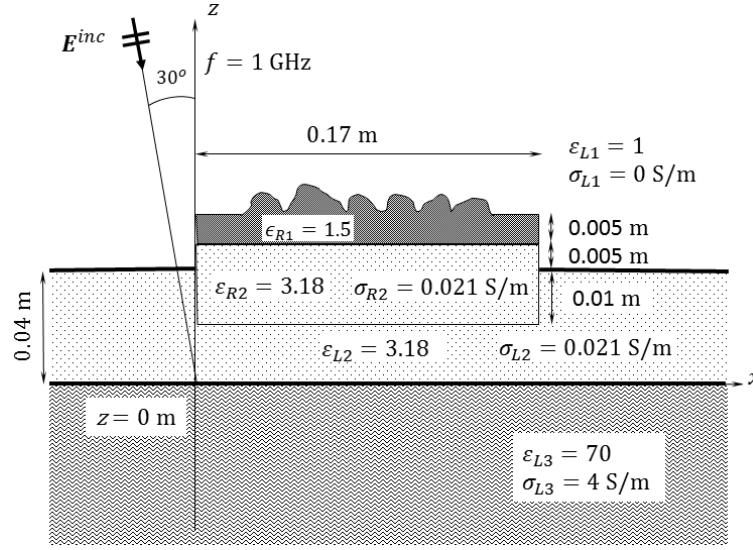


Figure 5.11: Depiction of a rough surface snow sea-ice model as a composite object. The top region of the model is covered by snow with 0.005 m thickness and complex relative permittivity of $\epsilon_{R1} = 1.5$ and the bottom region is sea-ice with 0.015 m thickness and relative permittivity and conductivity of $\epsilon_{R2} = 3.18$ and $\sigma_{R2} = 0.021 \text{ S/m}$ and is half buried in air and the sea-ice layer.

0.015 m, relative permittivity of $\epsilon_{R2} = 3.18$, and conductivity of $\sigma_{R2} = 0.021 \text{ S/m}$. The layer of the sea-ice has a thickness of 0.04 m with same material property as sea-ice region 2 of the object. The sea water layer has a relative permittivity of $\epsilon_{L3} = 70$ and conductivity of $\sigma_{L3} = 4.0 \text{ S/m}$. The model is excited by the same electric dipole as the one considered in the first and second numerical examples but operating at 1GHz. The total number of RWG functions and tetrahedrons of the discretized snow-sea-ice composite object are $I = 54,090$ and $N = 98,817$, respectively. The magnitude of the total electric field along the observation lines inside the object is depicted in Fig. 5.12 and obtained using the proposed SVS-EFIE formulation and FEKO. The considered observation lines are $(0.001 \leq x \leq 0.169, y = 0.085, z = 0.04) \text{ m}$, $(x = 0.085, 0.001 \leq y \leq 0.169, z = 0.04) \text{ m}$ and $(x = 0.085, y = 0.085, 0.031 \leq z \leq 0.049) \text{ m}$.

Next, the memory requirements and CPU time complexity of \mathcal{H} -matrix accelerated solution of the proposed SVS-EFIE solution for the rough surface snow sea-ice model are depicted in Fig. 5.13. In the composite snow-sea-ice model, the number of

tetrahedrons is discretized with $N = I^{1.1}$ ($\alpha = 1.1$).

Furthermore, the compression ratio (CR) for storage of each matrix block in (5.9) is calculated as

$$\text{CR} = \left(1 - \frac{\text{Mem. } \mathcal{H}\text{-matrix SVS-EFIE}}{\text{Mem. naïve MoM SVS-EFIE}} \right) \times 100\%. \quad (5.12)$$

The CR is 93.78% for the volume to surface operator matrix blocks (associated with MoM interactions with layered medium Green's function) for the scattering problem of the rough surface snow sea-ice model buried in the layered media. The scattering problem of the same snow sea-ice object in free space has CR equal to 93.83%. This confirm that creating clusters of elements crossing the dielectric interfaces between the layers preserve compressibility of the corresponding \mathcal{H} -matrix blocks. The matrix blocks of the same integral operator for the problem of capsule buried in the layered media has CR = 89.19%, while in the radiation problem for the same object in free space the CR equal to CR = 89.12%. Also, for the radiation problem of the coated sphere in layered media the volume-to-surface operator has CR = 91.42% while for the radiation problem of the same object in free space the CR is equal to CR = 91.50%.

5.6 Conclusion

Formulation of Surface-Volume-Surface Electric Field Integral Equation (SVS-EFIE) is proposed for solution of radiation and scattering problems on multi-region composite dielectric objects situated in planar multilayered medium with arbitrary composition of the layers. Materials of the object regions as well as the layers are assumed to be non-magnetic and isotropic. Since the SVS-EFIE utilizes only electric current to the electric field relationships, the electric field dyadic Green's function of the multilayered media is formulated in Michalski-Zheng's mixed-potential form, for which evaluation procedure for the Method of Moments (MoM) interactions has been well developed. Fast direct solution of the MoM matrix equation is enabled through use of hierarchical matrices (\mathcal{H} -matrices). For scatterers of moderate electrical sizes the CPU and memory complexity are bounded by $O(I^\alpha \log I)$ in the regimes outside

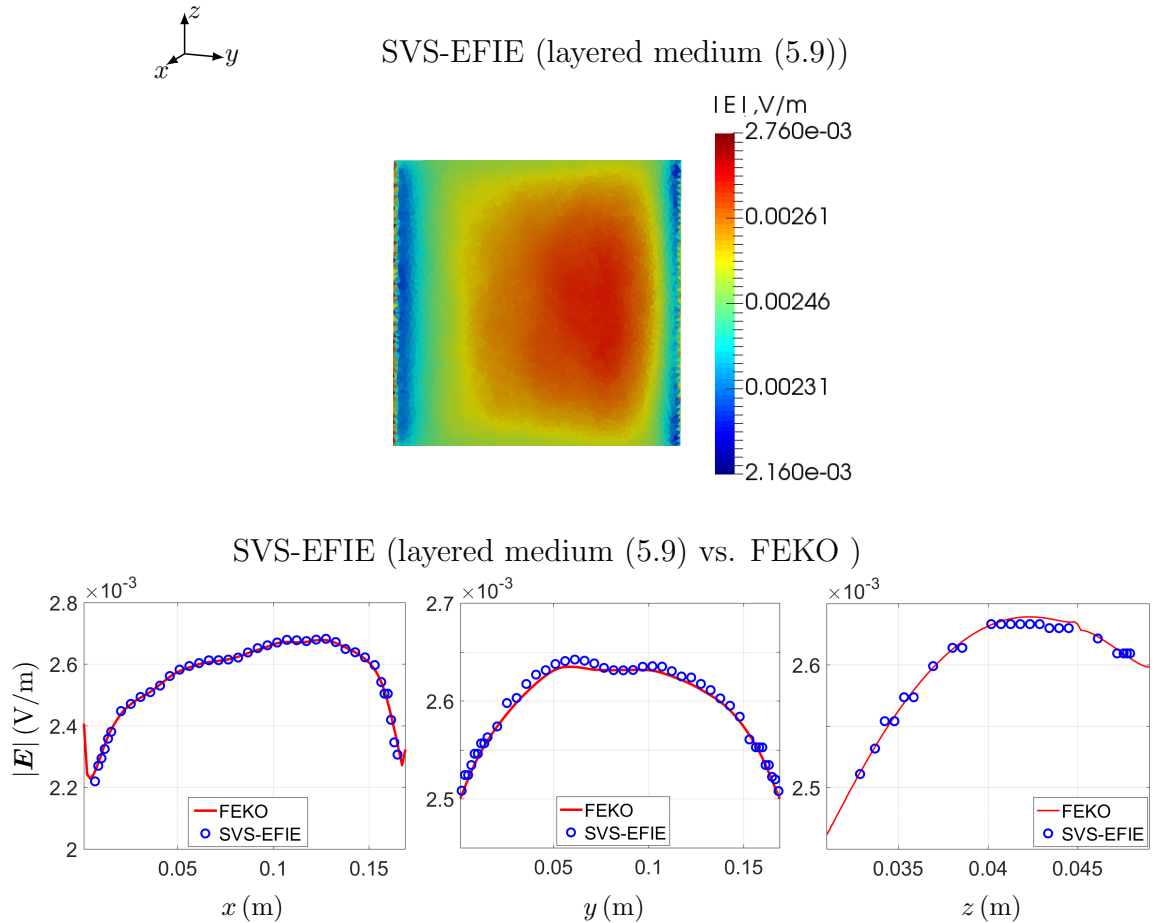


Figure 5.12: Magnitude of the total electric field inside the model of rough surface snow sea-ice model (Fig. 5.11) at 1GHz. The field distribution inside the model is shown in the left where the observation surface is on the interface between air layer and the sea ice layer $z = 0.04$ m. The fields computed using FEKO are shown in the right for comparison with observation lines at $(0.001 \leq x \leq 0.169, y = 0.085, z = 0.04)$ m, $(x = 0.085, 0.001 \leq y \leq 0.169, z = 0.04)$ m and $(x = 0.085, y = 0.085, 0.031 \leq z \leq 0.049)$ m.

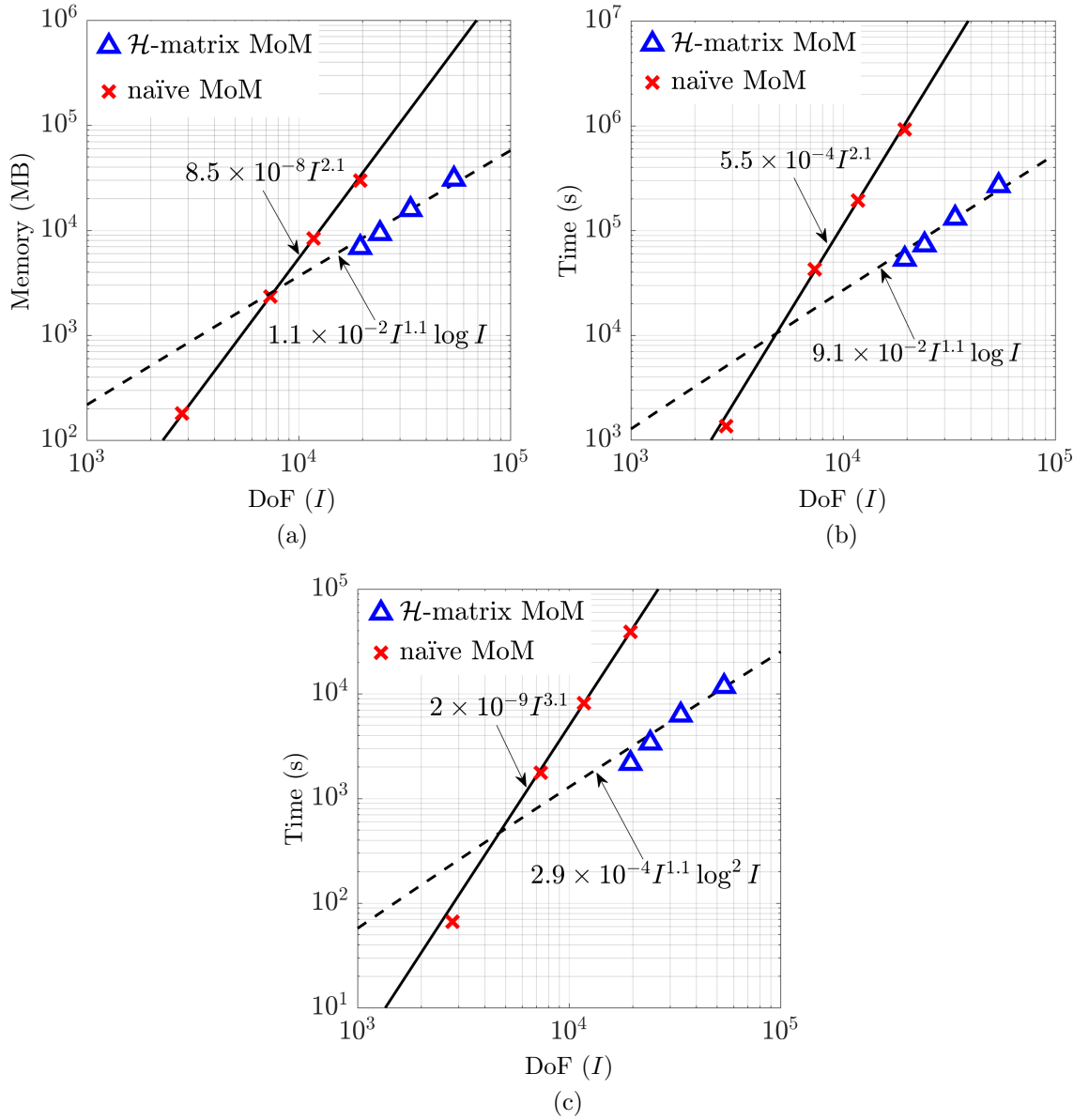


Figure 5.13: Memory cost and CPU time complexity of both \mathcal{H} -matrix (dashed lines) and naïve (solid lines) MoM discretization of SVS-EFIE for the scattering problem of the snow sea-ice model buried in layered medium. (a) Memory. (b) Fill time. (c) Direct solve time (including of creation of final \mathcal{Z}_{SVS} , block \mathcal{H} -LU decomposition, and block \mathcal{H} -substitution).

the low frequency and oversampling breakdowns, I being the number of unknowns in discretization of the surface currents and $1 < \alpha < 1.5$ is a geometry defined constant.

Numerical examples validate proposed formulation through comparison of computed fields against those obtained by commercial layered medium MoM solver based on traditional surface integral equations.

6

Fast Direct Error-Controlled Solution of Scattering problem via \mathcal{H} -matrix Accelerated Locally Corrected Nyström Discretization of Magnetic Field Integral Equation

6.1 Abstract

A fast direct high-order (HO) Locally Corrected Nyström (LCN) discretization of the magnetic field integral equation (MFIE) is proposed for radiation problem on perfect electric conductor (PEC) sphere. The method is based on the error-controlled hierarchical (\mathcal{H})-matrix with a significantly reduced computational cost. The accuracy of the proposed cost reduction method is validated with the analytical Mie-series solution and is shown to produce the HO results. The memory cost and CPU time complexity of the new computational framework is analyzed numerically

in detail.

6.2 Introduction

Solution of the large scattering and radiation problems has been critically important to development of stealth technologies [97], design for electromagnetic compatibility in the systems mounted on electrically large platforms [98], prediction of channels capacity in 5G communication networks [99], and other practical applications [100]. Due to large electrical sizes of the involved models, accurate solutions for such problems can only be obtained through discretization of the integral equations (IEs) which result in dense matrix equations. Hence, the sophisticated iterative [17, 21, 26] and direct [30, 31, 36] fast algorithms can be used to accelerate the solution of practically interesting problems. Commonly used iterative fast methods such as Multi-Level-Fast-Multipole-Algorithm (MLFMA) applied to acceleration of low-order Rao-Wilton-Glisson Method of Moments (RWG-MoM) solution [56], however, often fail to provide desired accuracy. Objects of interest are typically open metal structures with sharp edges, multiscale features, and plethora of complex physical resonant phenomena making conditioning of the pertinent matrix equations very poor. Wide dynamic range of the field levels due to shading effect caused by electrically large size further exacerbates the situation by imposing requirements of effective error controllability on both the discretization scheme and the fast algorithm. However, the fast direct algorithms are largely insensitive to the poor conditioning associated with the discretized IE operators.

In this work, we introduce a fast direct method using hierarchical (\mathcal{H})-matrix-based mathematical framework [36, 62] to reduce the computational complexity of the Locally Corrected Nyström (LCN) solution of the magnetic field integral equation (MFIE) for perfect electric conductor (PEC) objects. The \mathcal{H} -matrix acceleration implemented in this work accelerates the matrix fill time, LU decomposition, and backsubstitution. Numerical results validate the superior performance of the proposed fast direct error-controlled solver compared to conventional direct LCN solution.

6.3 Synopsis OF Locally Corrected Nyström Discretization Of MFIE

In this section, we review the background of this work including the LCN discretization of the MFIE. The time-harmonic MFIE for the PEC scatterer with surface ∂V situated in free-space is expressed as

$$\hat{\mathbf{n}} \times \mathbf{H}^{\text{inc}}(\mathbf{r}) = \frac{1}{2} \mathbf{J}(\mathbf{r}) - \hat{\mathbf{n}} \times \nabla \times \int_{\partial V} G_0(\mathbf{r}, \mathbf{r}') \cdot \mathbf{J}(\mathbf{r}') ds', \quad \mathbf{r} \in \partial V \quad (6.1)$$

where $G_0(\mathbf{r}, \mathbf{r}') = e^{-ik_0|\mathbf{r}-\mathbf{r}'|}/(4\pi|\mathbf{r}-\mathbf{r}'|)$ is the dyadic 3-D Green's functions of free-space with observation and source locations \mathbf{r} and \mathbf{r}' , $\hat{\mathbf{n}}$ is the unit vector normal to ∂V and \mathbf{H}^{inc} is the incident field. In order to numerically solve the MFIE (6.1) with LCN, the surface of the PEC scatterer is discretized with N_e curvilinear elements (pathces). Thus, (6.1) can be written as

$$\hat{\mathbf{n}} \times \mathbf{H}^{\text{inc}}(\mathbf{r}) = \frac{1}{2} \mathbf{J}(\mathbf{r}) - \hat{\mathbf{n}} \times \nabla \times \sum_{e=1}^{N_e} \int_{\partial V_e} G_0(\mathbf{r}, \mathbf{r}') \cdot \mathbf{J}(\mathbf{r}') ds', \quad \mathbf{r} \in \partial V. \quad (6.2)$$

In LCN, the unknown surface current density $\mathbf{J}(\mathbf{r})$ is expanded as

$$\mathbf{J} = J^1(\mathbf{r}) \mathbf{a}_1(\mathbf{r}) + J^2(\mathbf{r}) \mathbf{a}_2(\mathbf{r}) \quad (6.3)$$

where $\mathbf{a}_1(\mathbf{r}) = \partial \mathbf{r} / \partial \xi$ and $\mathbf{a}_2(\mathbf{r}) = \partial \mathbf{r} / \partial \eta$ are the covariant unitary vectors tangential to the surface ∂V_e which is locally defined by a 2-D space (ξ, η) [101]. Testing the integral equation in (6.2) by means of the covariant unitary vectors followed by substitution of (6.3) into (6.2) yields a pair of integral equations as

$$\begin{aligned} \mathbf{a}_{q,i}^m \cdot \hat{\mathbf{n}}_q^m \times \mathbf{H}^{\text{inc}}(\mathbf{r}_q^m) &= \frac{1}{2} \mathbf{a}_{q,i}^m \cdot (J^1(\mathbf{r}_q^m) \mathbf{a}_{q,1}^m + J^2(\mathbf{r}_q^m) \mathbf{a}_{q,2}^m) \\ &\quad - \mathbf{a}_{q,i}^m \cdot \hat{\mathbf{n}}_q^m \times \nabla \times \sum_{e=1}^{N_e} \int_{\partial V_e} G_0(\mathbf{r}_q^m, \mathbf{r}') \cdot (J^1(\mathbf{r}') \mathbf{a}_1^e(\mathbf{r}') + J^2(\mathbf{r}') \mathbf{a}_2^e(\mathbf{r}')) ds' \end{aligned} \quad (6.4)$$

where $i = 1, 2$ and the superscript $m = 1, \dots, N_e$ is corresponding to the observation patch and \mathbf{r}_q^m is the observation point which is chosen to be at the position-vector of the q th quadrature point on the observation patch m . Next, the integral over ∂V_e in (6.4) can be performed using a Q -point quadrature rule. Therefore, (6.4) is approximated as

$$\begin{aligned} \mathbf{a}_{q,i}^m \cdot \hat{\mathbf{n}}_q^m \times \mathbf{H}^{\text{inc}}(\mathbf{r}_q^m) &= \frac{1}{2} \mathbf{a}_{q,i}^m \cdot (J^1(\mathbf{r}_q^m) \mathbf{a}_{q,1}^m + J^2(\mathbf{r}_q^m) \mathbf{a}_{q,2}^m) \\ &\quad + \sum_{e=1}^{N_e} \sum_{q'=1}^Q \omega_{q,m,q',e}^{i,1} \cdot J^1(\mathbf{r}_{q'}^e) + \omega_{q,m,q',e}^{i,2} J^2(\mathbf{r}_{q'}^e) \end{aligned} \quad (6.5)$$

where $\mathbf{r}_{q'}^e$ is the q' th source point on source patch e , chosen to be at the position-vector of the q' th quadrature point. In (6.5) $\omega_{q,m,q',e}^{i,j}$ are regular weights defined as

$$\omega_{q,m,q',e}^{i,j} = -\mathbf{a}_{q,i}^m \cdot \hat{\mathbf{n}}_q^m \times [\nabla \times (G_0(\mathbf{r}, \mathbf{r}_{q'}^e) \cdot \mathbf{a}_{q',j}^e)] \Big|_{\mathbf{r}=\mathbf{r}_q^m} \quad (6.6)$$

where $j = 1, 2$ specifies the projection of unknown surface current \mathbf{J} on $\mathbf{a}_{q',j}^e$.

However, due to the singular behavior of $G_0(\mathbf{r}_q^m, \mathbf{r}_{q'}^e)$ for the near interactions, the regular weights formulation in (6.6) yields an inaccurate result for the integral in (6.2) over patches with singular behavior. Thus, the computation of the integral for near interactions should be computed through the local correction procedure [102, 103]. Therefore, (6.6) should be modified as

$$\begin{aligned}
& \frac{1}{2} \mathbf{a}_{q,i}^m \cdot (J^1(\mathbf{r}_q^m) \mathbf{a}_{q,1}^m + J^2(\mathbf{r}_q^m) \mathbf{a}_{q,2}^m) + \sum_{e \in \text{far}(m)} \sum_{q'=1}^Q \omega_{q,m,q',e}^{i,1} \cdot J^1(\mathbf{r}_{q'}^e) + \omega_{q,m,q',e}^{i,2} J^2(\mathbf{r}_{q'}^e) \\
& + \sum_{e \in \text{near}(m)} \sum_{q'=1}^Q \tilde{\omega}_{q,m,q',e}^{i,1} \cdot J^1(\mathbf{r}_{q'}^e) + \tilde{\omega}_{q,m,q',e}^{i,2} J^2(\mathbf{r}_{q'}^e) = \mathbf{a}_{q,i}^m \cdot \hat{\mathbf{n}}_q^m \times \mathbf{H}^{\text{inc}}(\mathbf{r}_q^m)
\end{aligned} \tag{6.7}$$

The locally corrected weights in (6.7) can be computed through solving

$$\sum_{q=1}^Q \tilde{\omega}_{q,m,q',e}^{i,j} F_k(\mathbf{r}_{q'}^e) = -\mathbf{a}_{q,i}^m \cdot \hat{\mathbf{n}}_q^m \times \nabla \times \int_{\partial V_e} G_0(\mathbf{r}_q^m, \mathbf{r}') \cdot (F_k(\mathbf{r}') \cdot \mathbf{a}_{q',j}^e) d\mathbf{r}', \quad k = 1, \dots, Q \tag{6.8}$$

where F_k are the polynomials and their matrix format in left-hand side is the Vandermonde matrix [21] with size of $Q \times Q$. This relatively small size system can be solved directly in order to obtain the locally corrected weights.

In LCN discretization of MFIE, in order to partition the interaction set to the near and far interactions, the calculated integral over ∂V_e in (6.2) must meet the desired precision using either the locally corrected weights in (6.8) or the regular quadrature rule computation. In this work, we use a fast tree-based search approach implemented in [104]. The idea behind this method is to efficiently find the LCN effective radius R_{LCN} as the minimum distance $|\mathbf{r}_q^m - \mathbf{r}'|$ for a given observation point \mathbf{r}_q^m until the integral in (6.2) obtained by the regular quadrature rule matches the value obtained by the locally corrected weights to the desired accuracy. In order to accomplish this goal, we consider the largest patch element and move it away from the observation point \mathbf{r}_q^m while checking if the error between two methods is smaller than the desired accuracy. Then, we consider this distance as the LCN effective radius R_{LCN} . Next, a tree-based search is performed to find patches with $|\mathbf{r}_q^m - \mathbf{r}'| > R_{\text{LCN}}$. Such patches with are then classified to belong to the far interaction set of the corresponding observer point \mathbf{r}_q^m (i.e. $\mathbf{r}' \in \partial V_{\mathbf{r}_q^m}^{\text{far}}$). Otherwise, they belong to the near interaction set $\mathbf{r}' \in \partial V_{\mathbf{r}_q^m}^{\text{near}}$ with respect to the observation quadrature point \mathbf{r}_q^m . The CPU time

complexity of this approach is $\mathcal{O}(N)$ as reported in [104].

Finally, the LCN discretization of MFIE in (6.7) yields a system of linear equations of $Z_{\text{LCN}} \cdot J = H$ with respect to the unknown coefficients vectors J_1 and J_2 with the total size of $2N_e Q \times 1$ and right-hand-side vectors H_1 and H_2 as

$$Z_{\text{LCN}} \cdot \begin{bmatrix} J_1 \\ J_2 \end{bmatrix} = \begin{bmatrix} H_1 \\ H_2 \end{bmatrix} \quad (6.9)$$

where impedance matrix $[Z_{\text{LCN}}]$ is a dense matrix of size $2N_e Q \times 2N_e Q$ and has the form of

$$Z_{\text{LCN}} = \begin{bmatrix} Z_{1,1} & Z_{1,2} \\ Z_{2,1} & Z_{2,2} \end{bmatrix} = \begin{bmatrix} Z_{1,1}^{\text{far}} & Z_{1,2}^{\text{far}} \\ Z_{2,1}^{\text{far}} & Z_{2,2}^{\text{far}} \end{bmatrix} + \begin{bmatrix} Z_{1,1}^{\text{near}} & Z_{1,2}^{\text{near}} \\ Z_{2,1}^{\text{near}} & Z_{2,2}^{\text{near}} \end{bmatrix}. \quad (6.10)$$

Conventional storage of the LCN matrices, their products, and LU decomposition lead to heavy memory and CPU time usage. To reduce computational time and memory complexities we developed an acceleration scheme based on \mathcal{H} -matrices. The proposed scheme features fast direct based \mathcal{H} -LU decomposition of the resultant matrices followed by the back-substitution while maintaining the HO performance of the conventional (unaccelerated) LCN method.

6.4 \mathcal{H} -Matrix-Based Fast Direct Solution of LCN-MFIE

6.4.1 Geometry Partitioning and Construction of the \mathcal{H} -matrix

The implementation of the \mathcal{H} -matrix acceleration scheme for the LCN-MFIE starts with partitioning of the source/test quadrature into an L -level hierarchy of clusters until the number of points in each leaf cluster is no greater than the predetermined *leafsize* n_{min} parameter. Hence, the Orthogonal Recursive Bisectioning (ORB) [35] is applied on the full set of the quadrature-sampled vector currents defined in (6.2) to create cluster tree T . Next, we create \mathcal{H} -matrix structure for the LCN impedance

matrix arising from the interaction trees. Therefore, using the observer and source interaction trees, the LCN impedance matrix can be decomposed into subblocks each representing the interaction between a cluster of the observer quadrature points and a cluster of the source quadrature points. These interaction sets can be classified as admissible and inadmissible by checking the following admissibility condition

$$\min\{\text{diam}(\mathcal{B}_{\text{obs}}), \text{diam}(\mathcal{B}_{\text{src}})\} \leq \eta \text{dist}(\mathcal{B}_{\text{obs}}, \mathcal{B}_{\text{src}}). \quad (6.11)$$

Here, \mathcal{B}_{obs} and \mathcal{B}_{src} are the bounding boxes which contain the observer and the source unknowns of the corresponding clusters, $\text{diam}(\cdot)$ and $\text{dist}(\cdot, \cdot)$ denote the Euclidean diameter and minimum distance between these bounding boxes, respectively. Also, η is an admissibility parameter with real positive value. While inadmissible blocks will be stored in a full-matrix format using conventional LCN, the admissible blocks will be approximated using Adaptive Cross Approximation (ACA) [23, 24] algorithm and stored in a compressed low-rank matrix format. The accuracy of the rank revealed blocks is controlled by the ACA truncation tolerance τ_{ACA} , which in this work is set to be above the error level associated with the error occurring during numerical evaluation of the adaptive integration method used in calculation of the locally-corrected weights in (6.7).

6.4.2 Direct Solution Using Block \mathcal{H} -LU Decomposition

After creation of the \mathcal{H} -matrices for LCN-MFIE (6.7), in order to solve the linear system using the fast direct \mathcal{H} -matrix scheme, block \mathcal{H} -LU decomposition followed by block \mathcal{H} -substitutions are applied to \mathcal{Z}_{LCN} . The block \mathcal{H} -LU decomposition can be computed as

$$\mathcal{Z}_{\text{LCN}} = \begin{bmatrix} \mathcal{Z}_{1,1} & \mathcal{Z}_{1,2} \\ \mathcal{Z}_{2,1} & \mathcal{Z}_{2,2} \end{bmatrix} = \begin{bmatrix} \mathcal{L}_{1,1} & \\ \mathcal{L}_{2,1} & \mathcal{L}_{2,2} \end{bmatrix} \cdot \begin{bmatrix} \mathcal{U}_{1,1} & \mathcal{U}_{1,2} \\ & \mathcal{U}_{2,2} \end{bmatrix} = \mathcal{L} \cdot \mathcal{U} \quad (6.12)$$

where \mathcal{Z}_{LCN} is the \mathcal{H} -matrix representation of the conventional LCN impedance matrix Z_{LCN} in (6.10). Detailed implementation of the block \mathcal{H} -LU algorithm is described

in [39]. Next, the vector of unknowns J can be computed as

$$\begin{bmatrix} \mathcal{L}_{1,1} & \\ \mathcal{L}_{2,1} & \mathcal{L}_{2,2} \end{bmatrix} \cdot \begin{bmatrix} \mathcal{U}_{1,1} & \mathcal{U}_{1,2} \\ & \mathcal{U}_{2,2} \end{bmatrix} \cdot \begin{bmatrix} J_1 \\ J_2 \end{bmatrix} = \begin{bmatrix} H_1 \\ H_2 \end{bmatrix}. \quad (6.13)$$

In order to solve (6.13), first, the block \mathcal{H} -LowerTriSolver procedure

$$\mathcal{L} \cdot \mathcal{W} = \begin{bmatrix} \mathcal{L}_{1,1} & \\ \mathcal{L}_{2,1} & \mathcal{L}_{2,2} \end{bmatrix} \cdot \begin{bmatrix} \mathcal{W}_1 \\ \mathcal{W}_2 \end{bmatrix} = \begin{bmatrix} H_1 \\ H_2 \end{bmatrix} \quad (6.14)$$

is invoked to find \mathcal{W}_1 and \mathcal{W}_2 . Next, these solutions are considered as the RHS in

$$\mathcal{U} \cdot J = \begin{bmatrix} \mathcal{U}_{1,1} & \mathcal{U}_{1,2} \\ & \mathcal{U}_{2,2} \end{bmatrix} \cdot \begin{bmatrix} J_1 \\ J_2 \end{bmatrix} = \begin{bmatrix} \mathcal{W}_1 \\ \mathcal{W}_2 \end{bmatrix} \quad (6.15)$$

to solve for the vector of unknowns J_1 and J_2 via block \mathcal{H} -UpperTriSolver procedure.

6.5 Numerical Results

To investigate the accuracy of the proposed fast direct error-controlled LCN solver, we performed comparison of its numerical solution against analytic Mie series [71] for the problem of electric dipole radiation near a PEC sphere. The \mathcal{H} -matrix parameters of the solver are chosen empirically. For the numerical examples of this thesis these parameters are the optimized values for $\eta = \{2, 3, 4, 5\}$ and $n_{\min} = \{16, 32, 64\}$. Also, the truncation tolerance of the ACA algorithm τ_{ACA} is set to the desired accuracy of the HO solution. As an example, in order to have 4 digits of accuracy in the solution, the ACA tolerance is set to $\tau_{\text{ACA}} = 10^{-4}$. In order to show the efficiency of the proposed solver, its memory and time complexities are also studied. All numerical results presented in this section are obtained using a single Intel Xeon X5650 Processor running with a single core at 2.66 GHz.

The PEC sphere is centered at the origin with radius of 1.0 m and excited by a radial \hat{z} -directed electric dipole with moment $I \cdot \ell = 1$ [A · m] situated at (0, 0, 10.0) m. The frequency of excitation is chosen to be 100 MHz. The number of surface patches is

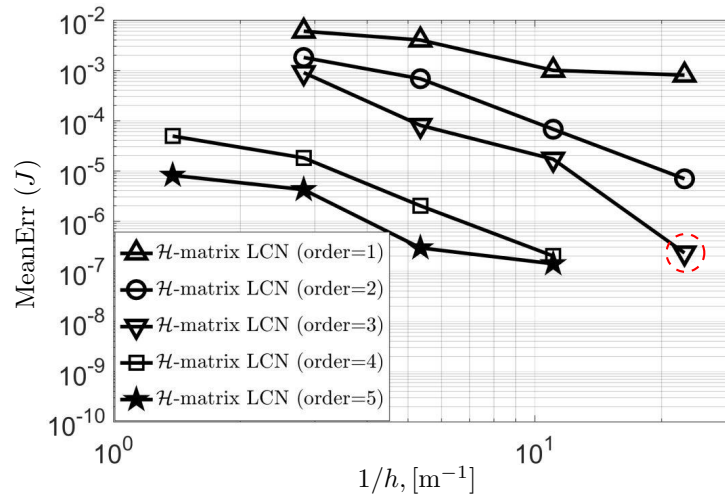


Figure 6.1: The mean relative error in the current as a function of the element size and solution order in the \mathcal{H} -matrix acceleration of LCN discretization of MFIE. The relative error is computed using $\text{MeanErr}(J) = \frac{1}{2QN_e} \sum_{i=0}^{2QN_e} \frac{|J_i^{\text{LCN}} - J_i^{\text{Ref}}|}{|J_i^{\text{Ref}}|}$ with respect to the Mie-series analytic solution as a reference.

varying from $N_e = 24$ to $N_e = 6,144$. This discretization produces mesh size varying from $h = 0.7236$ to $h = 0.0441$. The average relative error in the surface current is shown in Fig. 6.1 as a function of the solution order, p , and the mesh size, h , where $p+1$ is the requested number of digits of accuracy. As an example, the solution shown in Fig. 6.1 with a dashed red circle has number of elements equal to $N_e = 6,144$ and number of points per element equal to $Q = 16$ which results in $N = 196,608$ number of unknowns ($N = 2N_eQ$).

Next, in order to examine the memory and CPU time complexity performance of the proposed solver, we provide the memory and CPU time requirements of the computed results in Fig. 6.1 and compare them with their conventional LCN solution. Fig. 6.2(a) shows the memory requirements of the proposed solver up to solution order $p = 5$ with respect to the number of unknowns N . The memory cost of the conventional LCN with solution order $p = 1$ is shown in the same figure with scale $\mathcal{O}(N^2)$ for comparison. As shown in Fig. 6.2(a) the complexity of the \mathcal{H} -matrix LCN for the first-order solution is validated to scale as $\mathcal{O}(N \log N)$. From this figure one can see that the memory cost of the proposed solver is significantly reduced in

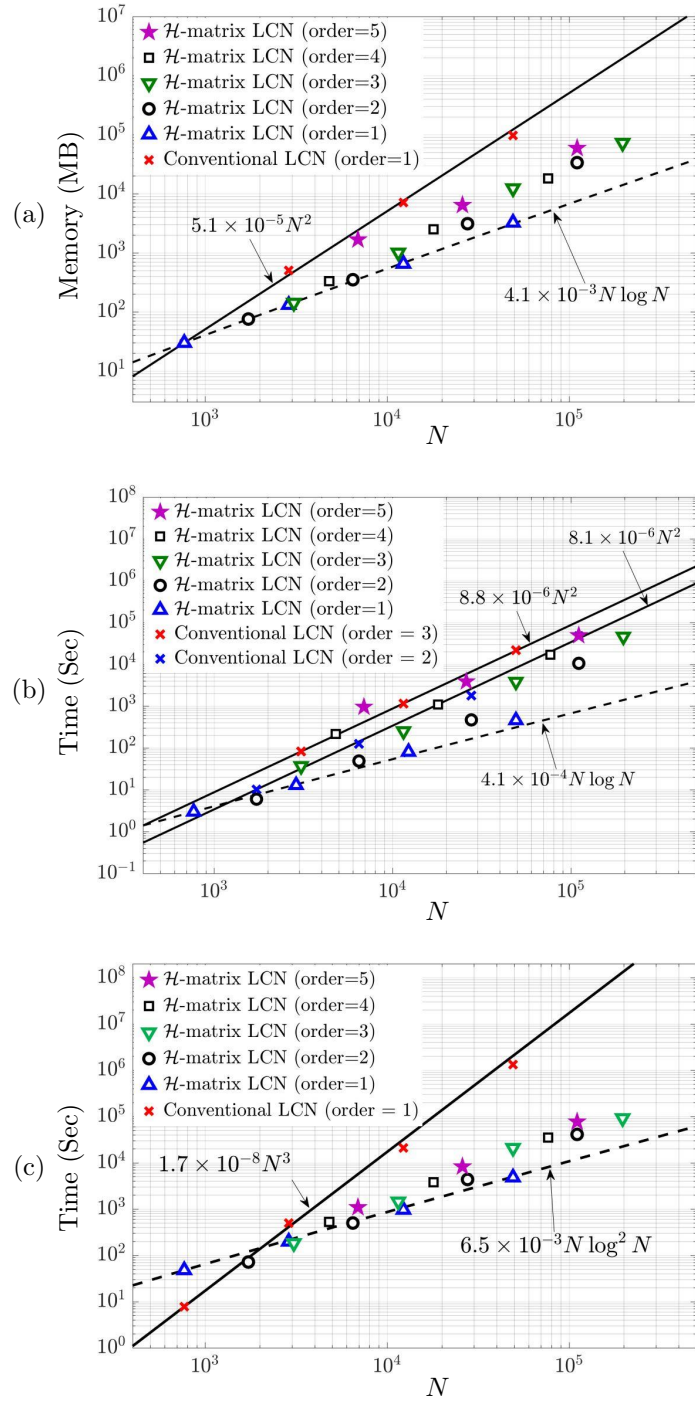


Figure 6.2: Memory cost and CPU time complexity performance of the \mathcal{H} -matrix accelerated LCN discretization of MFIE for the results in Fig. 6.1 as a function of the total number of unknowns N and solution order p . (a) Memory cost. (b) Fill time (time to construct the LCN matrices in (6.7)). (c) Solution time (using block \mathcal{H} -LU direct algorithm). The complexity of the conventional LCN discretization (solid line) of MFIE is also plotted for comparison.

Table 6.1: Memory compression ratio (5.12) for the results in Fig. 6.1 using the proposed solver as a function of the solution order p and the number of elements N_e

Order	CR %, τ_{ACA} ($N_e = 360$)	CR %, τ_{ACA} ($N_e = 1,536$)	CR %, τ_{ACA} ($N_e = 6,144$)
1	45.24, 10^{-3}	82.60, 10^{-3}	94.27, 10^{-3}
2	71.13, 10^{-4}	88.33, 10^{-4}	95.34, 10^{-5}
3	77.54, 10^{-4}	88.81, 10^{-6}	96.93, 10^{-6}
4	80.01, 10^{-5}	92.24, 10^{-6}	—
5	81.47, 10^{-6}	93.45, 10^{-7}	—

comparison to the conventional LCN.

Also, the CPU time required to fill the \mathcal{H} -matrices of the LCN in cases of Fig. 6.1 is depicted in Fig. 6.2(b) and compared with conventional LCN with solution order $p = 2$ and $p = 3$ plotted in the same figure with scale $\mathcal{O}(N^2)$. The numerical experiments show that for a fixed solution order p , increasing the number of elements N_e results in sufficient growth of the effective radius R_{LCN} . Hence, one can see that the constant behind the \mathcal{H} -matrix scale is growing rapidly in Fig. 6.2(b). Furthermore, the computational time to solve the equation includes the block \mathcal{H} -LU and block \mathcal{H} -backsubstitution which are depicted in Fig. 6.2(c). The scaling of $\mathcal{O}(N \log^2 N)$ is observed. The CPU time is compared with that of the conventional LCN with solution order $p = 1$ in the same figure. The latter scales as $\mathcal{O}(N^3)$.

Furthermore, the compression ratio (CR) for the memory storage of LCN matrices in (6.7) is calculated as

$$CR = \left(1 - \frac{\text{Mem. } \mathcal{H}\text{-matrix LCN MFIE}}{\text{Mem. naïve LCN MFIE}} \right) \times 100\%. \quad (6.16)$$

The CR's for the results in Fig. 6.1 are shown in Table 6.1 as a function of the solution order and the number of the mesh elements in order to show the averaged compressibility of the \mathcal{H} -matrix blocks. The ACA truncation tolerance τ_{ACA} for each simulation is also shown in the same table.

Next, in order to show the performance of the proposed solver for the problems

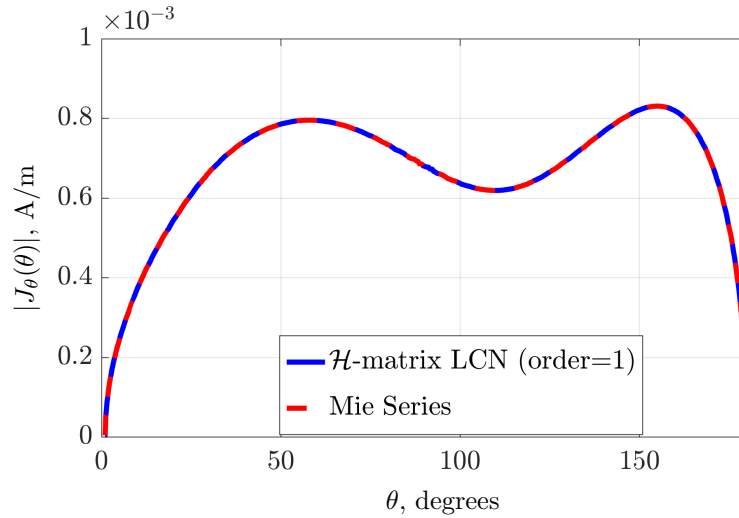


Figure 6.3: The magnitude of the surface current density J on the PEC sphere as a function of θ using the proposed solver and the Mie-series analytic solution at $f = 100$ MHz for the first-order solution with $N = 786,432$ number of unknowns.

with large number of unknowns, we conducted two numerical experiments. In the first experiment the sphere with number of elements $N_e = 98,304$ and solution order $p = 1$ resulting in $N = 786,432$ unknowns is considered. The simulation required 107 GB of memory for the \mathcal{H} -matrix parameters of $\eta = 5$, $n_{\min} = 32$, and $\tau_{ACA} = 10^{-4}$. The magnitude of the surface current density along the meridian of the PEC sphere ($\theta = 0^\circ - 180^\circ$) is depicted in Fig. 6.3. The result is compared against the Mie series. It produces average relative error of 2.3×10^{-4} . The CR in this experiment is equal to CR = 99.35%. In the second experiment, we consider the sphere with number of elements $N_e = 24,576$ and solution order $p = 2$, which results in $N = 442,368$ unknowns. The simulation required 130 GB of memory. The \mathcal{H} -matrix parameters are set to $\eta = 5$, $n_{\min} = 64$ and $\tau_{ACA} = 10^{-4}$. The solution produces the mean relative error of 7.0×10^{-5} in magnitude of the surface current density compared to the Mie series. The CR of the matrix in this experiment is equal to CR = 98.84%.

6.6 Conclusion

In this work, we proposed a fast direct error-controlled computational framework for scattering problem on PEC objects using \mathcal{H} -matrix acceleration of the LCN discretization of the MFIE. Numerical results validate the HO error behaviour in the proposed solver. The error studies are conducted by comparing the computed currents against those obtained using analytical Mie series solution. The reduction in memory requirement and CPU time of the proposed solver makes it suitable for fast direct solution of large-scale problem in the cases exhibiting strong physical resonances and/or multiscaling.

7

Conclusions, Comments and Future Work

7.1 Conclusions

This thesis presents \mathcal{H} -matrix based strategies for acceleration of the MoM solution of a single source integral equation known as SVS-EFIE as well as acceleration of the LCN solution of the traditional IEs. In the first stage, the fast direct and iterative \mathcal{H} -matrix based frameworks are developed for the SVS-EFIE for full-wave electromagnetic analysis of scattering and radiation problems on 3-D homogeneous dielectric objects. The new computational framework improves the capability, performance, and efficiency of the solver and enable it for solution of moderate electrical size problems. Next, the SVS-EFIE is developed for electromagnetic analysis of a 3-D composite dielectric objects made of an arbitrary number of piece-wise homogeneous non-magnetic dielectric regions. A new \mathcal{H} -matrix based direct method is developed to accelerate matrix-matrix multiplications, LU decomposition, and back-substitution of the new formulation. Furthermore, a new formulation of the SVS-EFIE is developed for the electromagnetic analysis of the 3-D composite metal-dielectric objects. The new formulation introduces independent surface electric current density on the boundary of each region. The \mathcal{H} -matrix accelerated direct method is also implemented to accelerate the conventional MoM solution of the proposed new formulation. Next,

the SVS-EFIE composite dielectric formulation is generalized for the case of multiregion objects situated in the layered medium and the method is accelerated using the \mathcal{H} -matrix framework. Numerical solutions confirm that the proposed layered medium solver preserve compressibility of the pertinent \mathcal{H} -matrix blocks. Finally, the error-controlled fast direct computational framework is developed using the higher-order LCN discretization of MFIE. The proposed algorithm demonstrate a significant reduction of memory consumption and a considerable speedup for CPU time compared to conventional LCN method while preserving the higher-order performance of the conventional LCN.

7.2 Addressing Prof. Peterson's Comments

7.2.1 Comment 1

Prof. Peterson: *My understanding is that even if a matrix block is not admissible one can still use the ACA compressed representation, which for a full rank block will eventually involve 2 full matrices instead of sparse factors. It would be interesting to know how the parameter eta in (2.10) or (3.19) is related to the efficiency of the ACA compression – in other words, is there a relation between the η factor and the realized CR factor? Have you looked into this or has your experience given you nay insight into this relation? A related question is: How much rank deficiency is considered necessary to make it worthwhile to compress the block?*

Response: The admissibility criterion η controls the distance at which the clustering of two given groups occurs. Hence, it also controls the number of admissible and inadmissible blocks. It is usually problem dependent and chosen empirically. In this thesis, this parameter is the optimized values from $\eta = \{1, 2, 3, 4, 5\}$ set for all numerical examples which is a type of standard η -admissibility criterion (i.e. the geometrical based criteria). In our solver, if the rank of ACA $k \geq \frac{1}{2} \min\{n(\ell), m(\ell)\}$, $n(\ell)$ and $m(\ell)$ being the number of rows and columns of the admissible block, the rank deficient representation of the admissible block is deemed to be not efficient. In such case, the rank deficient block is converted to the full block by simply multiplying

the two matrices of A and B^H . The experience shows that this situation may happen under the condition of selection of large η or/and having an electrically large problem.

7.2.2 Comment 2

Prof. Peterson: *I understand that you are not proposing the SVS-EFIE approach, this has been developed by previous students in your group. However, it would be nice to provide some sort of insight into how the overall efficiency of this technique compares to traditional surface-only formulations (even for traditional solvers). Since you make comparisons with PMCHWT in several chapters, you should be in a position to draw some conclusions about the relative efficiency of the SVS-EFIE approach. At the very minimum, you should be able to summarize the computational costs of the two approaches. However I don't see an explicit discussion about that anywhere.*

Response: The summary of the computational complexity and memory performance of the SVS-EFIE is shown in Table 3.1 where it is compared to that of PMCHWT solution [11]. Both naïve direct MoM and \mathcal{H} -matrix accelerated MoM solutions are considered. The data in this Table, however, only provides the asymptotic bounds. It is also for the case of composite object with a fixed number of regions \mathcal{L} . Hence, the formulations in this table do not show scaling with the number of regions. To answer this question, we have to consider the case of a composite dielectric object with variable number of regions \mathcal{L} . In SVS-EFIE formulation there is a coupling between all dielectric regions. However, in PMCHWT formulation surface currents couple only to the regions with common boundaries. Therefore, memory and CPU time scale in the PMCHWT formulation as $O(\mathcal{L})$ with the number of regions \mathcal{L} , while in SVS-EFIE they scales as $O(\mathcal{L}^2)$, provided fast algorithms are employed. For small number of regions, however, the complexity scaling is highly geometry dependent. Ability of the SVS-EFIE formulations to discretize each region independently based on its respective material property and to use non-conformal meshes contribute favorably to its performance.

Below we provide more detailed complexity analysis which accounts for variable number of regions \mathcal{L} in the particular case of composite scatterer in the form of a

Table 7.1: Scaling in fill time with number of regions \mathcal{L} in SVS-EFIE and PMCHWT formulations.

\mathcal{L}	SVS-EFIE ($\#S^2S$)	SVS-EFIE ($\#V^2S + \#S^2V$)	PMCHWT ($\#S^2S$)
1	1	2	4
2	2	6	16
4	4	20	40
8	8	72	88
16	16	272	184

multilayered sphere with \mathcal{L} layers. In order to simplify the analysis the number of RWG functions P discretizing a given current on surface of each layer of the layered sphere object is assumed to be same in both PMCHWT and SVS-EFIE formulations.

As discussed in the thesis, the time use in the solvers can be partitioned into three major groups, as follows:

1. **Fill time:** Time to fill the matrix in the PMCHWT formulation can be estimated as:

$$\text{Fill time(PMCHWT)} = (12\mathcal{L} - 8) \times \text{time(fill } P \times P \text{ size matrix)}, \quad (7.1)$$

where P is the number of RWG functions discretizing a given current on the surface of a layer. Also, for the SVS-EFIE we have

$$\begin{aligned} \text{Fill time(SVS-EFIE)} = & \mathcal{L} \times \text{time(fill } P \times P \text{ size matrix)} \\ & + \mathcal{L}^2 \times \text{time(fill } P \times 3N \text{ size matrix)} \\ & + \mathcal{L} \times \text{time(fill } 3N \times P \text{ size matrix)}. \end{aligned} \quad (7.2)$$

where N is the number of tetrahedrons in each layer of the layered sphere object (N is assumed to be the same for all layers). The results in Table 7.1 shows the number of key matrix operations performed by SVS-EFIE and PMCHWT formulations during matrix fill as a function of number of regions \mathcal{L} .

2. **Solve time:** by stepping through the block \mathcal{H} -LU algorithm (Algorithm 3), we can determine the time to apply the algorithm on a $2\mathcal{L}P \times 2\mathcal{L}P$ \mathcal{H} -matrix for PMCHWT formulation (factor 2 in PMCHWT formulation is due to doubling of the unknowns), as follow:

$$\begin{aligned} \text{Block}\mathcal{H}\text{-LU time(PMCHWT)} &= 2\mathcal{L} \times \text{time}(\mathcal{H}\text{-LU time on } P \times P \text{ size matrix}) \\ &\quad + f(2\mathcal{L}) \times \text{time}(\text{MulAdd}(\dots) \text{ of } P \times P \text{ size matrices}), \end{aligned} \quad (7.3)$$

where $f(2\mathcal{L}) = 8\mathcal{L}^3/3 - 6\mathcal{L}^2 + 2\mathcal{L}/6 + 12\mathcal{L} - 8$ in PMCHWT formulation.

On the other hands, for SVS-EFIE, the problem of a composite object with \mathcal{L} regions starts with creation of final Z_{svs} which needs the creation of \mathcal{L}^2 \mathcal{H} -matrices with $P \times P$ size. Next, one has to solve an \mathcal{H} -matrix with $\mathcal{L}P \times \mathcal{L}P$ size. Therefore, the time to solve for surface unknowns in SVS-EFIE is:

$$\begin{aligned} \text{Block}\mathcal{H}\text{-LU time(SVS-EFIE)} &= \mathcal{L}^2 \times \text{time}(\text{MulAdd}(\dots) \text{ of } N \times P \text{ size matrices}) \\ &\quad + \mathcal{L} \times \text{time}(\mathcal{H}\text{-LU time on } P \times P \text{ size matrix}) \\ &\quad + f(\mathcal{L}) \times \text{time}(\text{MulAdd}(\dots) \text{ of } N \times P \text{ size matrices}), \end{aligned} \quad (7.4)$$

where $f(\mathcal{L}) = \mathcal{L} \cdot (\mathcal{L} - 1) \cdot (2\mathcal{L} - 1)/6 = \mathcal{L}^3/3 - \mathcal{L}^2/2 + \mathcal{L}/6$ for SVS-EFIE. One can see from the result in Table 7.2 that the coefficient $f(\mathcal{L})$ for PMCHWT is much larger than that in SVS-EFIE.

3. **Time to compute field in the volume:** in order to compute the field throughout the volume in PMCHWT formulation, one must construct surface-to-volume \mathcal{H} -matrix. Also, due to doubling of the unknowns in the PMCHWT formulation one has to generate surface-to-volume \mathcal{H} -matrix for both electric and magnetic surface unknowns and then to perform the MVP with a vector of electric and magnetic current unknowns to find the field inside the volume. Therefore, the CPU time complexity of computing field throughout the volume in the PMCHWT formulation for a problem of composite object with \mathcal{L} regions

Table 7.2: Scaling in solve time with number of regions \mathcal{L} in SVS-EFIE and PMCHWT formulations.

\mathcal{L}	SVS-EFIE (# <i>MulAdd</i> of $N \times P$)	SVS-EFIE (# \mathcal{H} -LU on $P \times P$)	SVS-EFIE (# <i>MulAdd</i> of $P \times P$)	PMCHWT (# \mathcal{H} -LU on $P \times P$)	PMCHWT (# <i>MulAdd</i> of $P \times P$)
1	1	1	0	2	1
2	4	2	1	4	14
4	16	4	14	8	116
8	64	8	140	16	1,072
16	256	16	1,240	32	9,576

is:

$$\begin{aligned}
& \text{Time to compute field in volume(PMCHWT)} = \\
& 2\mathcal{L} \times \text{fill(S2V } 3N \times P \text{ size matrix)} \\
& + 2\mathcal{L} \times \text{time(MVP of } 3N \times P \text{ size matrix)}.
\end{aligned} \tag{7.5}$$

As explained in the thesis, the complexity of finding the field in the volume for SVS-EFIE is just a matrix vector product of \mathcal{L} \mathcal{H} -matrices.

$$\begin{aligned}
& \text{Time to compute field in volume(SVS-EFIE)} = \\
& + \mathcal{L} \times \text{time(MVP of } 3N \times P \text{ size matrix)}.
\end{aligned} \tag{7.6}$$

As leading terms in fill time complexity of SVS-EFIE and PMCHWT scale as \mathcal{L}^2 and \mathcal{L} , respectively, with number of regions \mathcal{L} , the PMCHWT shows more favorable scaling for large number of regions. However, until the number of regions \mathcal{L} reaches at least 10 the number of matrix fill operations in SVS-EFIE remains below that of PMCHWT. Also, the number of operations on the matrices such as multiplication-addition scale as $\mathcal{O}(8\mathcal{L}^3/3)$ in PMCHWT and $\mathcal{O}(\mathcal{L}^3)$ in SVS-EFIE. The number of \mathcal{H} -LU decompositions, however, which is the heaviest matrix solve operation scales as $\mathcal{O}(2\mathcal{L})$ in PMCHWT formulation and as $\mathcal{O}(\mathcal{L})$ for SVS-EFIE.

7.2.3 Comment 3

Prof. Peterson: *In the later chapters (such as around page 90) when you are looking at the cost of doing the compressed operations, you use the number of RWG basis functions as the order of the matrices arising from the surface integral equations, and the number of tetrahedral cells as the order of the matrices arising from the volume integral equations. I may have missed it, but I did not see the details of the volume discretization – what kind of basis functions, and how they relate to the order of the associated matrix. If Schaubert-Wilton-Glisson (SWG) functions were used to discretize the volume EFIE, the order of the matrices would be the number of faces in the mesh, not the number of cells. If piecewise-constant basis functions were used, the accuracy would presumably be lower, but even in that case the associated matrices would be three times the number of tetrahedrons (due to the 3 vector components per cell), not just the number of tetrahedrons. It appears that in Figure 2.4, separate systems are illustrated for the x , y , and z components of the volume operator. Can you clarify what kind of discretization is used for the volume operator?*

Response: In this thesis, the scalar pulse basis/test functions are used to expand the polarization current density inside the volume of the objects and as mentioned in the comment the matrix structure in Fig. (2.4) represents the number of associated basis/test functions with x , y , and z components. Detailed description of the standard MoM procedure of the SVS-EFIE can be found in [13]. The benefit of using SWG basis functions in terms of performance and accuracy has not been explored in this thesis and remains to be in the scope of future work.

7.2.4 Comment 4

Prof. Peterson: *In several places you use spherical targets to illustrate the approach. However, it is well known that spherical problems avoid some of the pathological cases where ACA fails. (These are well documented in Bebendorf's book and other papers.) This is especially true for the MFIE in Chap 6, which is known to produce ACA failures when portions of a structure are planar. Thus the sphere turns out to be a relatively easy case. Any comment?*

Response: The author agree that the ACA suffers from a potential break-down, which may happen when compressed blocks are in a predominantly block-diagonal form with a weak coupling between the blocks. In our codes we have a standard implementation of the ACA used with no mechanisms in place to detect such break-downs (except for monitoring the closeness of the final solution to some independent reference). The \mathcal{H} -matrix accelerated solution for fairly complex objects which were studied in the thesis such as the scattering problem of the snow sea-ice rough surface model in chapter 5 with CR = 94% and the radiation problem of the homogeneous human head model in chapter 3 no issues with such breakdown have been observed. The best approach to dealing with this potential ACA breakdown would be to implement alternative robust compression algorithms such as Hybrid Cross Approximation (HCA), which is free from this break-down and comparable in performance to the ACA. The implementation of \mathcal{H} -matrix with HCA should be considered in the future work.

7.2.5 Comment 5

Prof. Peterson: *Comparing your results with FEKO is fine in general to verify that your code is performing as expected. However, since it is likely that FEKO is based on a similar integral equation formulation, comparing with FEKO may be misleading in cases where FEKO may also fail to some extent. As an example, on page 98 you state that Figure 4.6d shows that your code accurately reconstructs the field singularity simply because your code and FEKO produce a result that increases near an edge. Purists might argue that neither code is very accurate in that situation!*

Response: Indeed, with the use of low order MoM approximation of the SVS-EFIE solution (and FEKO solution) we could only detect that the proposed formulation picks up the singular behavior of the current at the sharp edge. The exponent in the singular behavior has not been studied nor has it been verified to be correct. Error-controlled higher-order solution with either adaptive h-p refinement or special singular basis functions would be required to properly study the edge singularity in the SVS-EFIE solution. Construction of such high-precision solution methods is out

of scope of this thesis.

7.2.6 Comment 6

Prof. Peterson: *Table 2.1 shows an improved CR as the cell dimensions get smaller. Presumably the matrix orders increase by at least the square of the reciprocal of the cell dimension, which suggests that the overall efficiency is a more complicated function.*

Response: The purpose of the numerical results in Table 2.1 is two-fold. First, it shows that for a fixed mesh size (the numerical results of a certain column of Table 2.1), decreasing the ACA truncation tolerance significantly reduce the memory performance of the solver. Second, for an object with a fixed electrical size under the condition of a quasi-dynamic simulation scenarios and fixed value of the ACA truncation tolerance, the CR improves due to appearance of the compressible blocks with larger number of degrees of freedom. Under these conditions, the smaller mesh size produces improved CR. Effect of other factors on the CR in the considered examples is of secondary nature.

7.2.7 Comment 7

Prof. Peterson: *In contrast to the behavior reported in Table 2.1, which seems intuitively correct, in Table 6.1 it appears that the CR factor improves as the tolerance tau gets tighter. How can this be?*

Response: It is important to emphasize that the numerical results in Table 6.1 is for different number of unknowns ($N = 2QN_e$) which is assigned with the solution order p and the number of elements N_e . For example, the value of $CR = 96.93\%$ in row 3 and column 4 is for problem with $N = 196,608$ unknowns and the value of the $CR = 95.34\%$ in row 2 and column 4 is for problem with $N = 110,592$ unknowns. Again, same as the numerical results reported in Table 2.1, increasing the number of unknowns produces the larger admissible blocks which under the condition of the same electrical size results in improved CR.

7.2.8 Comment 8

Prof. Peterson: *Comparing Tables 3.2 and 3.3, why is the solve time for the PMCHWT method so much larger relative to the fill time in Table 3.2 than it is in Table 3.3?*

Response: As explained in the answer of the comment 2, the solve time of the PMCHWT formulation using the block \mathcal{H} -LU algorithm scales as $\mathcal{O}(8\mathcal{L}^3/3)$ for the objects with the number of regions \mathcal{L} whereas the fill time scales as $\mathcal{O}(12\mathcal{L})$. As $\mathcal{L} = 1$ in Table 3.3 case and $\mathcal{L} = 3$ in Table 3.2 case, significant increase in the CPU time is expected with the tripled number of regions.

7.2.9 Comment 9

Prof. Peterson: *On page 80 you make a reference to multiscale problems, have you tried any truly multiscale meshes with your approach?*

Response: As shown in the numerical results of chapter 4, the ratio of the finest mesh to the coarsest mesh in the multiscale mesh structure of the bifurcated sphere model is 1 to 10. In this thesis, we did not work with large degrees of multiscaling due to increased computational costs which became prohibitive within available to us resources. Studies of solutions under higher degrees of multiscaling should be addressed in future work.

7.2.10 Comment 10

Prof. Peterson: *From a perusal of your results, it appears that the largest problems you have solved using the ACA compression involved about 1,000,000 degrees of freedom. Is that correct?*

Response: Yes, using SVS-EFIE fast direct solver, we could solve a problem with 1 M DoFs. The largest problem solved in chapter 6 with \mathcal{H} -matrix accelerated direct solution of LCN discretized MFIE has 786,432 unknowns.

Thank you for all the valuable comments.

7.3 Future Works

The possible future research that can be conducted is, as follows:

1. It is known that the EFIE has low-frequency break down problem. Since the surface-to-surface operator of the SVS-EFIE is the same as surface-to-surface operator of regular EFIE, therefore, SVS-EFIE is also suffering from the low-frequency breakdown. Since SVS-EFIE is a class of SSSIE, one can implement the loop-tree and loop-star basis functions in order to overcome the low-frequency breakdown problem.
2. As discussed in Section 1.1.5, the SVS-EFIE formulations in this thesis is a particular case of constants $a = 1$ and $b = 0$. The problem of internal resonance is well-known for EFIE and the remedy is to use a combined field integral equation (CFIE), which has contribution from both electric and magnetic surface currents. Therefore, the SVS-EFIE in this paper is also not free of internal resonance problem. Hence, one can extend the SVS-EFIE formulation for the case of different values of weighting coefficients a and b .
3. The \mathcal{H} -matrix framework is not suggesting for the electrically large scale problems (usually objects with electrical size larger than 10λ) due to the rank growth issue of the admissible blocks. Therefore, one can implement the \mathcal{H}^2 -matrix framework for different formulations of SVS-EFIE of this thesis in order to preserve the computational complexity of the solver for larger scale problems.
4. In this thesis we implement the \mathcal{H} -matrix fast direct solution of SVS-EFIE using low-order MoM. One can extend the proposed solver for high-order MoM discretization and study the higher-order performance of the SVS-EFIE solver for the large-scale problems.
5. The ACA algorithm is implemented in this thesis to compress the admissible blocks of the pertinent \mathcal{H} -matrices. One can study the implementation of the Hybrid Cross Approximation (HCA) or other grid-based compression algorithms to accelerate the CPU time of the \mathcal{H} -matrix SVS-EFIE solver.

6. Another future work of this thesis includes parallelization of the sophisticated \mathcal{H} -matrix direct method for distributed memory multiprocessors communicating over the message passing interface (MPI). That would make the SVS-EFIE framework capable of solving practically large-scale problems such as SAR calculation of full human body model in bioelectromagnetics or scattering problems on practical rough surface sea ice models in remote sensing.
7. Application of the \mathcal{H} -matrix SVS-EFIE formulation in layered medium for broadband interconnect modeling which accurately handles conductor loss and utilizes the delta-gap port excitation formulation in SVS-EFIE.
8. The error-controlled fast direct LCN solver is demonstrated in this thesis for MFIE in the case of PEC scatterers. One can adopt this computational strategy for implementation of the fast direct LCN solution of both SVS-EFIE as well as traditional surface integral equation formulations (e.g. CFIE, PMCHWT, etc.) for homogeneous, composite dielectric-dielectric, and composite metal-dielectric objects situated in free space.
9. The generalized formulation of the SVS-EFIE for composite metal-dielectric objects is implemented in this thesis for the object in free space. One can study the implementation of the generalized formulation of SVS-EFIE in layered medium background in order to solve some interesting electromagnetics problem in characterization of 3-D microwave circuits and interconnect structures embedded in dielectric substrates featuring finite dielectric inclusions.

References

- [1] M. Ostadrahimi, P. Mojabi, S. Noghianian, L. Shafai, S. Pistorius, and J. LoVetri, “A novel microwave tomography system based on the scattering probe technique,” *IEEE Trans. Instrum. Meas.*, vol. 61, no. 2, pp. 379–390, Feb. 2012.
- [2] K. M. S. Thotahewa, J. M. Redouté, and M. R. Yuce, “SAR SA and temperature variation in the human head caused by IR-UWB implants operating at 4 GHz,” *IEEE Trans. Microw. Theory Techn.*, vol. 61, no. 5 pp. 2161–2169, May 2013.
- [3] D. Ferreira, P. Pires, R. Rodrigues, and R. F. S. Caldeirinha, “Wearable textile antennas: examining the effect of bending on their performance,” *IEEE Antennas Propag. Mag.*, vol. 59, no. 3, pp. 54–59, June 2017.
- [4] N. Ojaroudiparchin, M. Shen, S. Zhang, and G. F. Pedersen, “A switchable 3-D-coverage-phased array antenna package for 5G mobile terminals,” *IEEE Antennas Wireless Propag. Lett.*, vol. 15, pp. 1747–1750, Feb. 2016.
- [5] D. Isleifson, “Simulation and measurement techniques for microwave remote sensing of sea ice,” Ph.D. dissertation, Univ. Manitoba, Winnipeg, Canada, 2010. [Online]. Available: <http://hdl.handle.net/1993/4812>.
- [6] U. R. Patel and P. Triverio, “Skin effect modeling in conductors of arbitrary shape through a surface admittance operator and the contour integral method,” *IEEE Trans. Microw. Theory Techn.*, vol. 64, no. 9, pp. 2708–2717, Sept. 2016.
- [7] R. Mittra, *Computational Electromagnetics: Recent Advances and Engineering Applications*, 3rd ed. New York, Springer, 2014.

-
- [8] A. Taflove and S. C. Hagness, *Computational Electrodynamics: The Finite-Difference Time-Domain Method*, 3rd ed. Boston, MA: Artech House, 2005.
- [9] J. M. Jin, *The Finite Element Method in Electromagnetics*, 3rd ed. Wiley-IEEE Press, 2015.
- [10] R. Harrington, *Field Computation by Moment Methods*, New York: IEEE Press, 1993.
- [11] A. Peterson, S. Ray, and R. Mittra, *Computational Methods for Electromagnetics*, IEEE Press, 1998.
- [12] O. Ergul and L. Gurel, "Comparison of integral-equation formulations for the fast and accurate solution of scattering problems involving dielectric objects with MLFMA," *IEEE Trans. Antennas Propag.*, vol. 57, no. 1, pp. 176–187, Jan 2009.
- [13] F. L. S. Hosseini, A. Menshov, R. Gholami, J. Mojolagbe, and V. Okhmatovski, "Novel single-source integral equation for scattering problems by 3D dielectric objects," *IEEE Trans. Antennas Propag.*, vol. 66, no. 2, pp. 797–807, Feb. 2018.
- [14] F. L. S. Hosseini, "Novel single source integral equation for analysis of electromagnetic scattering by penetrable objects," Ph.D. dissertation, Dept. Elect. Comput. Eng., Univ. Manitoba, Winnipeg, MB, Canada, 2017. [Online]. Available: <https://mspace.lib.umanitoba.ca/handle/1993/32362>.
- [15] W. C. Chew, E. Michielssen, J. M. Song, and J. M. Jin, *Fast and Efficient Algorithms in Computational Electromagnetics*, Norwood, MA: Artech House, 2001.
- [16] R. Coifman, V. Rokhlin, and S. Wandzura, "The fast multipole method for the wave equation: a pedestrian prescription," *IEEE Antennas Propag. Mag.*, vol. 35, no. 3, pp. 7–12, Jun. 1993.
- [17] N. A. Gumerov and R. Duraiswami, *Fast Multipole Methods for the Helmholtz Equation in Three Dimensions*. Amsterdam, The Netherlands: Elsevier, 2006.

-
- [18] O. Ergül and L. Gürel, *The Multilevel Fast Multipole Algorithm (MLFMA) for Solving Large-Scale Computational Electromagnetics Problems*, Wiley-IEEE Press, 2014.
- [19] J. Aronsson and V. Okhmatovski, "Vectorial low-frequency MLFMA for the combined field integral equation," *IEEE Antennas Wireless Propag. Lett.*, vol. 10, pp. 532–535, 2011.
- [20] M. F. Catedra, R. F. Torres, J. Basterrechea, and E. Gago, *The CG-FFT method: Application of Signal Processing Techniques to Electromagnetics*, Boston, MA: Artech House, 1995.
- [21] E. Bleszynski, M. Bleszynski, and T. Jaroszewicz, "AIM: adaptive integral method for solving large-scale electromagnetic scattering and radiation problems," *Radio Sci.*, vol. 31, pp. 1255–1251, Sep.–Oct. 1996.
- [22] K. Yang and A. Yilmaz, "A three-dimensional adaptive integral method for scattering from structures embedded in layered media," *IEEE Trans. Geo. Remote Sens.*, vol. 50, no. 4, pp. 1130–1139, Apr. 2012.
- [23] M. Bebendorf and S. Rjasanow, "Adaptive low-rank approximation of collocation matrices," *Computing*, vol. 70, no. 1, pp. 1–24, Mar. 2003.
- [24] K. Zhao, M. N. Vouvakis, and J.-F. Lee, "The adaptive cross approximation algorithm for accelerated method of moments computations of EMC problems," *IEEE Trans. Electromagn. Compat.*, vol. 47, no. 4, pp. 763–773, Nov. 2005.
- [25] Y. Saad and M. H. Schultz, "GMRES: A generalized minimal residual algorithm for solving non-symmetric linear systems," *SIAM J. Sci. Stat. Comput.*, vol. 7, no. 3, pp. 856–869, Jul. 1986.
- [26] H. A. van der Vorst, "Bi-CGSTAB: a fast and smoothly converging variant of Bi-CG for the solution of nonsymmetric linear systems," *SIAM J. Sci. Stat. Comput.*, vol. 13, no. 2, pp. 631–644, 1992.

-
- [27] L. Grasedyck and W. Hackbusch, “Construction and arithmetics of \mathcal{H} -matrices,” *Computing*, vol. 70, no. 4, pp. 295–334, Aug. 2003.
- [28] P. G. Martinsson and V. Rokhlin “A fast direct solver for boundary integral equations in two dimensions,” *J. Comput. Phys.*, vol. 205, no. 1, pp. 1–23, May 2005.
- [29] H. Guo, J. Hu, and E. Michielssen, “On MLMDA/Butterfly compressibility of inverse integral operators,” *IEEE Antennas Wireless Propag. Lett.*, vol. 12, pp. 31–34, 2013.
- [30] J. Shaeffer, “Direct solve of electrically large integral equations for problem sizes to 1 M unknowns,” *IEEE Trans. Antennas Propag.*, vol. 56, no. 8, pp. 2306–2313, Aug. 2008.
- [31] Y. Brick, V. Lomakin, and A. Boag, “Fast direct solver for essentially convex scatterers using multilevel non-uniform grids,” *IEEE Trans. Antennas Propag.*, vol. 62, no. 8, pp. 4314–4324, Aug. 2014.
- [32] F. P. Andriulli, F. Vipiana, and G. Vecchi, “Hierarchical bases for nonhierarchical 3-D triangular meshes,” *IEEE Trans. Antennas Propag.*, vol. 56, no. 8, pp. 2288–2297, Aug. 2008.
- [33] E. Corona, A. Rahimian, and D. Zorin “A Tensor-Train accelerated solver for integral equations in complex geometries, *J. Comput. Phys.*, vol. 334, pp. 145–169, Apr. 2017.
- [34] I. V. Oseledets, “Tensor-Train decomposition, *SIAM J. Sci. Comput.*, vol. 33, no. 5, pp. 2295–2317, 2011.
- [35] R. Gholami, J. Mojolagbe, A. Menshov, F. Sheikh Hosseini Lori, and V. Okhmatovskii, “ \mathcal{H} -matrix arithmetic for fast direct and iterative method of moment solution of surface-volume-surface EFIE for 3-D radiation problems,” *Progress In Electromagnetics Research B*, Vol. 82, pp. 189–210, 2018.

-
- [36] W. Hackbusch, *Hierarchical Matrices: Algorithms and Analysis*, Berlin, Germany: Springer, 2015.
- [37] S. Zheng, R. Gholami, and V. Okhmatovski, "Surface-volume-surface electric field integral equation for solution of scattering problems on 3-D dielectric objects in multilayered media," *IEEE Trans. Microw. Theory Tech.*, vol. 66, no. 12, pp. 5399–5414, Dec. 2018.
- [38] Z. Chen, R. Gholami, J. Mojolagbe, and V. Okhmatovski, "Formulation of surface-volume-surface-EFIE for solution of 3D scattering problems on composite dielectric objects," *IEEE Antennas Wireless Propag. Lett.*, vol. 17, no. 6, pp. 1043–1047, Jun. 2018.
- [39] R. Gholami, A. Menshov, and V. Okhmatovski, " \mathcal{H} -matrix accelerated solution of surface-volume-surface EFIE for fast analysis of scattering on composite dielectric objects," *IEEE J. Multiscale and Multiphys. Comput. Techn.*, vol. 4, no. 1, pp. 152–162, May 2019.
- [40] R. Gholami and V. Okhmatovski, "Surface-volume-surface EFIE formulation for fast direct solution of scattering problem on 3-D composite metal-dielectric Objects," *IEEE Trans. Antennas Propag.*, (under review)
- [41] P. Yla-Oijala, M. Taskinen, and J. Sarvas, "Surface integral equation method for general composite metallic and dielectric structures with junctions," *Prog. Electromagn. Res.*, vol. 52, pp. 81–108, 2005.
- [42] M. Carr, E. Topsakal, and J. L. Volakis, "A procedure for modeling material junctions in 3-D surface integral equation approaches," *IEEE Trans. Antennas Propag.*, vol. 52, no. 5, pp. 1374–1379, May. 2004.
- [43] R. Gholami, S. Zheng, and V. Okhmatovski, "Surface-Volume-Surface EFIE for electromagnetic analysis of 3-D composite dielectric objects in multilayered media," *IEEE J. Multiscale and Multiphys. Comput. Techn.*, (under review)

- [44] M. Shafieipour, “Efficient error-controllable high-order electromagnetic modelling of scattering on electrically large targets with the Locally Corrected Nyström method,” Ph.D. dissertation, Dept. Elect. Comput. Eng., Univ. Manitoba, Winnipeg, MB, Canada, 2016. [Online]. Available: <https://mspace.lib.umanitoba.ca/handle/1993/31181>.
- [45] C. T. Tai, *Dyadic Green Functions in Electromagnetic Theory*, 2nd ed. New York: IEEE Press, 1994.
- [46] D. Swatek, “Investigation of single source surface integral equation for electromagnetic wave scattering by dielectric bodies,” Ph.D. dissertation, Univ. Manitoba, Winnipeg, Canada, 1999. [Online]. Available: <http://hdl.handle.net/1993/1699>.
- [47] J. Kornprobst and T. F. Eibert, “A combined source integral equation with weak form combined source condition,” *IEEE Trans. Antennas Propag.*, vol. 66, no. 14, pp. 2151–2155, Apr. 2018.
- [48] T. Wu, T. S. Rappaport, and C. M. Collins, “The human body and millimeter-wave wireless communication systems: interactions and implications,” in *IEEE Int. Conf. Commun. (ICC)*, Jun. 2015, pp. 2423–2429.
- [49] L. O. Fichte, “Interaction of biological tissue with electromagnetic waves in the RF range,” in *Asia-Pacific Conf. Env. Electromag. (CEEM)*, Nov. 2015, p. 10.
- [50] K. Agarwal and Y. X. Guo, “Interaction of electromagnetic waves with humans in wearable and biomedical implant antennas,” in *Asia-Pacific Symp. on Electromag. Compat. (APEMC)*, May 2015, pp. 154–157.
- [51] V. De Santis, M. Feliziani, and F. Maradei, “Safety assessment of UWB radio systems for body area network by the FD²TD method,” *IEEE Trans. Mag.*, vol. 46, no. 8, pp. 3245–3248, Aug. 2010.
- [52] E. Aguirre, J. Arpón, L. Azpilicueta, S. de Migue, V. Ramos, and F. Falcone, “Evaluation of electromagnetic dosimetry of wireless systems in complex indoor

- scenarios with human body interaction,” *Prog. Electromagn. Res. B*, vol. 43, pp. 189–209, Sep., 2012.
- [53] “*Ansoft HFSS 11.1 User’s Guide*,” ANSYS Inc., Pittsburg, PA, USA, 2009.
- [54] “*XFDTD 7.3 User’s Manual*,” Remcom Inc., State College, PA, USA, 2012.
- [55] J. W. Massey, Chang Liu, Anton Menshov, and Ali E. Yilmaz, “Bioelectromagnetic benchmarks,” 2016. [Online]. Available: <http://bit.ly/BioEM-Benchmarks>
- [56] R. Mittra and C. Li, “The art and science of matrix preconditioning—a review,” in *IEEE Int. Conf. Comput. EM (ICCEM)*, Feb. 2016, pp. 17–19.
- [57] F. Vico, L. Greengard, and M. Ferrando, “Decoupled field integral equations for electromagnetic scattering from homogeneous penetrable obstacles,” *J. Communications in Partial Differential Equations*, vol. 43, no. 2, pp. 159–184, Mar. 2018.
- [58] Q. S. Liu, S. Sun, and W. C. Chew, “An integral equation method based on vector and scalar potential formulations,” in *Proc. USNC-URSI Radio Sci. Meeting*, Jul. 2015, pp. 744–745.
- [59] F. Valdes, F. P. Andriulli, H. Bagci, and E. Michielssen, “On the discretization of single source integral equations for analyzing scattering from homogeneous penetrable objects,” in *IEEE Antennas and Propag. Soc. Int. Symp.*, Jul. 2008, pp. 1–4.
- [60] H. Contopanagos *et al.*, “Well-conditioned boundary integral equations for three-dimensional electromagnetic scattering,” *IEEE Trans. Antennas Propag.*, vol. 50, no. 12, pp. 1824–1930, Dec. 2002.
- [61] K. Cools, F. P. Andriulli, and E. Michielssen, “A Calderon multiplicative preconditioner for the PMCHWT integral equation,” *IEEE Trans. Antennas Propag.*, vol. 59, no. 12, pp. 4579–4587, Dec. 2011.

-
- [62] W. Hackbusch, “A sparse matrix arithmetic based on \mathcal{H} -matrices. Part I. Introduction to \mathcal{H} -matrices,” *Computing*, vol. 62, no. 2, pp. 89–108, 1999.
- [63] J. Mojolagbe, R. Gholami, and V. Okhmatovski, “On complexity reduction in solution of scattering problems on well-conducting 3D objects with Surface-Volume-Surface EFIE,” in *Appl. Comput. Electromag. Conf. (ACES)*, May 2018, pp. 1–2.
- [64] Z. G. Qian, W. C. Chew, and R. Suaya, “Generalized impedance boundary condition for conductor modeling in surface integral equation,” *IEEE Trans. Microw. Theory Techn.*, vol. 55, no. 11, pp. 2354–2364, Nov. 2007.
- [65] C. Müller, *Foundations of the Mathematical Theory of Electromagnetic Waves*, Berlin, Heidelberg, New York: Springer-Verlag, 1969.
- [66] A. Kishk and L. Shafai, “Different formulations for numerical solution of single or multibodies of revolution with mixed boundary conditions,” *IEEE Trans. Antennas Propag.*, vol. 34, no. 5, pp. 666–673, May 1986.
- [67] S. M. Rao, D. R. Wilton, and A. W. Glisson, “Electromagnetic scattering by surfaces of arbitrary shape,” *IEEE Trans. Antennas Propag.*, vol. 30, no. 3, pp. 409–418, May 1982.
- [68] P.-G. Martinsson, V. Rokhlin, and M. Tygert, “A randomized algorithm for the decomposition of matrices,” *Appl. Comput. Harmon. Anal.*, vol. 30, no. 1, pp. 47–68, Jan. 2011.
- [69] Y. Brick and A. Yilmaz, “Fast multilevel computation of low-rank representation of \mathcal{H} -matrix blocks,” *IEEE Trans. Antennas Propag.*, vol. 64, no. 12, pp. 5326–5334, Dec. 2016.
- [70] S. Börm, L. Grasedyck, and W. Hackbusch, *Hierarchical Matrices*, Technical Report 21, Max Planck Institute for Mathematics in the Sciences, 2006.
- [71] W. C. Chew, *Waves and Fields in Inhomogeneous Media*, Wiley-IEEE Press, 1999.

-
- [72] “*FEKO User’s Manual*,” EM Software & Syst. Inc., Stellenbosch 7600, South Africa, 2014.
- [73] A. C. Woo, H. T. G. Wang, and M. J. Schuh, “Benchmark radar targets for the validation of computational electromagnetics programs,” *IEEE Antennas Propag. Mag.*, vol. 35, no. 1, pp. 84–89, Feb. 1993.
- [74] *IEEE Recommended Practice for Determining the Peak Spatial-Average Specific Absorption Rate (SAR) in the Human Head from Wireless Communications Devices: Measurement Techniques*, IEEE Std 1528-2013 (Rev. IEEE Std 1528-2003), Sep. 2013.
- [75] L. J. Gomez, A. C. Yucel, and E. Michielssen, “The ICVSIE: a general purpose integral equation method for bio-electromagnetic analysis,” *IEEE Trans. Biomed. Eng.*, vol. 65, no. 3, pp. 565–574, Mar. 2018.
- [76] O. Bottauscio, M. Chiampì, and L. Zilberti, “A hybrid FE–BE method for SAR estimate in voxel based human models undergoing MRI,” *Eng. Anal. Bound. Elem.*, vol. 49, pp. 15–21, Dec. 2014.
- [77] R. Mitharwal and F. P. Andriulli, “A regularised boundary element formulation for contactless SAR evaluations within homogeneous and inhomogeneous head phantoms,” *Comptes Rendus Physique*, vol. 16, no. 9, pp. 776–788, Nov. 2015.
- [78] G. H. Golub and C. F. Van Loan, *Matrix Computation*, 3rd ed. Baltimore, MD, USA: The Johns Hopkins Univ. Press, 1996.
- [79] J. S. Zhao and W. C. Chew, “Integral equation solution of Maxwell’s equations from zero frequency to microwave frequencies,” *IEEE Trans. Antennas Propag.*, vol. 48, no. 10, pp. 1635–1645, Oct. 2000.
- [80] S. Y. Chen, W. C. Chew, J. M. Song, and J. S. Zhao “Analysis of low-frequency scattering from penetrable scatterers,” *IEEE Trans. Geosci. Remote Sensing*, vol. 39, no. 4, pp. 726–735, Apr. 2001.

-
- [81] P. Yla-Oijala, M. Taskinen, and S. Jarvenpaa, "Analysis of surface integral equations in electromagnetic scattering and radiation problems," *Eng. Anal. Boundary Elements*, vol. 32, pp. 196–209, 2008.
- [82] K. A. Michalski and D. Zheng, "Electromagnetic scattering and radiation by surfaces of arbitrary shape in layered media. Part I: Theory," *IEEE Trans. Antennas Propag.*, vol. 38, no. 3, pp. 335–344, Mar. 1990.
- [83] P. Kristensen, J. Mork, P. Lodahl, and S. Hughes, "Decay dynamics of radiatively coupled quantum dots in photonic crystal slabs", *Phys. Rev. B*, vol. 83, no. 7, pp. pp. 075305-1–075305-10, Feb. 2011.
- [84] V. Okhmatovski, M. Yuan, I. Jeffrey, and R. Phelps, "A three-dimensional precorrected FFT algorithm for fast method of moments solutions of the mixed-potential integral equation in layered media," *IEEE Trans. Microw. Theory Tech.*, vol. 57, no. 12, pp. 3505–3517, Dec. 2009.
- [85] Y. Baba and V. Rakov, "Electromagnetic models of the lightning return stroke," *J. Geophys. Res.*, vol. 112, pp. 1–17, Feb. 2007.
- [86] N. Firoozy, *et al.*, "A controlled experiment on oil release beneath thin sea ice and Its electromagnetic detection," *IEEE Trans. Geosci. Remote Sens.*, vol. 56, no. 8, pp. 4406–4419, Aug. 2018.
- [87] N. A. Khizhnyak, "Green's function of Maxwell equations in inhomogeneous media," (*in Russian*), *J. Tech. Phys.*, vol. 28, no. 7, pp. 1592–1609, 1958.
- [88] P. Yla-Oijala and M. Taskinen, "Well-conditioned Muller formulation for electromagnetic scattering by dielectric objects," *IEEE Trans. Antennas Propag.*, vol. 53, pp. 3316–3323, Oct. 2005.
- [89] Y. P. Chen, L. Jiang, S. Sun, W. C. Chew, and J. Hu, "Calderon preconditioned PMCHWT equations for analyzing penetrable objects in layered medium," *IEEE Trans. Antennas Propag.*, vol. 62, no. 11, pp. 5619–5627, Nov. 2014.

-
- [90] A. Colliander and P. Yla-Oijala, “Electromagnetic scattering from rough surface using single integral equation and adaptive integral method,” *IEEE Trans. Antennas Propag.*, vol. 55, no. 12, pp. 3639–3646, Dec. 2007.
- [91] H. L. Sun and C. M. Tong, “Analysis of scattering from composite conductor and dielectric objects using single integral equation method and FG-FFT,” *J. Electromagn. Waves Appl.*, vol. 31, no. 2, pp. 225–240, Jan. 2017.
- [92] Y. L. Chow, J. J. Yang, D. G. Fang, and G. E. Howard, “A closed-form spatial Green’s function for the thick microstrip substrate,” *IEEE Trans. Microw. Theory Tech.*, vol. 39, pp. 588–592, Mar 1991.
- [93] M. I. Aksun, “A robust approach for the derivation of closed-form Green’s functions,” *IEEE Trans. Microw. Theory Tech.*, vol. 44, no. 5, pp. 651–658, May 1996.
- [94] R. Gholami, S. Zheng, and V. Okhmatovski, “ \mathcal{H} -Matrix accelerated MoM solution of surface-volume-surface electric field integral equation for scattering problems on homogenous dielectric objects in multilayered medium,” *2019 IEEE MTT-S Intl. Conf. Num. Electromagn. Multiphys. Mod. Optimization*.
- [95] K. Butt, I. Jeffrey, F. Ling, and V. Okhmatovski, “Parallel discrete complex image method for Barnes-Hut accelerated capacitance extraction in multilayered substrates,” in *IEEE Top. Meet. Electr. Perform. Electron. Packaging*, Oct. 2007, pp. 333–336.
- [96] M. Abramovitz and I. Stegun, *Handbook of Mathematical Functions*, 7th ed. New York: Dover, 1970.
- [97] S. Cadirci, “RF Stealth (or Low Observable) and Counter? RF Stealth Technologies: Implications of Counter-RF Stealth Solutions for Turkish Air Force,” MSc Thesis, Naval Postgraduate School, Monterey, CA, 2009.

-
- [98] D. Weston, "Comparison of Techniques for Prediction and Measurement of Antenna to Antenna Coupling on an Aircraft," in *Int. Symp. Electromagn. Compatibility (EMC)*, York, UK, Sept. 2011, pp. 228–233.
- [99] C. E. Lim, "Computational electromagnetic modeling for wireless channel characterization," Ph.D. dissertation, The Ohio State University, Columbus, OH, 2006.
- [100] K. Butt, I. Jeffrey, M. Al-Qedra, F. Ling, and V. Okhmatovski, "Accurate capacitance extraction in the entire package model using a parallel kernel independent hierarchical extractor," in *Proc. IEEE Workshop Signal Propag. Interconnects (SPI)*, Ruta Di Camogli (Genova), Italy, May 13–16, 2007, pp. 149–152.
- [101] J. A. Stratton, *Electromagnetic Theory*, Piscataway, NJ, USA: IEEE Press, 2007.
- [102] L. Canino, *et al.*, "Numerical solution of the Helmholtz equation in 2D and 3D using a high-order Nystrom discretization," *J. Comput. Phys.*, vol. 146, no. 2, pp. 627–663, Nov. 1998.
- [103] S. D. Gedney, "On deriving a locally corrected Nyström scheme from a quadrature sampled moment method," *IEEE Trans. Antennas Propag.*, vol. 51, no. 9, pp. 2402–2412, Sep. 2003.
- [104] I. Jeffrey, J. Aronsson, M. Shafieipour, and V. Okhmatovski, "Error controllable solutions of large scale problems in electromagnetics: MLFMA accelerated Locally Corrected Nyström solutions of CFIE in 3D," *IEEE Antennas Propag. Mag.*, vol. 55, no. 3, pp. 294–308, June. 2013.